HEAT TRANSFER AND FLUID FLOW OF NANOFLUIDS IN ENCLOSURES WITH ENTROPY GENERATION AND INNER SOLID

MUHAMAD SAFWAN BIN ISHAK

UNIVERSITI KEBANGSAAN MALAYSIA

HEAT TRANSFER AND FLUID FLOW OF NANOFLUIDS IN ENCLOSURES WITH ENTROPY GENERATION AND INNER SOLID

MUHAMAD SAFWAN BIN ISHAK

THESIS SUBMITTED IN FULFILMENT FOR THE DEGREE OF DOCTOR OF PHILOSOPHY

FACULTY OF SCIENCE AND TECHNOLOGY
UNIVERSITI KEBANGSAAN MALAYSIA
BANGI

2025

PEMINDAHAN HABA DAN ALIRAN BENDALIR DALAM RONGGA DENGAN NANOCECAIR PENJANA ENTROPI DAN PEPEJAL DALAMAN

MUHAMAD SAFWAN BIN ISHAK

TESIS YANG DIKEMUKAKAN UNTUK MEMPEROLEH IJAZAH
DOKTOR FALSAFAH

FAKULTI SAINS DAN TEKNOLOGI
UNIVERSITI KEBANGSAAN MALAYSIA
BANGI

2025

DECLARATION

I hereby declare that the work in this thesis is my own except for quotations and summaries which have been duly acknowledged.

7 March 2025

MUHAMAD SAFWAN BIN ISHAK
P90284

007733

PERAKUAN TESIS SARJANA / DOKTOR FALSAFAH
(DECLARATION OF MASTER / DOCTOR OF PHILOSOPHY THESIS)

A. MAKLUMAT PELAJAR/*STUDENT DETAILS*

B. PERAKUAN / *DECLARATION*

the thesis is the property of UKM as described below

Sila tandakan (✓) pada salah satu pilihan berikut / *Please tick (✓) one of the following options*

RAHSIA *CONFIDENTIAL*	Mengandungi maklumat rahsia di bawah AKTA RAHSIA RASMI 1972 *Consisting of classified information under the OFFICIAL SECRETS ACT 1972*
TERHAD *RESTRICTED*	Mengandungi maklumat TERHAD yang telah ditentukan oleh organisasi / badan di mana penyelidikan dijalankan *Consisting of RESTRICTED information which has been determined by the organisation/body where the research was conducted*
AKSES TERBUKA/ TIDAK TERHAD *OPEN ACCESS/ NON-RESTRICTED*	Saya membenarkan tesis ini diterbitkan secara akses terbuka, teks penuh atau dibuat salinan untuk tujuan pengajian, pembelajaran & penyelidikan sahaja *I give permission for this thesis to be published through open access, full text or copied only for study, learning, and research purposes*

Saya mengakui maklumat & hasil yang dikemukakan adalah benar & terkini

I acknowledge the information & the thesis provided are correct & current

Tandatangan Pelajar
Student's Signature

Tarikh / Date 5/3/2025

PROF DR ISHAK BIN HASHIM
JABATAN SAINS MATEMATIK
FAKULTI SAINS & TEKNOLOGI
UNIVERSITI KEBANGSAAN MALAYSIA

10/3/25

C. PENGESAHAN FAKULTI/INSTITUT | *VERIFICATION OF FACULTY/INSTITUTE*

Tandatangan/Signature
Nama/Name PROF MADYA DR ABDUL GHANI ABU MERAD
Tarikh/Date 10/3/2025
Cop Rasmi/Official Stamp

**Kuatkuasa 15 Julai 2021

ACKNOWLEDGEMENTS

In the name of Allah, Most Gracious, Most Merciful. Praise be to Allah who gave me strength, inspiration and prudence to bring this thesis to a close. Peace be upon His messenger Muhammad and his honorable family.

First and foremost, I would like to express my deepest appreciation to my supervisor, Prof. Dr. Ishak Hashim, for his immense wisdom, patience and constructive comments throughout my journey of study and writing. His careful guidance and critical views at times have made my research work improve tremendously. Also, special thanks to my co-supervisor Dr. Ammar Alsabery (The Islamic University, Iraq) and Dr. Mohd Almie bin Alias. Their knowledge imparted and kind assistance is greatly appreciated and acknowledged. I would also like to show my gratitude and greatest appreciation to Dr. Habibis Saleh for his guidance, generous contribution of knowledge and experience.

For all those who stood beside me and cooperated with me during my study, all the staff at the Faculty of Science and Technology, Universiti Kebangsaan Malaysia, especially the staff at the School of Mathematical Sciences and I gratefully acknowledge the financial support received from the grants.

I would like to thank both of my dearest parent Ishak bin Md Noor and Kelthum binti Abu, whom without they prayer and vision I never will embark nor finish the journey. To all my four sibling Khairunnisa binti Ishak, Muhamad Arshad bin Ishak, Nurul Hidayah binti Ishak and Muhamad Ariffuddin bin Ishak who always motivate, challenge and support me in every way possible.

I also like to express my highest appreciation to all my fellow colleague, Pn Nur Aimi Syaqilah binti Aziz, Dr. Husni binti Mohd Radzi and Mohd Fadlihisyam bin Ishak, who has always being ready to step up on my behalf when I am unable to fill in the task due to my commitment in chasing my dream. To my Dean of College of Engineering (COE), UNITEN, my utmost appreciation for giving me the permission to do my doctoral degree. To my course mates for always inspiring and assisting me till the end, Dr. Fatin Munirah binti Azizul and Dr. Nur Asiah binti Mohd Makhatar.

Last but not least to all my student, friends, and lecturers I would like to express my thankfulness to all the cooperation, assistance and support that they have given me.

ABSTRAK

Memahami ciri-ciri pemindahan haba dan aliran bendalir adalah penting dalam banyak aplikasi kejuruteraan, termasuk mereka-bentuk penukar haba yang cekap, pengurusan haba dalam peranti elektronik, dan pengoptimuman dinamik bendalir dalam aerodinamik dan hidrodinamik. Pelbagai model matematik dan teknik pengkomputasian seperti dinamik bendalir pengkomputasian (CFD), digunakan untuk menganalisis dan meramalkan tingkah laku pemindahan haba dan aliran bendalir dalam sistem yang kompleks. Dengan menganalisis aliran bendalir dan fenomena pemindahan haba, CFD membolehkan jurutera dan saintis untuk mereka-bentuk sistem tenaga yang mengoptimumkan kadar pemindahan haba. Tesis ini memberi tumpuan kepada penyelidikan prestasi pemindahan haba dan penjanaan entropi menggunakan gabungan antara olakan semula jadi dan campuran dalam pelbagai jenis rongga. Keadaan aliran yang dipertimbangkan adalah laminar, Newtonan, dan dua dimensi, sementara nanobendalir digunakan sebagai bendalir kerja. Untuk memodelkan masalah secara matematik, persamaan sempadan dan kawalan adalah dinormalisasikan, menghasilkan set persamaan pembeza separa tak linear. Persamaan model berangka diterima menggunakan kaedah beza terhingga dan elemen, yang dilaksanakan dalam perisian COMSOL Multiphysics. Untuk mengesahkan penyelesaian berkomputasi, hasilnya dibandingkan dengan kajian terdahulu. Dapatan tesis ini dikemukakan secara grafik melalui visualisasi seperti garisan arus, isoterma, plot isentropik, taburan nombor Nusselt tempatan, nombor Nusselt purata, penghasilan entropi global, dan nombor Bejan. Kes pertama memberi tumpuan kepada suatu rongga segi empat dengan masukkan pepejal yang diletakkan di tengah rongga, manakala sumber haba terletak di sepanjang dinding bawah manakala sebahagian dinding atas dan samping disejukkan. Keputusan menunjukkan bahawa dengan memasukkan pepejal yang lebih besar dan kekonduksian haba yang lebih rendah merencatkan pemindahan haba konvektif dalam rongga segi empat.Kemudian, kajian pemindahan haba di dalam satu rongga segi empat di mana dinding bawah dipanaskan manakala dinding di kedua dua belah disejukkan dengan menggunakan nanobendalir dipertimbangkan. Keputusan menunjukkan bahawa pemindahan haba konvektif meningkat dengan peningkatan panjang sumber haba pada dinding bawah dan dinding antara dalam kaviti segi empat. Seterusnya, sebuah rongga yang berbentuk trapezoid dengan silinder pepejal yang diletakkan di tengah rongga dengan menggunakan nanobendalir turut dikaji. Dinding atas bergerak dengan kelajuan seragam sambil dikekalkan pada suhu sejuk, dan dinding bawah dipanaskan. Hasil yang diperoleh menunjukkan peningkatan prestasi pemindahan haba apabila silinder pepejal diletakkan di tengah rongga. Akhirnya, sebuah rongga yang berbentuk segitiga dengan tiga silinder pepejal yang berputar diletakkan di dalam rongga dianalisis. Dinding bawah dipanaskan, sementara dinding sisi dikekalkan pada suhu sejuk. Hasil menunjukkan bahawa kehadiran silinder pepejal dalam rongga meningkatkan penjana entropi dan meningkatkan analisis pemindahan haba.

ABSTRACT

Understanding the heat transfer and fluid flow characteristics is crucial in many engineering applications, including designing efficient heat exchangers, thermal management in electronic devices, and optimizing fluid dynamics in aerodynamics and hydrodynamics. Various mathematical models and computational techniques, such as computational fluid dynamics (CFD), are used to analyze and predict heat transfer and fluid flow behavior in complex systems. By analyzing fluid flow and heat transfer phenomena, CFD enables engineers and scientists to design energy systems that optimize heat transfer rates. This thesis focuses on investigating heat transfer performance and entropy generation using both natural and mixed convection within different types of enclosures. The flow conditions considered are laminar, Newtonian, and two-dimensional, while nanofluid is employed as the working fluid. To mathematically model the problem, the boundary and governing equations are nondimensionalized, resulting in a set of nonlinear partial differential equations (PDEs). The numerical model equations are solved using the finite difference and element method, which is implemented in COMSOL Multiphysics software. To validate the computational solutions, the results are compared with previous studies. The findings of this thesis are presented graphically through visualizations such as streamlines, isotherms, isentropic plots, local Nusselt number distributions, average Nusselt numbers, global entropy generation, and Bejan numbers. The first case focuses on a square cavity with a solid insert placed on the center of the enclosure, while isothermal heat sources are located along the bottom wall and partially cold at the top and side walls. The results indicate that a larger solid insert and lower thermal conductivity hinder convective heat transfer within the square cavity. Next, a partially heated cavity with a nanofluid and a solid bottom wall is considered. The results show that convective heat transfer is enhanced with an increase in the heat source length on the bottom wall and the interface walls within the square cavity. Moving on, a trapezoidal enclosure with a localized solid cylinder positioned at the center of the cavity is studied. The top horizontal surface of the enclosure moves at a uniform velocity while being maintained at a cold temperature, and the bottom horizontal wall is thermally activated. The obtained results demonstrate an improvement in heat transfer performance when the solid cylinder is placed at the cavity's center. Lastly, a triangular enclosure with three inner rotating solid cylinders is analyzed. The bottom wall of the enclosure is heated, while the side walls are maintained at a cold temperature. The results reveal that the presence of rotating solid cylinders in the cavity enhances entropy generation and improves the heat transfer analysis.

TABLE OF CONTENTS

LIST OF FIGURES

LIST OF TABLES

LIST OF SYMBOLS

A	amplitude
C_p	specific heat capacity
D	aspect ratio of inner square cylinder width to outer square cylinder width
g	gravitational acceleration
h	interphase heat transfer coefficient
k	thermal conductivity
K_r	thermal conductivity ratio
L	width and height of enclosure
n	power-law index
Nu	Nusselt number
$\overline{Nu}$	average Nusselt number
p	pressure
Pr	Prandtl number
Be	Bejan number
Ra	Rayleigh number
Re	Reynold number
Ri	Richardson number
q	internal heat source
S	dimensionless solid wall thickness, dimensionless porous layer thickness
t	time
T	temperature
t	Time
u, v	dimensional velocity components in the x- and y-directions, respectively
U, V	dimensionless velocity components in the X- and

	Y-directions, respectively
$\mathbf{V}$	velocity vector
x, y	dimensional space coordinates
X, Y	dimensionless space coordinates
S_{GEN}	local entropy generation
GEG	global entropy generation

Greek symbols

α	thermal diffusivity
β	thermal expansion coefficient
γ	phase deviation
Γ	thermal diffusivity ratio
ϵ	the consistency coefficient
ε	dimensionless amplitude
Υ	modified conductivity ratio
μ	dynamic viscosity
ν	kinematic viscosity
ϕ	volume fraction of nanoparticles
φ	porosity of the porous medium
ψ	stream function
Ψ	dimensionless stream function
τ	dimensionless time
θ	dimensional temperature
λ_r	relaxation parameter
ξ	dimensionless scaled variable ($\xi = X - Y\tan(\omega)$)
ρ	density
Ω	dimensionless vorticity
ω	vorticity

Subscripts/superscripts

b	bottom
bf	base fluid
c	cold
f	fluid
h	hot
i	interface between the solid wall and the nanofluid
l	left
max	maximum
min	minimum
r	right
nf	nanofluid
sp	solid nanoparticle
t	top
w	wall

LIST OF ABBREVIATIONS

ADI	alternating direct implicit
CFD	computational fluids dynamics
CHT	conjugate heat transfer
Eq./Eqs.	equation/equations
et al.	(et alii): and others, and coworkers
i.e.	(id est): that is, in other words
Fig./Figs.	figure/figures
FDE	finite difference equation
FDM	finite difference method
FEM	finite element method
PDE	partial differential equation
SOR	successive over-relaxation
LTNE	local thermal non-equilibrium
TDMA	tridiagonal matrix algorithm, Thomas algorithm
NFI	nanofluid irreversibility
HTI	heat transfer irreversibility

CHAPTER I

INTRODUCTION

1.1 GENERAL INTRODUCTION

Natural convection, forced and combined convection heat transfer, and fluid momentum have been regarded as one of the most important research topics due to the wide range of applications, including lubrication systems, polymer processing, chemical processing equipment, hydro-dynamical machines, building ventilation, and electronic equipment. Furthermore, because of its numerous applications in industry, such as cooling electronic devices, food storage, and lubrication technologies, numerous studies have concentrated on mixed convection heat transfer in cavities in recent years. Despite its wide range of uses, convective heat transfer is known for its low efficiency, which is mostly due to the convective fluid's low thermal conductivity. Many numerical and experimental investigations have been conducted to improve the fluid's heat transfer characteristics, including the use of extended surfaces such as fins and microfins, swirl flow devices, jet impingement, electromagnetic field, ultra-high thermal conductivity composite materials, and phase-change devices. Furthermore, there are a number of ways to improve heat transfer efficiency.

1.2 FLUID DYNAMICS

Fluid mechanics is the branch of physics concerned with the mechanics of fluids and the forces on them. Fluid can be divided into two parts, which it is liquid and gas. Fluid mechanics helps us understand the behavior of fluid under various forces and at different atmospheric conditions, and to select the proper fluid for various applications. Fluid

mechanics has been divided into two parts. The first part is the fluid at rest which is called as fluid statics while the study of the effect of forces on fluid motion called as fluid dynamics.

Fluid dynamics is very important in industrial applications such as rocket engines, wind turbines, oil pipelines, and air conditioning systems. Fluid dynamics helps us understand in the movement of liquids and gases. It has several subdisciplines, including aerodynamics and hydrodynamics. A fluid dynamics problem is often solved by calculating various fluid characteristics as functions of space and time, such as flow velocity, pressure, density, and temperature.

The conservation rules, specifically conservation of mass, conservation of linear momentum, and conservation of energy, are the basic principles of fluid dynamics. These are based on classical mechanical and modified in quantum mechanics and general relativity. Furthermore, fluids are considered to follow the continuum assumption.

1.3 NANOFLUIDS

A nanofluid is a fluid in which nanometer-sized particles, suspended in the base fluid, form a colloidal solution of nanoparticles in a base fluid. The idea of nanofluid was first proposed by Choi and Eastman (1995) after performing experimental studies of various nanoparticle suspensions. The nanoparticles used in nanofluids are typically made of metals, oxides, carbides, or carbon nanotubes while the base fluids include water, ethylene glycol and oil.

Nanofluids can be considered as the future of heat transfer fluids in various heat transfer applications. They are expected to give better thermal performance than conventional fluids due to the presence of suspended nanoparticles which have high thermal conductivity.

Nanofluids are engineered suspensions of nanometer sized solid nanopaticles in a base fluid. Suspending small solid particles in the energy transmission fluids can improve their thermal conductivity and provides an effective and innovative way to enhance their

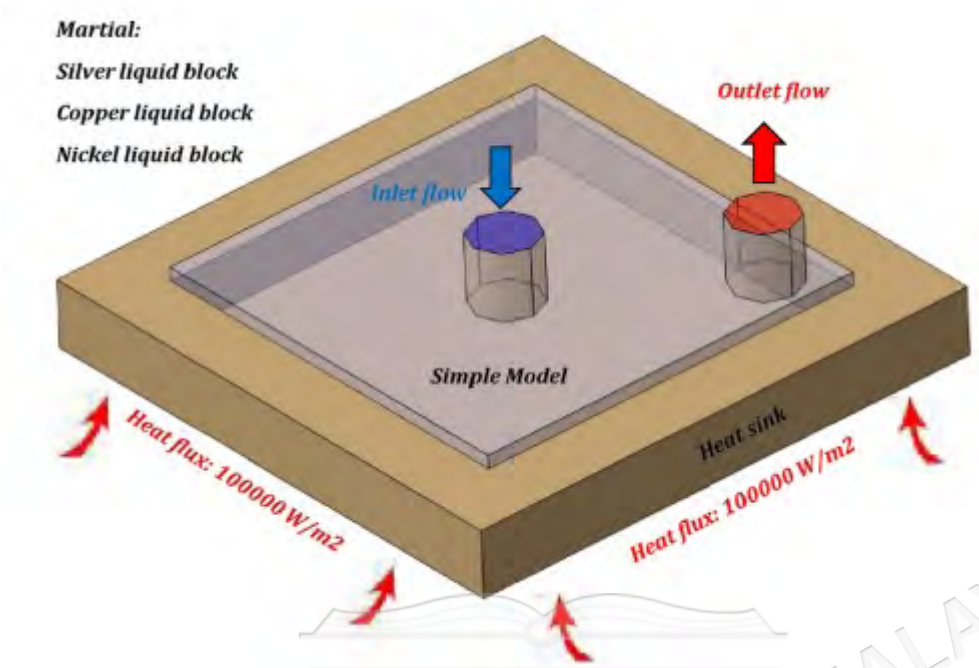

Figure 1.1 Application of electronic cooling devices having fin heat passing cooling technique.
Adapted from Siahchehrehghadikolaei et al. 2022

heat transfer characteristic significantly. Nanofluids can be applied to various industrial and engineering problems such as heat exchanging, cooling of electronic equipment, and chemical processes. Due to their increasing application in recent years, several researchers performed experimental and numerical studies to investigate the application of nanofluids to control heat transfer in a process. Figure 1.1 shows an application involves 3D heat nanofluid and novel design fin heat sinks passive cooling techniques on the thermal management of a CPU with an application in electronics cooling.

1.4 CONVECTION HEAT TRANSFER

Heat convection is a method of heat transmission in which heat is transferred through the mass motion of a fluid such as air. When the surrounding fluid of an item is heated, heat convection occurs, and energy is transported away from the source of heat. When the surface temperature of a fluid differs from that of the surrounding fluid, convective heat transfer occurs.

Heat is the transfer of energy from one body to another body when there are changes of temperatures between the objects. The generation, utilisation, conversion, and exchange of thermal energy across physical systems is the focus of heat transfer. There are 3 mechanisms in heat transfer, which is conduction, convection, and radiation.

Natural or free convection and forced convection are the two most common types of convective heat transfer. In natural convection, gravity is the driving force behind fluid motion, which is created by the buoyancy force caused by a change in density caused by a temperature difference in the fluid. The centrifugal force, which exists when there is an overall rotary motion, such as that which occurs in a spinning machine, is another cause of natural convection. The fluid motion in forced convection is induced by an external force such as a fan or a pump. Forced convection includes air conditioning, central heating, and fluid radiators in automobiles. When both free and forced convection occur at the same time, this is referred to as mixed convection. One example of mixed convection is the cooling reactor system. Both natural and mixed convection is applied in all problems in this thesis.

1.5 ENTROPY GENERATION

Entropy production is the amount of entropy which is produced in any irreversible processes such as heat and mass transfer processes including motion of bodies, heat exchange, fluid flow, substances expanding or mixing, anelastic deformation of solids, and any irreversible thermodynamic cycle, including thermal machines such as power plants, heat engines, refrigerators, heat pumps, and air conditioners.

The importance of avoiding irreversible processes was recognized by Carnot as early as 1824. He postulated that any machine with moving parts characterized by a "loss of moment" activity due to friction and "violet effects" (which in modern terms would include both a mechanical cause of inefficiency, namely the effects of vibrates, and a thermodynamic cause due to extreme non-equilibrium phenomena). In 1865, Rudolf Clausius expanded his previous work from 1854 on the concept of "unkompensirte Verwandlungen" (uncompensated transformations), which in our modern nomenclature,

would be called the entropy production. In the same article in which he introduced the name entropy, Clausius gives the expression for the entropy production (for a closed system) which he denotes by N, in which equation

$$N = S - S_0 - \int \frac{dQ}{T}. \tag{1.1}$$

where S is the entropy in the final state, S_0, is the entropy in the initial state, and Q is the heat flow rate.

Heat transfer processes are generally accompanied by thermodynamic irreversibility of entropy generation. The generation of entropy may be due to a variety sources, primarily heat transfer down temperature gradients and characteristic of convective heat transfer, viscous effects. With a better understanding of how entropy is being generated in heat transfer processes and engineering components for heat exchange it is possible to reduce the process irreversibility, thus registering saving in useful power. With this objective in mind, Bejan (2013) showed how the entropy generation rate can systemically be reduced in simple components.

1.6 NONDIMENSIONAL NUMBERS IN FLUIDS DYNAMICS AND HEAT TRANSFER

As is common with fluid dynamics and heat transfer analysis, a number of dimensionless parameters are employed to describe fluid flow and convective heat transfer. A summary of these parameters is included in the following lists (Bejan 2013):

1. Reynolds number

   The Reynolds number is the ratio of inertial forces to viscous forces. The Reynolds number is a dimensionless number used to categorize the fluid systems in which the effect of viscosity is important in controlling the velocities of the flow pattern of a fluid. The Reynolds number is used to determine whether a fluid is in laminar or turbulent flow.

2. Rayleigh number

   Rayleigh number is the ratio of the fluid buoyancy stress to the viscous stress

and it is related to the natural convection. When the value of Rayleigh number is lower than the critical value of the fluid, the heat transfer is mostly in the compose of the conduction, while the heat transfer is mostly in the compose of the convection when the value of Rayleigh number is higher than the critical value of the fluid.

3. Richardson number

   The Richardson number is the dimensionless number that expresses the ratio of the buoyancy term to the flow shear term. The Richardson number represents the importance of natural convection relative to the forced convection. It can be expressed by using a combination of the Grashof number and Reynolds number. Typically, the natural convection is negligible when $Ri < 0.1$, forced convection is negligible when $Ri > 10$, and neither is negligible when $0.1 < Ri < 10$. It may be noted that usually the forced convection is large relative to natural convection except in the case of extremely low forced flow velocities. However, buoyancy often plays a significant role in defining the laminar-turbulent transition of a mixed convection flow.

4. Nusselt number

   Nusselt number is the ratio of the heat that is transferred from the surface to the heat that is conducted away by the fluid. When Nusselt number equals one, it means conduction heat transfer is dominated. Whereas convection heat transfer is dominated when the values of Nusselt number is greater than one.

5. Bejan number

   Bejan number is a dimensionless number demonstrates the fraction of thermal entropy generation to the total entropy generation (thermal and frictional). The Bejan number has no effect on heat transfer but rather is a description of the entropy generated by heat transfer and fluid friction. For one thermal system, when Bejan values are close to one, it is indicates that thermal entropy generation is predominant on the total entropy generation compared with frictional entropy generation.

1.7 RESEARCH OBJECTIVES AND SCOPES

This thesis is motivated on the following objectives:

1. To develop mathematical models of fluid flow and heat transfer and a numerical solution in an enclosure with an inner cavity.
2. To perform a parametric study on fluid flow and heat transfer in an enclosure with an inner cavity.
3. To investigate the entropy generation in different type of enclosure with different shape of inner cavity.
4. To investigate the fluid flow and heat transfer with entropy generation with rotating inner solid.

Then, we solved numerical algorithms by using COMSOL Multiphysics for the following problems. The algorithms in this thesis will be developed to solve the convective heat transfer for both natural and mixed convection in various type of enclosure and inner solid. The research specifically focused on mixed and natural convection, two dimensional, Newtonian fluid, steady state and using Aluminium Oxide, Al_2O_3.

1.8 PROBLEM STATEMENT

Understanding convection and entropy generation is critical for energy efficiency and reliability in industrial applications such as gadgets, the environment, and structure. However, practical challenges limit its feasibility. Nanofluids, while enhancing thermal performance, face issues like stability, fouling, and corrosion. Designing and positioning heaters and rotating components require precise modeling for uniform heat transfer and efficiency, but real-world constraints such as material degradation, manufacturing limitation, and energy consumption pose significant challenges. Balancing natural and forced convection is essential but difficult electronic cooling and chemical processing. Furthermore, scaling experimental findings to industrial systems is challenging due to differences in size, materials, and operating conditions. Therefore, to answer this question, the effects of nanoparticle volume fraction, thermal conductivity ratio, length

and position of thermal heater, size, position and velocity of rotating inner solid, Rayleigh number, Reynolds number, Richardson number, and Grashof number are studied in this thesis.

1.9 RESEARCH MOTIVATION

Many experimental and theoretical studies has been studied involved the convective heat transfer and entropy generation in various type of enclosures. The research is very important in many industries and applications. However, natural convection and entropy generation in a square enclosure with a concentric solid insert have received attention over the decades. There are several research which considered the natural convection with entropy generation in partially heated square cavity with an isothermal heater is located on the bottom solid wall and partly cold sidewalls. Nevertheless, the research is extended to mixed convection and entropy generation with trapezoidal enclosure with inner solid cylinder. There is no study in mixed convection with entropy generation with more than one rotating inner solid cylinder (three) in triangular enclosure.

1.10 THESIS ORGANIZATION

This thesis is organized as follows:

Chapter 2 basically reviews on some work earlier for the studies of natural and mixed convection for all problems in this thesis. The discussion included the natural convection and mixed convection with various types of enclosure and various shape of inner solid. The entropy generation in enclosure with nanofluid are also highlighted. The chapter also presents the mathematical model of the convective heat transfer.

Chapter 3 is aimed to present the solution of mathematical model that discussed in Chapter 2 numerically by the finite difference method. The discussion include the governing equation of the natural and mixed convection in enclosure. This chapter also presents the solution methods for model problems using finite element method.

Chapter 4, 5, 6, and 7 cover the topics convective heat transfer in different enclosure with different inner solid and differentially heated enclosure. This thesis applied nanoparticle volume fraction, thermal conductivity ratio, length and position of thermal heater, size, position and velocity of rotating inner solid, Rayleigh number, Reynolds number, Richardson number, and Grashof number as parametric studies. The reason to use the parametric study to find the optimal heat transfer performance.

Chapter 8 draws the conclusion of this thesis. Contributions are highlighted and further works are suggested.

CHAPTER II

LITERATURE REVIEW

2.1 INTRODUCTION

Extensive and intensive analytical or numerical investigations have been carried out to study flow patterns and heat transfer characteristics of fluids dynamics and heat transfer problems. This chapter consists of two sections. The first section gives literature review on natural convection in enclosures. The second section is concerned with the basic mathematical formulations for model problems.

2.2 NATURAL CONVECTION IN RECTANGULAR ENCLOSURES

The analysis of fluid flow and heat transfer within cavities has become a prominent area of research due to its relevance in heat storage applications. Consequently, there has been a significant increase in research activities focused on convective heat transfer. The fluid motion is not generated by any external source called natural convection flow. Such mechanism is easily identified in various engineering applications such as electronic cooling, cooling of containment buildings, room ventilation, heat exchangers, storage tanks, double pane windows, solar collectors, and so on. Khanafer et al. (2003) has investigated natural convection within rectangular cavities filled with nanofluids. Utilizing the finite volume method, the study examined the impact of metallic nanoparticles on flow behavior and analyzed the heat transfer distribution, highlighting the enhancement of thermal conductivity. It was found that the suspended nanoparticles strong enhancement was produced on the heat transfer rate for all values of the Grashof number.

Similar findings were also found by Jou and Tzeng (2006) who carried out a numerical study of natural convection heat transfers in nanofluids occupying a rectangular cavity using the finite-difference approach also discovered similar findings. Santra et al. (2008) conducted a study on natural convection heat transfer in a differentially heated square cavity utilizing a copper-water nanofluid, considering the Oswald-de Waele model. The research applied the finite volume method to investigate the enhancement of heat transfer by incorporating copper particles of 100 nm size within a clear fluid. The results indicated that the heat transfer rate decreased with an increase in the solid volume fraction for a specific Rayleigh number. On the other hand, Alloui et al. (2011) conducted a study on the natural convection in a shallow rectangular cavity filled with nanofluids where have studied the natural convection in a shallow rectangular cavity filled with nanofluids. Öztop et al. (2015) presented an excellent review on natural convective heat transfer in cavities with localized heating, addressing both pure fluids and nanofluids. To analyse the optimization of the fractal-like architecture of porous fibrous materials concerning permeability, diffusivity, and thermal conductivity, Xiao et al. (2017b) applied an established theoretical model named fractal analytical. Their findings revealed that the ratio of the dimensionless total effective thermal conductivity to the dimensionless effective diffusivity increased as a function of the tortuosity fractal dimension.

Then, Alsabery et al. (2017b) investigated the effect of spatial side-wall temperature variation on transient natural convection of a nanofluid in a trapezoidal cavity. They apply the finite difference method to solve the mathematical model numerically. They revealed that the rate of the heat transfer the nanoparticles volume fraction increased the rate of heat transfer. Xiao et al. (2017a) conducted a research on the relative permeability of nanofibers, examining various parameters such as saturation, porosity, area fractal dimension for pores, the fractal dimension of tortuous capillaries, capillary pressure and microstructural of porous nanofibers by using the Fractal-Monte Carlo technique. Based on an experimental verification, Long and Xu (2017) derived a perforation-erosion model and studied the effect of this model on dimensions of the fracture, distribution of the fluid model and studied the effect of this model on dimensions of the fracture, distribution of the fluid and the drop of the

pressure. Then, Xiao et al. (2018) analytically studied the problem of water flow through unsaturated porous rocks using a derived model with the calculation of the capillary pressure and water relative permeability.

2.3 NATURAL CONVECTION WITH OBSTACLES INSIDE

Natural convection plays a crucial role in numerous industrial applications. The introduction of obstacles in the enclosure significantly affects the natural convection process. In industrial applications, strategically placing obstacles within an enclosure offers several benefits, particularly in enhancing heat transfer and optimizing fluid flow. House et al. (1990) have considered the effect of a centred heat-conducting square body on natural convection heat transfer in a square cavity. In this study, two vertical walls were maintained at two different constant temperatures and the horizontal walls were adiabatic. They found that the increase of the solid body size reduces the heat transfer. Man et al. (1999) have numerically investigated the effect of unsteady natural convective heat transfer processes in similar vertical cavities with a centered heat-conducting body. They found that the fluid flow distribution and convective heat transfer increases with increasing Rayleigh number at the cold and hot wall. Mezrhab et al. (2006) investigated the radiation-natural convection interaction in a differentially-heated cavity with an inner body. They discovered that the radiation exchange helps to homogenize the temperature within the cavity and significantly increases the average Nusselt number. Chen (2010) conducted a research on the effects of eccentricity and geometric configuration on heat transfer by natural convection in a Newtonian fluid numerically between a sphere and a vertical cylinder with isothermal boundary conditions. They realized that the heat and fluid flow patterns in the annulus are mainly influenced by the Rayleigh number, eccentricity and geometric configurations. Then, the transient natural convection of liquid gallum from a horizontal triangular cylinder to its coaxial cylinder enclosure was investigated by Yu et al. (2010). They found that the overall heat transfer is enhanced by horizontally positioning the top side of the inner triangular cylinder.

Mahmoodi and Sebdani (2012) also looked into the problem of natural convective

flow and heat transfer of Cu-water nanofluid inside a square cavity having an adiabatic square bodies at its center. The results obtained showed that for all values of the Rayleigh number investigated with the exception of $Ra = 10^4$, the average Nusselt number increased with an increase in the volume fraction of the nanoparticles. At $Ra = 10^4$, the average Nusselt number was a decreasing function of the nanoparticles volume fraction. Moreover, the rate of heat transfer decreased when the size of the adiabatic square body was increased at low Rayleigh numbers, whereas an increase in the heat transfer rate was observed at high Rayleigh numbers. Alsabery et al. (2016) have numerically studied the problem of transient natural convective heat transfer in a nanofluid-saturated porous square cavity with a concentric solid insert and sinusoidal boundary condition. The right wall was heated sinusoidally, while the left vertical wall of the cavity was maintained at a constant temperature and a solid square was inserted at the center of the cavity. The results showed that the overall heat transfer was significantly increased with relatively non-uniform heating. Hatami (2017) investigated the natural convection heat transfer of the nanofluids in a wavy-wall cavity is studied when a heated cylinder is located inside. It is concluded that increasing the cylinder diameter up to 1.0 enhances the Nusselt number due to the larger heated surface area. However, further increases in diameter lead to a decrease in natural convection heat transfer because the flow is obstructed in the narrow space between the wavy walls and the cylinder. The thermophoresis and Brownian diffusion in natural convection are numerically studied in a wavy cavity filled with Al_2O_3-water nanofluid by Hashim et al. (2019). This cavity contains a central heat-conducting solid block, which is influenced by a local heater positioned on the bottom wall. The results indicate that introducing nanoparticles and selecting an optimal number of oscillations enhance heat transfer within the cavity. Then, Salah et al. (2021) investigated the unsteady MHD natural convection flow in an inclined square cavity filled with nanofluid and containing a heated circular obstacle at its center with heat generation. They discovered that the average Nusselt number is sensitive to the central's obstacle's size, and it reduces sufficiently when the radious of the inner cylinder increases.

2.4 NATURAL CONVECTION AND ENTROPY GENERATION

Natural convection is a mode of heat transfer where it occurs due to buoyancy forces induced by temperature differences within a fluid. Entropy generation, on the other hand, is a measure of the irreversibility within a thermodynamic process. A lot of studies have been conducted to study the natural convection and entropy generation to designing efficient thermal systems. Kaluri and Basak (2011) have studied the entropy generation numerically in porous square cavities with distributed heated sources during laminar natural convection with fluid saturated porous medium. They considered the effect of the permeability of the porous medium, the distributed heating technique and Prandtl number by using the Galerkin finite element method. Using the finite volume method, Mahapatra et al. (2013) have numerically considered the study of heat transfer enhancement and entropy generation in a square cavity. This was done with the presence of an adiabatic block. Their results concluded that the heat transfer rate showed an enhancement with the increasing of the block size for low Rayleigh numbers. Lam and Prakash (2014) studied the problem of natural convection and entropy generation in a porous cavity with heat sources using the finite element method. They investigated the effect of heat sources, Darcy number, porosity of the media and Rayleigh number. They then discovered that the rate of the heat transfer was an increasing function of Rayleigh number.

Sheremet et al. (2015) numerically took into consideration the entropy generation analysis on natural convection of nanofluid inside a square cavity having hot solid block with the use of Tiwari and Das' model. Kefayati (2016) have analyzed the heat transfer and entropy generation of laminar convection of non-Newtonian nanofluids in a porous cavity by the Finite Difference Lattice Boltzmann Method. Kolsi et al. (2016) have considered the natural convection and entropy generation in an open cavity nanofluid filled with an adiabatic diamond shaped obstacle using the finite volume technique.Ismael et al. (2016) have investigated the entropy generation due to conjugate natural convection-conduction heat transfer in a square domain, which composed of porous cavity heated by a triangular solid wall and saturated with a CuO-water nanofluid. The results that they collected showed that both the average Nusselt number and the

entropy generation were increasing functions of the thermal conductivity ratio, while there were maxima at some critical values of the ratio of the length of the inner solid to that of the outer hollow. Bouchoucha et al. (2017) have investigated the entropy generation due to natural convection in a nanofluid-filled square cavity with a thick bottom wall. They found that the average Nusselt number decreased with increasing values of the thickness of the bottom wall Meanwhile, the local heat transfer decreases with increasing the wall thickness. Ghasemi and Siavashi (2017) have considered a numerical study on natural convection in a porous cavity filled with Cu-water nanofluid using the Lattice Boltzmann method (LBM). Nayak et al. (2016) have investigated the entropy generation analysis in the porous square cavity filled with nanofluid in natural convection using the lattice Boltzmann method considering a wide range of porosity and constant Darcy numbers with various volume fractions of nanoparticles. Manna et al. (2022) investigated the entropy generation with hybrid nanofluid in quarter circular cavity using the oriented magnetic fields. They discovered that both heat transfer and entropy generation are performed for a hybrid nanofluid flow in a quarter circular cavity considering different orientations of magnetic fields. While Selimefendigil et al. (2023) analyzed the impacts of using a rotating partition on the natural convection and entropy generation of nanofluid filled double annulus under magnetic field. They discovered that the location of the interface becomes closer to the outer surface of the annulus, reduction of the entropy generation up to 68% can be obtained.

2.5 NATURAL CONVECTION IN ENCLOSURES FILLED WITH NANOFLUIDS

Natural convection heat transfer in a cavity is investigated by many researchers due to its wide application areas. The usage of nanofluids as a working media on natural convection heat transfer in a cavity has gained attention of researchers in recent years due to the reason that nanofluids' excellent and adjustable properties including high thermal conductivity, stability, homogeneity and minimal clogging in flow passages due to small sizes and very large specific surface areas of the nano-sized particles. Khanafer et al. (2003) performed numerical studies on natural convection in cavities that are partially occupied by nanofluids. Meanwhile, Jou and Tzeng (2006) have

studied natural convective heat transfer in nanofluids which occupy a rectangular cavity. An experimental study on natural convection heat transfer of alumina-water nanofluid in vertical square cavity was studied by Ho et al. (2010). Alsabery et al. (2017) investigated the problem of transient natural convection heat transfer in a nanoliquid-saturated porous oblique cavity numerically. They found that the strength of the flow circulation increases for the relative concentration of nanofluid with the increment of the inclination angle to the positive direction. Baytas and Pop (2002) explained numerically the free convection flow and heat transfer in a square cavity bounded by isothermal vertical walls at different temperatures and adiabatic horizontal walls. Mobedi (2008) studied the conduction effect of horizontal walls on natural convection heat transfer in a square cavity numerically. The results indicated that the transfer rate decrease for high values of Rayleigh number and thermal conductivity ratio. Next, Alsabery et al. (2023) also apply the hybrid nanofluid with wavy enclosure via heatline approach. They found that the hybrid water nanofluid exhibits a higher Nusselt number than that corresponding to a pure water as well as other regular nanofluids. Furthermore, Tasnim et al. (2023) has been studied the effect of nanofluid in square enclosure with multiple heat generating elements and conducting solid elements. They discovered that the pure water manifests better heat transfer characteristics than nanofluid, with a higher Nusselt number and lower thermal performance criteria. Moreover, it reveals that the position of heat-generating elements and the inclination angle of the enclosure profoundly influence thermal performance. Then, Roy (2022) investigated the effect of a hybrid nanofluid in an enclosure with multiple heat sources with the presence of magnetic field applied to an angle with the horizontal axis. He found that the volume fraction of nanoparticles is more than 6%, the streamlines and the isotherms demonstrate distinct pattern form those for its lower value. Next, Rashid et al. (2023) examined effects of nanoparticles shape on nanofluid flow in a lid-driven square cavity. They found that the lamina shape nanoparticles have higher performance in temperature distribution and heat transfer.

2.6 MIXED CONVECTION HEAT TRANSFER IN ENCLOSURES

Mixed convective heat transfer in enclosures is very important in various engineering application such as solar panels, materials processor, solar ponds, heat exchangers and many more. The combination of shear effect and buoyancy force have been investigated by many researchers. Mixed convection in square or rectangles cavities have been investigated by Monisha et al. (2015), Arani et al. (2012), Khorasanizadeh et al. (2013), Sebdani et al. (2012), and Nayak et al. (2016). Some researchers have investigated numerical studies on mixed convection in trapezoidal cavities. Arefmanesh et al. (2016) concluded that the effective thermal conductivity of nanofluid leads in heat transfer and entropy generation inside the enclosure for a variable property model. Non isothermal bottom wall plays a pre-eminent role to multiple steady states in either natural convection dominated regime or mixed convection regime in convection dominated heat transport regime have been found by Bhattacharya et al. (2013). Tmartnhad et al. (2008) investigated mixed convection in two-dimensional trapezoidal cavity with two openings and heated from below. They concluded that heat transfer and flow structure pivot on the inlet opening site. Similar with Tmartnhad, Kareem et al. (2016) also investigated mixed convection in trapezoidal cavity but different types of nanofluid and no inlet opening site. The outcome shows that a wide range of nanofluids have higher Nusselt number compared with pure water. They also found that the Nusselt number increments as the volume fraction increases and the rotational angle decline yet diminishes as the measurement of the nanopacrticles of nanofluid increases. Selimefendigil and Oztop (2018) investigated mixed convection in a lid driven trapezoidal cavity filled with alumina-water nanofluid effect of an inclined magnetic field for three different electrical conductivity models. The result reveals that the value of Richardson number, strength of the magnetic field and solid particle volume fractions enhance and disparity between the average Nusselt number increases for system with various electrical conductivity models. Aghaei et al. (2016) investigated the effects of magnetic field in a trapezoidal enclosure on the flow field, heat transfer and entropy generation of Cu water nanofluid mixed convection. The top lid is cold and moves to the right or left, the bottom wall is warmer, and the side walls are separated from the horizon at various angles. They discovered that the convection of nanofluid

and strength of flow decrease while the flow tends toward numbers natural convection and finally towards pure conduction by introducing and enhancing the magnetic field while entropy generation due to friction is negligible and the total entropy generation is mainly due to irreversibility associated with heat transfer.

Al-Rashed et al. (2020) investigated the flow field and heat transfer of a water-copper nanofluid with variable properties in a trapezoidal enclosure saturated with porous media. They discovered that with increasing Reynolds number for all Darcy numbers, aspect ratios and volume fraction of nanoparticles, the average Nusselt number increases. The effect of the tilt angle of the cavity on the mixed convection heat transfer inside two separate lid-driven trapezoidal cavities was investigated by Hasib et al. (2015). One heated the wall on short base and the other heated the wall on a long base. They discovered that the heat transfer and flow characteristics inside the cavities depend strongly on Reynold and Grashof numbers. Chamkha et al. (2016) examined the mixed convection within a Cu-water nanofluid filled trapezoidal by the action of lid-driving of the right hot inclined side wall under the effect of a constant magnetic field. They found that, depending on the direction of the lid, the action of the Nusselt number varies from the Richardson number. The numerical results for heat transfer through mixed convection in an incompressible steady lid driven fluid flow inside a trapezoidal cavity in the presence of a uniform magnetic field were investigated by Javed et al. (2017). The findings show that for $Ra = 100,000$, the effects of moving lid become negligible, although increasing Rayleigh number leads to greater streamline circulation and convection dominant effects within the enclosure.While in another investigation, the results indicated that the average Nusselt number decreased as the Lewis number increased, while the total entropy production increased. Al-Rashed et al. (2018) examined mixed convection and entropy generation in a cubical heated up by a central isothermal block. Natural convection heat transfer and total entropy generation of nanofluid in a square cavity in presence of a refrigerant rigid body was considered by Rahimi et al. (2018). Recently, Man, Mi and Young (1999) investigated a three-dimensional free convection and entropy generation of Al_2O_3 water-based nanofluid in a cylindrical cavity. Natural convection and entropy generation in an air-filled cubical cavity with active lateral was studied by Alnaqi et al. (2018).

Probert and Thirst (1977) and Thirst and Probert (1978) initially investigated natural convection in triangular enclosure. Next, Ghasemi and Aminossadati (2010) investigated the convection using triangular cavity where the bottom wall moves to add another convection other buoyancy fluid driven. Then, Xiong et al. (2021) applied different Richardson number, Reynolds number, Hartmann number, and cold circular obstacle to investigate the thermal convection in the lid driven triangular cavity. Then, Shahid et al. (2021) applying multi collision time model to investigate the mixed convection in triangular cavity using incompressible fluid. Then, Hussein (2018) studied the heat transfer and fluid flow in right angle triangular cavity in a 3D air. They found that direction of the moving wall influence the flow filed inside the cavity. Hussein (2018) investigated the effects of moving wall on the mixed convection flow and heat transfer in a right-angle triangular cavity filled with a micropolar fluid. Bottom wall is thermally insulated and the right inclined wall is cold, whereas the vertical wall is adiabatic and moving upward and downward. Roy et al. (2017) studied the effects of horizontally moving walls on the thermal performance and fluid flow via heatline in porous entrapped triangular cavity. They found that the movement of walls significantly influenced the heat flow rates.

Soomro et al. (2020) have applied both the lid driven with magnetohydrodynamic to investigate the thermal in triangular enclosure where the upper wall is thermally insulated while the cooled cylinder placed at the cavity. They discovered that both the Richardson number and Hartmann number influenced the heat transfer. Selimefendigil and Oztop (2017) placed the internal heat generation with bottom wall moves and left wall heated while the inclined wall of the cavity is cooled and partially flexible. They found that the local and average heat transfer reduce as the Richardson number increase. Cherif et al. (2022) investigated the entropy generation and convection inside a 3D triangular porous cavity for nanofluid with a rotating cylinder. They recommend to have a low Hartmann number and higher Darcy number and high rotational speed for the cylinder in the flow direction. Next, Majdi et al. (2020) placed the circular body inside the triangular cavity with combined natural-forced convection and investigate it numerically. They found that the heat transfer affected by the nanoparticles volume fraction and Richardson number. Then, Khan et al. (2022) investigated the effect of

Casson fluid with different thermal boundary conditions inside the triangular cavity while the cylindrical obstacle located inside the cavity. The effect of rotation velocity, solid volume fraction, radius of the inner cylinder has been investigated by Wang et al. (2015) with ethylene glycol-silicon carbide. They found that the rotational velocity influence affects the thermal performances in a triangular enclosure.

2.7 MIXED CONVECTION IN ENCLOSURES FILLED WITH NANOFLUID

Researchers have been conducting the research with either base fluid or nanofluid or both. Gibanov et al. (2018) conducted conjugate mixed convection and entropy generation of alumina-water nanofluid in a lid driven cavity with a bottom solid wall. The outcome shows that bottom wall thickness and volume fraction of nanoparticles plays an important role in enhancing heat transfer. Astanina et al. (2018) studied the mixed convection of alumina-water nanofluid in a lid driven cavity with two porous layers with different thermal properties, permeability and porosity located on the bottom wall. They discovered that addition of nanoparticles contributes to the enhancement of heat transfer in natural convection while an increase in the volume fraction of nanoparticles leads to a reduction in heat transfer for mixed and forced convection. Abu-Nada and Chamkha (2010) investigated the mixed convection flow in a lid driven inclined square enclosure filled with alumina-water nanofluid. They found that due to the existence of nanoparticles, significant heat transfer enhancement can be achieved. Mehmood et al. (2017) examined the mixed convection in alumina-water nanoluid filled lid driven square cavity filled with an isothermally heated square blockage with magnetic filed effect. They found that as nanoparticle volume fraction increases, the average Nusselt number and kinetic energy increase. The findings also show that with a rise in the magnetic field, average Nusselt number, average entropy generation due to heat transfer, Bejan number, and kinetic energy decrease. Goodarzi et al. (2014) investigated the laminar and turbulent mixed convection heat transfer of water-Cu nanofluids in a rectangular shallow cavity utilizing a two phase mixture model. Increasing the volume fraction of nanoparticles is shown to increase the coefficient of convective heat transfer and thus the Nusselt number for specific Grashof

and Richardson number.

The laminar mixed convection flow in single and double lid square cavities filled with an alumina water nanofluid was investigated numerically by Chamkha and Abu-Nada (2012). Due to the existence of nanoparticles, it is observed that significant heat transfer enhancement can be accomplished and that this is accentuated by increasing the nanoparticles volume fraction at moderate and high Richardson number using both nanofluid models for single and double lid cavity configurations. Akbarinia and Behzadmehr (2007) conducted investigation on mixed convection of a nanofluid consisting of alumina water in a horizontal curved tube numerically. The result shows that buoyancy force has a negative influence on the Nusselt number for particular Reynolds number, whereas the concentration of nanoparticles has a positive effect on the enhancement of heat transfer. Alinia et al. (2011) investigated mixed convection of a nanofluid consisting of water and SiO_2 in an inclined enclosure cavity with the left and right walls maintained at different constant temperatures with moving lids and the upper and bottom walls. They concluded that the inclusion of nanoparticles greatly increases heat transfer in the cavity and induces major flow pattern changes. Shariat et al. (2011) conducted research on laminar mixed convection alumina water nanofluid flow in elliptic ducts with constant heat flux boundary by employing two phase mixture model. Results show that increasing solid nanoparticles volume fraction increases the Nusselt number in a given Reynolds and Richardson number while the skin friction decreases. Then, Oktay et al. (2024) focused on the entropy generation analysis of hybrid nanofluids in mixed convection conditions. The results highlighted the importance of operational parameters like nanoparticle volume fraction, Rayleigh number, and Prandtl number, as these factors directly impacted entropy generation. The analysis showed that adjusting these parameters could minimize entropy generation, leading to more efficient thermal systems. Next, Hussain et al. (2024) have expanded on the role of entropy generation in MHD mixed convection of hybrid nanofluids. They found that applying external magnetic fields, as well as optimizing the nanoparticle concentration, could reduce the entropy generation while simultaneously enhancing heat transfer. Then, Dutta et al. (2022) highlighted the role of nanoparticle type and concentration in improving the thermal conductivity of the fluid, which in turn

enhanced heat transfer performance. The study also considered the effects of different hybrid nanoparticle combinations and their influence on the heat transfer coefficient. It was found that hybrid nanofluids generally outperformed single nanofluids in heat transfer performance, with the highest enhancements observed in the presence of multi-type nanoparticle mixtures.

2.8 MIXED CONVECTION IN ENCLOSURE WITH OBSTACLE INSIDE

Apart from application of nanofluid and type of cavities, the heat transfer and fluid flow in cavities having an inside body has received considerable attention in the recent years due to its practical engineering applications. Free convection in cavities having square inner solid is discussed by Alsabery et al. (2018a), Alsabery et al. (2016), Mahmoodi and Sebdani (2012), and Sheremet et al. (2015). Alnajem et al. (2019) considered the entropy generation and natural convection in a wavy-wall filled with a nanofluid and containing solid inner cylinder with isothermal heat source at the left vertical wall and adiabatic at the horizontal wall, while the right wavy wall cooled isothermally. Their outcome indicates that the influence of the addition of nanoparticles on the rate of heat transfer rate is necessary for low Rayleigh number and number of undulations. Alsabery et al. (2019) investigated the time dependent mixed convection of alumina water nanoliquid in a differentially heated chamber with wavy upper wall and centered solid heat-conducting cylinder. They discovered that increase in the average Nusselt number at the hot wall depends on the moving parameter and the inner solid cylinder diameter.

Selimefendigil et al. (2017) numerically examined the mixed convection in a lid driven 3D flexible walled trapezoidal cavity with nanofluid. They observed that the differences in the Richardson number, elastic modulus of the side wall, and nanoparticle volume fraction for various side wall inclination angles of the trapezoidal cavity influenced the heat transfer and fluid flow characteristics. Liao and Lin (2014) investigated mixed convection in a square enclosure with an isothermally rotating circular cylinder. It has been observed that the heat transfer changer according to the Rayleigh number, the aspect ratio and Prandtl number. The mixed convection and

entropy generation in alumina-water nanofluid filling a wavy walled cavity containing a rotating conductive cylinder was investigated by Alsabery et al. (2018b). They discovered that the cylinder's rotation raises the rate of heat exchange at some Rayleigh number and increases with the volume fraction of the nanoparticles and the length of the heater segment. Rahman et al. (2009) investigated the mixed convection in a two dimensional rectangular cavity with a uniform heat source applied on the right vertical wall where a circular heat conducting horizontal cylinder is placed within the cavity. It is shown that both rate of heat transfer from the heated wall and the dimensionless temperature in the cavity was highly dependent on the system's governing parameters and configurations studied, such as size, location, thermal conductivity of the cylinder and position of the inflow and outflow opening. Rahman and Alim (2010) performed a research on the influence of magnetohydrodynamic (MHD) mixed convection flow in a vertical lid driven square enclosure including a heat conducting horizontal circular cylinder with joule heating. The investigation on the MHD mixed convection of Cu-water nanofluid filled triangular enclosure with a rotating cylinder was conducted by Shariat et al. (2014). Heat transfer and total entropy generation are shown to increase as the solid volume fraction of the nanoparticle increases. Rahman et al. (2008) invesigated the effects of cylinder size and Richardson number on mixed convection flow inside a vented square cavity with a heat conducting horizontal solid circular cylinder placed at the center of the cavity. The results show that the streamlines, isotherms, average Nusselt number on the heated surface, average temperature of the fluid in the cavity and the dimensionless temperature in the center of the cylinder strongly depend on both the Richardson number and the cylinder diameter. Chatterjee et al. (2014) conducted research on the mixed convective transport of CuH_2O nanofluid in a differentially heated and lid driven square enclosure in the presence of a rotating and thermally insulated circular cylinder placed centrally within the enclosure. They found that the heat transfer rate is substantially affected by the rotational speed of the cylinder, mixed convective strength and the nanoparticle concentration. Billah et al. (2011) investigated the mixed convection heat transfer in a lid driven cavity along with a heated circular hollow cylinder positioned at the center of the cavity. The result shows that the flow field and temperature distribution strongly depend on the cylinder diameter. Later, Maneengam et al. (2022) examinesd mixed

convection heat transfer in a porous trapezoidal enclosure with a rotating inner tube. This numerical study considered hybrid nanofluids with varying nanoparticle volume fractions and explored the effect of the rotation speed and the Darcy number on thermal performance. It found that the nanofluid's heat transfer performance was improved with higher nanoparticle concentrations and that rotation increased the overall heat transfer rate. Then, Jiang et al. (2023) investigated the mixed convective heat transfer in a three-dimensional triangular enclosure containing a rotating circular cylinder. The study used Fe_3O_4/MWCNT-water hybrid nanofluids and demonstrated the effect of parameters like Hartmann number, rotation speed, and Darcy number on heat transfer. The results suggested that higher rotation speeds enhanced the convective heat transfer while reducing the entropy generation. This kind of analysis is pivotal in understanding the fluid flow and thermal behaviors under mixed convection conditions.

CHAPTER III

METHODOLOGY

3.1 INTRODUCTION

In this chapter, the equations for natural convection in square cavity filled with nanofluid solved numerically. The fundamental equations of the convective heat transfer process, which are derived from the conservation of mass, momentum, and energy, are discussed in Subsection 3.1.1. The governing equations of the convection in a square cavity are discussed in Subsection 3.1.2. Section 3.2 presents the solution methods for model problems using , finite difference method, finite element method (FEM), interpolating function, and Galerkin weighted residual method.

3.1.1 Basic equation

The governing equation of natural convection is based on the conservation of mass, momentum, and energy. It is commonly referred to as the Navier-Stokes equations combined with the energy equation. The specific form of the equations depends on the assumptions made and the specific problem being considered.

For a Newtonian fluid the continuity equation, momentum and energy equation can be written as follows (Bejan 2013):

Continuity equation:

$$\frac{D\rho}{Dt} + \rho\nabla = 0. \tag{3.1}$$

Momentum equation:

$$\frac{D\mathbf{V}}{Dt} = -\frac{\nabla p}{\rho} + \upsilon \nabla^2 \mathbf{V} + \mathbf{F}. \tag{3.2}$$

Energy equation:

$$\frac{DT}{Dt} = \nabla . \left(\frac{\kappa \nabla T}{\rho C_p} \right). \tag{3.3}$$

When the fluid is filled in the cavity, the solid particles exert a force on the fluid which is equal and opposite to the drag force on the solid particles. This force must be balanced by the pressure gradient in the flow,

$$\mathbf{V} = -\frac{\kappa}{\nu} \left(\nabla p + \mathbf{F} \right). \tag{3.4}$$

For equations (3.1)–(3.4), $\frac{D}{Dt}$ is the material derivative, ρ is the fluid density, T is the local temperature, $\mathbf{F} = (f_x, f_y)$ is the body force per unit volume, p is the pressure, t is the time, μ is the dynamic viscosity, $\nu = \frac{\mu}{\rho}$ is the kinematic viscosity, C_p is the specific heat at constant pressure and κ is thermal conductivity. 2D problems are considered due to the geometric simplicity of the enclosure, the dominance of convective heat transfer, and the ability to effectively analyze fluid flow behavior and entropy generation while maintaining computational efficiency. Hence $\mathbf{V}$ represents the velocity vector involved (u, v) in the two coordinate directions x and y, respectively.

Other symbols are defined as:

$$\begin{aligned} \nabla &= \left(\frac{\partial}{\partial x}, \frac{\partial}{\partial y} \right), \\ \nabla \cdot \mathbf{V} &= \frac{\partial u}{\partial x} + \frac{\partial v}{\partial y}, \\ \frac{D}{Dt} &= \frac{\partial}{\partial t} + u\frac{\partial}{\partial x} + v\frac{\partial}{\partial y}, \\ \nabla^2 &= \frac{\partial^2}{\partial x^2} + \frac{\partial^2}{\partial y^2}. \end{aligned} \tag{3.5}$$

In natural convective mode, the body force is the only buoyancy force due

to differences in density caused by temperature variations. The body force in the $x-$direction is , $f_x = 0$, whereas the body force in the $y-$direction, $f_y = -g$, where g is the gravitational acceleration. The governing equations for mixed convective flow are coupled partial differential equations, which include complex equations that must be simplified. The density difference is calculated as follows (Acheson 1990):

$$\rho_0 - \rho = \rho\beta(T - T_0), \tag{3.6}$$

where ρ_0 and T_0 refers to references density and temperature respectively and β is the coefficient of thermal expansion. Oosthuizen and Naylor (1999) proposed the Boussinesq approximation (3.6), which performs simplification based on the smallness of the volume expansion coefficient. The differences in density are minor and can be neglected, but not for the variability density in the momentum equation's buoyancy term. The resulting acceleration from the body's force and inertial force can be quite huge, hence cannot be ignored in the momentum equation. As a result, the density behaved as a constant in all term motion equations except for the body force. This Boussinesq approximation has two components: (i) the density variation is ignored and (ii) the density difference is viewed as a pure temperature effect.

Initially, emphasis is restricted to a 2D model. The assumptions of Boussinesq approximation are used and incompressible fluid is assumed to have constant density and restricted to steady laminar flow with flow variables u, v and p that do not change with time. The governing equations expressed in Cartesian coordinates in the terms of x and y are simplified. Expanding equations (3.1) to (3.3) using Definitions (3.5) and (3.6), the 2D of mixed convective heat transfer of governing equations can be written as (Oosthuizen & Naylor 1999):

Continuity:

$$\frac{\partial u}{\partial x} + \frac{\partial v}{\partial y} = 0. \tag{3.7}$$

$x-$momentum:

$$u\frac{\partial u}{\partial x} + v\frac{\partial u}{\partial y} = \frac{1}{\rho}\frac{\partial p}{\partial x} + \nu\left(\frac{\partial^2 u}{\partial x^2} + \frac{\partial^2 u}{\partial y^2}\right). \tag{3.8}$$

$y-$momentum:

$$u\frac{\partial v}{\partial x} + v\frac{\partial v}{\partial y} = \frac{1}{\rho}\frac{\partial p}{\partial y} + \nu\left(\frac{\partial^2 v}{\partial x^2} + \frac{\partial^2 v}{\partial y^2}\right) + \beta g(T - T_0). \tag{3.9}$$

Energy:

$$u\frac{\partial T}{\partial x} + v\frac{\partial T}{\partial y} = \frac{\kappa}{\rho C_p}\left(\frac{\partial^2 T}{\partial x^2} + \frac{\partial^2 T}{\partial y^2}\right). \tag{3.10}$$

The concepts of equations (3.7) to (3.10) are fundamental to all mathematical formulations in this thesis, and the formulations for the three test problems are stated in the next section. These equations are given primitive variables u, v, p and T based on equations that include the vorticity ω, the stream function ψ, and the temperature T as variables that are easier to solve (Oosthuizen & Naylor 1999). The vorticity and stream functions are defined as:

$$u = \frac{\partial \psi}{\partial y}, \text{ and } v = -\frac{\partial \psi}{\partial x}, \tag{3.11}$$

$$\omega = \left(\frac{\partial v}{\partial x} - \frac{\partial u}{\partial y}\right). \tag{3.12}$$

The stream function (ψ) is the mathematical representation of the streamlines that is obtained from the velocity components, namely (u and v), in such a way that the continuity equation for the incompressible fluid is satisfied. The relationship between the velocity components (u and v are x and y component velocities, respectively) and stream function ψ in the Cartesian coordinates is as described in equation (3.11). ψ is a constant that has been used as a visualisation and analysis tool for the fluid flow. The vorticity equation is obtained by eliminating the pressure between the two momentum equations, i.e., by differentiating the $x-$derivatives of equation (3.9) and the $y-$ derivative

of equation (3.8). This gives

$$\frac{\partial u}{\partial x}\frac{\partial v}{\partial x} + u\frac{\partial^2 v}{\partial x^2} + v\frac{\partial^2 v}{\partial x \partial y} + \frac{\partial v}{\partial x}\frac{\partial v}{\partial y} = -\frac{1}{\rho}\frac{\partial^2 p}{\partial y \partial x} + \nu\left(\frac{\partial^3 v}{\partial x^3} + \frac{\partial^3 v}{\partial y^2 \partial x}\right) + \beta g\frac{\partial T}{\partial x}, \tag{3.13}$$

$$\frac{\partial u}{\partial y}\frac{\partial u}{\partial x} + u\frac{\partial^2 u}{\partial x \partial y} + v\frac{\partial^2 u}{\partial y^2} + \frac{\partial v}{\partial y}\frac{\partial u}{\partial y} = -\frac{1}{\rho}\frac{\partial^2 p}{\partial x \partial y} + \nu\left(\frac{\partial^3 u}{\partial x^2 \partial y} + \frac{\partial^3 u}{\partial y^3}\right). \tag{3.14}$$

Equation (3.14) is subtracted from equation (3.13), and simplified to

$$u\left(\frac{\partial^2 v}{\partial^2 x^2} - \frac{\partial^2 u}{\partial y \partial x}\right) + v\left(\frac{\partial^2 v}{\partial x \partial y} - \frac{\partial^2 u}{\partial y^2}\right) + \frac{\partial v}{\partial x}\left(\frac{\partial u}{\partial x} + \frac{\partial v}{\partial y}\right) - \frac{\partial u}{\partial y}\left(\frac{\partial u}{\partial x} + \frac{\partial v}{\partial y}\right) = \nu\left[\left(\frac{\partial^3 v}{\partial x^3} - \frac{\partial^3 u}{\partial y \partial x^2}\right) + \left(\frac{\partial^3 v}{\partial x \partial y^2} - \frac{\partial^3 u}{\partial y^3}\right)\right] + \beta g\frac{\partial T}{\partial x}. \tag{3.15}$$

Using the definition of vorticity equation (3.12) and using the continuity equation (3.7), equation (3.15) can be simplified to:

$$u\frac{\partial \omega}{\partial x} + v\frac{\partial \omega}{\partial y} = \nu\left(\frac{\partial^2 \omega}{\partial x^2} + \frac{\partial^2 \omega}{\partial y^2}\right) + \beta g\frac{\partial T}{\partial x}. \tag{3.16}$$

Applying the streamfunction equation (3.11), equation (3.16) can be written as follows:

$$\frac{\partial \psi}{\partial y}\frac{\partial \omega}{\partial x} - \frac{\partial \psi}{\partial x}\frac{\partial \omega}{\partial y} = \nu\left(\frac{\partial^2 \omega}{\partial x^2} + \frac{\partial^2 \omega}{\partial y^2}\right) + \beta g\frac{\partial T}{\partial x}. \tag{3.17}$$

Now, the vorticity (3.12) can be defined in terms of stream function as:

$$\left(\frac{\partial^2 \psi}{\partial x^2} + \frac{\partial^2 \psi}{\partial y^2}\right) = -\omega. \tag{3.18}$$

Neglecting the dissipation term, the 2D energy equation becomes:

$$\frac{\partial \psi}{\partial y}\frac{\partial T}{\partial x} - \frac{\partial \psi}{\partial x}\frac{\partial T}{\partial y} = \frac{\kappa}{\rho C_p}\left(\frac{\partial^2 T}{\partial x^2} + \frac{\partial^2 T}{\partial y^2}\right). \tag{3.19}$$

The boundary conditions following the stream function are:

$$\text{on} \quad x = 0, x = 1, \;\; 0 \le y \le 1, \;\; \psi = 0, \;\; T = T_c, \tag{3.20}$$

$$\text{on} \quad 0 \le x \le 1, \;\; y = 0, \;\; \psi = 0, \;\; T = T_h, \tag{3.21}$$

$$\text{on} \quad 0 \le x \le 1, \;\; y = 1, \;\; \psi = 0, \;\; \frac{\partial T}{\partial Y} = 0. \tag{3.22}$$

The following dimensionless forms are introduced and applied,

$$X = \frac{x}{L}, \;\; Y = \frac{y}{L}, \;\; \theta = \frac{T - Tc}{T_h - T_c}, \;\; \Psi = \frac{\psi Pr}{\nu}, \;\; \Omega = \frac{\omega L^2 Pr}{\nu},$$
$$U = \frac{u}{U_0}, \quad V = \frac{v}{V_0}, \;\; Re = \frac{U_0 L}{\nu}, \;\; Ri = \frac{Gr}{Re^2}, \;\; Gr = \frac{g\beta_f \left(T_h - T_c\right) L^3}{\nu_f^2},$$
$$\alpha = \frac{\kappa}{\rho C_p}, \;\; Pr = \frac{\nu}{\alpha}. \tag{3.23}$$

The vorticity equation (3.17) becomes:

$$\frac{\nu^2}{L^4 Pr^2}\left(\frac{\partial \Psi}{\partial Y}\frac{\partial \Omega}{\partial X} - \frac{\partial \Psi}{\partial X}\frac{\partial \Omega}{\partial Y}\right) = \frac{\nu^2}{L^4 Pr}\left(\frac{\partial^2 \Omega}{\partial X^2} + \frac{\partial^2 \Omega}{\partial Y^2}\right) - \beta g \frac{T_h - T_c}{L}\frac{\partial \theta}{\partial X}. \tag{3.24}$$

Equation (3.24) can be simplified as:

$$\frac{\partial \Psi}{\partial Y}\frac{\partial \Omega}{\partial X} - \frac{\partial \Psi}{\partial X}\frac{\partial \Omega}{\partial Y} = Pr\left(\frac{\partial^2 \Omega}{\partial X^2} + \frac{\partial^2 \Omega}{\partial Y^2}\right) - \frac{\beta g T_h - T_c L^3 Pr^2}{\nu^2}\frac{\partial \theta}{\partial X} \tag{3.25}$$

The Rayleigh number is defined based on the enclosure on the cavity width l, such that:

$$Ra = \frac{\beta g T_h - T_c L^3}{\nu^2} Pr. \tag{3.26}$$

Hence, the dimensionless vorticity of equation (3.25) can be written as:

$$\frac{\partial^2 \Omega}{\partial X^2} + \frac{\partial^2 \Omega}{\partial Y^2} = \frac{1}{Pr}\left(\frac{\partial \Psi}{\partial Y}\frac{\partial \Omega}{\partial X} - \frac{\partial \Psi}{\partial X}\frac{\partial \Omega}{\partial Y}\right) + Ra\frac{\partial \theta}{\partial X}. \tag{3.27}$$

Similarity to energy equation (3.19), the following is obtained:

$$\frac{\partial^2 \theta}{\partial X^2} + \frac{\partial^2 \theta}{\partial Y^2} = \frac{\partial \Psi}{\partial Y}\frac{\partial \theta}{\partial X} - \frac{\partial \Psi}{\partial X}\frac{\partial \theta}{\partial Y}. \tag{3.28}$$

3.1.2 Natural convection in a square cavity

Substituting the (3.1) until (3.3) in (3.23), the dimensionless become:

Continuity equation :

$$\frac{\partial U}{\partial X} + \frac{\partial V}{\partial Y} = 0. \tag{3.29}$$

Momentum equation in the $x-$direction:

$$U\frac{\partial U}{\partial X} + V\frac{\partial U}{\partial Y} = \frac{\partial P}{\partial X} + \frac{1}{Re}\left(\frac{\partial^2 U}{\partial X^2} + \frac{\partial^2 U}{\partial Y^2}\right). \tag{3.30}$$

Momentum equation in the $y-$direction:

$$U\frac{\partial V}{\partial X} + V\frac{\partial V}{\partial Y} = \frac{\partial P}{\partial Y} + \frac{1}{Re}\left(\frac{\partial^2 V}{\partial X^2} + \frac{\partial^2 V}{\partial Y^2}\right) + Ri\theta. \tag{3.31}$$

Energy equation:

$$U\frac{\partial \theta}{\partial X} + V\frac{\partial \theta}{\partial Y} = \frac{1}{PrRe}\left(\frac{\partial^2 \theta}{\partial X^2} + \frac{\partial^2 \theta}{\partial Y^2}\right). \tag{3.32}$$

3.2 SOLUTION METHOD

In this section, the numerical solution to the system of equation discussed in Section 2.1 are presented. Finite difference method and finite element method are used to solve the elliptic partial differential equation, continuity, momentum and energy equation. This section provides a brief overview of the numerical methods available for numerically solving a problem.

3.2.1 Finite difference method

Finite difference method is a numerical technique used to approximate solutions to differential equations. It was first utilised in 1768 by Euler. It involves discretizing the domain of problem into a grid of points and approximating the derivatives of the unknown function. The principle to employ a Taylor series expansion for the discretisation of the derivatives of the flow variables.

First, we set the first derivative $U(x)$ at some point. If we develop $U(x_0 + \Delta x)$ as a Taylor series in x, we obtain

$$U(x_0 + \Delta x) = U(x_0) + \Delta x \frac{\partial U}{\partial x}(x_0) + \ldots \tag{3.33}$$

Then, the first derivative of U can be approximated as

$$\frac{\partial U}{\partial x}(x_0) = \frac{U(x_0 + \Delta x)}{\Delta x} + \vartheta(\Delta x) \tag{3.34}$$

To apply the finite difference method, we must to:

1. Discretize the domain by dividing the domain into a set grid of points.
2. Approximate the derivatives of the unknown function at each grid point.
3. Boundary conditions are applied to the grid points at the boundaries of the domain.
4. Solution of equations.
5. Post-computation of solution and quantities of interest.

By applying this method, the dimensionless governing equations (3.7)–(3.10) subject to the boundary conditions (3.20)–(3.22) are numerically formulated. The grid–points distribution at the conducting wall and the enclosure is shown in Figure 3.1 where ND + 1 is number of nodal points in the vertical axis in the wall, NX + 1 is number of nodal points in the X axis and NY + 1 is number of nodal points in the Y axis. By solving the governing equations in the stream function–vorticity formulation in Alsabery et al. (2018c), the finite difference form of the equation related to the dimensionless vorticity

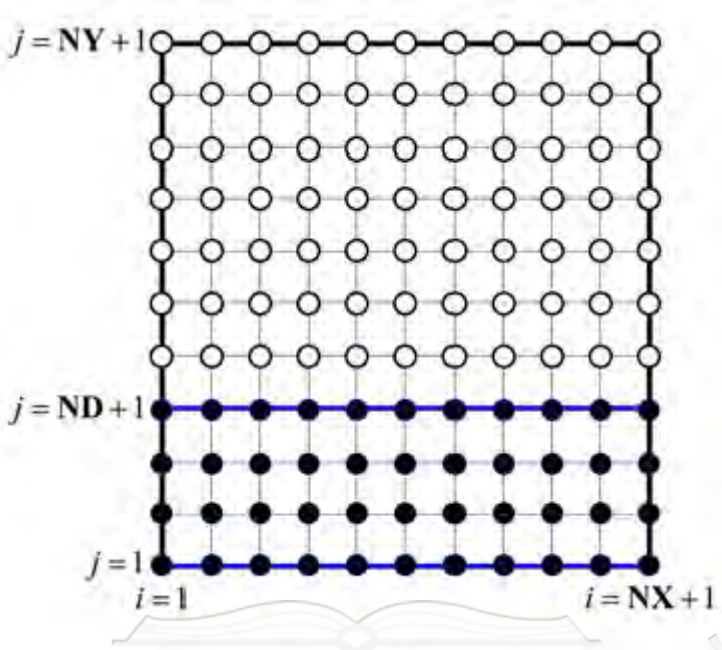

Figure 3.1 Grid-point distributions in the conducting wall ($j \leq$ ND + 1) and cavity ($j >$ ND + 1).

is:

$$\frac{\Omega_{i+1,j} - 2\Omega_{i,j} + \Omega_{i-1,j}}{(\Delta X)^2} + \frac{\Omega_{i,j+1} - 2\theta_{i,j} + \Omega_{i,j-1}}{(\Delta Y)^2} - (S_\Omega)_{i,j} = 0 \tag{3.35}$$

with

$$\begin{aligned}(S_\Omega)_{i,j} \;=\; & \frac{1}{\mathrm{Pr}}\left[\left(\frac{\Psi_{i,j+1} - \Psi_{i,j-1}}{2\Delta Y}\right)\left(\frac{\Omega_{i+1,j} - \Omega_{i-1,j}}{2\Delta X}\right)\right. \\ & \left. -\left(\frac{\Psi_{i+1,j} - \Psi_{i-1,j}}{2\Delta X}\right)\left(\frac{\Omega_{i,j+1} - \Omega_{i,j-1}}{2\Delta Y}\right)\right] \\ & +Ra_f\left(\frac{\theta_{i+1,j} - \theta_{i-1,j}}{2\Delta X}\right)\end{aligned} \tag{3.36}$$

To solve the value of Ω at the grid point i and j, the values of Ω at the right-hand side must be provided, $B = \frac{\Delta X}{XY}$. This method is known as the point Gauss–Seidel method. The general formulation of the method provides:

$$\begin{aligned}\Omega_{i,j}^{k+1} \;=\; & \Omega_{i,j}^{k} + \frac{\lambda_r}{2(1+B^2)}\left[\Omega_{i+1,j}^{k} + \Omega_{i-1,j}^{k+1} + B^2(\Omega_{i,j+1}^{k} + \Omega_{i,j-1}^{k+1})\right. \\ & \left. -2(1+B^2)\Omega_{i,j}^{k} - (\Delta X)^2(S_\Omega)_{i,j}^{k}\right]\end{aligned} \tag{3.37}$$

The computations is assumed to move through the grid points from left to right and

bottom to top. Where the superscript k denotes the iteration number. We make partition in the solution domain in the $X-Y$ plane into equal rectangles of sides ΔX and ΔY. The values of the relaxation parameter λ_r must lie in the range $0 < \lambda_r < 2$ for convergence. The range $0 < \lambda_r < 1$ corresponds to under-relaxation, $1 < \lambda_r < 2$ over-relaxation and $\lambda_r = 1$ refers to the Gauss-Seidel iteration. The finite difference form of equation relating the stream function, energy and volume fraction could be treated in the same way.

The finite difference equation of the dimensionless energy equation of the solid wall is written in the Gaussian successive over-relaxation formulation as:

$$\begin{aligned}(\theta_w)_{i,j}^{k+1} &= (\theta_w)_{i,j}^{k} + \frac{\lambda_r}{2(1+B^2)}\Big[(\theta_w)_{i+1,j}^{k} + (\theta_w)_{i-1,j}^{k+1} + B^2((\theta_w)_{i,j+1}^{k} \\ &\quad +(\theta_w)_{i,j-1}^{k+1}) - 2(1+B^2)(\theta_w)_{i,j}^{k}\Big] \end{aligned} \tag{3.38}$$

The conditions at the solid-nanofluid interfaces boundary are:

$$\begin{aligned}(\theta)_{i,\mathrm{ND}+1}^{k+1} &= (\theta_w)_{i,\mathrm{ND}+1}^{k} \\ (\theta_w)_{i,\mathrm{ND}+1}^{k+1} &= \left[\left(\frac{1}{K_r}\right)\left(-(\theta)_{i,\mathrm{ND}+3}^{k} + 4(\theta)_{i,\mathrm{ND}+2}^{k} - 3(\theta)_{i,\mathrm{ND}+1}^{k}\right)\right. \\ &\quad \left. +4(\theta_w)_{i,\mathrm{ND}}^{k} - (\theta_w)_{i,\mathrm{ND}}^{k}\right]/3 \end{aligned} \tag{3.39}$$

3.2.2 Finite element method

The finite-element method, as it is in general applied to the solution of the Euler/Navier-Stokes equations, starts with a subdivision of the physical space into discrete elements(mostly triangular or quadrilateral shapes in 2D, and tetrahedral or hexahedral shapes in 3D). Thus, an unstructured grid has to be generated. Depending on the element type and the required accuracy, a certain number of points at the boundaries and/or inside an element is specified, where the solution of the flow problem has to be found. The total number of points multiplied with the number of unknowns determines the number of degrees of freedom. Furthermore, the shape functions have to be defined, which represent the variation of the solution inside each

element. In practical implementations, linear or higher-order elements are employed (linear elements use just the grid nodes.) The shape functions are then either linear or higher-order distributions, whose values is zero outside the corresponding element. This results in second and higher order accurate representation of the solution on regular grids.

Within the finite-element method, it is necessary to transform the governing equations from the differential into an equivalent integral form. This can be accomplished in two different ways. The first one is based on the variational principle, that is, a physical solution is sought, for which a certain functional possess an extremum. The second possibility is known as the method of weighted residuals or the weak formulation. Here, it is required that the weighted average of the residuals is identically zero over the physical domain. The residuals can be viewed as the errors of the approximation of the solution. The weak formulation has the same advantage as the finite-volume discretization of the conservation laws – it allows the treatment of discontinuities such as shocks. Therefore, the weak formulation is preferred over the variational methodology. The discontinuous Galerkin scheme differs form the classical finite-element method with respect to the mass matrix, which is defined as being local to the generating element. This makes it possible for the discontinuous Galerkin scheme to temporally evolve the unknown solution coefficients by using simple explicit methods.

The finite-element method is attractive because of its integral formulation and the use of unstructured grids, which are both preferable for flows in or around complex geometries. Besides aerocoustics, the method is also particularly suitable for the treatment of non-Newtonian fluids. The finite-element method has a very rigorous mathematical foundation, particularly for elliptic and parabolic problems. Although it can be shown that in certain cases the method is mathematically equivalent to the finite-volume discretization, the numerical effort is noticeably higher. This may explain why the finite volume method became more popular for standard flow problems. However, both methods are sometimes combined – particularly on unstructured grids. So, for example, the treatment of the boundaries and the discretization of the viscous fluxes is usually “borrowed” from the finite-element method.

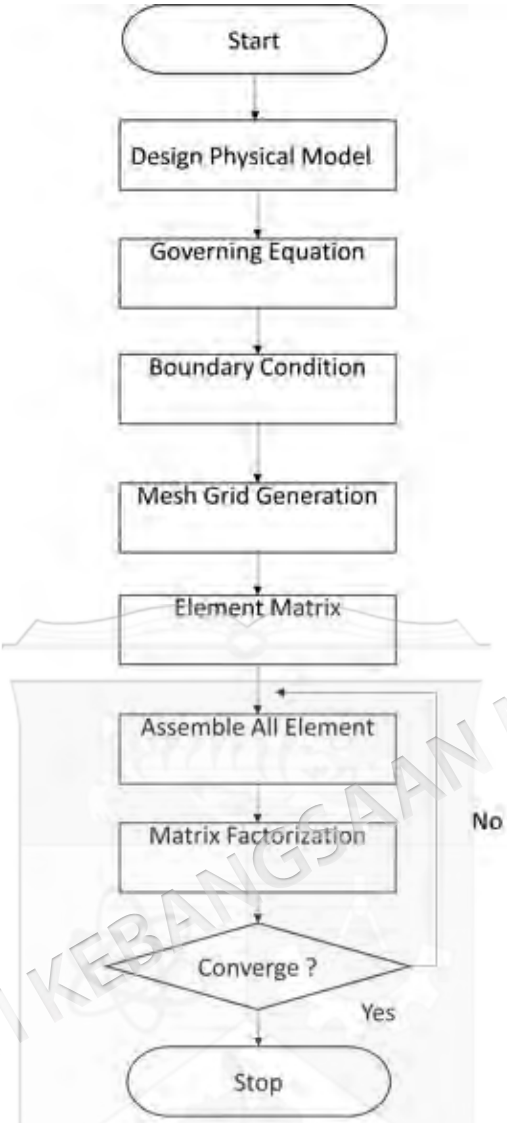

Figure 3.2 The flowchart of numerical simulation in FEM.

The basic idea of the finite element method is to view a given domain as an assemblage of simple geometric shapes. It is possible to systematically generate the approximation functions needed in the solution of differential equations by any of the variational and weighted residual methods. The approximation functions are often constructed using ideas from interpolation theory.The steps is shown in Figure 3.2.

The major steps in the finite element formulation and analysis are:

1. Discretize the domain by dividing the domain into a set grid of points.
2. Construction of a statement, often a weighted-integral or weak form statement

that is equivalent to the differential equation.

3. Development of the finite element model using the weighted-integral statement or weak form over an element.
4. Assembly of finite elements to obtain the global system of algebraic equations.
5. Imposition of boundary conditions.
6. Solution of equations.
7. Post-computation of solution and quantities of interest.

3.2.3 Interpolating function

There are three types of elements in finite element method used for meshing. There are simplex, complex and multiplex. Simplex elements are the basic building blocks where they are simple and straightforward shape such as triangles in 2D or tetrahedral in 3D. The interpolating function, u, for 2D triangular elements is :

$$u = c_1 + c_2 x + c_3 y. \tag{3.40}$$

where x and y are the spatial coordinates, and c_1, c_2 and c_3 are coefficients determined by the nodal values.

The interpolating function shows that the 2D triangular elements has 3 nodes. Complex elements, also known as higher-order elements, are more sophisticated than simplex elements. Complex elements are typically defined by additional interpolation points within each element such as the quadratic elements. The quadratic elements interpolating function as following:

$$u = c_1 + c_2 x + c_3 y + c_4 xy + c_5 x^2 + c_6 y^2. \tag{3.41}$$

From the equation (3.41), the element has 6 nodes c_i for $i = 1, 2, .., 6$ and it goes to second order interpolation functions.

Consider a three noded triangular element as Figure 3.3 , and each nodes labelled

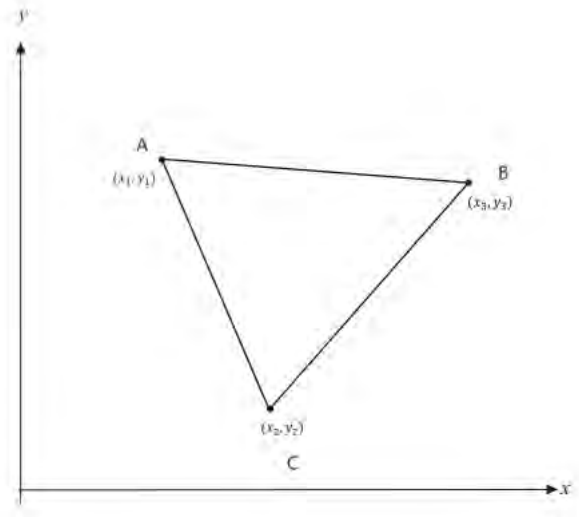

Figure 3.3 A 2D linear triangular element. Adaptef from Pepper and Heinrich (2017)

as coordinates A, B and C. In each nodes, each become:

$$A(x_1, y_1) \tag{3.42}$$
$$B(x_2, y_2)$$
$$C(x_3, y_3)$$

Since it is 2D problem, we can express the general polynomial to represent the solution of the problem as:

$$u_1 = c_0 + c_1 x_1 + c_2 y_1, \tag{3.43}$$
$$u_2 = c_0 + c_1 x_2 + c_2 y_2,$$
$$u_3 = c_0 + c_1 x_3 + c_2 y_3.$$

This general polynomial form can be expressed in matrix form:

$$\begin{bmatrix} u_1 \\ u_2 \\ u_3 \end{bmatrix} = \begin{bmatrix} 1 & x_1 & y_1 \\ 1 & x_2 & y_2 \\ 1 & x_3 & y_3 \end{bmatrix} \begin{bmatrix} c_0 \\ c_1 \\ c_2 \end{bmatrix}. \tag{3.44}$$

By changing the position, equation 3.44 become,

$$\begin{bmatrix} c_0 \\ c_1 \\ c_2 \end{bmatrix} = \begin{bmatrix} 1 & x_1 & y_1 \\ 1 & x_2 & y_2 \\ 1 & x_3 & y_3 \end{bmatrix}^{-1} \begin{bmatrix} u_1 \\ u_2 \\ u_3 \end{bmatrix}. \tag{3.45}$$

Finding the values for c_1, c_2, and c_3 as a function of the values u_1, u_2, and u_3 is now a simple task. These are:

$$\begin{aligned} c_1 &= \frac{1}{2A^{(e)}} \left[(x_2y_3 - x_3y_2)u_1 + (x_3y_1 - x_1y_3)u_2 + (x_1y_2 - x_2y_1)u_3\right], \\ c_2 &= \frac{1}{2A^{(e)}} \left[(y_2 - y_3)u_1 + (y_3 - y_1)u_2 + (y_1 - y2)u_3\right], \\ c_3 &= \frac{1}{2A^{(e)}} \left[(x_3 - x_2)u_1 + (x_1 - x_3)u_2 + (x_2 - x1)u_3\right], \end{aligned} \tag{3.46}$$

where the area, $A^{(e)}$, is defined by

$$2A^{(e)} = (x_1y_2 - x_2y_1) + (x_3y_1 - x_1y_3) + (x_2y_3 - x_3y_2). \tag{3.47}$$

Notice that the area of the element is defined in terms of the nodal coordinates. To obtain the shape functions, we approximate u as a function of the three nodal values such that

$$u = N_1u_1 + N_2u_2 + N_3u_3, \tag{3.48}$$

just as in the one-dimensional element. The shape functions are formally defined as

$$N_1^{(e)}(x, y) = \frac{1}{2A^{(e)}}[(x_2y_3 - x_3y_2) + (y_2 - y_3)x + (x_3 - x_2)y], \tag{3.49}$$

$$N_2^{(e)}(x, y) = \frac{1}{2A^{(e)}}[(x_3y_1 - x_1y_3) + (y_3 - y_1)x + (x_1 - x_3)y], \tag{3.50}$$

$$N_3^{(e)}(x, y) = \frac{1}{2A^{(e)}}[(x_1y_2 - x_2y_1) + (y_1 - y_2)x + (x_2 - x_1)y], \tag{3.51}$$

which conforms to the general relations expressed by equation (3.40). As an example, the value of N_1 at node 1 can be obtained by substituting $x = x_1$ and $y = y_1$ into equation (3.49), it become

$$N_1 = \frac{1}{2A}(x_2y_3 - x_3y_2 + y_2x_1 - y_3x_1 + x_3y_1 - x_2y_1), \tag{3.52}$$

where N_1 is zero at nodes 2 and 3 and all points on a line passing through these nodes. We also note that the value in parentheses in equation (3.52) is also equal to 2A. Hence

$$\begin{aligned} N_1 = \frac{2A}{2A} = 1 \qquad & \text{at } x = x_1, y = y_1 \\ N_1 = 0 \qquad & \text{at } x = x_2, y = y_2 \text{ and at } x = x_3, y = y_3 \end{aligned} \tag{3.53}$$

The gradient of the variable u is given by the expression

$$\begin{aligned} \frac{\partial u}{\partial x} &= \frac{\partial N_1}{\partial x}u_1 + \frac{\partial N_2}{\partial x}u_2 + \frac{\partial N_3}{\partial x}u_3, \\ \frac{\partial u}{\partial y} &= \frac{\partial N_1}{\partial y}u_1 + \frac{\partial N_2}{\partial y}u_2 + \frac{\partial N_3}{\partial y}u_3, \end{aligned} \tag{3.54}$$

The value of $\frac{\partial N_1}{\partial x}$, for example, is easily determined from equation (3.52):

$$\frac{\partial N_1}{\partial x} = \frac{y_2 - y_3}{2A}. \tag{3.55}$$

The remaining derivatives for the shape functions are obtained in a straightforward manner. The value of $\frac{\partial u}{\partial x}$ becomes

$$\frac{\partial u}{\partial x} = \frac{1}{2A}[(y_2 - y_3)u_1 + (y_3 - y_1)u_2 + (y_1 - y_2)u_3]. \tag{3.56}$$

3.2.4 Weighted residual method

The Galerkin weighted residual along with finite element methods are employed to investigate the control equations (3.29)–(3.32) subject to the boundary conditions equations (3.20)–(3.22). The finite element analysis of the momentum equations (3.30) and (3.31) is showing by the following procedure:

Primary, we apply the penalty finite element method by excluding the pressure (P) including a penalty parameter (λ) as the following:

$$P = -\lambda \left(\frac{\partial U}{\partial X} + \frac{\partial V}{\partial Y} \right).$$

Leads to the following momentum equations toward the X and Y-directions:

$$U\frac{\partial U}{\partial X} + V\frac{\partial U}{\partial Y} = \frac{\partial \lambda}{\partial X}\left(\frac{\partial U}{\partial X} + \frac{\partial V}{\partial Y} \right) + \frac{1}{Re}\left(\frac{\partial^2 U}{\partial X^2} + \frac{\partial^2 U}{\partial Y^2} \right),$$
$$U\frac{\partial V}{\partial X} + V\frac{\partial V}{\partial Y} = \frac{\partial \lambda}{\partial Y}\left(\frac{\partial U}{\partial X} + \frac{\partial V}{\partial Y} \right) + \frac{1}{Re}\left(\frac{\partial^2 V}{\partial X^2} + \frac{\partial^2 V}{\partial Y^2} \right) + \frac{Gr}{Re^2}\theta.$$

The weak (or weighted-integral) formulation regarding the momentum equations by multiplying the equation by an internal domain (Φ) and integrating it over the computational domain which is discretised toward small triangular elements.

The following weak formulations are obtained:

$$\int_\Omega \left(\Phi_i U^k \frac{\partial U^k}{\partial X} + \Phi_i V^k \frac{\partial U^k}{\partial Y} \right) \mathrm{d}X\mathrm{d}Y = \lambda \int_\Omega \frac{\partial \Phi_i}{\partial X}\left(\frac{\partial U^k}{\partial X} + \frac{\partial V^k}{\partial Y} \right) \mathrm{d}X\mathrm{d}Y$$
$$+\frac{1}{Re}\int_\Omega \Phi_i \left(\frac{\partial^2 U^k}{\partial X^2} + \frac{\partial^2 U^k}{\partial Y^2} \right) \mathrm{d}X\mathrm{d}Y,$$
$$\int_\Omega \left(\Phi_i V^k \frac{\partial V^k}{\partial X} + \Phi_i V^k \frac{\partial V^k}{\partial Y} \right) \mathrm{d}X\mathrm{d}Y = \lambda \int_\Omega \frac{\partial \Phi_i}{\partial Y}\left(\frac{\partial U^k}{\partial X} + \frac{\partial V^k}{\partial Y} \right) \mathrm{d}X\mathrm{d}Y$$
$$+\frac{1}{Re}\int_\Omega \Phi_i \left(\frac{\partial^2 V^k}{\partial X^2} + \frac{\partial^2 V^k}{\partial Y^2} \right) \mathrm{d}X\mathrm{d}Y + \frac{Gr}{Re^2}\int_\Omega \Phi_i \theta^k \mathrm{d}X\mathrm{d}Y.$$

Selection about the interpolation functions as implementing an approximation toward the velocity distribution and temperature distribution as:

$$U \approx \sum_{j=1}^{m} U_j \Phi_j(X,Y), \quad V \approx \sum_{j=1}^{m} V_j \Phi_j(X,Y), \quad \theta \approx \sum_{j=1}^{m} \theta_j \Phi_j(X,Y).$$

The nonlinear residual equations for the momentum equations that obtained from the Galerkin weighted residual finite-element method are:

$$R(1)_i = \sum_{j=1}^{m} U_j \int_\Omega \left[\left(\sum_{j=1}^{m} U_j \Phi_j \right) \frac{\partial \Phi_j}{\partial X} + \left(\sum_{j=1}^{m} V_j \Phi_j \right) \frac{\partial \Phi_j}{\partial Y} \right] \Phi_i \mathrm{d}X\mathrm{d}Y$$

$$+\lambda\left[\sum_{j=1}^{m} U_j \int_{\Omega} \frac{\partial \Phi_i}{\partial X}\frac{\partial \Phi_j}{\partial X}\mathrm{d}X\mathrm{d}Y + \sum_{j=1}^{m} V_j \int_{\Omega} \frac{\partial \Phi_i}{\partial X}\frac{\partial \Phi_j}{\partial Y}\mathrm{d}X\mathrm{d}Y\right]$$
$$+\frac{1}{Re}\sum_{j=1}^{m} U_j \int_{\Omega}\left[\frac{\partial \Phi_i}{\partial X}\frac{\partial \Phi_j}{\partial X} + \frac{\partial \Phi_i}{\partial Y}\frac{\partial \Phi_j}{\partial Y}\right]\mathrm{d}X\mathrm{d}Y,$$

$$R(2)_i = \sum_{j=1}^{m} V_j \int_{\Omega}\left[\left(\sum_{j=1}^{m} U_j\Phi_j\right)\frac{\partial \Phi_j}{\partial X} + \left(\sum_{j=1}^{m} V_j\Phi_j\right)\frac{\partial \Phi_j}{\partial Y}\right]\Phi_i\mathrm{d}X\mathrm{d}Y$$
$$+\lambda\left[\sum_{j=1}^{m} U_j \int_{\Omega} \frac{\partial \Phi_i}{\partial Y}\frac{\partial \Phi_j}{\partial X}\mathrm{d}X\mathrm{d}Y + \sum_{j=1}^{m} V_j \int_{\Omega} \frac{\partial \Phi_i}{\partial Y}\frac{\partial \Phi_j}{\partial Y}\mathrm{d}X\mathrm{d}Y\right]$$
$$+\frac{1}{Re}\sum_{j=1}^{m} V_j \int_{\Omega}\left[\frac{\partial \Phi_i}{\partial X}\frac{\partial \Phi_j}{\partial X} + \frac{\partial \Phi_i}{\partial Y}\frac{\partial \Phi_j}{\partial Y}\right]\mathrm{d}X\mathrm{d}Y$$
$$+\frac{Gr}{Re^2}\int_{\Omega}\left(\sum_{j=1}^{m}\theta_j\Phi_j\right)\Phi_i\mathrm{d}X\mathrm{d}Y,$$

where the superscript k is the relative index, subscripts i, j and m are the residual number, node number and iteration number, respectively. For clarifying the nonlinear terms into the momentum equations, a Newton-Raphson iteration algorithm was employed. The convergence of the solution is allowed through the relative error to any of the variables does satisfy the resulting convergence criteria:

$$\left|\frac{\Gamma^{m+1} - \Gamma^{m}}{\Gamma^{m+1}}\right| \leq 10^{-5}.$$

Figure 3.4 shows the flowchart of the used numerical code of the Galerkin weighted residual method FEM and all the numerical code is implied into COMSOL Mutliphysics software to produce results of contour streamlines, isotherms and isentropic with graphs of local and average Nusselt number with Bejan number.

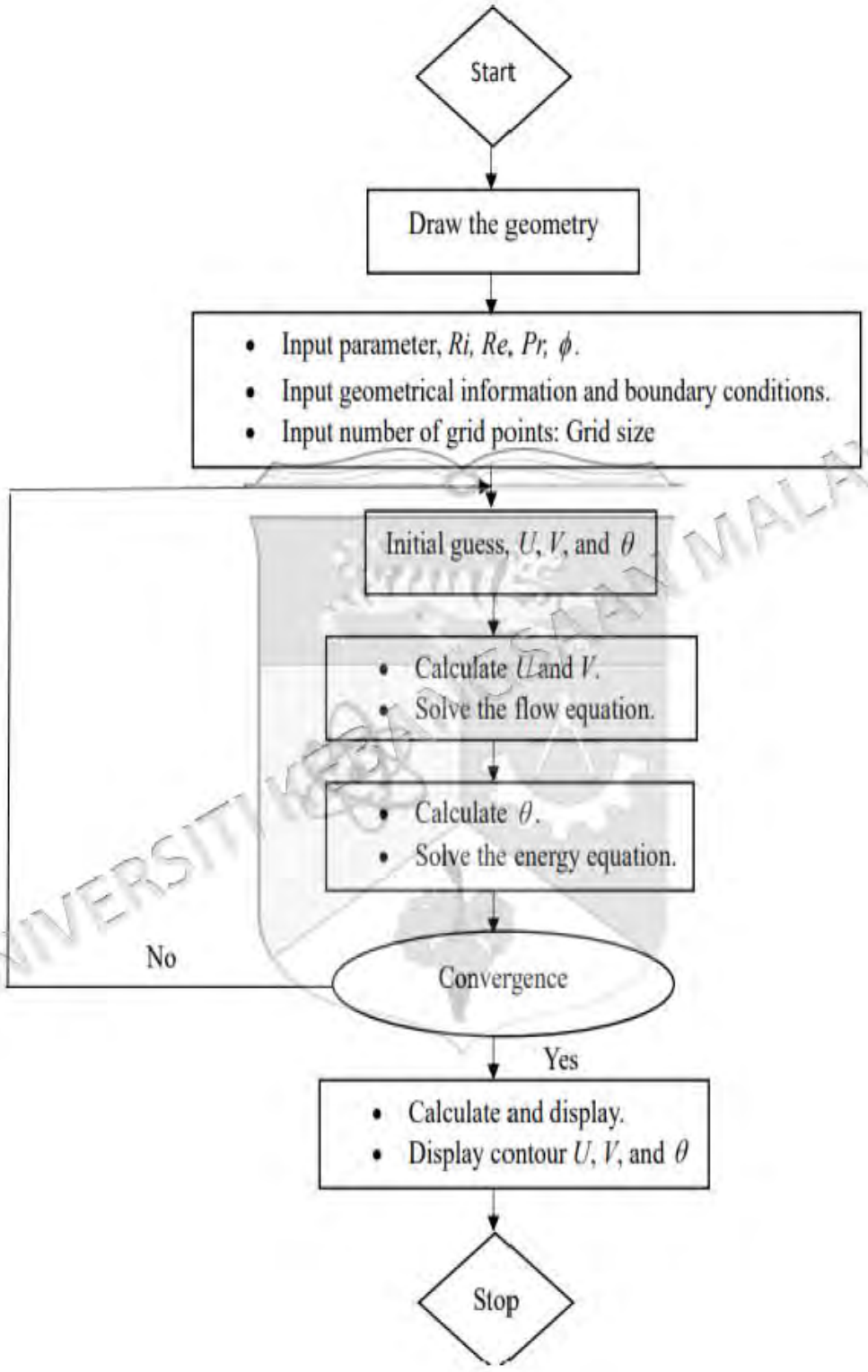

Figure 3.4 The flowchart of numerical simulation in FEM.

CHAPTER IV

ENTROPY GENERATION ANALYSIS AND NATURAL CONVECTION IN A NANOFLUID-FILLED SQUARE CAVITY WITH A CONCENTRIC SOLID INSERT AND DIFFERENT TEMPERATURE DISTRIBUTIONS

4.1 INTRODUCTION

Fluid flow and heat transfer analysis in cavities have become popular areas of research related to heat storage applications. As a result, the increase in research activities regarding convection heat transfer is significant. When the fluid motion is not generated by any external source, the flow is characterized by natural convection flow. Such a mechanism is easily identified in various engineering applications such as electronic cooling, cooling of containment buildings, room ventilation, heat exchangers, storage tanks, double pane windows, solar collectors and so on. Many researchers are interested in the use of nanofluids in the natural convection flow because of nanofluids' excellent and adjustable properties including high thermal conductivity, stability, homogeneity and minimal clogging in flow passages due to small sizes and very large specific surface areas of the nanosized particles. Nevertheless, many researchers have focused their attention on studying the convective heat transfer within cavities one or more obstacles inside. Many researchers have applied the heat transfer and entropy generation in various cavities using different methods.

Based on the studies mentioned above and to the authors' best knowledge, the problem of entropy generation analysis and natural convection in a nanofluid-filled square cavity with a concentric solid insert and different temperature distribution is yet to be investigated. Hence, this study aims to investigate the entropy generation analysis and natural convection in nanofluid-filled square cavity with a concentric solid insert

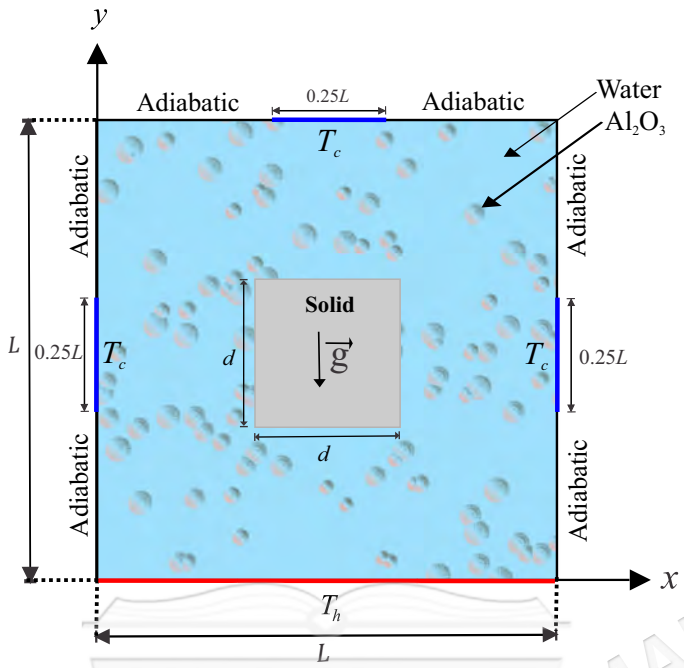

Figure 4.1 Physical model of convection in a square cavity together with the coordinate system.

and different temperature distribution. A square cavity with an isothermal hot bottom wall and partly cold sidewalls and partly cold top wall are important problems in thermal processing applications, for example, in molten metals infiltration, drying and transport of gases, enhanced oil recovery by hot-water flooding and combustion of heavy oils. Therefore, the authors believe that the present work is a valuable contribution in improving the thermal performance and the heat transfer enhancement in some engineering instruments.

4.2 MATHEMATICAL FORMULATION

The steady two-dimensional natural convection problem in a square cavity with length L and with the cavity center inserted by a solid square with side d, as illustrated in Figure 4.1.

The Rayleigh number range chosen in the study keeps the nanofluid flow laminar and two-dimensional. Isothermal cold sources are distributed along the top wall and side

walls of the square cavity at a constant cold temperature T_c, which are showed by thick blue lines with length of $0.25L$. While the remainder of these walls are kept adiabatic. The bottom wall of the cavity is maintained at a constant hot temperature T_h. The boundaries of the annulus are assumed to be impermeable, the fluid within the cavity is a water-based nanofluid having Al_2O_3 nanoparticles. The Boussinesq approximation is applicable. By considering these assumptions, the continuity, momentum and energy equations for the laminar and steady state natural convection can be written as follows (Alsabery et al. (2017b); Roslan, Saleh & Hashim (2011)):

$$\frac{\partial u}{\partial x} + \frac{\partial v}{\partial y} = 0, \tag{4.1}$$

$$u\frac{\partial u}{\partial x} + v\frac{\partial u}{\partial y} = -\frac{1}{\rho_{nf}}\frac{\partial p}{\partial x} + \frac{\mu_{nf}}{\rho_{nf}}\left(\frac{\partial^2 u}{\partial x^2} + \frac{\partial^2 u}{\partial y^2}\right), \tag{4.2}$$

$$u\frac{\partial v}{\partial x} + v\frac{\partial v}{\partial y} = -\frac{1}{\rho_{nf}}\frac{\partial p}{\partial y} + \frac{\mu_{nf}}{\rho_{nf}}\left(\frac{\partial^2 v}{\partial x^2} + \frac{\partial^2 v}{\partial y^2}\right) + \beta_{nf} g\left(T_h - T_c\right), \tag{4.3}$$

$$u\frac{\partial T_{nf}}{\partial x} + v\frac{\partial T_{nf}}{\partial y} = \alpha_{nf}\left(\frac{\partial^2 T_{nf}}{\partial x^2} + \frac{\partial^2 T_{nf}}{\partial y^2}\right). \tag{4.4}$$

The energy equation of the inner solid wall is

$$\frac{\partial^2 T_w}{\partial x^2} + \frac{\partial^2 T_w}{\partial y^2} = 0, \tag{4.5}$$

where x and y are the Cartesian coordinates measured in the horizontal and vertical directions respectively, g is the acceleration due to gravity, α_{nf} is the effective thermal diffusivity of the nanofluids and ρ_{nf} is the effective density of the nanofluids, which are defined as Nasrin & Parvin (2012)

$$\begin{aligned} \alpha_{nf} &= \frac{k_{nf}}{(\rho C_p)_{nf}}, \\ \rho_{nf} &= (1-\phi)\rho_{bf} + \phi\rho_{sp}, \end{aligned} \tag{4.6}$$

where ϕ is the solid volume fraction of nanoparticles and the heat capacitance of the nanofluids $(\rho C_p)_{nf}$ is given as (Nasrin & Parvin 2012)

$$(\rho C_p)_{nf} = (1-\phi)(\rho C_p)_{bf} + \phi(\rho C_p)_{sp}. \tag{4.7}$$

The thermal expansion coefficient of the nanofluids can be determined by Nasrin & Parvin (2012):

$$\beta_{nf} = (1-\phi)(\beta)_{bf} + \phi\beta_{sp}, \tag{4.8}$$

$$(\rho\beta)_{nf} = (1-\phi)(\rho\beta)_{bf} + \phi(\rho\beta)_{sp}. \tag{4.9}$$

The dynamic viscosity ratio of Al_2O_3-water nanofluids for 36nm particle-size in the ambient condition was derived by Nguyen et al. (2007) as follows:

$$\frac{\mu_{nf}}{\mu_{bf}} = 1 + 0.025\phi + 0.015\phi^2. \tag{4.10}$$

The temperature dependence of water viscosity μ_{bf} is expressed by Chon et al. (2005) as

$$\mu_{bf} = 2.414 \times 10^{-5} 10^{247.8/(T-140)}. \tag{4.11}$$

The thermal conductivity ratio of Al_2O_3-water nanofluids calculated by the Chon model as Chon et al. (2005) is

$$\frac{k_{nf}}{k_{bf}} = 1 + 64.7\phi^{0.7640} \left(\frac{d_{bf}}{d_{sp}}\right)^{0.7476} \mathrm{Pr}_T^{0.9955} \mathrm{Re}^{1.2321}. \tag{4.12}$$

Here Pr_T and Re are defined as

$$\mathrm{Pr}_T = \frac{\mu_{bf}}{\rho_{bf}\alpha_{bf}}. \tag{4.13}$$

$$\mathrm{Re} = \frac{\rho_{bf} k_b T}{3\pi\mu_{bf}^2 l_{bf}}, \tag{4.14}$$

where $k_b = 1.380648 \times 10^{-23}(J/K)$ is the Boltzmann constant, $l_{bf} = 0.17$nm is the mean path of the used fluid (water) for the entire tested temperature range (from 21 to 71 °C) (Chon et al. 2005), and d_{bf} is the molecular diameter of water given as Corcione (2011)

$$d_{bf} = \frac{6M}{N\pi\rho_{bf}}. \tag{4.15}$$

Here M is the molecular weight of the base fluid, N is the Avogadro number and ρ_{bf} is the density of the base fluid at standard temperature (310K). Accordingly and basing on

water as a base fluid, the value of d_{bf} is (Corcione 2011):

$$d_{bf} = \left(\frac{6 \times 0.01801528}{6.022 \times 10^{23} \times \pi \times 998.26} \right)^{1/3} = 3.85 \times 10^{-10}\text{m}. \tag{4.16}$$

Now define the stream function ψ and the vorticity ω in the usual waw

$$u = \frac{\partial \psi}{\partial y}, \quad v = -\frac{\partial \psi}{\partial x}, \tag{4.17}$$

$$\omega = \frac{\partial v}{\partial x} - \frac{\partial u}{\partial y}, \tag{4.18}$$

and introduce the following non-dimensional variables:

$$X = \frac{x}{L}, \quad Y = \frac{y}{L}, \quad \Omega = \frac{\omega L^2}{\alpha_{bf}}, \quad \Psi = \frac{\psi}{\alpha_{bf}}, \quad \theta_{nf} = \frac{T_{nf} - T_c}{T_h - T_c},$$
$$\theta_w = \frac{T_w - T_c}{T_h - T_c}. \tag{4.19}$$

Substituting the non-dimensional variables (4.19) into the governing equations (4.1)–(4.5) we obtain the following dimensionless equations:

$$\frac{\partial^2 \Psi}{\partial X^2} + \frac{\partial^2 \Psi}{\partial Y^2} = -\Omega, \tag{4.20}$$

$$\frac{\partial \Psi}{\partial Y}\frac{\partial \Omega}{\partial X} - \frac{\partial \Psi}{\partial X}\frac{\partial \Omega}{\partial Y} = \frac{\mu_{nf}}{\mu_{bf}} \left[\frac{\text{Pr}}{(1-\phi) + \phi \frac{\rho_{sp}}{\rho_{bf}}} \right] \left(\frac{\partial^2 \Omega}{\partial X^2} + \frac{\partial^2 \Omega}{\partial Y^2} \right)$$
$$+ \frac{\beta_{nf}}{\beta_{bf}} Ra\text{Pr} \left(\frac{\partial \theta}{\partial X} \right), \tag{4.21}$$

$$\frac{\partial \Psi}{\partial Y}\frac{\partial \theta_{nf}}{\partial X} - \frac{\partial \Psi}{\partial X}\frac{\partial \theta_{nf}}{\partial Y} = \frac{(\rho C_p)_{bf}}{(\rho C_p)_{nf}} \frac{k_{nf}}{k_{bf}} \left(\frac{\partial^2 \theta_{nf}}{\partial X^2} + \frac{\partial^2 \theta_{nf}}{\partial Y^2} \right), \tag{4.22}$$

$$\frac{\partial^2 \theta_w}{\partial X^2} + \frac{\partial^2 \theta_w}{\partial Y^2} = 0, \tag{4.23}$$

where $Ra = g\rho_{bf}\beta_{bf}(T_h - T_c)L^3/(\mu_{bf}\alpha_{bf})$ is the Rayleigh number for the base fluid and $\text{Pr} = \nu_{bf}/\alpha_{bf}$ is the Prandtl number for the base fluid. The dimensionless boundary conditions of equations (4.20) and (4.23) are:

$$\Psi = 0, \text{ on all solid boundaries,} \tag{4.24}$$

$$\theta_{nf}(X, 0) = 1, \text{ (for the hot bottom wall),} \tag{4.25}$$

$$\theta_{nf}(X,Y) = 0, \text{ (for the cold regimes in the side and top walls)} \quad (4.26)$$

$$\frac{\partial\theta(X,Y)}{\partial Y} = 0, \text{ (for the adiabatic part of the remainder walls)} \quad (4.27)$$

$$\theta_{nf} = \theta_w, \text{ at the outer solid square surface,} \quad (4.28)$$

$$\frac{\partial\theta_{nf}}{\partial X} = K_r\frac{\partial\theta_w}{\partial X}, \quad 0 \le X \le D, \quad (4.29)$$

$$\frac{\partial\theta_{nf}}{\partial Y} = K_r\frac{\partial\theta_w}{\partial Y}, \quad 0 \le Y \le D, \quad (4.30)$$

where $K_r = k_w/k_{nf}$ is the thermal conductivity ratio and $D = d/L$ is the aspect ratio of inner square cylinder width to outer square cylinder width.

The local Nusselt number evaluated at the bottom wall is defined by

$$Nu_{nf} = -\frac{k_{nf}}{k_{bf}}\left(\frac{\partial\theta_{nf}}{\partial Y}\right)_{Y=0}. \quad (4.31)$$

Finally, the average Nusselt number evaluated at the bottom wall which is given by:

$$\overline{Nu}_{nf} = \int_0^1 Nu_{nf}\,\mathrm{d}X. \quad (4.32)$$

The entropy generation relation is given by

$$S = \frac{k_{nf}}{T_0^2}\left[\left(\frac{\partial T}{\partial x}\right)^2 + \left(\frac{\partial T}{\partial y}\right)^2\right] + \frac{\mu_{nf}}{T_0}\left[2\left(\frac{\partial u}{\partial x}\right)^2 + 2\left(\frac{\partial v}{\partial y}\right)^2 + \left(\frac{\partial u}{\partial x} + \frac{\partial v}{\partial x}\right)^2\right]. \quad (4.33)$$

In dimensionless form, the local entropy generation can be expressed as:

$$S_{\mathrm{GEN}} = \frac{k_{nf}}{k_{bf}}\left[\left(\frac{\partial\theta}{\partial X}\right)^2 + \left(\frac{\partial\theta}{\partial Y}\right)^2\right] + \frac{\mu_{nf}}{\mu_{bf}}N_\mu\left[4\left(\frac{\partial^2\Psi}{\partial X\partial Y}\right)^2 + \left(\frac{\partial^2\Psi}{\partial Y^2} - \frac{\partial^2\Psi}{\partial X^2}\right)^2\right], \quad (4.34)$$

where, $N_\mu = \frac{\mu_{bf}T_0}{k_{bf}}\left(\frac{\alpha_{bf}}{L(\Delta T)}\right)^2$ is the irreversibility distribution ratio and $S_{\mathrm{GEN}} = S_{\mathrm{gen}}\frac{T_0^2L^2}{k_{bf}(\Delta T)^2}$. The terms of equation (4.34) can be rewritten in the following form:

$$S_{\mathrm{GEN}} = S_\theta + S_\Psi, \quad (4.35)$$

where S_θ and S_Ψ are the entropy generation due to heat transfer irreversibility (HTI) and

nanofluid friction irreversibility (NFI), respectively,

$$S_\theta = \frac{k_{nf}}{k_{bf}}\left[\left(\frac{\partial\theta}{\partial X}\right)^2 + \left(\frac{\partial\theta}{\partial Y}\right)^2\right], \tag{4.36}$$

$$S_\Psi = \frac{\mu_{nf}}{\mu_{bf}} N_\mu \left[4\left(\frac{\partial^2\Psi}{\partial X\partial Y}\right)^2 + \left(\frac{\partial^2\Psi}{\partial Y^2} - \frac{\partial^2\Psi}{\partial X^2}\right)^2\right]. \tag{4.37}$$

By integrating equation (4.35) over the domain, the global entropy generation (GEG) for the present two-dimensional study is obtained

$$\text{GEG} = \int S_{\text{GEN}}\,\mathrm{d}X\mathrm{d}Y = \int S_\theta\,\mathrm{d}X\mathrm{d}Y + \int S_\Psi\,\mathrm{d}X\mathrm{d}Y. \tag{4.38}$$

We mention now the Bejan number to display dominance between heat transfer or nanofluid friction irreversibility:

$$Be = \frac{\int S_\theta\,\mathrm{d}X\mathrm{d}Y}{\int S_{\text{GEN}}\,\mathrm{d}X\mathrm{d}Y}. \tag{4.39}$$

Since Bejan number is the ratio between heat transfer irreversibility (HTI) with the global entropy generation, then when Be > 0.5, the heat transfer irreversibility (HTI) is dominant, while when Be < 0.5, the nanofluid friction irreversibility (NFI) is dominant.

4.3 SOLUTION METHOD

The governing dimensionless equations (4.20)–(4.23) subject to the boundary conditions (4.24)–(4.30) are solved numerically by the finite difference method (FDM). In this study, several grid testings are performed: 10×10, 20×20, 40×40, 60×60, 80×80, 100×100, 120×120, 140×140 and 160×160. Table 4.1 shows the calculated strength of the flow circulation ($\Psi_{\min}$) and average Nusselt number ($\overline{Nu}_{nf}$) at different grid sizes for $Ra = 10^5$, $\phi = 0.04$, $K_r = 1$ and $D = 0.25$. The results show insignificant differences for the 140×140 grids and above. Therefore, for all computations in this study for similar problems to this subsection, the 140×140 uniform grid is employed.

For the validation of data, the results are compared with previously published

Table 4.1 Grid testing for $\Psi_{\min}$ and $\overline{Nu}_{nf}$ at different grid size for $Ra = 10^5$, $\phi = 0.04$, $K_r = 1$ and $D = 0.25$.

Grid size	$\Psi_{\min}$	$\overline{Nu}_{nf}$
10×10	−0.76597	3.7233
20×20	−0.76613	3.7569
40×40	−0.76653	3.7802
60×60	−0.76658	3.7979
80×80	−0.76761	3.8014
100×100	−0.76878	3.8016
120×120	−0.76897	3.8018
140×140	−0.76956	3.8019
160×160	−0.76968	3.8019

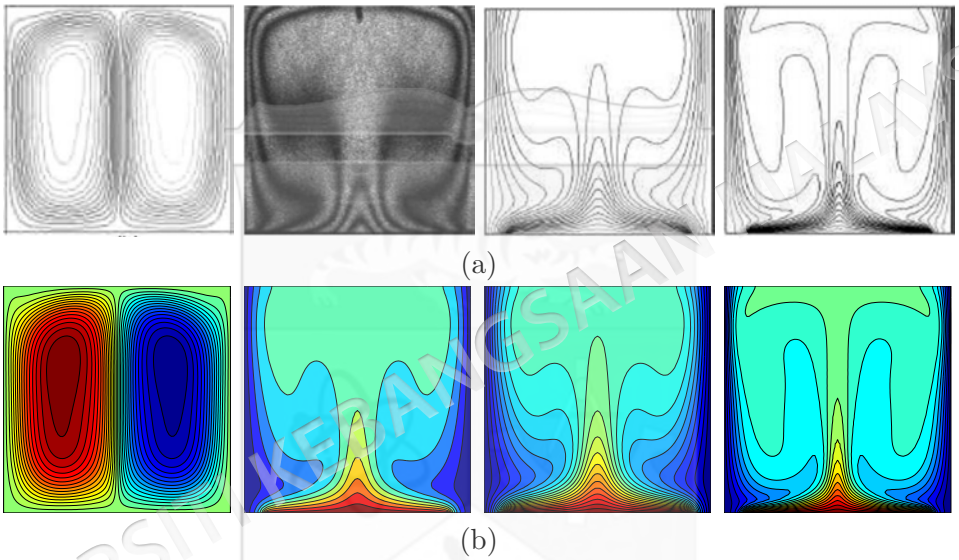

Figure 4.2 Streamlines at $Ra = 10^6$, isotherms at $Ra = 1.836 \times 10^5$, isotherms at $Ra = 10^5$ and isotherms at $Ra = 10^6$ (a) numerical and experimental results of Calcagni et al. (2005) and (b) numerical results of the present study for $\phi = 0$ and $D = 0$.

numerical and experimental results obtained by Calcagni et al. (2005) for the case of natural convection heat transfer in a square cavity partially heated from below, as shown in Figure 4.2. A second validation presented a comparison between the current results and previous published numerical results obtained by Kaluri and Basak (2011) for the case of entropy generation analysis and natural convection in a discretely heated porous square cavity, as shown in Figure 4.3. In addition, a comparison made between the present streamlines, isotherms, local entropy generation due to heat transfer and entropy generation due to fluid friction results and the numerical one presented by Mahapatra et al. (2013) for the case of entropy generation analysis and natural convection in a

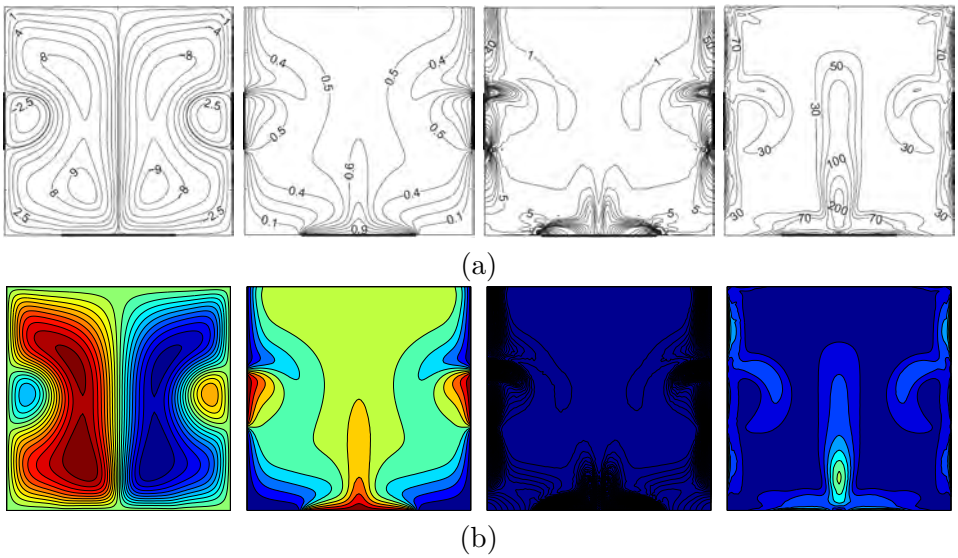

Figure 4.3 Streamlines, isotherms, local entropy generation due to heat transfer and due to fluid friction (a) Kaluri and Basak (2011) and (b) present study for $Ra = 10^6$, $Da = 10^{-3}$, $\phi = 0$ and $D = 0$.

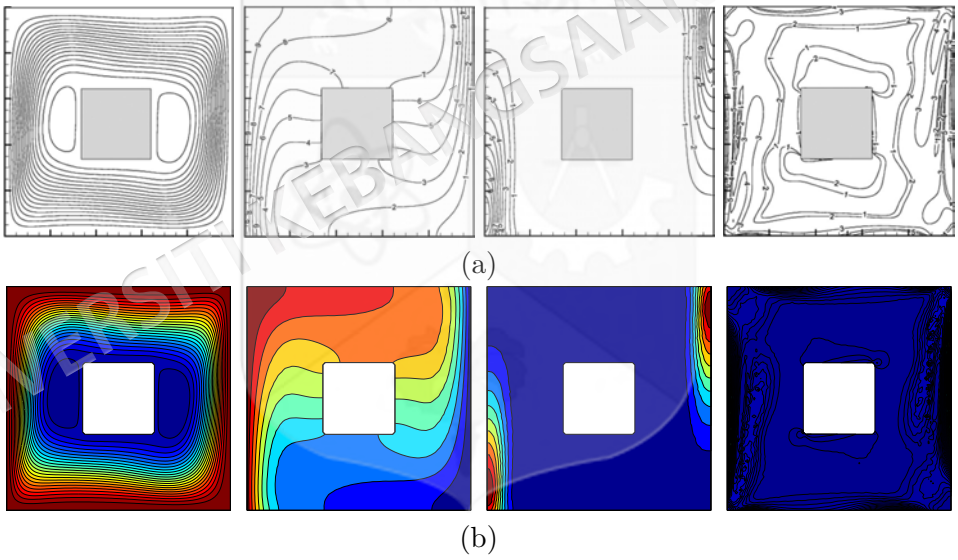

Figure 4.4 Streamlines, isotherms, local entropy generation due to heat transfer and due to fluid friction (a) Mahapatra et al. (2013) and (b) present study for $Ra = 10^5$, $\phi = 0$ and $D = 0.25$.

square cavity in the presence of an adiabatic block, as demonstrated in Figure 4.4. The validation was mainly done by visually comparing how the fluid flows and heat moves in the system. The streamlines were checked to see if the swirling motion, flow direction, and patterns looked similar to those in previous studies. Likewise, the temperature distribution was compared to make sure the heat spread in the expected way. The areas

Table 4.2 Thermo-physical properties of water with Al_2O_3 nanoparticles as Roslan et al. (2011).

Physical properties	Fluid phase (water)	Al_2O_3
Cp (J/kgK)	4179	765
ρ (kg/m^3)	997.1	3970
k (Wm^{-1}K^{-1})	0.613	25
$\beta \times 10^5$ (1/K)	21	0.85
d_p (nm)	3.85	36

where energy is lost due to heat transfer and fluid movement were also examined to see if they appeared in the right places and at the right intensity. Since the visual results closely matched the published ones, this gives strong confidence that the current numerical method is accurate.

4.4 RESULTS AND DISCUSSION

In this section, we present numerical results for the streamlines, isotherms and isentropic lines (the local dimensionless entropy generation) with various values of the nanoparticles volume fraction ($0 \leq \phi \leq 0.09$), the Rayleigh number ($10^3 \leq Ra \leq 10^6$), thermal conductivity ratio (K_r = 0.44, 1, 2.40, 9.90 and 23.8) (epoxy-water: 0.44, brickwork-water: 1, glass-water: 2.40, epoxy-air: 9.90, stainless steel-water: 23.8) and the length of the inner solid ($0 \leq D \leq 0.6$). The values of the average Nusselt number, global entropy generation GEG, overall Bejan number Be are calculated for various values of Ra, ϕ and D. The thermophysical properties of the base fluid (water) and solid Al_2O_3 phases are tabulated in Table 4.2.

Figure 4.5 presents the effect of various volume fraction of nanoparticles on the streamlines (left), isotherms (middle), and isentropic (right) evolution for $Ra = 10^5$, $K_r = 1$ and $D = 0.25$. It is evident that the temperature distribution and flow behaviour of the square cavity are influenced by heating the bottom wall to a constant hot temperature and then dispersing the isothermal cold sources over the top and side walls. Two cells rotate in a clockwise direction at the top left and bottom right of the cavity, while two more cells rotate in an anticlockwise way at the top right and bottom left of the cavity, creating the appearance of a flow inside the cavity. It can be seen that the high

intensity located at the bottom of the cavity was affected by the constant exposure to high temperature on the bottom of the wall. Heating the bottom wall of the cavity causes the appearance of the curved lines in the isotherm patterns with high intensity in nanofluid. As the volume fraction of nanoparticles increases, the strength of the streamlines is augmented due to the combined effects on viscosity and inertial forces. This increase in volume fraction enhances the thermal conductivity of the fluid medium, thereby improving heat transfer and subsequently strengthening the flow. Consequently, a new cell emerges, and its size increases in tandem with the rising volume fraction of nanoparticles. Meanwhile, it is apparent that there is no discernible changing in the isotherm patterns. The intensity of the isentropic patterns tends to increase with the increment of nanoparticles volume fraction resulting to the high thermal conductivity of nanoparticles.

Figure 4.6 shows the result of various Rayleigh number on the streamlines (left), isotherms (middle) and isentropic (right) for $\phi = 0.04$, $K_r = 1$ and $D = 0.25$. At the low Ra value (10^3),the flow inside the cavity exhibits two streamlined rotating cells: an anticlockwise fluid heat flow on the left side and a clockwise fluid heat flow on the right side around the solid square. This phenomenon is attributed to the impact of the vertical walls on the temperature distribution variations. The isotherm patterns exhibit curved lines near the cold sources, with a high intensity of isotherms at the bottom of the wall, indicating the influence of the hot source. The isentropic patterns manifest as spot shapes at both the right and left edges of the cavity walls. As the Rayleigh number increases, the intensity of the streamlines along with the amount and size of the cells increase caused by the strong buoyancy forces compared to the viscous forces. The strength of the flow circulation increase with the Rayleigh numbers being affected by the increment of buoyancy force and convection intensity. As illusrtated in Figure 4.6(d), the flow behavior and temperature distribution are significantly affected at a higher Rayleigh number value. It is observed that the intensity of the nanofluid isotherm patterns increases and occupies more space within the cavity. These isotherm patterns are present at both the hot and cold sources. The intensity of the isotherm patterns within the inner solid also increased with the increase in the Rayleigh number. Even though the intensity of the isentropic patterns of the nanofluid increase until the Rayleigh numbers

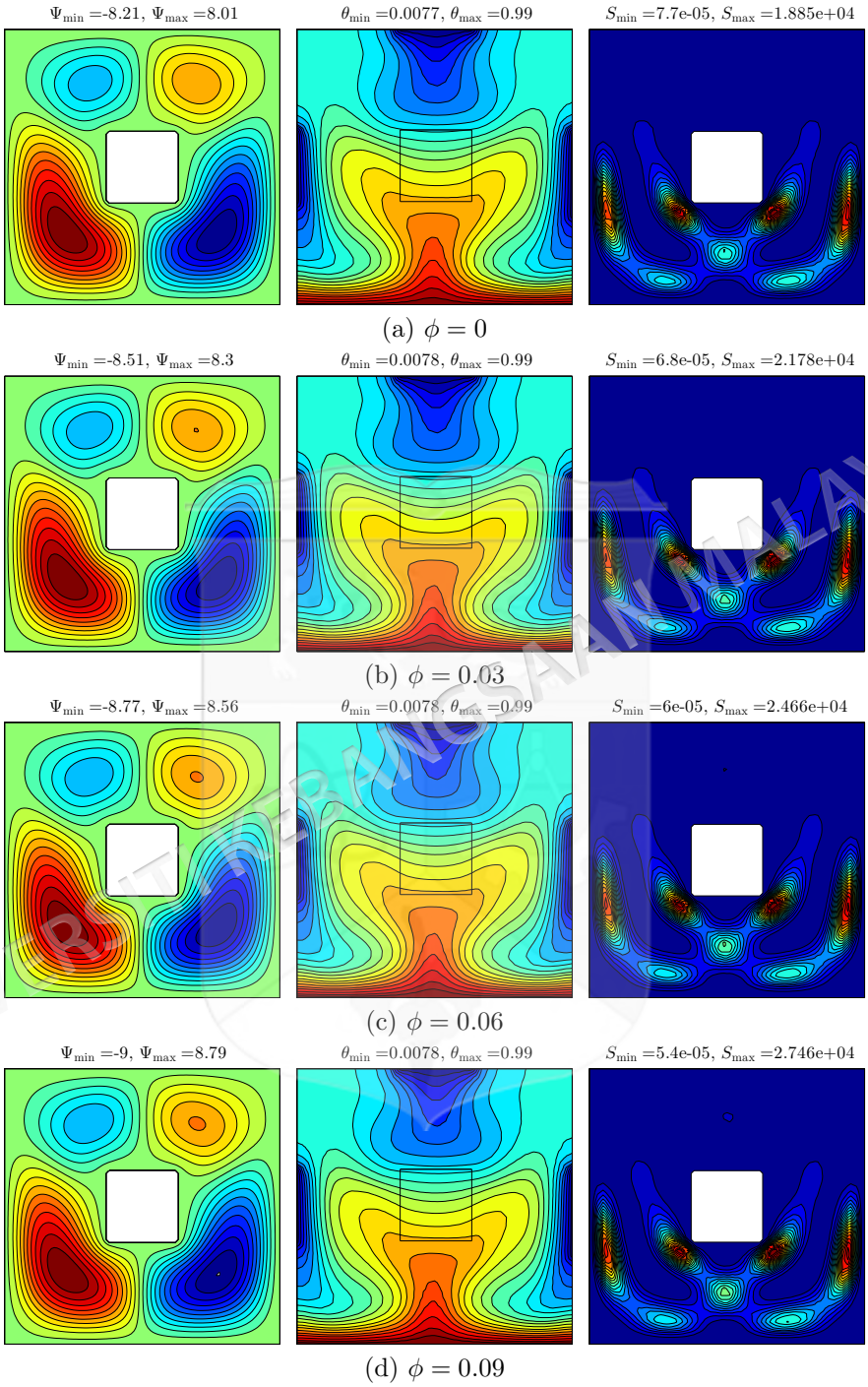

Figure 4.5 Variation of the streamlines (left), isotherms (middle), and isentropic (right) evolution by the solid volume fraction (ϕ) for $Ra = 10^5$, $K_r = 1$ and $D = 0.25$.

at 10^5., the intensity decline after the Rayleigh number at 10^6.

Figure 4.7 demonstrates the effect of various thermal conductivity ratios on the streamlines (left), isotherms (middle) and isentropic (right) for $Ra = 10^5$, $\phi = 0.04$ and $D = 0.25$. At a low thermal conductivity ratio, four rotating cells are evident, with high intensity observed on the bottom wall of the cavity. The isotherm patterns exhibit curved lines along the vertical and bottom walls of the cavity, while the isentropic patterns also display curved lines with high intensity at the bottom of the cavity. This phenomenon is caused by the varied temperature distributions along the vertical and horizontal walls. As thermal conductivity ratio increases, the strength and intensity of the streamlines decrease while we observed that the cell at top right vertical wall disappeared due to the fact that the resistance of the solid inner cavity inclines to reduce the thermal conductivity ratio. Additionally, the intensity of the isotherm patterns decreased due to the reduction in the thermal resistance of the solid inner square, which facilitated greater heat transfer within the cavity as a result of the increased thermal conductivity ratio. Meanwhile, the intensity of isentropic patterns along with the size of cells increase as thermal conductivity ratio increases.

Figure 4.8 depicts the effect of various lengths of the inner solid square on the streamlines (left), isotherms (middle) and isentropic (right) for $Ra = 10^5$, $\phi = 0.04$ and $K_r = 1$. Figure 4.8(a) shows the flow behaviour and temperature distribution within the cavity in the absence of the inner solid square ($D = 0$). It can be observed that the streamline within the cavity tends to form a primary cell located in the center of the cavity, with a secondary cell adjacent to the left vertical side. The minimum strength of the flow circulation decreases with the insertion of the inner solid square. Meanwhile, the maximum strength of the flow circulation increases. This phenomenon is influenced by the viscosity and the inertial force in addition to the higher resistance of the inner solid. Consequently, increasing the length of the inner solid wall significantly affects the distribution of the flow and temperature profiles. The vertical expansion of the primary streamline enables the formation of two additional cells on the solid inner square. On the contrary, the secondary cell expand vertically with the increase of the inner solid length because of the thermal property of the solid insert. The intensity and number of isotherm patterns of the nanofluid are distinctly increased within the solid inner square.

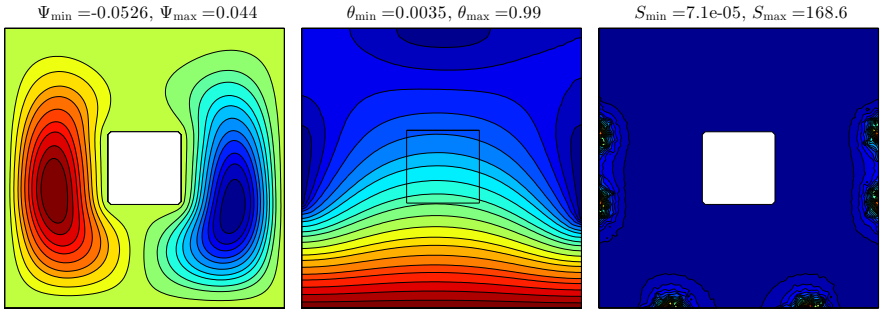

(a) $Ra = 10^3$

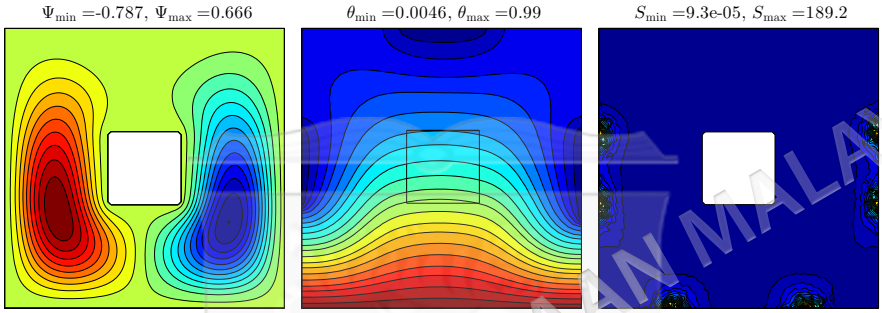

(b) $Ra = 10^4$

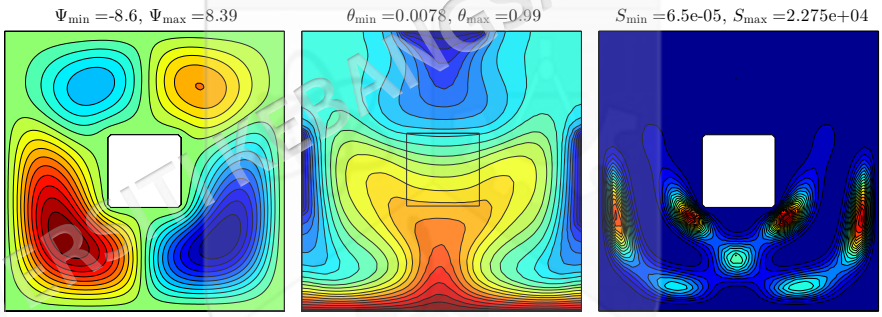

(c) $Ra = 10^5$

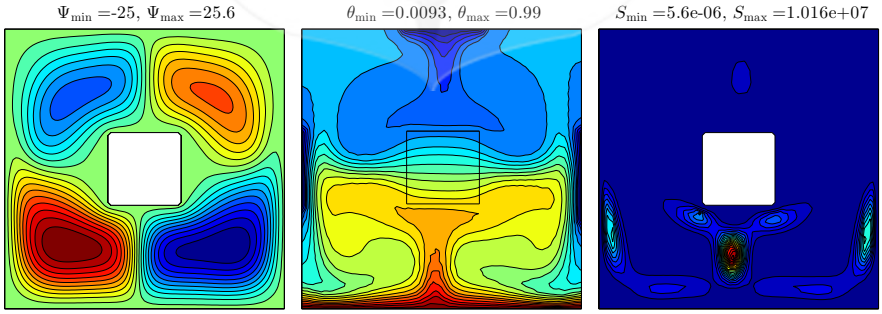

(d) $Ra = 10^6$

Figure 4.6 Variation of the streamlines (left), isotherms (middle), and isentropic (right) evolution by Rayleigh number (Ra) for $\phi = 0.04$, $K_r = 1$ and $D = 0.25$.

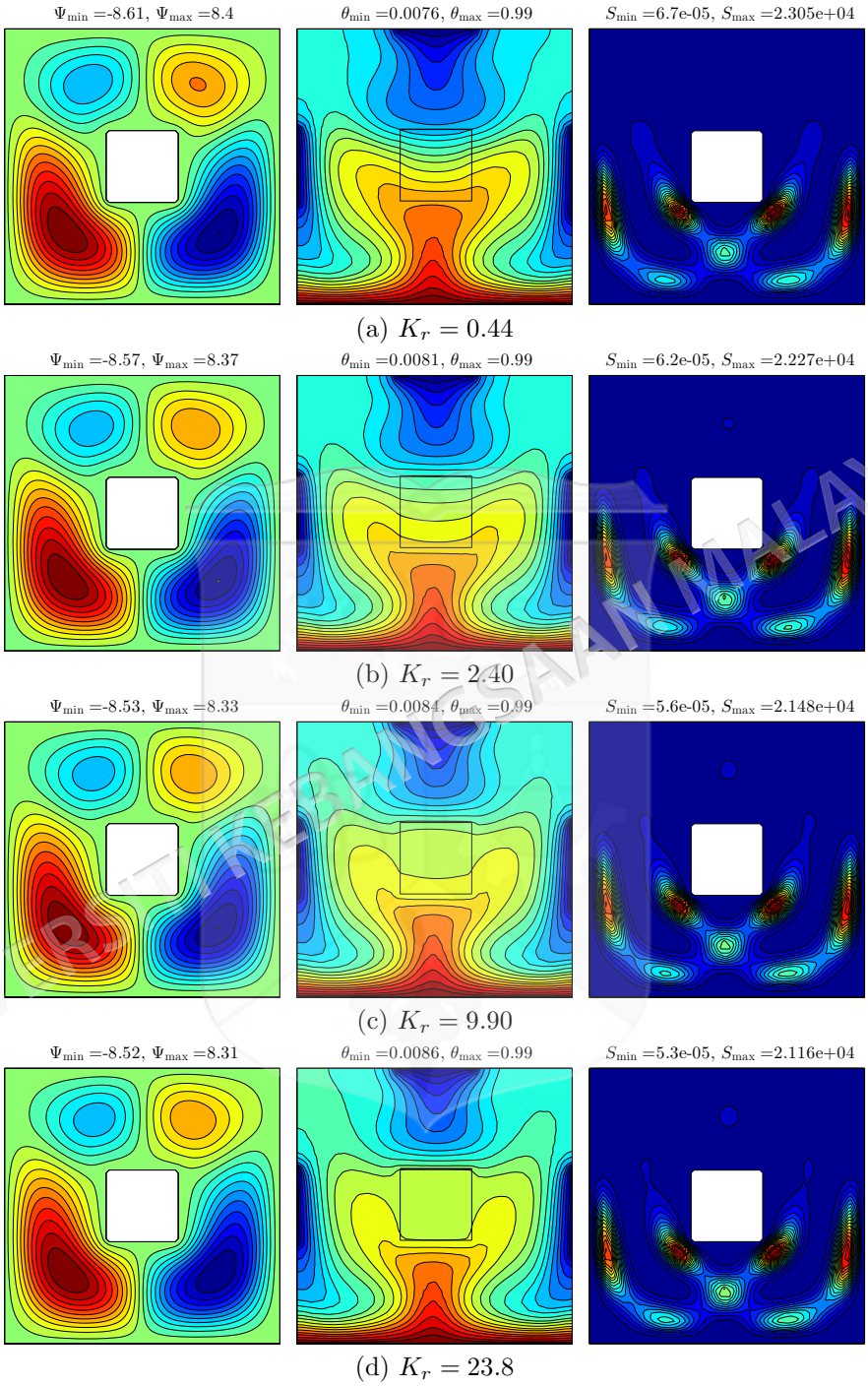

Figure 4.7 Variation of the streamlines (left), isotherms (middle), and isentropic (right) evolution by thermal conductivity ratio (K_r) for $Ra = 10^5$, $\phi = 0.04$ and $D = 0.25$.

This is attributed to the difference between the thermal conductivity of the nanofluid and the thermal conductivity of the solid insert, leading to greater heat absorption by the medium with higher thermal conductivity. Meanwhile, the intensity of the isentropic lines reduces as the length of the inner cavity increases.

Figure 4.9 illustrates the effects of various values of the Rayleigh numbers and the volume fraction of nanoparticles on the local Nusselt number, and along the X coordinates for $K_r = 1$ and $D = 0.25$. Due to the presence of a heated source at the bottom wall and cooled sources on the left, right, and top walls of the cavity, the local Nusselt numbers exhibit a sinusoidal pattern for all Rayleigh numbers and nanoparticle volume fractions. Increasing the Rayleigh numbers enhances the local heat transfer as illustrated in Figure 4.9(a). Meanwhile, the convective heat transfer increases by the augmentation of nanoparticles volume fraction, as illustrated in Figure 4.9(b).

Figure 4.10 illustrates the effects of various values of the thermal conductivity ratio and the length of inner cavity on the local Nusselt number, and along the X coordinates for $Ra = 10^5$ and $\phi = 0.04$. Similar to the preceding figure, the local Nusselt number exhibits a sinusoidal pattern across all thermal conductivity ratios and inner solid lengths due to the varying heating systems on the cavity walls. The maximum value of the local Nusselt number is achieved at $K_r = 2.40$ while in Figure 4.10(b), the absence of an inner solid results in the highest local Nusselt number, attributed to the lack of heat resistance from the inner solid square.

A comprehensive imagination about the overall heat transfer is illustrated by the average Nusselt number. Hence, Figure 4.11 indicates the average Nusselt number with different Rayleigh numbers on (a) nanoparticles volume fraction, (b) the thermal conductivity ratio and (c) the length of the inner cavity. We clearly observe that the convective heat transfer increases when Rayleigh numbers is 10^4 for all figures. This is due to the strong buoyancy forces compared to the viscous forces at higher Rayleigh numbers. In Figs. 4.11(a) and 4.11(b), the application of the higher nanoparticles volume fraction (a) and the higher thermal conductivity ratio (b) significantly increase the heat transfer rate, which results in a maximum average Nusselt number. Furthermore, the application of lower inner of cavity increases the heat transfer rate, which results

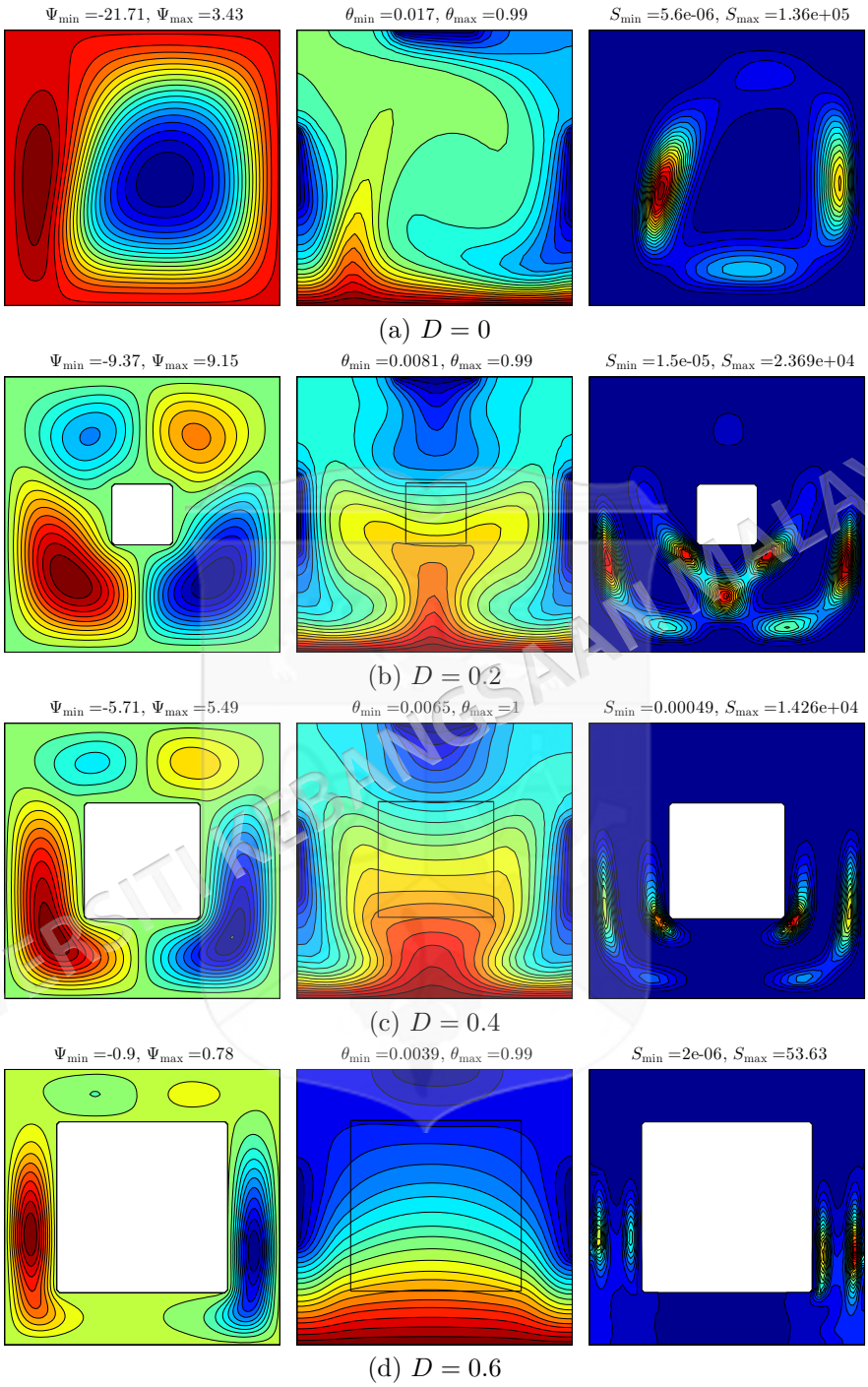

Figure 4.8 Variation of the streamlines (left), isotherms (middle), and isentropic (right) evolution by the length of the inner solid (D) for $Ra = 10^5$, $\phi = 0.04$ and $K_r = 1$.

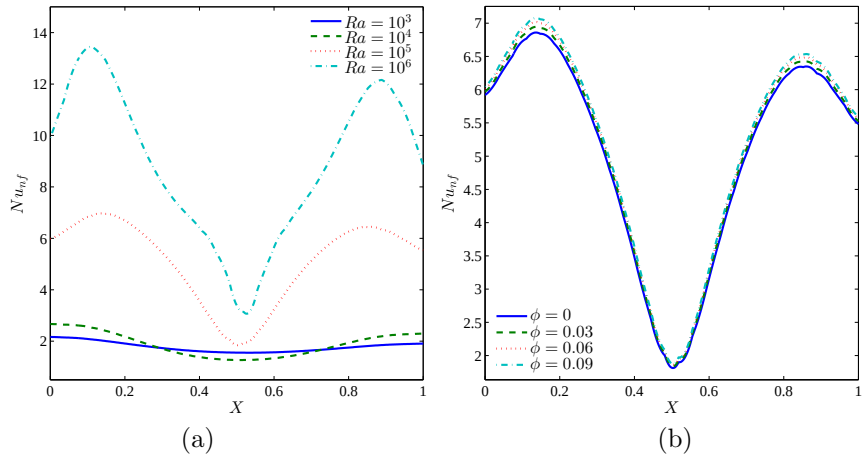

Figure 4.9 Variation of local Nusselt number interfaces with X for different (a) Ra and (b) ϕ at $K_r = 1$ and $D = 0.25$.

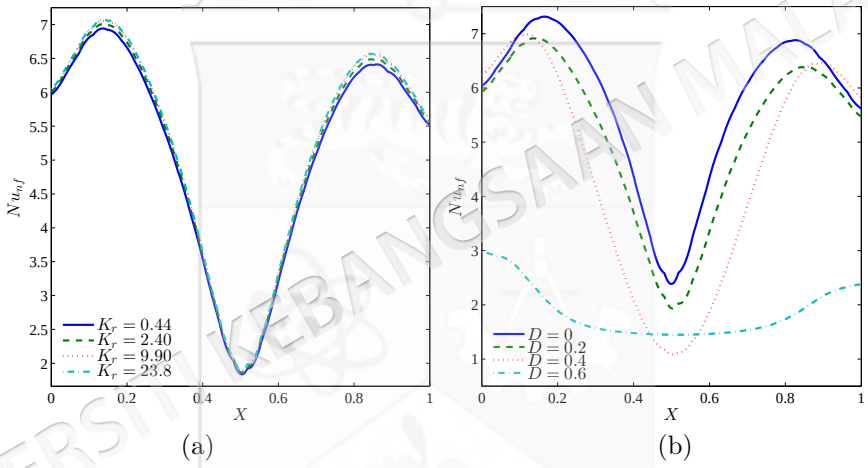

Figure 4.10 Variation of local Nusselt number interfaces with X for different (a) K_r and (b) D at $Ra = 10^5$ and $\phi = 0.04$.

in a maximum average Nusselt number. However, a diverse behaviour appears on the heat transfer rate with the increase of Rayleigh number in $[4.83 \times 10^5, 10^6]$ for the case of $D = 0.4$. The rate of the heat transfer shows a reduction function with an increment of Rayleigh number in $[4.83 \times 10^5, 6.95 \times 10^5]$, while beyond that when the value of Ra is between $[6.95 \times 10^5, 10^6]$, the heat transfer rate tends to enhance. This phenomenon is attributed to the significant enhancement of convective heat transfer by the inner solid. A larger inner solid insert reduces the gap between the cavity wall and the inner solid, resulting in accelerated fluid flow, which increases convective heat transfer at relatively low Rayleigh numbers. However, as the Rayleigh number

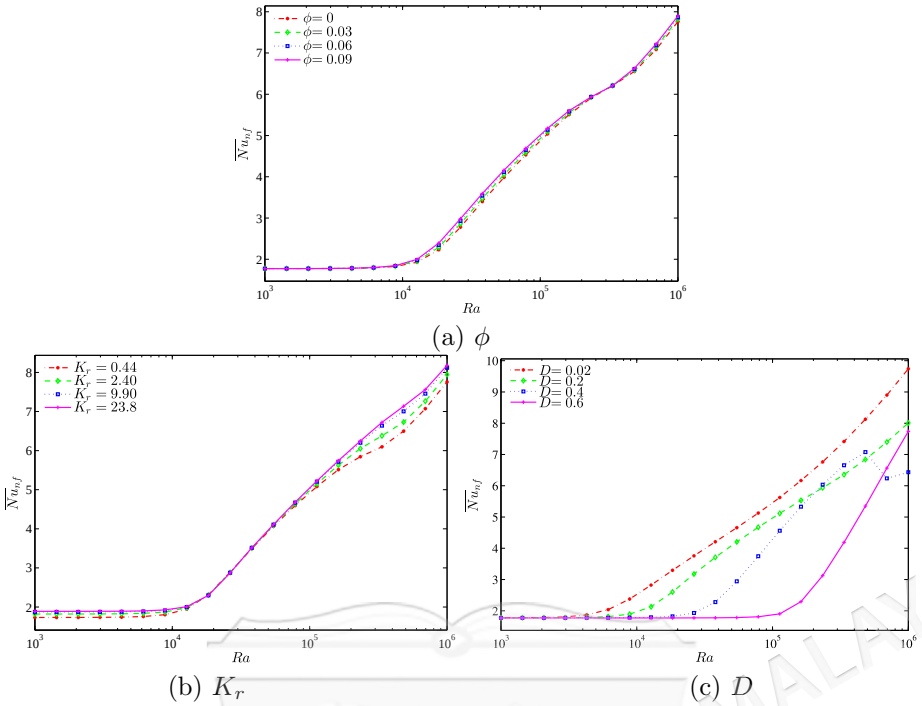

Figure 4.11 Variation of average Nusselt number with Ra for different (a) ϕ, (b) K_r and (c) D.

increases, a contrasting behavior is observed. In the narrow gap between the wall and the inner solid block, a relatively high Rayleigh number induces high fluid velocity, which subsequently slows down the heat transfer process. The unexpected increase in heat transfer at very high Rayleigh numbers can be attributed to the onset of turbulent convection in the narrow space between the wall and the inner solid, where the dynamics become spatio-temporally chaotic.

In Figure 4.12, we observe an interesting result in relation to the influence of the Rayleigh numbers, thermal conductivity ratio and the length of the inner cavity on the average Nusselt number with different nanoparticles volume fractions. It is observed that convective heat transfer is minimally impacted by the increase in nanoparticle volume fractions. However, the heat transfer rate increases with rising Rayleigh numbers. Furthermore, a substantial enhancement in the heat transfer rate is observed when the Rayleigh number increases from 10^4 to 10^5 compared to other values of the Rayleigh number. This is attributed to the significant increase in buoyancy forces relative to viscous forces within this Rayleigh number range, clearly demonstrating a notable improvement in the heat transfer rate.in comparison to other values of Rayleigh

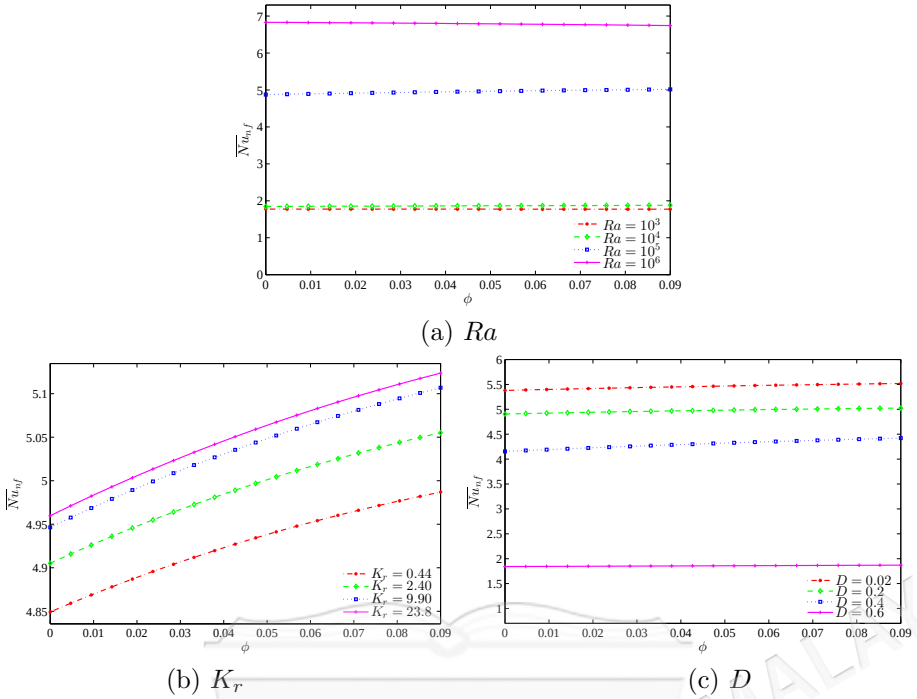

(a) Ra

(b) K_r (c) D

Figure 4.12 Variation of average Nusselt number with ϕ for different (a) Ra, (b) K_r and (c) D.

number. Figure 4.12(b) illustrates the effect of various thermal conductivity ratios on the average Nusselt number with different nanoparticles volume fractions. In line with prior findings, the overall heat transfer remains relatively unaffected by variations in nanoparticle volume fraction. However, convective heat transfer is notably enhanced with increasing nanoparticle volume fractions, primarily due to their superior thermal conductivity. Moreover, it is evident that heat transfer rates increase proportionally with higher thermal conductivity ratios, as this reduces thermal resistance due to the reduction of the thermal resistance and facilitates greater heat transfer within the cavity. Figure 4.12(c) depicts the effect of various lengths of the inner solid square on the average Nusselt number with different nanoparticles volume fractions. An increase in nanoparticle volume fraction results in heightened convective heat transfer owing to enhanced thermal conductivity. It is evident from our observations that the overall heat transfer is minimally impacted by increments in nanoparticle volume fraction. In addition to that, the overall heat transfer decreases with an increase in the length of the inner cavity due to higher heat resistance of the solid inner square, which in result decreases the temperature gradient and the resulting in less heating effect.

Figure 4.13 demonstrates the effect of various Rayleigh numbers, volume of nanoparticles and thermal conductivity ratios on the average Nusselt number with different inner solid lengths. We observed from Figure 4.13(a) that by increasing the length of the inner solid square, it causes the reduction in average Nusselt number at high Rayleigh numbers. This is due to the higher resistance occured by the increase in the inner solid length. On the other hand, at lower Rayleigh numbers, we clearly observe that the average Nusselt number is less affected with an increase in inner solid length. Figure 4.13(b) depicts the effect of various nanoparticles volume fraction on the average Nusselt number with different inner solid length. As the length of the inner solid square increases, the overall heat transfer consequently decreases for all nanoparticles volume fractions. Furthermore, we clearly observe that due to the higher thermal conductivity of nanoparticles, the convective heat transfer increases with an increase in the nanoparticles volume fraction. Figure 4.13(c) illustrates the effect of the various thermal conductivity ratio on the average Nusselt number with different inner solid length. By increasing the length of the inner cavity up to the low value ($D \leq 0.55$), the convective heat transfer decreases for all thermal conductivity ratios affected by the resistance of the solid inner cavity, which reduces the convective heat transfer. However, we can observe the increment of the average Nusselt number with an increase in D in $[0.55, 0.7]$, particularly for high thermal conductivity ratios.

Figure 4.14 depicts the variation in global entropy generation and the Bejan number across different Rayleigh numbers (Ra) and various nanoparticles voluma fractions. In Figure 4.14(a), the global entropy generation remains constant at low Rayleigh numbers $Ra < 10^5$. While in the range of ($Ra > 10^5$). However, as Ra exceeds $Ra > 10^5$, GEG increases across all nanoparticle volume fractions, particularly notable at higher fraction ($\phi = 0.09$). This is because of the intensified inertia and viscous effects within the nanofluid. Conversely, Figure 4.14(b) illustrates that nanoparticles mitigate heat transfer irreversibility (HTI) over a broad range of Rayleigh numbers considered.

The effects of the inner solid length towards global entropy generation and Bejan number are presented as a function of the Rayleigh number in Figure 4.15. At lower Rayleigh numbers, no changes are observed in global entropy generation across all

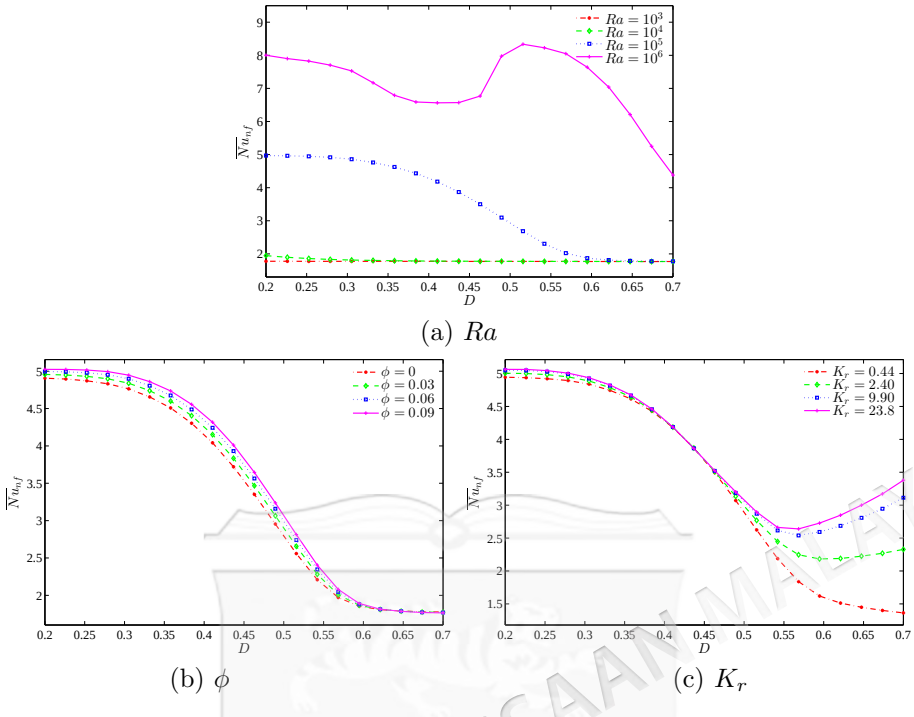

(a) Ra

(b) ϕ (c) K_r

Figure 4.13 Variation of average Nusselt number with D for different (a) Ra, (b) ϕ and (c) K_r.

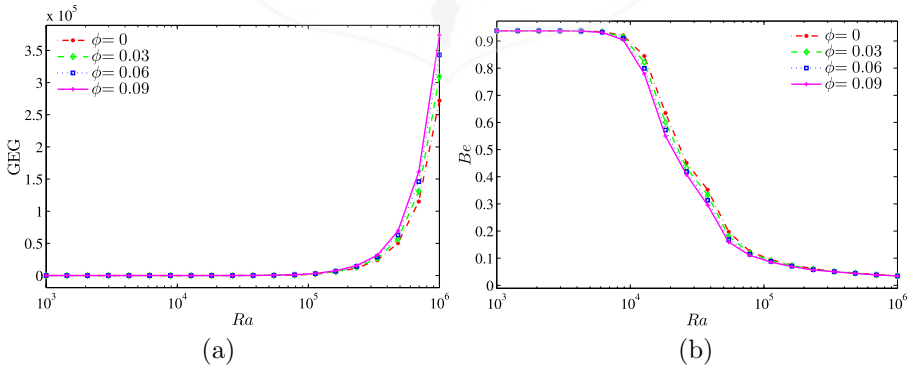

(a) (b)

Figure 4.14 Variation of (a) the global entropy generation (GEG) and (b) Bejan number (Be) with Ra for different values of ϕ at $K_r = 1$ and $D = 0.25$.

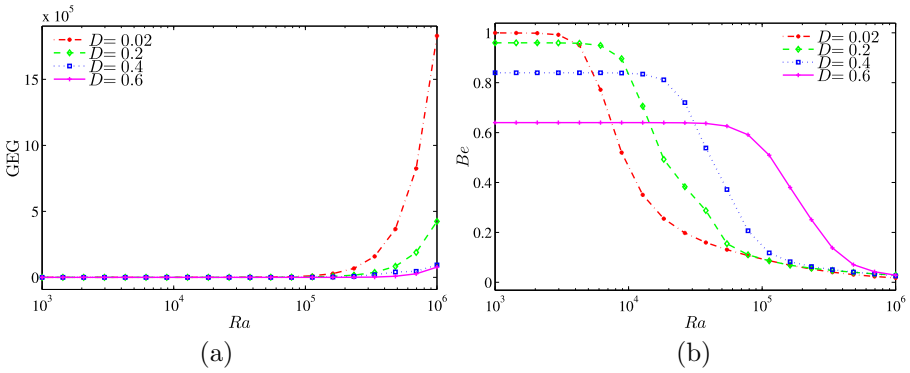

Figure 4.15 Variation of (a) the global entropy generation (GEG) and (b) Bejan number (Be) with Ra for different values of D at $\phi = 0.04$ and $K_r = 1$.

inner solid lengths. However, for $Ra \geq 10^5$, global entropy generation increases for all inner solid lengths, particularly pronounced at shorter lengths ($D = 0.02$). On the other hand, the Bejan number decreases with the increasing inner solid length. Heat transfer irreversibility predominates ($Be > 0.5$) at lower Rayleigh number while nanofluid friction irreversibility (NFI) dominates at higher Rayleigh numbers.

Figure 4.16 presents the variation of global entropy generation (GEG) and Bejan number with nanoparticles volume fraction across different thermal conductivity ratio. In Figure 4.16(a), the graph indicates that the GEG increases with rising nanoparticles volume fraction for all thermal conductivity ratio with higher value observed at lower thermal conductivity ratio due to the reduced thermal conductivity. Figure 4.16(b) indicates that nanofluid irreversibility is dominant across all thermal conductivity ratios.

Figure 4.17 shows the variation of the global entropy generation (GEG) and Bejan number with nanoparticles volume fraction for different inner solid length. An increase in global entropy generation with rising nanoparticle volume fractions is observed only for the smaller inner cavity length ($D = 0.02$), whereas global entropy generation remains constant for larger inner solid lengths. In Figure 4.17(b), the Bejan number is lower at shorter inner solid lengths but increases as the inner solid length increases. This indicates that heat transfer irreversibility is dominant at longer inner solid lengths, while nanofluid friction irreversibility (NFI) is more prominent at shorter inner solid lengths.

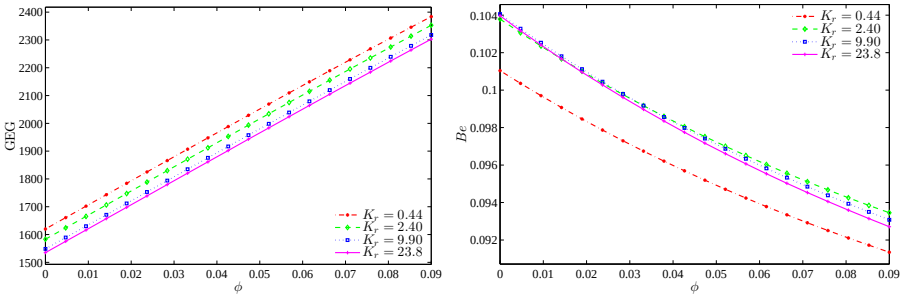

(a) (b)

Figure 4.16 Variation of (a) the global entropy generation (GEG) and (b) Bejan number (Be) with ϕ for different values of K_r at $Ra = 10^5$ and $D = 0.25$.

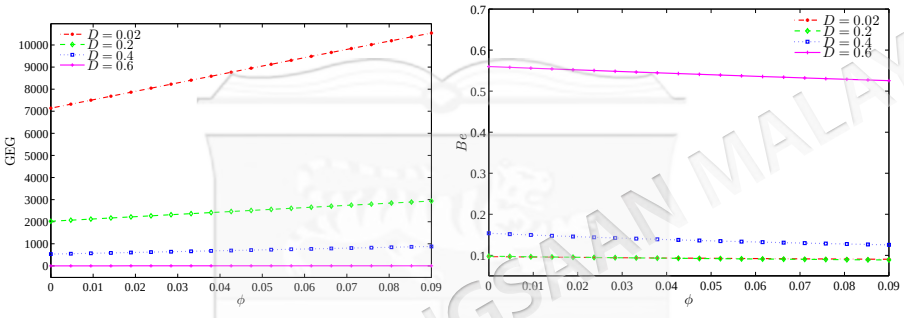

(a) (b)

Figure 4.17 Variation of (a) the global entropy generation (GEG) and (b) Bejan number (Be) with ϕ for different values of D at $Ra = 10^5$ and $K_r = 1$.

Figure 4.18 shows the variation of the global entropy generation (GEG) and Bejan number with the size of the inner solid for different values of Rayleigh numbers at $\phi = 0.04$ and $K_r = 1$. There has been no augmentation on the global entropy generation at low Rayleigh numbers. However, at the higher Rayleigh number ($Ra = 10^6$) the global entropy generation tends to enhance. The GEG is a decreasing function as the inner solid increases. In Figure 4.18(b), we observe that the Bejan number exhibits high values when the Rayleigh numbers are low. However, as the Rayleigh numbers increase, there is a noticeable decline in the Bejan number. It shows that the HTI is dominant at the higher Rayleigh number while NFI is dominant at the smaller Rayleigh number. However, at $Ra = 10^5$, the HTI dominant is switched to NFI as the inner solid increases.

Figure 4.19 presents the variation of the global entropy generation (GEG) and

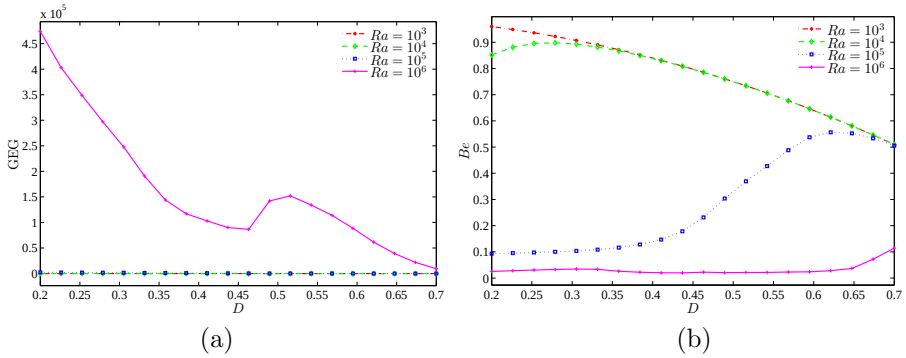

Figure 4.18 Variation of (a) the global entropy generation (GEG) and (b) Bejan number (Be) with D for different values of Ra at $\phi = 0.04$ and $K_r = 1$.

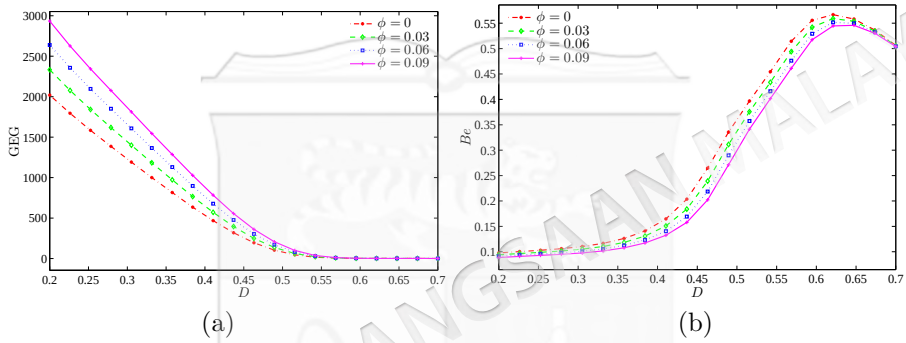

Figure 4.19 Variation of (a) the global entropy generation (GEG) and (b) Bejan number (Be) with D for different values of ϕ at $Ra = 10^5$ and $K_r = 1$.

Bejan number with D for different values of ϕ at $Ra = 10^5$ and $K_r = 1$. This figure shows that the GEG is a decreasing function for all nanoparticles volume fractions as the inner solid increases. However, there is no changes observed on the global entropy generation for the high inner solid ($D \geq 0.5$). The global entropy generation is strong at the higher nanoparticles volume fraction due to the high thermal conductivity of nanoparticles. Meanwhile in Figure 4.19(b) it shows that the Bejan number is very weak with the small inner solid and for all nanoparticles volume fractions. Also, this figure indicates that the NFI is dominant for all nanoparticles volume fraction at the small inner solid. However, for all nanoparticles volume fraction, the system is HTI dominant at $D = 0.55$.

Figure 4.20 shows that the global entropy generation (GEG) and Bejan number with D for different values of thermal conductivity ratio at $Ra = 10^5$ and $\phi = 0.04$. The GEG is decreasing for all thermal conductivity ratios as the inner solid increases. The

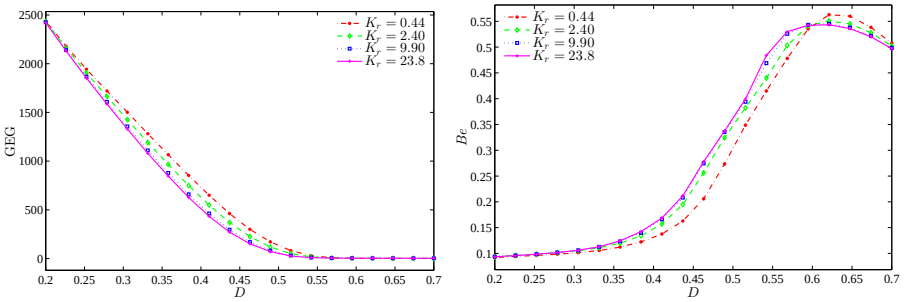

(a) (b)

Figure 4.20 Variation of (a) the global entropy generation (GEG) and (b) Bejan number (Be) with D for different values of K_r at $Ra = 10^5$ and $\phi = 0.04$.

GEG does not exist for the high inner solid ($D \geq 0.55$). Figure 4.20(b) shows that the NFI is dominant for all thermal conductivity ratio for a small inner solid. However, the NFI dominance is changed to HTI dominance as the inner solid reaches up to 0.55.

4.5 CONCLUSIONS

In the present numerical study, the finite difference method (FDM) is employed to analyze the entropy generation analysis and natural convection in a nanofluid square cavity with a concentric solid insert and different temperature distributions. The detailed computational results for the streamlines, isotherms and local entropy generation within the considered cavity for the laminar flow, and the local and average Nusselt numbers are shown graphically for different values of volume fraction of nanoparticles, Rayleigh number, thermal conductivity ratio, and inner solid length. Some important conclusions from the study are given below:

1. The insertion of the inner solid significantly impacts the flow behavior, temperature distribution, and local entropy generation. This effect is primarily due to the resistance introduced by conductive heat transfer within the solid inner square, which alters the thermal and fluid dynamics within the system.
2. A substantial enhancement in heat transfer rate is observed with the increasing of Rayleigh number from 10^4 to 10^5 as compared to the other values. The enhancement happened because of a significant increment of the buoyancy forces

compared to the viscous forces in the specific range of Rayleigh number.

3. The rate of heat transfer is notably affected by both the thermal property and the size of the inner solid square. When a larger solid insert is present, it restricts convective heat transfer within the square cavity, especially when the solid insert possesses lower thermal conductivity. Meanwhile the higher thermal conductivity of the solid promotes increased the heat transfer rate by facilitating more efficient thermal energy transport within the cavity.
4. As the Rayleigh number increases, there is a corresponding increase in the global entropy generation, indicating a positive correlation between these variables. In contrast, the average Bejan number exhibits a contrasting behavior, showing a tendency to decrease as the Rayleigh number rises.
5. There is a notable reduction in global entropy generation when the size of the inner solid increases for the case of intensive convection regime ($Ra \geq 10^5$), while average Bejan number is a growth function of the size of the inner solid of the same regime.
6. Global entropy generation is reduced by a larger solid insert characterized by high thermal resistance. On the other hand, global entropy generation exhibits strength at higher nanoparticle volume fractions, while a relatively larger solid insert positively impacts the average Bejan number.

CHAPTER V

EFFECT OF FINITE WALL THICKNESS ON ENTROPY GENERATION AND NATURAL CONVECTION IN A NANOFLUID-FILLED PARTIALLY HEATED SQUARE CAVITY

5.1 INTRODUCTION

Natural convection heat transfer in a cavity is investigated by many researchers because of its wide application areas. The usage of nanofluids as working media on natural convection heat transfer in a cavity has gained attention of researchers in recent years. The problem of natural convection with various thermal boundary conditions in closed cavities filled with nanofluids has been given considerable attention by several studies. Entropy generation because of natural convection is an important issue in engineering applications because it gives information about local and global losses of energy because of heat transfer and fluid friction irreversibility. Conjugate convection is the convection because of thermal interaction between fluids and solids. In the recent years, much attention was received by the conjugate convection heat transfer in cavities because of its significance in various engineering systems.

According to past researches mentioned above and to the authors' best knowledge, the gap regarding the problem with entropy generation analysis and natural convection in partially heated square cavity has yet to be filled. Due to this, this study aims to investigate the entropy generation analysis as well as the natural convection in nanofluid-filled square cavity which was heated partially. A square cavity with an isothermal heater is located on the bottom solid horizontal wall of the cavity and partly cold sidewalls are important problems in thermal processing applications. Hence, the authors believe that this present work will be a valuable contribution in improving the thermal performance.

5.2 MATHEMATICAL FORMULATION

The steady two-dimensional natural convection problem in a square cavity with length L and having a solid wall placed at the bottom with length d, as illustrated in Figure 5.1. An isothermal heater is placed on the bottom solid horizontal wall of the cavity with length h while the wavy vertical walls are maintained at a constant cold temperature T_c. The remainder of the bottom wall and the top wall are kept adiabatic. The boundaries of the domain are assumed to be impermeable, the fluid within the cavity is a water-based nanofluid having Al_2O_3 nanoparticles. The Boussinesq approximation is applicable. By considering these assumptions, the continuity, momentum and energy equations for the Newtonian fluid, laminar and steady state flow can be written as follows:

$$\frac{\partial u}{\partial x} + \frac{\partial v}{\partial y} = 0, \tag{5.1}$$

$$u\frac{\partial u}{\partial x} + v\frac{\partial u}{\partial y} = -\frac{1}{\rho_{nf}}\frac{\partial p}{\partial x} + \nu_{nf}\left(\frac{\partial^2 u}{\partial x^2} + \frac{\partial^2 u}{\partial y^2}\right), \tag{5.2}$$

$$u\frac{\partial v}{\partial x} + v\frac{\partial v}{\partial y} = -\frac{1}{\rho_{nf}}\frac{\partial p}{\partial y} + \nu_{nf}\left(\frac{\partial^2 v}{\partial x^2} + \frac{\partial^2 v}{\partial y^2}\right) + \beta_{nf}\cdot g(T_{nf} - T_0), \tag{5.3}$$

$$u\frac{\partial T}{\partial x} + v\frac{\partial T}{\partial y} = \alpha_{nf}\left(\frac{\partial^2 T}{\partial x^2} + \frac{\partial^2 T}{\partial y^2}\right). \tag{5.4}$$

The energy equation of the solid wall is:

$$\frac{\partial^2 T_w}{\partial x^2} + \frac{\partial^2 T_w}{\partial y^2} = 0, \tag{5.5}$$

where x and y are the Cartesian coordinates measured in the horizontal and vertical directions respectively, g is the acceleration due to gravity, ρ_{nf} is the density of the nanofluid and ν_{nf} is the kinematic viscosity of the nanofluid. The thermo-physical properties of the nanofluid including heat capacitance $(\rho C_p)_{nf}$, effective thermal diffusivity α_{nf}, effective density ρ_{nf}, thermal expansion coefficient β_{nf}, can be explained respectfully as the following:

$$(\rho C_p)_{nf} = (1-\phi)(\rho C_p)_f + \phi(\rho C_p)_p, \tag{5.6}$$

$$\alpha_{nf} = \frac{k_{nf}}{(\rho C_p)_{nf}}, \tag{5.7}$$

$$\rho_{nf} = (1-\phi)\rho_f + \phi\rho_p, \tag{5.8}$$

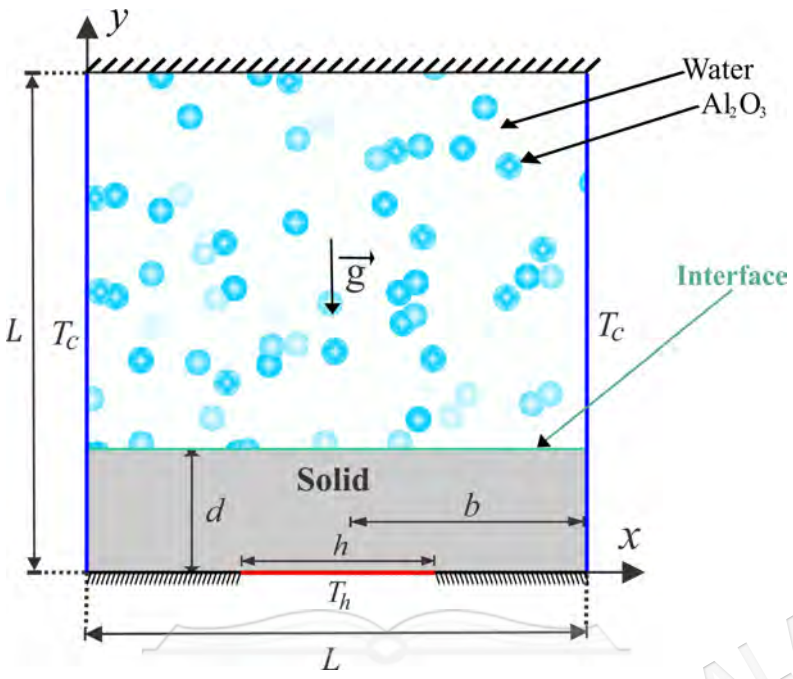

Figure 5.1 Physical model of convection in a square cavity together with conducting wall and coordinate system.

$$(\rho\beta)_{nf} = (1-\phi)(\rho\beta)_f + \phi(\rho\beta)_p. \tag{5.9}$$

While the dynamic viscosity ratio of water-Al_2O_3 nanofluids for 33nm particle-size in the ambient condition is described by Corcione (2011) as follows.

$$\frac{\mu_{nf}}{\mu_f} = 1/\left(1 - 34.87\left(d_p/d_f\right)^{-0.3}\phi^{1.03}\right). \tag{5.10}$$

And the thermal conductivity ratio of water-Al_2O_3 nanofluids is calculated by Corcione (2011) as the following:

$$\frac{k_{nf}}{k_f} = 1 + 4.4\mathrm{Re}_B^{0.4}\mathrm{Pr}^{0.66}\left(\frac{T}{T_{fr}}\right)^{10}\left(\frac{k_p}{k_f}\right)^{0.03}\phi^{0.66}, \tag{5.11}$$

where Re_B is defined as

$$\mathrm{Re}_B = \frac{\rho_f u_B d_p}{\mu_f}, \quad u_B = \frac{2k_bT}{\pi\mu_f d_p^2}, \tag{5.12}$$

where $k_b = 1.380648 \times 10^{-23}(J/K)$ is the Boltzmann constant. $l_f = 0.17\mathrm{nm}$ is the mean path of fluid particles. d_f is the molecular diameter of water given as Corcione

(2011)

$$d_f = \frac{6M}{N\pi\rho_f}, \tag{5.13}$$

where M is the molecular weight of the base fluid, N is the Avogadro number and ρ_f is the density of the base fluid at standard temperature (310K). Accordingly, and basing on water as a base fluid, the value of d_f is obtained:

$$d_f = \left(\frac{6 \times 0.01801528}{6.022 \times 10^{23} \times \pi \times 998.26}\right)^{1/3} = 3.85 \times 10^{-10}\text{m}. \tag{5.14}$$

Now we introduce the following non-dimensional variables:

$$X = \frac{x}{L}, \quad Y = \frac{y}{L}, \quad U = \frac{uL}{\alpha_f}, \quad V = \frac{vL}{\alpha_f}, \quad \theta = \frac{T - T_c}{T_h - T_c}, \quad \theta_w = \frac{T_w - T_c}{T_h - T_c},$$
$$D = \frac{d}{L}, \quad \text{Pr} = \frac{\nu_f}{\alpha_f}, \quad Ra = \frac{g\beta_f (T_h - T_c) L^3}{\nu_f \alpha_f}, \quad P = \frac{pL^2}{\rho_f \alpha_f^2}, \quad H = \frac{h}{L}. \tag{5.15}$$

The dimensionless governing equations are obtained as:

$$\frac{\partial U}{\partial X} + \frac{\partial V}{\partial Y} = 0, \tag{5.16}$$

$$U\frac{\partial U}{\partial X} + V\frac{\partial U}{\partial Y} = -\frac{\partial P}{\partial X} + \text{Pr}\,\frac{\rho_f}{\rho_{nf}}\frac{\mu_{nf}}{\mu_f}\left(\frac{\partial^2 U}{\partial x^2} + \frac{\partial^2 U}{\partial Y^2}\right), \tag{5.17}$$

$$U\frac{\partial V}{\partial X} + V\frac{\partial V}{\partial Y} = -\frac{\partial P}{\partial Y} + \text{Pr}\,\frac{\rho_f}{\rho_{nf}}\frac{\mu_{nf}}{\mu_f}\left(\frac{\partial^2 V}{\partial X^2} + \frac{\partial^2 V}{\partial Y^2}\right) + \frac{(\rho\beta)_{nf}}{\rho_{nf}\beta_f} Ra\,\text{Pr}\,\theta, \tag{5.18}$$

$$U\frac{\partial \theta}{\partial X} + V\frac{\partial \theta}{\partial Y} = \frac{(\rho C_p)_f}{(\rho C_p)_{nf}}\frac{k_{nf}}{k_f}\left(\frac{\partial^2 \theta}{\partial X^2} + \frac{\partial^2 \theta}{\partial Y^2}\right), \tag{5.19}$$

$$\frac{\partial^2 \theta_w}{\partial X^2} + \frac{\partial^2 \theta_w}{\partial Y^2} = 0. \tag{5.20}$$

The dimensionless boundary conditions of equations (5.16)–(5.20) are:

On the heated part of the bottom horizontal wall:

$$U = V = 0, \;\; \theta = 1, \;\; Y = 0, \;\; (1 - H)/2 \le X \le (1 + H)/2, \tag{5.21}$$

On the adiabatic parts of the bottom wall:

$$U = V = 0,\ \frac{\partial \theta}{\partial Y} = 0,\ Y = 0,\ 0 \le X \le (1-H)/2 \text{ and } (1+H)/2 \le X \le 1, \tag{5.22}$$

On the left vertical wall:

$$U = V = 0,\ \theta = 0,\ X = 0,\ 0 \le Y \le 1, \tag{5.23}$$

On the right vertical wall:

$$U = V = 0,\ \theta = 0,\ X = 1,\ 0 \le Y \le 1, \tag{5.24}$$

On the adiabatic top wall:

$$U = V = 0,\ \frac{\partial \theta}{\partial Y} = 0,\ 0 \le X \le 1,\ Y = 1, \tag{5.25}$$

$$\theta = \theta_w, \text{ at the interface wall,} \tag{5.26}$$

$$U = V = 0,\ \theta(X, D) = \theta_w(X, D); \frac{\partial \theta(X, S)}{\partial Y} = K_r \frac{\partial \theta_w(X, D)}{\partial Y}, \tag{5.27}$$

where $K_r = k_w/k_{nf}$ is the thermal conductivity ratio and over the surface of the solid wall. The local Nusselt number evaluated at the heated part of the bottom horizontal wall, which is defined by

$$Nu_w = -\left(\frac{\partial \theta}{\partial Y}\right)_{Y=0}, \tag{5.28}$$

also, the local Nusselt number along the interface between the solid wall and the nanofluid region is defined as

$$Nu_i = -\frac{k_{nf}}{k_f}\left(\frac{\partial \theta}{\partial Y}\right)_{Y=D}. \tag{5.29}$$

Finally, the average Nusselt number evaluated at the heated part of the bottom horizontal wall of the cavity which is given by:

$$\overline{Nu}_w = \int_{B-(0.5H)}^{B+(0.5H)} Nu_{nf}\, \mathrm{d}X, \tag{5.30}$$

and the average Nusselt number evaluated at the interface surface is given by:

$$\overline{Nu}_i = \int_0^1 Nu_i\, \mathrm{d}X. \tag{5.31}$$

The entropy generation relation is given by:

$$S = \frac{k_{nf}}{T_0^2}\left[\left(\frac{\partial T}{\partial x}\right)^2 + \left(\frac{\partial T}{\partial y}\right)^2\right] + \frac{\mu_{nf}}{T_0}\left[2\left(\frac{\partial u}{\partial x}\right)^2 + 2\left(\frac{\partial v}{\partial y}\right)^2 + \left(\frac{\partial u}{\partial x} + \frac{\partial v}{\partial x}\right)^2\right]. \tag{5.32}$$

In dimensionless form, local entropy generation can be expressed as:

$$S_{GEN} = \frac{k_{nf}}{k_f}\left[\left(\frac{\partial\theta}{\partial X}\right)^2 + \left(\frac{\partial\theta}{\partial Y}\right)^2\right] + \frac{\mu_{nf}}{\mu_f}N_\mu\left\{2\left[\left(\frac{\partial U}{\partial X}\right)^2 + \left(\frac{\partial V}{\partial Y}\right)^2\right] + \left(\frac{\partial^2 U}{\partial Y^2} + \frac{\partial^2 V}{\partial X^2}\right)^2\right\}, \tag{5.33}$$

where, $N_\mu = \frac{\mu_f T_0}{k_f}\left(\frac{\alpha_f}{L(\Delta T)}\right)^2$ is the irreversibility distribution ratio and $S_{GEN} = S_{gen}\frac{T_0^2 L^2}{k_f(\Delta T)^2}$.

The terms of equation (5.33) can be separated to the following form:

$$S_{GEN} = S_\theta + S_\Psi, \tag{5.34}$$

where S_θ and S_Ψ are the entropy generation due to heat transfer irreversibility (HTI) and fluid friction irreversibility (FFI), respectively.

$$S_\theta = \frac{k_{nf}}{k_f}\left[\left(\frac{\partial\theta}{\partial X}\right)^2 + \left(\frac{\partial\theta}{\partial Y}\right)^2\right], \tag{5.35}$$

$$S_\Psi = \frac{\mu_{nf}}{\mu_f}N_\mu\left\{2\left[\left(\frac{\partial U}{\partial X}\right)^2 + \left(\frac{\partial V}{\partial Y}\right)^2\right] + \left(\frac{\partial^2 U}{\partial Y^2} + \frac{\partial^2 V}{\partial X^2}\right)^2\right\}. \tag{5.36}$$

By Integrating equation (5.34) over the domain, the global entropy generation (GEG) for the present two-dimensional study is obtained as the following:

$$GEG = \int S_{GEN}\,\mathrm{d}X\mathrm{d}Y = \int S_\theta\,\mathrm{d}X\mathrm{d}Y + \int S_\Psi\,\mathrm{d}X\mathrm{d}Y. \tag{5.37}$$

It is appropriate to mention Bejan number in order to determine which is the dominant, heat transfer or fluid friction irreversibility. Bejan number is defined as:

$$Be = \frac{\int S_\theta\,\mathrm{d}X\mathrm{d}Y}{\int S_{GEN}\,\mathrm{d}X\mathrm{d}Y}. \tag{5.38}$$

When $Be > 0.5$, the HTI is the dominant, while when $Be < 0.5$, the FFI is the dominant.

5.3 METHOD OF SOLUTION

The dimensionless governing equations equations (5.16)–(5.20) subject to the boundary conditions equations (5.21)–(5.27) are numerically formulated using the Finite Difference (FD) scheme consisting of the Alternating Direction Implicit (ADI) method. The grid–points distribution at the conducting wall and the enclosure is shown in Figure 5.2 where ND + 1 is number of nodal points in the vertical axis in the wall, NX + 1 is number of nodal points in the X axis and NY + 1 is number of nodal points in the Y axis.

The finite dimensionless energy of equation (5.20) written in the Gaussian SOR formulation is:

$$\begin{aligned}(\theta_w)_{i,j}^{k+1} &= (\theta_w)_{i,j}^{k} + \frac{\lambda_r}{2(1+B^2)}\Big[(\theta_w)_{i+1,j}^{k} + (\theta_w)_{i-1,j}^{k+1} + B^2((\theta_w)_{i,j+1}^{k} \\ &\quad +(\theta_w)_{i,j-1}^{k+1}) - 2(1+B^2)(\theta_w)_{i,j}^{k}\Big]. \end{aligned} \tag{5.39}$$

The conditions at the solid-nanofluid interfaces boundary are:

$$\begin{aligned}(\theta)_{i,\mathrm{ND}+1}^{k+1} &= (\theta_w)_{i,\mathrm{ND}+1}^{k} \\ (\theta_w)_{i,\mathrm{ND}+1}^{k+1} &= \left[\left(\frac{1}{K_r}\right)\left(-(\theta)_{i,\mathrm{ND}+3}^{k} + 4(\theta)_{i,\mathrm{ND}+2}^{k} - 3(\theta)_{i,\mathrm{ND}+1}^{k}\right)\right. \\ &\quad \left. +4(\theta_w)_{i,\mathrm{ND}}^{k} - (\theta_w)_{i,\mathrm{ND}}^{k}\right]/3. \end{aligned} \tag{5.40}$$

For the purpose of validating the data, we have compared the present results with the previous experimental and numerical findings that presented by Calcagni et al. (2005) for the problem of free convective flow and heat transfer in a square cavity that filled with pure fluid and partially heated from below, as explained in Figures 5.3 and 5.4. In addition, a comparison is made between the resulting figures and the one provided by Ilis et al. (2008) for the case of entropy generation and natural convection in a square cavity fully heated from sides, as shown in Figure 5.5. Figure 5.6 shows alternative comparisons regarding the enhancement in the thermal conductivity due to the addition of the Al_2O_3 nanoparticles with two different experimental results and the

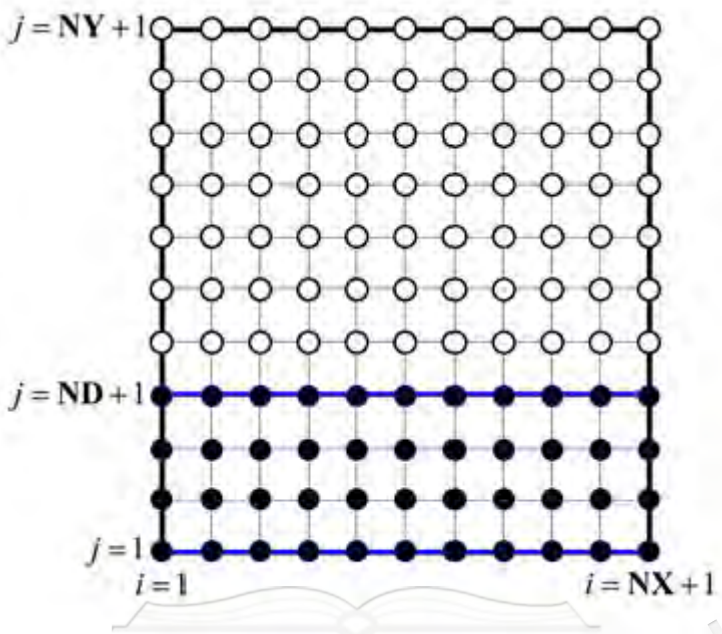

Figure 5.2 Grid-point distributions in the conducting wall ($j \leq$ ND + 1) and cavity ($j >$ ND + 1).

numerical results of Corcione et al. (2013) as well. These results provide confidence to the accuracy of the present numerical method.

5.4 RESULTS AND DISCUSSION

This section presents numerical results for the streamlines, isotherms and isentropic lines (the local dimensionless entropy generation) with various values of Rayleigh number ($Ra = 10^3$ and 10^6), nanoparticles volume fraction ($0 \leq \phi \leq 0.04$), solid wall thermal conductivity (k_w = 0.28, 0.76, 1.95, 7 and 16) (epoxy: 0.28, brickwork: 0.76, granite: 1.95, solid rock: 7, stainless steel: 16), solid wall thickness ($0.01 \leq D \leq 0.5$), heat source length ($0.2 \leq H \leq 0.8$), heat source position ($0.25 \leq B \leq 0.75$), where the value of Prandtl number is fixed at $Pr = 4.623$. The values of the average Nusselt number, overall Bejan number (Be) and global entropy generation (GEG) are calculated for various values of Ra and D. The thermophysical properties of the used base fluid (water) and solid Al_2O_3 phases are described in Table 5.1.

Figure 5.7 shows the effects of various Rayleigh numbers on the streamlines,

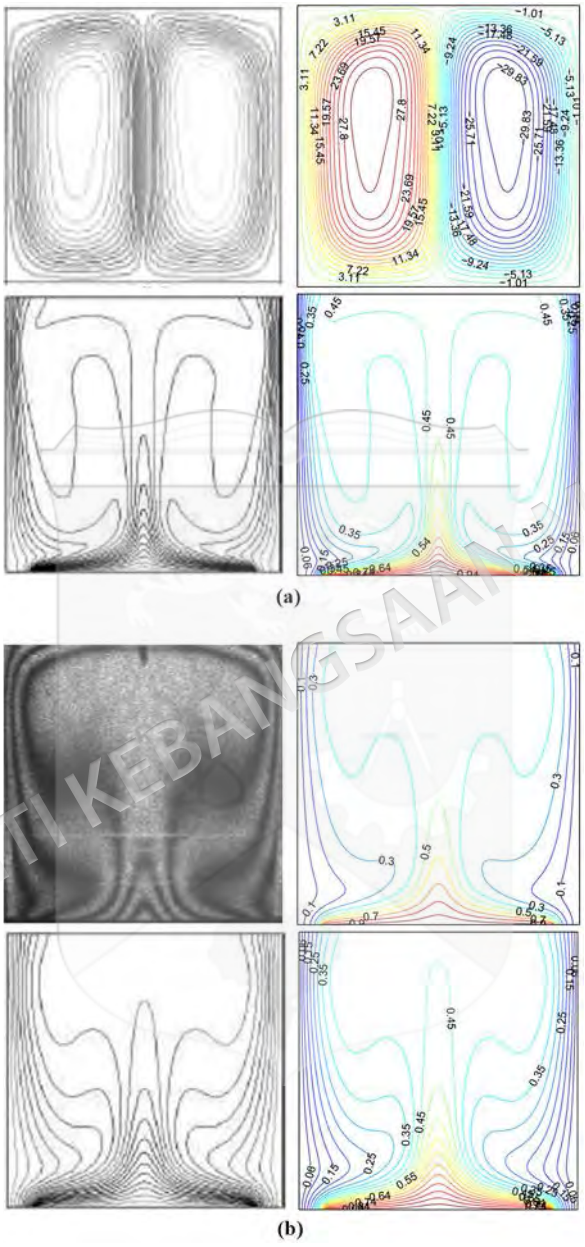

Figure 5.3 (left) Calcagni et al. (2005) and (right) present study for (a) streamlines at $Ra = 10^6$ and $H = 0.4$, (b) isotherms at $Ra = 10^5$ and $H = 0.8$ for the case of numerical and experimental results of Calcagni et al. (2005) at $\phi = 0$ and $D = 0$.

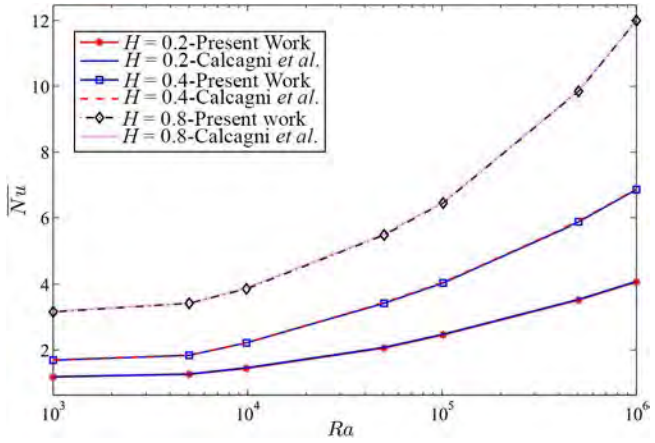

Figure 5.4 Comparison of the average Nusselt number interface with Ra for different H with Calcagni et al. (2005) at $\phi = 0$ and $D = 0$.

Table 5.1 Thermo-physical properties of water with Al_2O_3 nanoparticles at T = 310K (Bergman et al. 2011).

Physical properties	Fluid phase (water)	Al_2O_3
C_p (J/kgK)	4178	765
ρ (kg/m^3)	993	3970
k (Wm^{-1}K^{-1})	0.628	40
$\beta \times 10^5$ (1/K)	36.2	0.85
$\mu \times 10^6$ (kg/ms)	695	–
d_p (nm)	0.385	33

isotherm and isentropic of the nanoliquid phase for $k_w = 0.76$, $D = 0.2$, $H = 0.5$, $B = 0.5$, $\phi = 0$ (solid lines) and $\phi = 0.02$ (dashed lines). By heating up the bottom solid horizontal walls and constant cold temperature on the vertical walls with having a solid wall placed at the bottom clearly affects the flow behaviour and the distribution of temperature. There are two streamlined rotating cells appear inside the cavity where one in anti-clockwise direction located at the right solid wall and one in clockwise direction located at the left solid wall at low Rayleigh number. This phenomenon happened because the effect of bottom solid horizontal walls and vertical walls with variation in the distribution of temperatures. The direction and strength of the fluid heat flow are defined by the contour level labels. A positive value of $\Psi_{\min}$ denotes an anti-clockwise fluid heat flow, in contrast to the negative value indicating a clockwise fluid heat flow. $\Psi_{\min}$ represents the optimal stream function. These values are significant in showing the minimum change of the flow. The usage of the nanoparticle volume fraction has

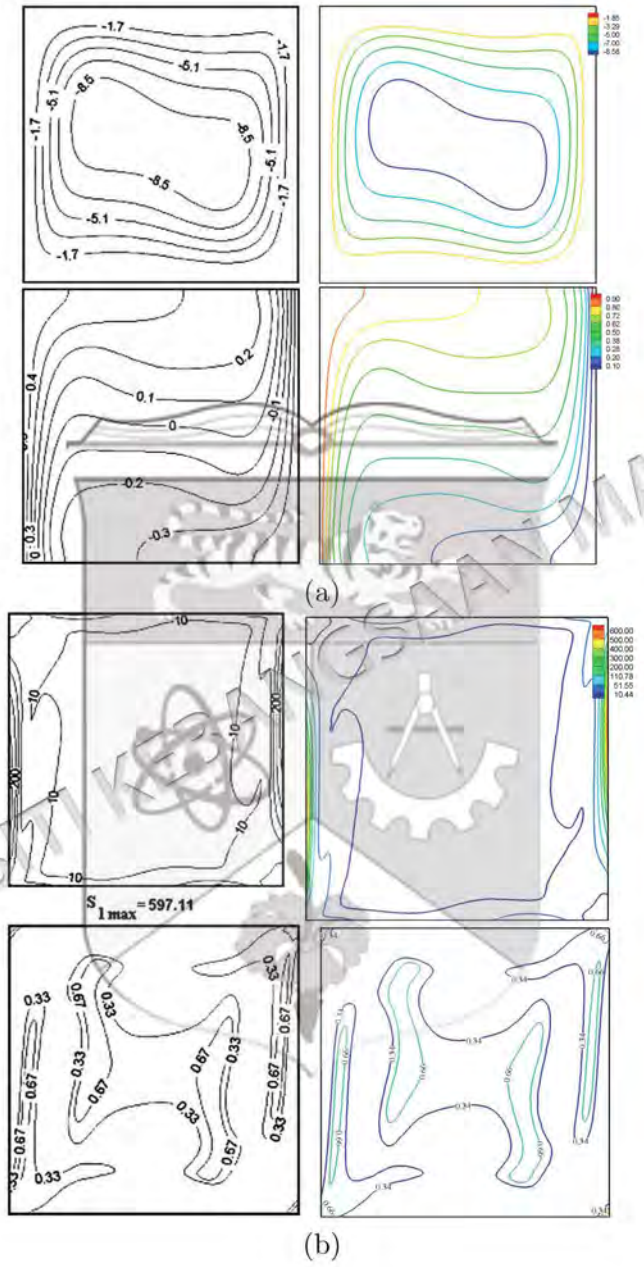

Figure 5.5 Streamlines and isotherms (a), global entropy generation and Bejan number (b), Ilis et al. (2008) (left), present study (right), for $Ra = 10^5$, $\phi = 0$, D and $H = 1$.

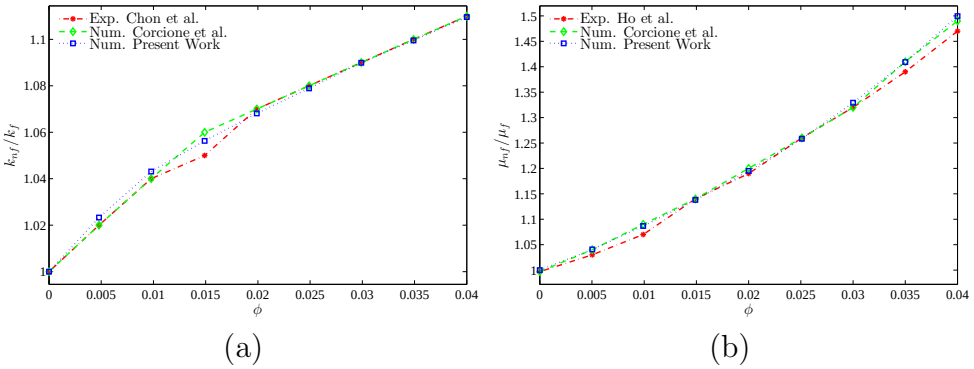

Figure 5.6 Comparison of (a) thermal conductivity ratio with Chon et al. (2005) and Corcione et al. (2013) and (b) dynamic viscosity ratio with Ho et al. (2010) and Corcione et al. (2013).

the tendency to reduce the strength of the flow circulation, which was influenced by the viscosity forces and the inertial force. The intensity of the streamlines increases as the Rayleigh number rise together with the cells size. The reason why it happened is because the system has strong buoyancy forces in comparison to the viscous forces. Both clockwise and anti-clockwise circulation of the streamlined cells for pure liquid are larger than that for nanoliquid. The strength of the flow circulation tends to increase with the Rayleigh numbers being affected by the increment of the buoyancy force and convection intensity. The isotherm patterns within appear with a high density within the solid wall as illustrated in Figure 5.7(a). By the increase of Rayleigh number, the isotherm patterns within the solid wall show a greater density.

Figures 5.8 (a) and 5.8 (b) depict the effects of Rayleigh number for, respectively bottom and interface wall on the local Nusselt number and along the X coordinate of water-AL_2O_3 at $\phi = 0.02$, $k_w = 0.76$, $D = 0.2$, $H = 0.5$ and $B = 0.5$. The local Nusselt number exhibits a consistent pattern at bottom wall across all Rayleigh number. The local Nusselt number decrease until it reaches minimum at $X = 0.25$. After that, the local heat transfer increase. Meanwhile, for all Rayleigh numbers, the local Nusselt number profiles exhbit a sinusoidal shape at interface wall take a sinusoidal shape. It is observed that the convective heat transfer are elevated at higher Rayleigh number. Figures 5.9 (a) and 5.9 (b) present the effects of various values of volume fraction on the local Nusselt number for, respectively, bottom and interface wall and along the X-coordinate at $Ra = 10^5$, $k_w = 0.76$, $D = 0.2$, $H = 0.5$, and $B = 0.5$. Higher volume

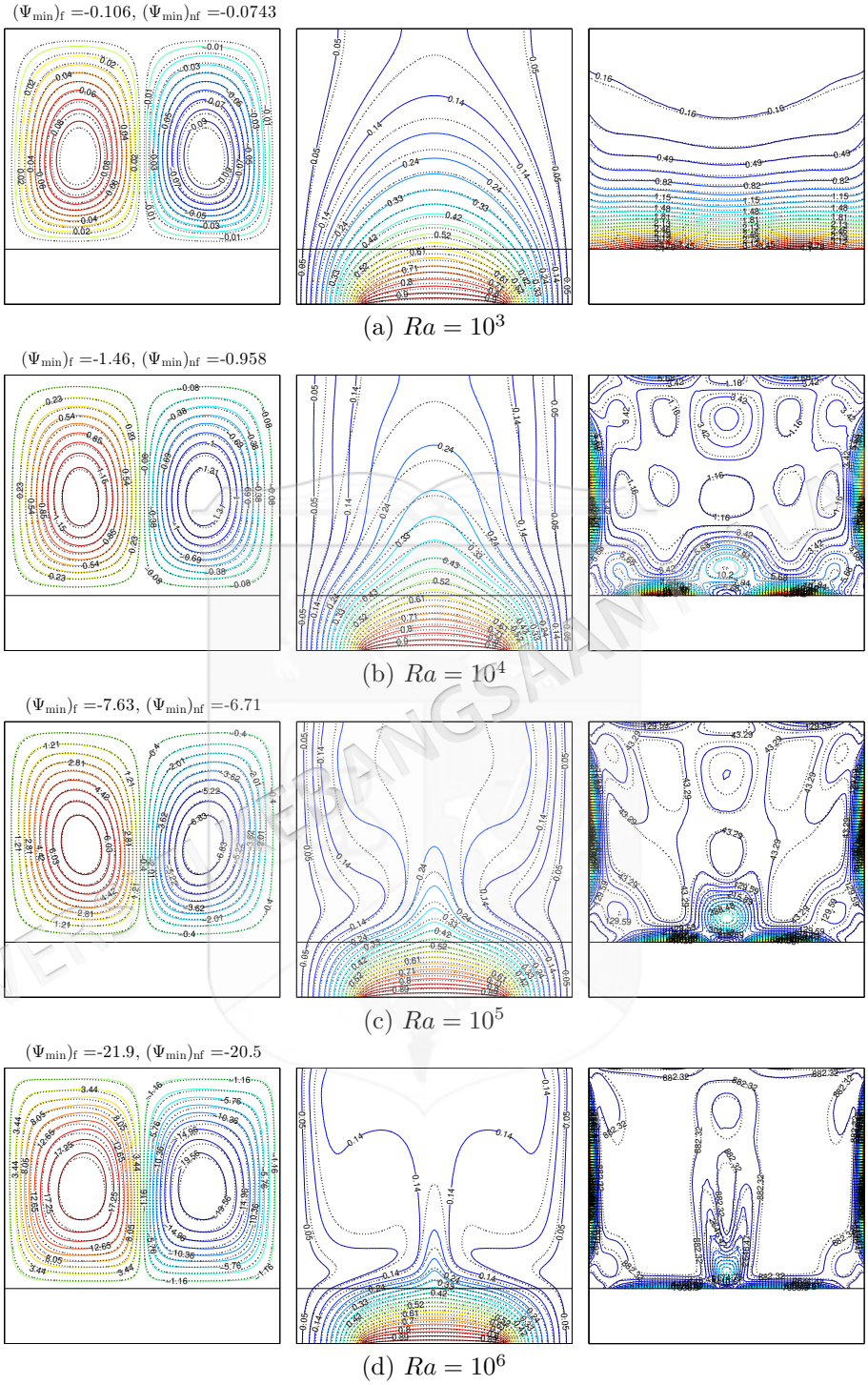

Figure 5.7 Variation of the streamlines (left), isotherms (middle), and isentropic (right) evolution by Rayleigh number (Ra) for $k_w = 0.76$, $D = 0.2$, $H = 0.5$, $B = 0.5$, $\phi = 0$ (solid lines) and $\phi = 0.02$ (dashed lines).

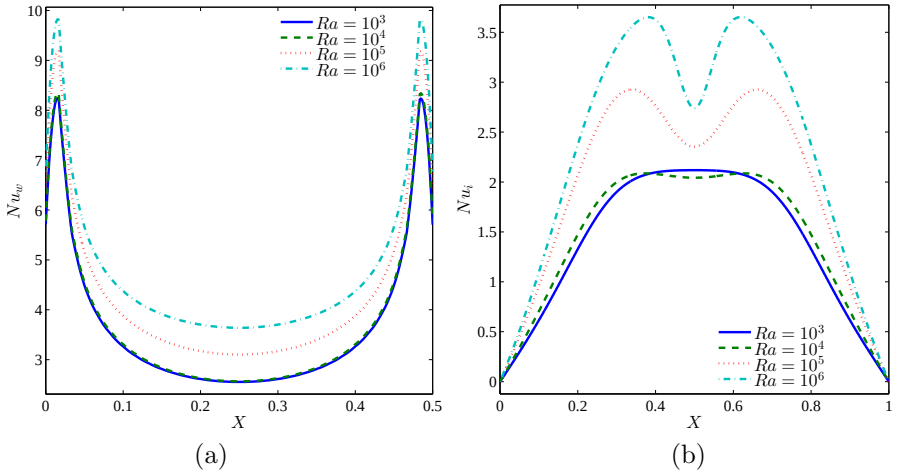

Figure 5.8 Variation of local Nusselt number interfaces with (a) bottom wall and (b) interface wall for different Ra at $\phi = 0.02$, $k_w = 0.76$, $D = 0.2$, $H = 0.5$ and $B = 0.5$.

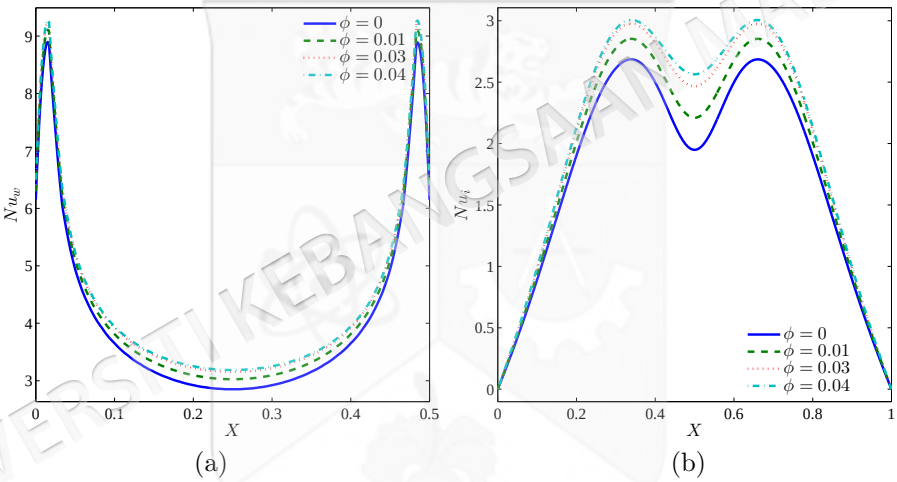

Figure 5.9 Variation of local Nusselt number interfaces with (a) bottom wall and (b) interface wall for different ϕ at $Ra = 10^5$, $k_w = 0.76$, $D = 0.2$, $H = 0.5$ and $B = 0.5$.

fraction significantly enhances heat transfer owing to the increased thermal conductivity. Moreover, higher volume fraction influences the local heat transfer, giving the maximum local Nusselt number.

Figures 5.10 (a) and 5.10 (b) show the effect of various nanoparticle volume fractions for, respectively bottom and interface walls on the average Nusselt number with different Rayleigh number at $k_w = 0.76$, $D = 0.2$, $H = 0.5$, and $B = 0.5$. Clearly, the convective heat transfer augmented by the Rayleigh number for both interface and bottom

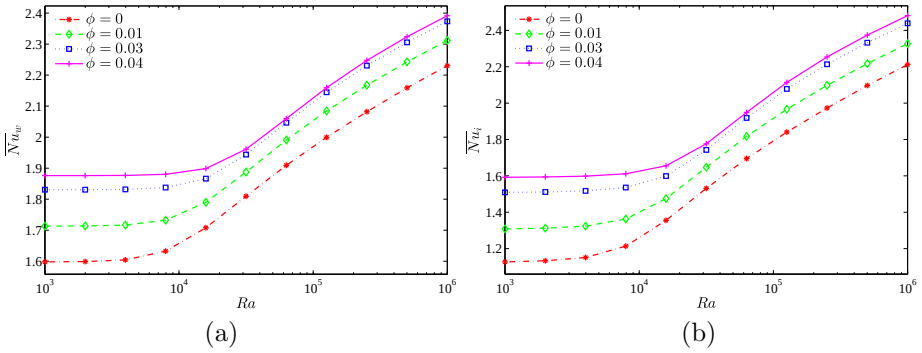

Figure 5.10 Variations of the average Nusselt number of (a) bottom wall and (b) interface wall with Ra for different ϕ at $k_w = 0.76$, $D = 0.2$, $H = 0.5$ and $B = 0.5$.

walls and this is attributed to a higher nanoparticle volume fractions. The application of a higher nanoparticle volume fraction significantly enhances the heat transfer rate, leading to a peak average Nusselt number. This effect is due to the greater temperature gradient and magnitude which are provided by the sinusoidal right boundary condition. On the contrary, the lower nanoparticle volume fraction has a weaker influence on the convective heat transfer, which obtained the minimum average Nusselt number.

Figure 5.11(a) and (b) present the effect of various nanoparticle volume fractions on the Bejan number and global entropy generation with different Rayleigh number at $k_w = 0.76$, $D = 0.2$, $H = 0.5$, and $B = 0.5$. The average Bejan number signifies the significance of entropy generation due to heat transfer or fluid friction irreversibilities. As mentioned earlier, $Be > 0.5$ indicates that heat transfer irreversibility is dominant whereas $Be < 0.5$ indicates fluid friction dominant entropy generation. A consitent trend of decreasing in Bejan number with Rayleigh number is observed for all nanoparticle volume fraction. At low Rayleigh number, the Bejan number are maximum value, indicates that entropy generation in the cavity is predominantly driven by heat transfer irreversibility. Higher nanoparticle volume fraction elevate the Bejan number due to the higher influence on the convective heat transfer. At higher Rayleigh number, the Bejan number decrease to 0, indicating that entropy generation in the cavity is due to fluid friction irreversibility. In Figure 5.11(b) depict the effect of nanoparticle volume fraction on the global entropy generation with different Rayleigh number. At $Ra = 10^5$, there is an increase in global entropy generation due to the significant of entropy generation

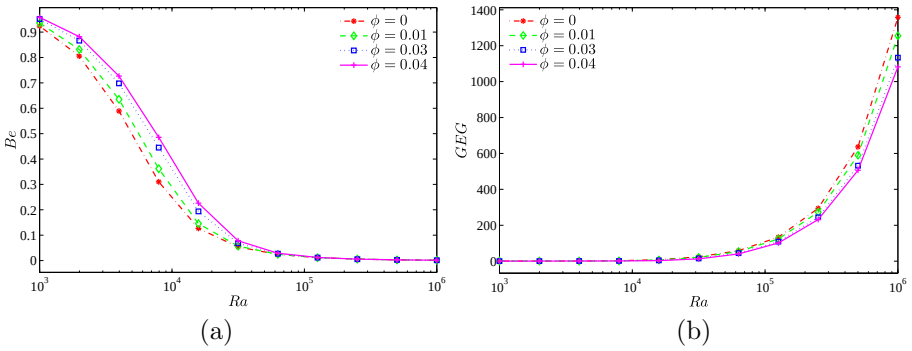

Figure 5.11 Variation of (a) Bejan number (Be) and (b) the global entropy generation (GEG) with Ra for different values of ϕ at $k_w = 0.76$, $D = 0.2$, $H = 0.5$ and $B = 0.5$.

primarily due to the fluid friction. Lower nanoparticle volume fraction manifest better global entropy generation significant to entropy generation because of high heat transfer at higher nanoparticles volume fraction.

Figure 5.12 exemplifies the results of different thermal conductivity of solid wall on the streamlines, isotherm and isentropic of the global nanoliquid phases for $Ra = 10^5$, $D = 0.2$, $H = 0.5$, $B = 0.5$, $\phi = 0$ (solid lines) and $\phi = 0.02$ (dashed lines). The isotherm patterns of the nanofluid phases exhibit higher density near the solid wall due to its lower thermal conductivity. The intensity of flow circulation tends to increase with higher thermal conductivity of the solid wall. Meanwhile, the isotherm patterns within the solid wall decrease by increasing the thermal conductivity ratio of solid wall. This phenomenon happened because of thermal resistance of the solid wall is reduced. Regarding the isentropic, the patterns of isentropic are high at the left and right wall as well as at the interface between the wall and solid insert. The amplitudes of isentropic lines decreases as the thermal conductivity ratio increases.

Figure 5.13 illustrates the effects of various solid wall thickness on the streamlines, isotherm and isentropic for $Ra = 10^5$, $k_w = 0.76$, $H = 0.5$, $B = 0.5$, $\phi = 0$ (solid lines) and $\phi = 0.02$ (dashed lines). Figure 5.13(a) illustrates the flow behavior and the temperature distribution within the porous cavity with the absence of the solid wall. It can be seen that the streamlines within the cavity tend to appear with two streamlined rotating cell, in which one appears in the clockwise direction next to the left vertical of the cavity while the other appears in the anti-clockwise direction next to

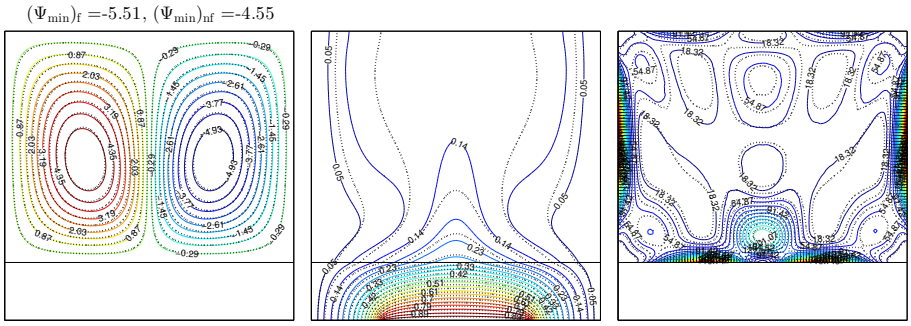

(a) $k_w = 0.28$

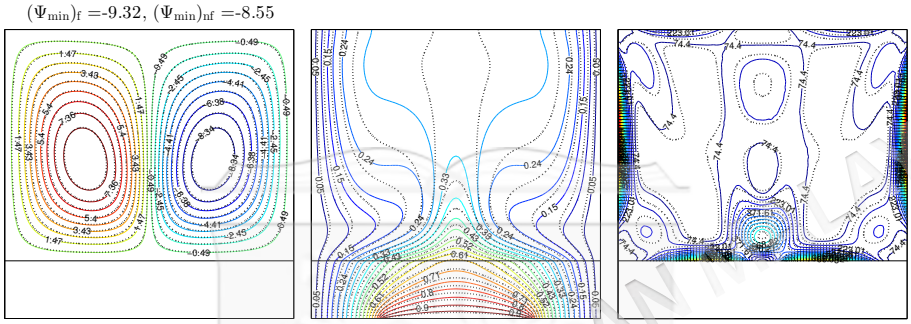

(b) $k_w = 1.95$

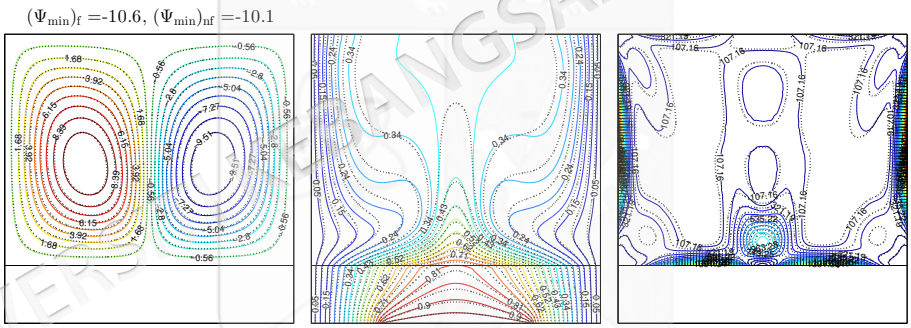

(c) $k_w = 7$

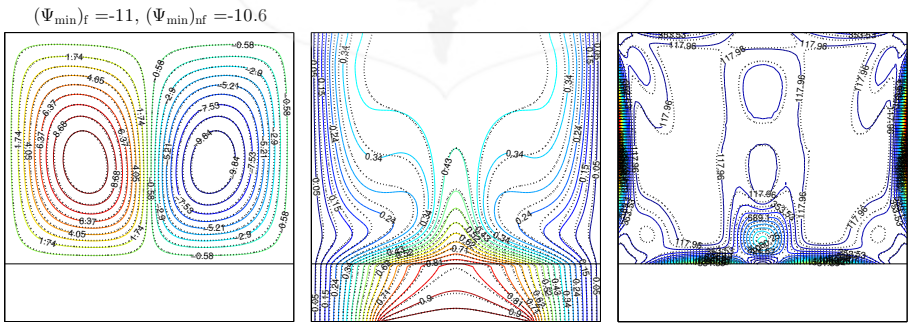

(d) $k_w = 16$

Figure 5.12 Variation of the streamlines (left), isotherms (middle), and isentropic (right) evolution by thermal conductivity of the solid wall (k_w) for $Ra = 10^5$, $D = 0.2$, $H = 0.5$, $B = 0.5$, $\phi = 0$ (solid lines) and $\phi = 0.02$ (dashed lines).

the right vertical of the cavity. Because of the various temperature distribution, the density of the isotherm pattern appears high near both the left and right as well as the bottom walls of the cavity. The streamlines are then moved from there towards the adiabatic walls with the presence of a solid finite thickness walls as the top wall of the cavity. In addition, both cell tends to shrink vertically. The strength of the flow circulation decreases (see Ψ_{min} values) due to the solid wall which has a higher thermal resistance. Due to the viscosity forces and the inertial force, the strength of the flow circulation decreases with the addition of the 5% nanoparticles. By increasing the thickness of the solid wall, it influences the distribution of flow behavior as well as the temperature profiles. The amount and density of the isotherm pattern are vividly increased within the solid wall, as the solid wall offers a high resistance. This, in turn, leads to the low temperature.

Figures 5.14 (a) and (b) illustrate the effects of various values of thermal conductivity for, respectively bottom and interface walls on the local Nusselt number and along the X coordinate of water-Cu at $Ra = 10^5$, $\phi = 0.02$, $D = 0.2$, $H = 0.5$, and $B = 0.5$. It is observed that the convective heat transfer is significantly effected by the variatons of the thermal conductivity at both walls. An increase in thermal conductivity results in a higher local Nusselt number, with this enhancement being particularly evident at the interface wall. However, lower thermal conductivity leads to a maximum local Nusselt number at the bottom wall.

Figures 5.15 (a) and (b) present the outcome of various thermal conductivity ratio for, respectively bottom and interface walls on the average Nusselt number with different length of solid wall at $Ra = 10^5$, $\phi = 0.02$, $H = 0.5$, and $B = 0.5$. It shows that the increment in length of the solid wall at both the bottom and interface wall affects the convective heat transfer. At bottom wall, it is observed that the convective heat transfer tends to increase with an increase in the length of solid wall particularly for a high thermal conductivity ratio. Due to lower thermal conductivity ratio, it was clearly observed that the convective heat transfer reduces. At the interface wall, the overall heat transfer reduces significantly with the increased in length of solid wall due to the resistance of the solid wall. The convective heat transfer is strongly enhanced with the lower thermal conductivity ratio because of the lower thermal conductivity.

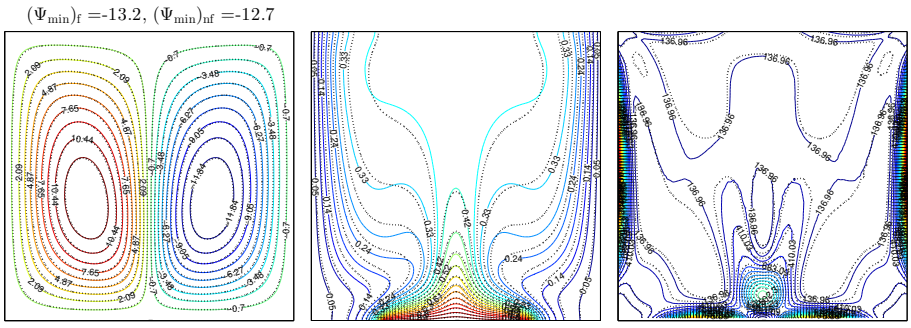

(a) $D = 0.01$

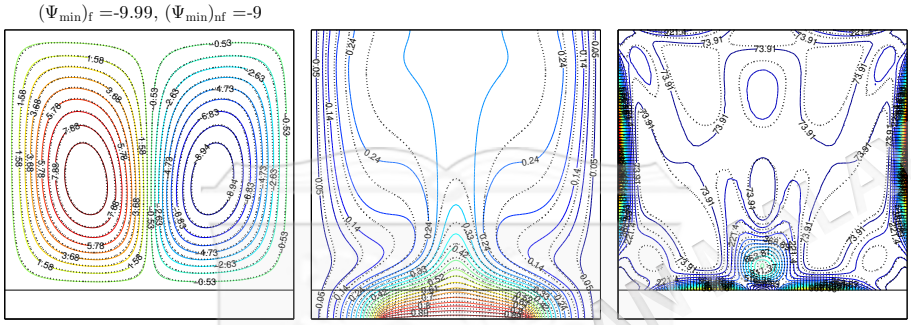

(b) $D = 0{,}1$

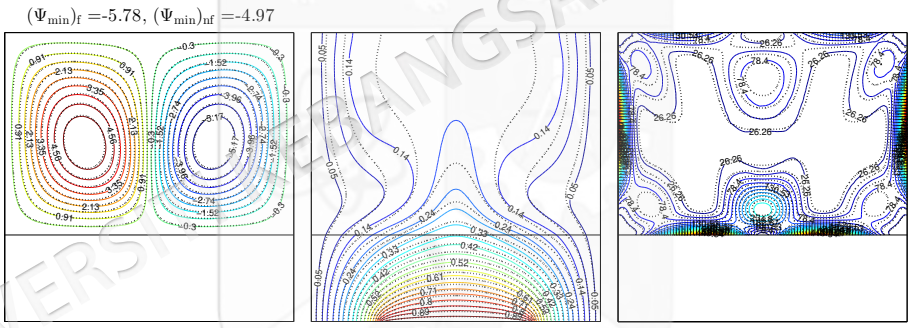

(c) $D = 0.3$

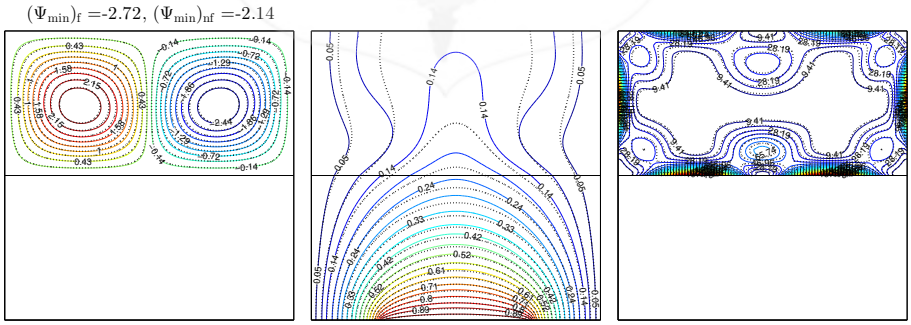

(d) $D = 0.5$

Figure 5.13 Variation of the streamlines (left), isotherms (middle), and isentropic (right) evolution by the solid wall thickness (D) for $Ra = 10^5$, $k_w = 0.76$, $H = 0.5$, $B = 0.5$, $\phi = 0$ (solid lines) and $\phi = 0.02$ (dashed lines).

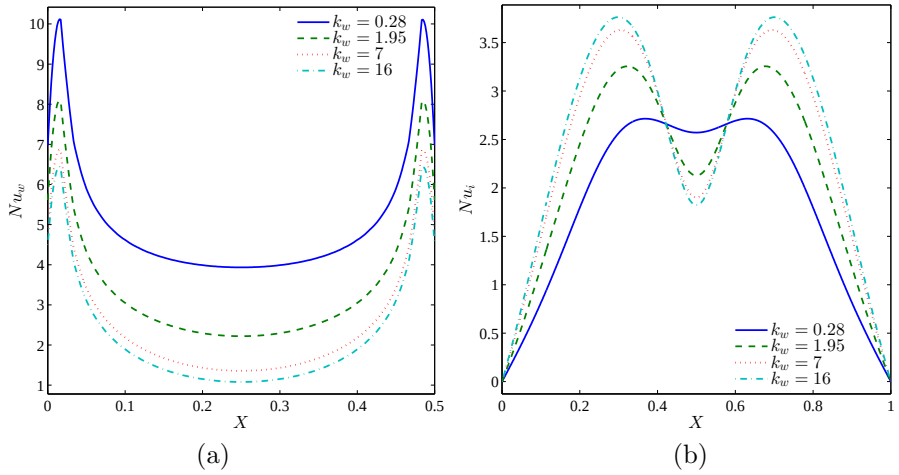

Figure 5.14 Variation of local Nusselt number interfaces with (a) bottom wall and (b) interface wall for different k_w at $Ra = 10^5$, $\phi = 0.02$, $D = 0.2$, $H = 0.5$ and $B = 0.5$.

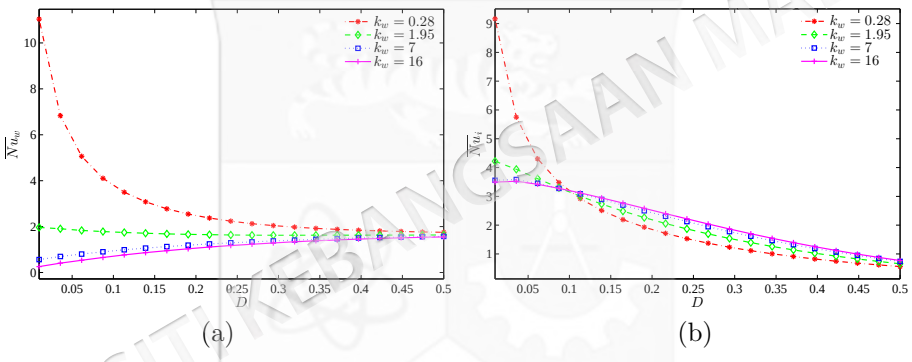

Figure 5.15 Variations of the average Nusselt number of (a) bottom wall and (b) interface wall with D for different k_w at $Ra = 10^5$, $\phi = 0.02$, $H = 0.5$ and $B = 0.5$.

Figures 5.16 (a) performs the effect of various thermal conductivity ratio on the Bejan number with different length of size enclosure at $Ra = 10^5$, $\phi = 0.02$, $H = 0.5$, and $B = 0.5$. We noticed that the value of Bejan number are below than 0.5 for all thermal conductivity ratio indicating that fluid friction irreversibility is dominant over the heat transfer irreversibility for all thermal conductivity ratio. However, the Bejan number increases, particularly at higher thermal conductivity ratio. Figure 5.16 (b) demonstrates the global entropy generation affected by various thermal conductivity ratio for different enclosure sizes. The figure shows that the global entropy generation decrease as the size of enclosure increase due to the weak of fluid friction. However, higher thermal conductivity ratio manifest best performance for global entropy generation.

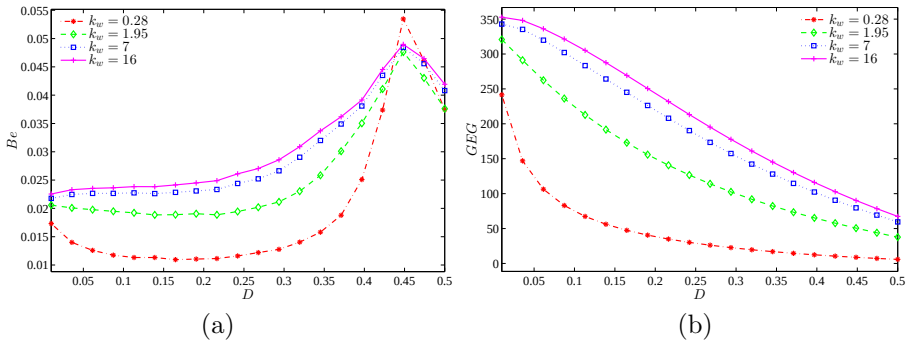

Figure 5.16 Variation of (a) Bejan number (Be) and (b) the global entropy generation (GEG) with D for different k_w at $Ra = 10^5$, $\phi = 0.02$, $H = 0.5$ and $B = 0.5$.

Figures 5.17 (a) and (b) demonstrate the effect of varying lengths of solid wall for, respectively bottom and interface walls on average Nusselt number with different Rayleigh number at $\phi = 0.02$, $k_w = 0.76$, $H = 0.5$, and $B = 0.5$. It was observed that the convective heat transfer is significantly influenced by the increase in Rayleigh number for both bottom and interface walls. Lower inner length of solid wall will increase the convective heat transfer because the resistance of the solid wall. When the higher inner length of heat source applied, the convective heat transfer are slightly increase as the Rayleigh number increase. It occur to both bottom and interface walls.

Figure 5.18 depicts the effect of various sizes of enclosure on the (a) Bejan number and (b) global entropy generation with different Rayleigh number at $\phi = 0.02$, $k_w = 0.76$, $H = 0.5$, and $B = 0.5$. The suppression effect on the heat transfer irreversibility is significantly influenced by the nanoparticles across a wide range of Rayleigh number, particularly when $Ra > 10^5$. On the other hand, two distinct stages of the nanofluid effect on global entropy generation GEG was observed; stage 1 is for low Rayleigh number where the nanoparticles action can be ignored as seen in Figure 5.18 (b). Stage 2 for $Ra > 10^5$ where the nanoparticles exist in the enclosure and it stimulates the global entropy generation. This is because of the enhanced viscous and inertia effects associated with the length of enclosure.

Figure 5.19 depicts the effects of various length of heat source on the streamlines, isotherms and isentropic for $Ra = 10^5$, $k - w = 0.76$, $D = 0.2$, $B = 0.5$, $\phi = 0$ (solid lines) and $\phi = 0.02$ (dashed lines). The temmperature distribution and flow behaviour

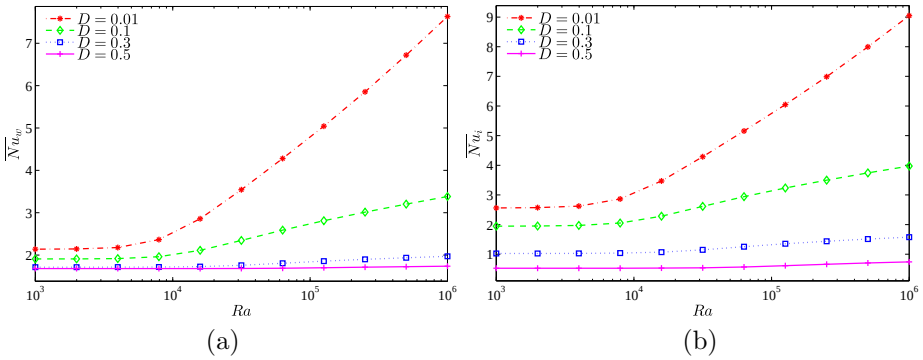

Figure 5.17 Variations of the average Nusselt number of (a) bottom wall and (b) interface wall with Ra for different D at $\phi = 0.02$, $k_w = 0.76$, $H = 0.5$ and $B = 0.5$.

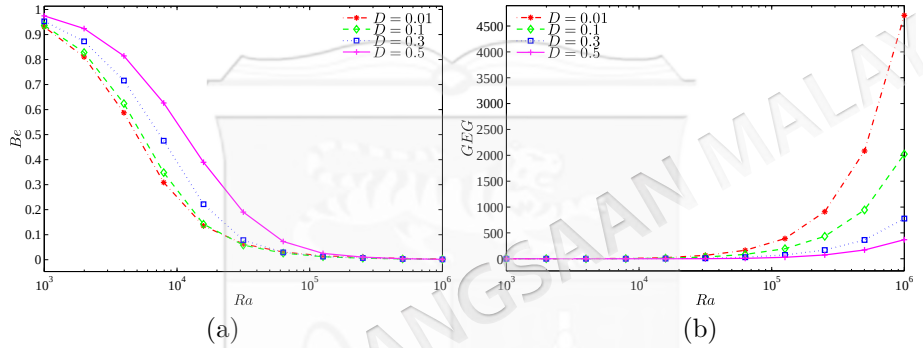

Figure 5.18 Variation of (a) Bejan number (Be) and (b) the global entropy generation (GEG) with Ra for different D at $\phi = 0.02$, $k_w = 0.76$, $H = 0.5$ and $B = 0.5$.

inside the cavity with 0.2 length of heater are shown in Figure 5.19 (a). The streamlines exhibit a tendency to form two primary cells: a clockwise cell on the left side of the cavity and an anticlockwise cell near the right vertical side. The horizontal heating wall intensifies the isotherm patterns of the nanoliquid within the solid insert. As the heat source length increases, the strength of flow circulation diminishes, and the isotherm patterns elongate horizontally. Due to the varied temperature distribution, isentropic lines are prominent on the left, right, and at the interface between the cavity and the solid insert. The amplitudes of isentropic increase as the heater source increase.

Figure 5.20 demonstrate the effect of various of heat source position on streamlines, isotherms and isentropic for $Ra = 10^5$, $k_w = 0.76$, $D = 0.2$, $H = 0.5$, $\phi = 0$ (solid lines) and $\phi = 0.02$ (dashed lines). The outcome from changing the heat source position on the bottom walls of the cavity is illustrated in Figure 5.20 (a). The

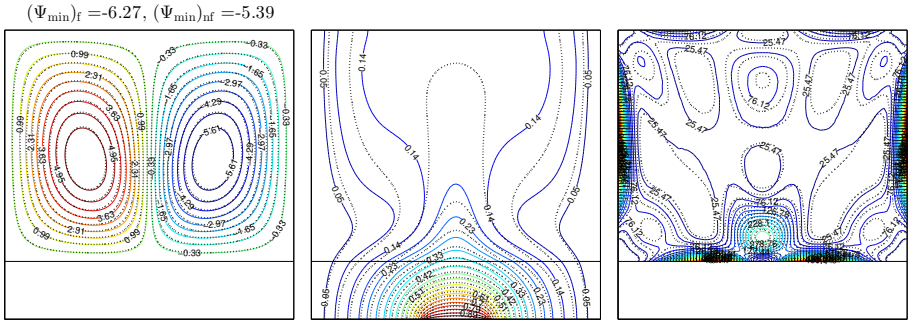

(a) $H = 0.2$

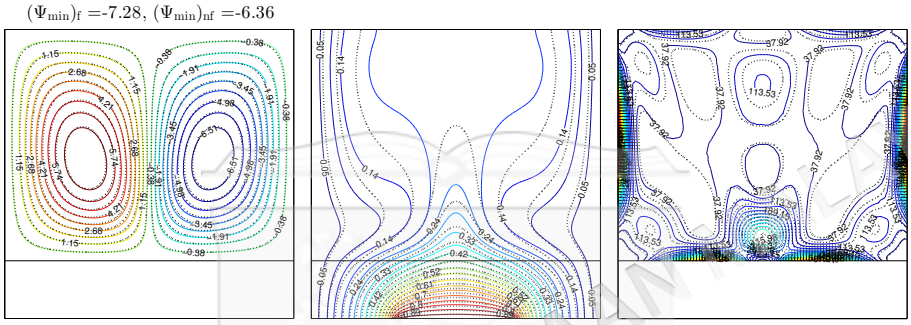

(b) $H = 0.4$

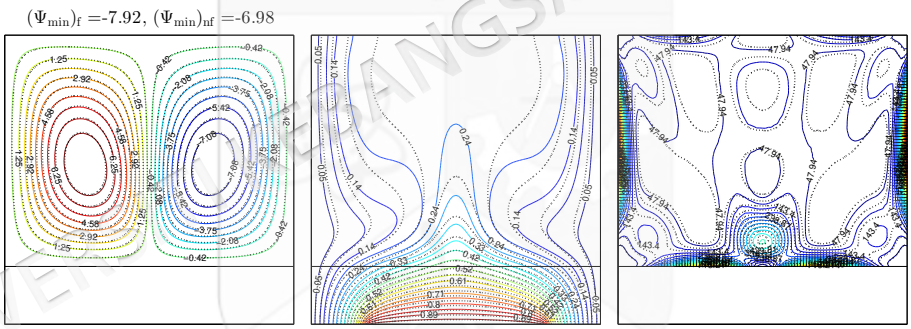

(c) $H = 0.6$

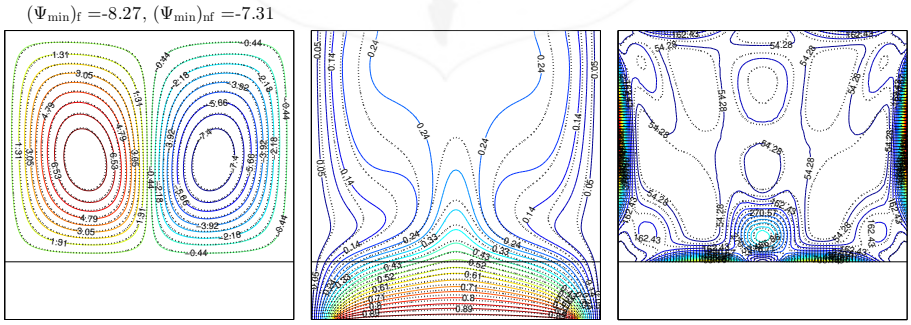

(d) $H = 0.8$

Figure 5.19 Variation of the streamlines (left), isotherms (middle), and isentropic (right) evolution by heat source length (H) for $Ra = 10^5$, $k_w = 0.76$, $D = 0.2$, $B = 0.5$, $\phi = 0$ (solid lines) and $\phi = 0.02$ (dashed lines).

streamlines has the tendency to appear with high intensity on the right side of the cavity and low intensity at the left side of the cavity. This distribution shows a significant variation in the flow behavior across the cavity. The isotherm pattern of the nanofluid are highly concentrated within the solid insert due to the heating at the bottom wall of the cavity. This heating creates a strong temperature gradient, leading to pronounced isotherm patterns. Isentropic field illustrates zones of entropy generation resulting from heat transfer and fluid friction. It is noted that the high entropy generation zones are primarily located at the right and left of the heater where the cold wave collides with the hot temperature. This collision creates regions of intense thermal gradients and fluid friction, contributing to higher entropy generation. The isentropic lines are also highly concentrated at the location of the heat source.

Figures 5.21 (a) and (b) present the effects of various values of length heat source on the local Nusselt number and along the X-coordinate of water-Cu at $Ra = 10^5$, $k_w = 0.76$, $\phi = 0.02$, $D = 0.2$, and $B = 0.5$ for bottom and interface wall. The local Nusselt number occurs according to the size of heat source at the bottom wall. Clearly, the convective heat transfer is significantly influenced by the changes of the length heat source at both walls. Additionally, a longer heat source length enhances local heat transfer, resulting in a maximum local Nusselt number.

Figures 5.22 (a) and (b) illustrate the effect of various length of inner solid for $Ra = 10^5$, $k_w = 0.76$, $\phi = 0.02$, and $B = 0.5$, respectively bottom and interface walls on average Nusselt number with different length of heat source. Increasing the length of inner solid significantly affects overall heat transfer rate in which it reduces the convective heat transfer for all length of heat source which is attributed due to the resistance posed by the solid inner cavity. This resistance markedly reduces convective heat transfer. Furthermore, a longer length of heat source leads to the greatest enhancement of the overall heat transfer, achieving the maximum weighted average Nusselt number.

Figure 5.23 depicts variants of global entropy generation, GEG, and Bejan number, Be with the size of inner solid for different length of heat source at $Ra = 10^5$, $k_w = 0.76$, $\phi = 0.02$, and $B = 0.5$. Figure 5.23 (a) demonstrates that for all size of heat source, the fluid friction irreversibility dominates over the heat transfer irreversibility.

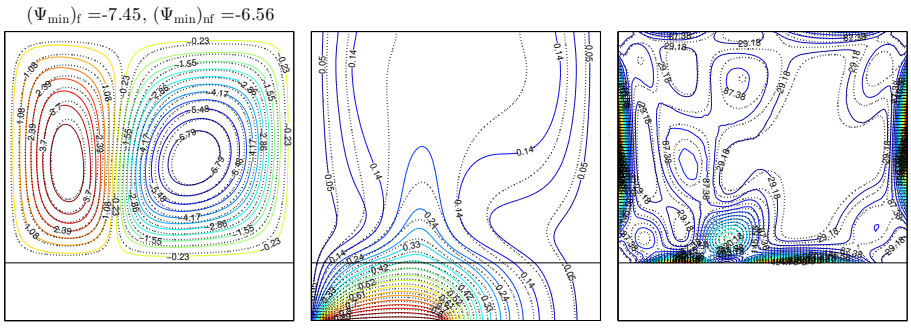

(a) $B = 0.25$

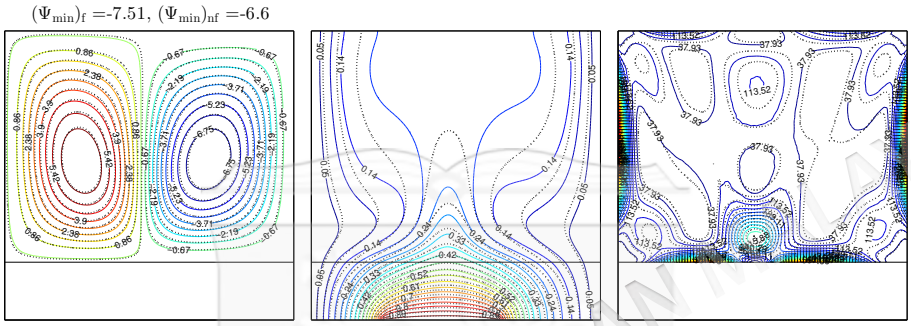

(b) $B = 0.45$

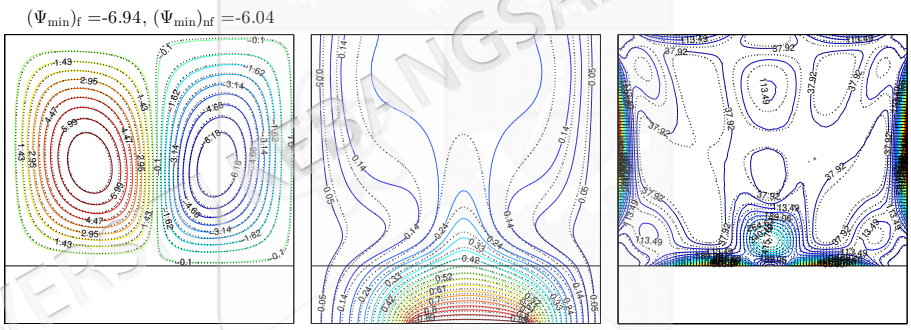

(c) $B = 0.55$

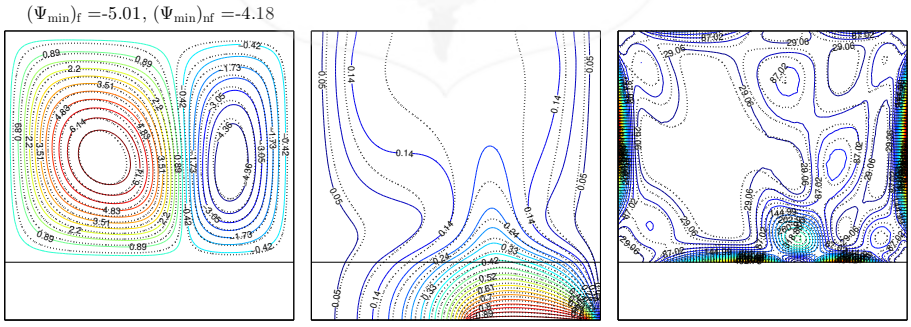

(d) $B = 0.75$

Figure 5.20 Variation of the streamlines (left), isotherms (middle), and isentropic (right) evolution by heat source position (B) for $Ra = 10^5$, $k_w = 0.76$, $D = 0.2$, $H = 0.5$, $\phi = 0$ (solid lines) and $\phi = 0.02$ (dashed lines).

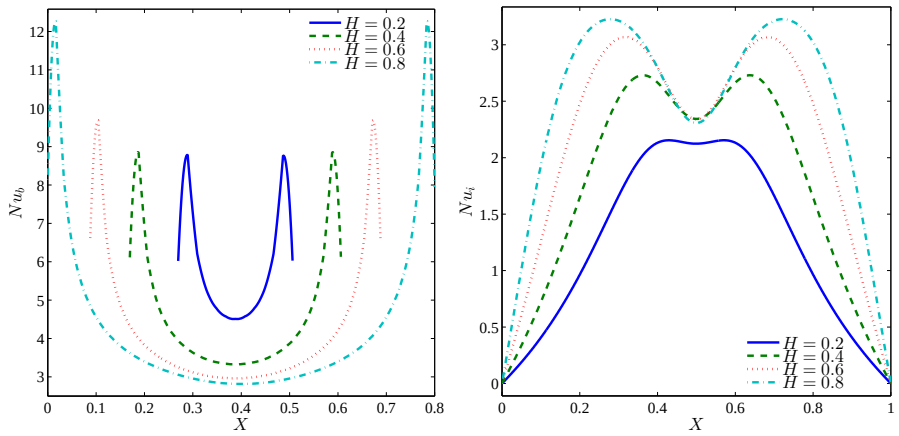

Figure 5.21 Variation of local Nusselt number interfaces with (a) bottom wall and (b) interface wall for different H at $Ra = 10^5$, $\phi = 0.02$, $k_w = 0.76$, $D = 0.2$ and $B = 0.5$.

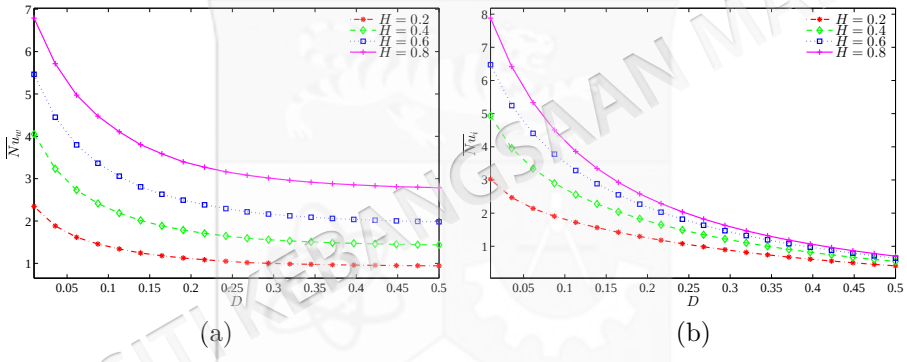

Figure 5.22 Variations of the average Nusselt number of (a) bottom wall and (b) interface wall with D for different H at $Ra = 10^5$, $\phi = 0.02$, $k_w = 0.76$ and $B = 0.5$.

However, a continuous increase of Be with D is recorded for all H. On the other hand, it is noted that the GEG decrease as the size of enclosure for all heat source lengths. This phenomenon can be attributed to the two concentrators of entropy generation localized at the two edges of the wall-porous interface. Hence, when D increases, the available space for vortex rotation become, leading to a reduction in vortex strength, hence less irreversibility will come from the fluid friction. At the same time, this reduction also weakens global entropy generation.

Figure 5.24 (a) and (b) display the effects of various of heat position for bottom and interface walls on average Nusselt number with different sizes of inner solid at

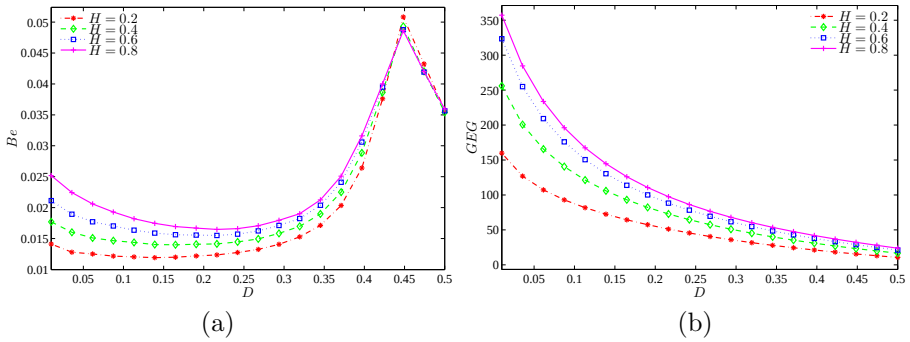

Figure 5.23 Variation of (a) Bejan number (Be) and (b) the global entropy generation (GEG) with D for different H at $Ra = 10^5$, $\phi = 0.02$, $k_w = 0.76$ and $B = 0.5$.

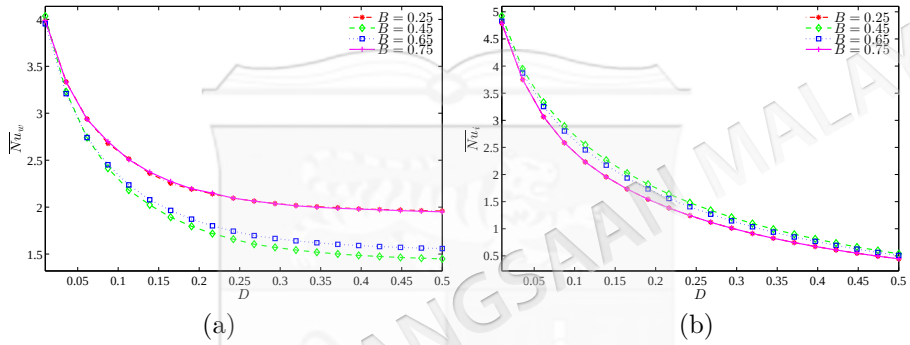

Figure 5.24 Variations of the average Nusselt number of (a) bottom wall and (b) interface wall with D for different B at $Ra = 10^5$, $\phi = 0.02$, $k_w = 0.76$ and $H = 0.5$.

$Ra = 10^5$, $k_w = 0.76$, $\phi = 0.02$, and $H = 0.5$. It is observed that the convective heat transfer decreases as the size of solid wall increases for all heat sources position on both walls. The highest position of the heat source yields the maximum average Nusselt number at the bottom wall. However, at interface wall, a lower position of the heat source results in the maximum weighted average Nusselt number. The variations of global entropy generation, GEG and Bejan, Be number with the size of cavity for different heat source position presented in Figure 5.25 for $Ra = 10^5$, $k_w = 0.76$, $\phi = 0.02$, and $H = 0.5$. When the value of B is low, it means that the position of heat source at the right of bottom cavity. Figure 5.25(a) shows that the nanofluid friction is dominant since the Bejan number is lower than 0.5. Meanwhile Figure 5.25 (b) indicates that GEG decreases for all position of heat source as the cavity size increases.

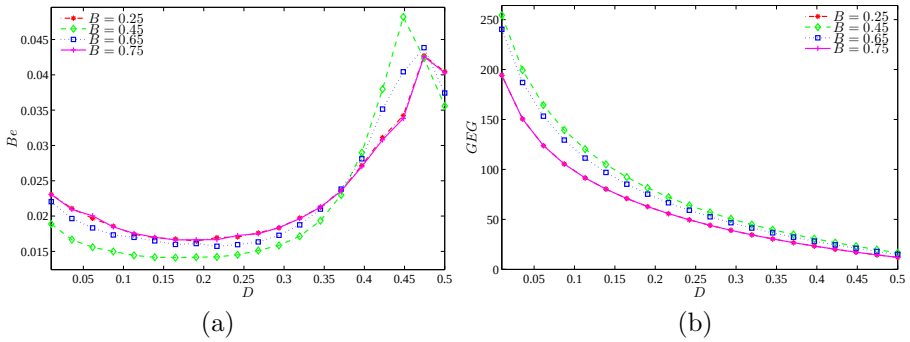

(a) (b)

Figure 5.25 Variation of (a) Bejan number (Be) and (b) the global entropy generation (GEG) with D for different B at $Ra = 10^5$, $\phi = 0.02$, $k_w = 0.76$ and $H = 0.5$.

5.5 CONCLUSIONS

In the current numerical work, the finite difference method (FDM) is used to analyze the entropy generation analysis and natural convection in partially heated square cavity filled with Al_2O_3-water nanofluid and having solid bottom wall. The detailed computational results for the streamlines, isotherms and local entropy generation for different values of Rayleigh number, nanoparticles volume fraction, solid wall thermal conductivity, solid wall thickness, heat source length and heat source position. Some important conclusions from the study are given below:

1. Increase the solid wall tends to influence the flow behavior: local entropy generation and temperature distribution influenced by the resistance due to the conductive heat transfer in the solid wall.
2. A significant enhancement is observed on the heat transfer rate with the increasing of Rayleigh number from 10^4 to 10^6 as compared to the other values. This is because a significant increment of the buoyancy forces compared to the viscous forces in this range of Rayleigh number
3. The thermal property and the size of the solid bottom wall significantly influenced the heat transfer rate. The convective heat transfer inhibited with the presence of a thick solid wall within the enclosure, as well as a low thermal conductivity of the solid wall. Whilst the higher thermal conductivity of the solid wall increases the rate of the heat transfer.

4. Convective heat transfer improves with an increase in the heat source length on both the bottom wall and interface walls within the square cavity. Similarly, this enhancement is observed in the global entropy generation and the average Bejan number.
5. The global entropy generation shows an increasing trend with the augmentation of the Rayleigh number, indicating that higher thermal and fluid motion contributes to greater entropy production within the system.Meanwhile, the average Bejan number demonstrates a different result. As the Rayleigh number rises, the average Bejan number tends to reduce. It shows that a diminishing role of heat transfer irreversibility relative to fluid friction irreversibility.
6. For the case of intensive convection regime ($Ra \geq 10^5$), the global entropy generation is a decreasing function of the size of the inner solid. In contrast, the average Bejan number is an increasing function of the size of the inner solid of the same regime.
7. Finally, the global entropy generation inhibited by a thick solid wall with a high thermal resistance . However, the global entropy generation is significant when the solid wall has higher thermal conductivity while a relatively thick solid wall has positive impact on the average Bejan number.
8. Some other directions in future work could include non-Newtonian fluids, three dimensional problems and non-uniform heating. Including the non-Darcy effect in the formulation of the porous medium problem is also a considerable future work.

CHAPTER VI

ENTROPY PRODUCTION AND MIXED CONVECTION WITHIN TRAPEZOIDAL CAVITY HAVING NANOFLUIDS AND LOCALISED SOLID CYLINDER

6.1 INTRODUCTION

Mixed convective heat transfer is a combination of natural convection and force convection. Mixed convective heat transfer inside cavities acts as an extensive rule in various engineering applications such as solar panels, material processors, solar ponds, heat exchangers and many more. Several researchers have investigated the combination of the shear effect and buoyancy force.

Based on the studies mentioned above and to the best of our knowledge, no investigation has been performed on entropy generation and mixed convection of nanofluids within a lid-driven trapezoidal cavity containing an inner solid cylinder. The heat and fluid flow can be affected significantly by the inclusion of an inner body (like a square or a cylinder) without consuming extra energy. Therefore, this investigation intends a lid-driven trapezoidal cavity having water-Al_2O_3 nanofluids. The outcomes shall be reported for various Reynolds number, Richardson number, nanoparticles volume fraction, the solid cylinder's dimensionless radius and location toward streamlines, isotherms, isentropic, local and average Nusselt number, Bejan number, and the global entropy generation. .

6.2 MATHEMATICAL FORMULATION

Two-dimensional geometric model of mixed convection flow and heat transfer inside a trapezoidal cavity with bottom wall of length L and top wall with range $L/2$, with

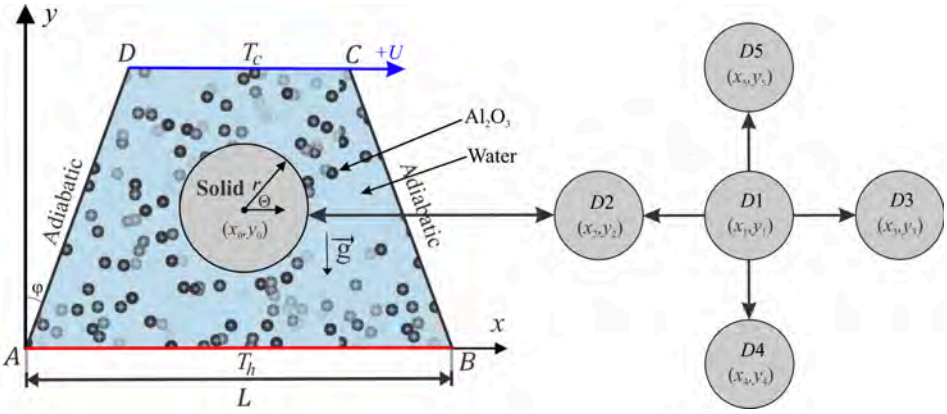

Figure 6.1 Physical model of convection in a trapezoidal cavity together with conducting wall and coordinate system

an internal solid cylinder with dimensional radius r that located in different locations as described schematically in Figure 6.1. The bottom surface assumed to be heated into a constant temperature of T_h, and the top surface slide with uniform velocity from left to right at $+U$ and preserved at a constant cold temperature, T_c. Meanwhile, both sloping surfaces with length $0.65L$ and inclination angle φ are saved in adiabatic rule. The fluid flow in the trapezoidal cavity is examined to hold steady, laminar, and loaded with an alumina-water nanofluids. The governing equations of Navier-Stokes equations and the energy equations toward the viscous incompressible flow can indicate into the dimensional model as the following :

$$\frac{\partial u}{\partial x}+\frac{\partial v}{\partial y}=0, \tag{6.1}$$

$$u\frac{\partial u}{\partial x}+v\frac{\partial u}{\partial y}=-\frac{1}{\rho_{nf}}\frac{\partial p}{\partial x}+\nu_{nf}\left(\frac{\partial^2 u}{\partial x^2}+\frac{\partial^2 u}{\partial y^2}\right),$$

$$u\frac{\partial v}{\partial x}+v\frac{\partial v}{\partial y}=-\frac{1}{\rho_{nf}}\frac{\partial p}{\partial y}+\nu_{nf}\left(\frac{\partial^2 v}{\partial x^2}+\frac{\partial^2 v}{\partial y^2}\right)+\beta_{nf}\,g(T-T_0), \tag{6.2}$$

$$u\frac{\partial T}{\partial x}+v\frac{\partial T}{\partial y}=\alpha_{nf}\left(\frac{\partial^2 T}{\partial x^2}+\frac{\partial^2 T}{\partial y^2}\right). \tag{6.3}$$

The heat equation of the solid inner body remains as:

$$\frac{\partial^2 T_s}{\partial x^2}+\frac{\partial^2 T_s}{\partial y^2}=0, \tag{6.4}$$

where x and y are the Cartesian coordinates measured in the horizontal and vertical directions respectively, g is the acceleration due to gravity, ρ_{nf} is the density of the

nanofluid and ν_{nf} is the kinematic viscosity of the nanofluid. The thermo-physical properties of the nanofluid including heat capacitance $(\rho C_p)_{nf}$, effective thermal diffusivity α_{nf}, effective density ρ_{nf}, thermal expansion coefficient β_{nf}, can be explained respectfully as the following:

$$(\rho C_p)_{nf} = (1-\phi)(\rho C_p)_f + \phi(\rho C_p)_p, \tag{6.5}$$

$$\alpha_{nf} = \frac{k_{nf}}{(\rho C_p)_{nf}}, \tag{6.6}$$

$$\rho_{nf} = (1-\phi)\rho_f + \phi\rho_p, \tag{6.7}$$

$$(\rho\beta)_{nf} = (1-\phi)(\rho\beta)_f + \phi(\rho\beta)_p. \tag{6.8}$$

While the dynamic viscosity ratio of water-Al_2O_3 nanofluids for 33nm particle-size in the ambient condition is described by Corcione (2011) as follows.

$$\frac{\mu_{nf}}{\mu_f} = 1/\left(1 - 34.87\left(d_p/d_f\right)^{-0.3}\phi^{1.03}\right). \tag{6.9}$$

And the thermal conductivity ratio of water-Al_2O_3 nanofluids is calculated by Corcione (2011) as the following:

$$\frac{k_{nf}}{k_f} = 1 + 4.4\mathrm{Re}_B^{0.4}\mathrm{Pr}^{0.66}\left(\frac{T}{T_{fr}}\right)^{10}\left(\frac{k_p}{k_f}\right)^{0.03}\phi^{0.66}. \tag{6.10}$$

where Re_B is defined as

$$\mathrm{Re}_B = \frac{\rho_f u_B d_p}{\mu_f}, \quad u_B = \frac{2k_b T}{\pi\mu_f d_p^2}, \tag{6.11}$$

where $k_b = 1.380648 \times 10^{-23}(J/K)$ is the Boltzmann constant. $l_f = 0.17$nm is the mean path of fluid particles. d_f is the molecular diameter of water given as Corcione (2011)

$$d_f = \frac{6M}{N\pi\rho_f}, \tag{6.12}$$

where M is the molecular weight of the base fluid, N is the Avogadro number and ρ_f is the density of the base fluid at standard temperature (310K).

Now we introduce the following non-dimensional variables:

$$X = \frac{x}{L}, \quad Y = \frac{y}{L}, \quad U = \frac{u}{U_0}, \; V = \frac{v}{U_0}, \quad \theta = \frac{T - T_c}{T_h - T_c}, \quad \theta_s = \frac{T_s - T_c}{T_h - T_c},$$
$$D = \frac{d}{L}, \quad \mathrm{Pr} = \frac{\nu_f}{\alpha_f}, \quad P = \frac{pL^2}{\rho_f \alpha_f^2}. \tag{6.13}$$

This then yields the dimensionless governing equations are:

$$\frac{\partial U}{\partial X} + \frac{\partial V}{\partial Y} = 0, \tag{6.14}$$

$$U\frac{\partial U}{\partial X} + V\frac{\partial U}{\partial Y} = -\frac{\partial P}{\partial X} + \frac{1}{Re}\frac{\rho_f}{\rho_{nf}}\frac{\mu_{nf}}{\mu_f}\left(\frac{\partial^2 U}{\partial x^2} + \frac{\partial^2 U}{\partial Y^2}\right), \tag{6.15}$$

$$U\frac{\partial V}{\partial X} + V\frac{\partial V}{\partial Y} = -\frac{\partial P}{\partial Y} + \frac{1}{Re}\frac{\rho_f}{\rho_{nf}}\frac{\mu_{nf}}{\mu_f}\left(\frac{\partial^2 V}{\partial X^2} + \frac{\partial^2 V}{\partial Y^2}\right) + \frac{(\rho\beta)_{nf}}{\rho_{nf}\beta_f}\frac{Gr}{Re^2}\theta, \tag{6.16}$$

$$U\frac{\partial \theta}{\partial X} + V\frac{\partial \theta}{\partial Y} = \frac{\alpha_{nf}}{\alpha_f}\frac{1}{\mathrm{Pr}\,Re}\left(\frac{\partial^2 \theta}{\partial X^2} + \frac{\partial^2 \theta}{\partial Y^2}\right), \tag{6.17}$$

$$\frac{\partial^2 \theta_s}{\partial x^2} + \frac{\partial^2 \theta_s}{\partial y^2} = 0, \tag{6.18}$$

where $Ri = \frac{Gr}{Re^2}$ shows the Richardson number. The dimensionless boundary conditions regarding equations (6.14) and (6.18) are:

On the bottom heated surface (AB):

$$U = V = 0, \;\; \theta = 1, \;\; 0 \le X \le 1, \;\; Y = 0, \tag{6.19}$$

On the top moving cold surface (DC):

$$U = 1, \; V = 0, \;\; \theta = 0, \;\; 0 \le X \le 1, \;\; Y = 0.65, \tag{6.20}$$

On the left and right sloping surfaces (AD and BC):

$$U = V = 0, \;\; \frac{\partial \theta}{\partial (X, Y)} = 0, \;\; \forall X, \;\; \forall Y, \tag{6.21}$$

$$\theta = \theta_s, \;\; \text{at the outer solid cylinder surface,} \tag{6.22}$$

$$U = V = 0, \;\; \frac{\partial \theta}{\partial n} = K_r \frac{\partial \theta_s}{\partial n}, \tag{6.23}$$

where $K_r = k_s/k_{nf}$ keeps the thermal conductivity ratio above the covering of the internal body. The local Nusselt number evaluated at the heated bottom horizontal

surface, which is defined by

$$Nu_{nf} = -\left(\frac{\partial \theta}{\partial X}\right)_{Y=0}, \tag{6.24}$$

Finally, the average Nusselt number evaluated at the heated part of the bottom horizontal surface of the cavity which is given by:

$$\overline{Nu}_{nf} = \int_A^B Nu_{nf}\, \mathrm{d}Y, \tag{6.25}$$

The entropy generation relation is given by Ilis et al. (2008) and Alsabery et al. (2018d):

$$S = \frac{k_{nf}}{T_0^2}\left[\left(\frac{\partial T}{\partial x}\right)^2 + \left(\frac{\partial T}{\partial y}\right)^2\right] + \frac{\mu_{nf}}{T_0}\left[2\left(\frac{\partial u}{\partial x}\right)^2 + 2\left(\frac{\partial v}{\partial y}\right)^2 + \left(\frac{\partial u}{\partial x} + \frac{\partial v}{\partial x}\right)^2\right]. \tag{6.26}$$

In dimensionless form, local entropy generation can be expressed as:

$$\begin{aligned} S_{\mathrm{GEN}} = {} & \frac{k_{nf}}{k_f}\left[\left(\frac{\partial \theta}{\partial X}\right)^2 + \left(\frac{\partial \theta}{\partial Y}\right)^2\right] \\ & + \frac{\mu_{nf}}{\mu_f} N_\mu \left\{2\left[\left(\frac{\partial U}{\partial X}\right)^2 + \left(\frac{\partial V}{\partial Y}\right)^2\right] + \left(\frac{\partial^2 U}{\partial Y^2} + \frac{\partial^2 V}{\partial X^2}\right)^2\right\}, \end{aligned} \tag{6.27}$$

where, $N_\mu = \frac{\mu_f T_0}{k_f}\left(\frac{\alpha_f}{L(\Delta T)}\right)^2$ is the irreversibility distribution ratio and $S_{\mathrm{GEN}} = S_{gen}\frac{T_0^2 L^2}{k_f(\Delta T)^2}$.

The terms of equation (6.27) can be separated to the following form:

$$S_{\mathrm{GEN}} = S_\theta + S_\Psi, \tag{6.28}$$

where S_θ and S_Ψ are the entropy generation due to heat transfer irreversibility (HTI) and fluid friction irreversibility (FFI), respectively.

$$S_\theta = \frac{k_{nf}}{k_f}\left[\left(\frac{\partial \theta}{\partial X}\right)^2 + \left(\frac{\partial \theta}{\partial Y}\right)^2\right], \tag{6.29}$$

$$S_\Psi = \frac{\mu_{nf}}{\mu_f} N_\mu \left\{2\left[\left(\frac{\partial U}{\partial X}\right)^2 + \left(\frac{\partial V}{\partial Y}\right)^2\right] + \left(\frac{\partial^2 U}{\partial Y^2} + \frac{\partial^2 V}{\partial X^2}\right)^2\right\}. \tag{6.30}$$

By Integrating equation (6.28) over the domain, the global entropy generation (GEG)

for the present two-dimensional study is obtained as the following:

$$\text{GEG} = \int S_{GEN}\,\mathrm{d}X\mathrm{d}Y = \int S_{\theta}\,\mathrm{d}X\mathrm{d}Y + \int S_{\Psi}\,\mathrm{d}X\mathrm{d}Y. \tag{6.31}$$

It is appropriate to mention Bejan number in order to determine which is the dominant, heat transfer or fluid friction irreversibility. Bejan number is defined as:

$$Be = \frac{\int S_{\theta}\,\mathrm{d}X\mathrm{d}Y}{\int S_{GEN}\,\mathrm{d}X\mathrm{d}Y}. \tag{6.32}$$

When $Be > 0.5$, the HTI is the dominant, while when $Be < 0.5$, the FFI is the dominant.

6.3 METHOD OF SOLUTION

The finite element based on Galerkin weighted residual are applied to investigate the control equations (6.14)–(6.18) subject to the boundary conditions equations (6.19)–(6.23). We analyse the momentum equations (6.15) and (6.16) by using the finite element analysis.

First, we apply the penalty finite element method by excluding the pressure (P) including a penalty parameter (λ) as the following:

$$P = -\lambda\left(\frac{\partial U}{\partial X} + \frac{\partial V}{\partial Y}\right). \tag{6.33}$$

Then we have the following momentum equations towards the X and Y-directions:

$$U\frac{\partial U}{\partial X} + V\frac{\partial U}{\partial Y} = \frac{\partial \lambda}{\partial X}\left(\frac{\partial U}{\partial X} + \frac{\partial V}{\partial Y}\right) + \frac{\rho_f}{\rho_{nf}}\frac{\mu_{nf}}{\mu_f}\frac{1}{Re}\left(\frac{\partial^2 U}{\partial X^2} + \frac{\partial^2 U}{\partial Y^2}\right), \tag{6.34}$$

$$\begin{aligned} U\frac{\partial V}{\partial X} + V\frac{\partial V}{\partial Y} &= \frac{\partial \lambda}{\partial Y}\left(\frac{\partial U}{\partial X} + \frac{\partial V}{\partial Y}\right) + \frac{\rho_f}{\rho_{nf}}\frac{\mu_{nf}}{\mu_f}\frac{1}{Re}\left(\frac{\partial^2 V}{\partial X^2} + \frac{\partial^2 V}{\partial Y^2}\right) \\ &\quad + \frac{(\rho\beta)_{nf}}{\rho_{nf}\beta_f}\frac{Gr}{Re^2}\theta_{nf}. \end{aligned} \tag{6.35}$$

The weak (or weighted-integral) formulation regarding the momentum equations by

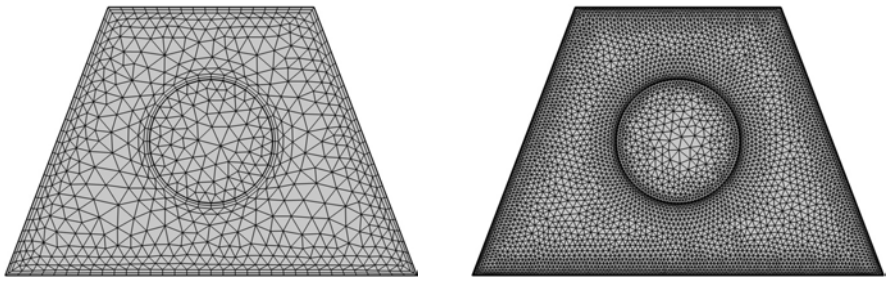

(a) (b)

Figure 6.2 Grid-points distribution for the grid size of (a) 1339 and (b) 9846 elements.

multiplying the equation by an internal domain (Φ) and integrating it over the computational domain which is discretised toward small triangular elements as revealed in Figure 6.2.

The following weak formulations are as follows:

$$\int_{\Omega}\left(\Phi_i U^k\frac{\partial U^k}{\partial X}+\Phi_i V^k\frac{\partial U^k}{\partial Y}\right)\mathrm{d}X\mathrm{d}Y=\lambda\int_{\Omega}\frac{\partial\Phi_i}{\partial X}\left(\frac{\partial U^k}{\partial X}+\frac{\partial V^k}{\partial Y}\right)\mathrm{d}X\mathrm{d}Y$$
$$+\frac{\rho_f}{\rho_{nf}}\frac{\mu_{nf}}{\mu_f}\frac{1}{Re}\int_{\Omega}\Phi_i\left(\frac{\partial^2 U^k}{\partial X^2}+\frac{\partial^2 U^k}{\partial Y^2}\right)\mathrm{d}X\mathrm{d}Y, \tag{6.36}$$

$$\int_{\Omega}\left(\Phi_i V^k\frac{\partial V^k}{\partial X}+\Phi_i V^k\frac{\partial V^k}{\partial Y}\right)\mathrm{d}X\mathrm{d}Y=\lambda\int_{\Omega}\frac{\partial\Phi_i}{\partial Y}\left(\frac{\partial U^k}{\partial X}+\frac{\partial V^k}{\partial Y}\right)\mathrm{d}X\mathrm{d}Y$$
$$+\frac{\rho_f}{\rho_{nf}}\frac{\mu_{nf}}{\mu_f}\frac{1}{Re}\int_{\Omega}\Phi_i\left(\frac{\partial^2 V^k}{\partial X^2}+\frac{\partial^2 V^k}{\partial Y^2}\right)\mathrm{d}X\mathrm{d}Y+\frac{(\rho\beta)_{nf}}{\rho_{nf}\beta_f}\frac{Gr}{Re^2}\int_{\Omega}\Phi_i\theta_{nf}^k\mathrm{d}X\mathrm{d}Y. \tag{6.37}$$

Selection about the interpolation functions as implementing an approximation toward the velocity distribution and temperature distribution as:

$$U\approx\sum_{j=1}^{m}U_j\Phi_j(X,Y),\quad V\approx\sum_{j=1}^{m}V_j\Phi_j(X,Y),\quad\theta\approx\sum_{j=1}^{m}\theta_j\Phi_j(X,Y). \tag{6.38}$$

The nonlinear residual equations for the momentum equations that obtained from the Galerkin weighted residual finite-element method are:

$$R(1)_i=\sum_{j=1}^{m}U_j\int_{\Omega}\left[\left(\sum_{j=1}^{m}U_j\Phi_j\right)\frac{\partial\Phi_j}{\partial X}+\left(\sum_{j=1}^{m}V_j\Phi_j\right)\frac{\partial\Phi_j}{\partial Y}\right]\Phi_i\mathrm{d}X\mathrm{d}Y$$

$$+\lambda\left[\sum_{j=1}^{m} U_j \int_{\Omega} \frac{\partial \Phi_i}{\partial X}\frac{\partial \Phi_j}{\partial X}\mathrm{d}X\mathrm{d}Y + \sum_{j=1}^{m} V_j \int_{\Omega} \frac{\partial \Phi_i}{\partial X}\frac{\partial \Phi_j}{\partial Y}\mathrm{d}X\mathrm{d}Y\right] \tag{6.39}$$

$$+\frac{\rho_f}{\rho_{nf}}\frac{\mu_{nf}}{\mu_f}\frac{1}{Re}\sum_{j=1}^{m} U_j \int_{\Omega}\left[\frac{\partial \Phi_i}{\partial X}\frac{\partial \Phi_j}{\partial X} + \frac{\partial \Phi_i}{\partial Y}\frac{\partial \Phi_j}{\partial Y}\right]\mathrm{d}X\mathrm{d}Y,$$

$$R(2)_i = \sum_{j=1}^{m} V_j \int_{\Omega}\left[\left(\sum_{j=1}^{m} U_j\Phi_j\right)\frac{\partial \Phi_j}{\partial X} + \left(\sum_{j=1}^{m} V_j\Phi_j\right)\frac{\partial \Phi_j}{\partial Y}\right]\Phi_i\mathrm{d}X\mathrm{d}Y$$

$$+\lambda\left[\sum_{j=1}^{m} U_j \int_{\Omega} \frac{\partial \Phi_i}{\partial Y}\frac{\partial \Phi_j}{\partial X}\mathrm{d}X\mathrm{d}Y + \sum_{j=1}^{m} V_j \int_{\Omega} \frac{\partial \Phi_i}{\partial Y}\frac{\partial \Phi_j}{\partial Y}\mathrm{d}X\mathrm{d}Y\right] \tag{6.40}$$

$$+\frac{\rho_f}{\rho_{nf}}\frac{\mu_{nf}}{\mu_f}\frac{1}{Re}\sum_{j=1}^{m} V_j \int_{\Omega}\left[\frac{\partial \Phi_i}{\partial X}\frac{\partial \Phi_j}{\partial X} + \frac{\partial \Phi_i}{\partial Y}\frac{\partial \Phi_j}{\partial Y}\right]\mathrm{d}X\mathrm{d}Y$$

$$+\frac{(\rho\beta)_{nf}}{\rho_{nf}\beta_f}\frac{Gr}{Re^2}\int_{\Omega}\left(\sum_{j=1}^{m}\theta_j\Phi_j\right)\Phi_i\mathrm{d}X\mathrm{d}Y,$$

where the superscript k is the relative index, subscripts i, j and m are the residual number, node number and iteration number, respectively. For clarifying the nonlinear terms into the momentum equations, a Newton-Raphson iteration algorithm was employed. The convergence of the solution is allowed through the relative error to any of the variables does satisfy the resulting convergence criteria:

$$\left|\frac{\Gamma^{m+1} - \Gamma^m}{\Gamma^{m+1}}\right| \leq 10^{-5}. \tag{6.41}$$

For the purpose of validating the data, we have compared the present results with the previous numerical findings that presented by Khanafer & Aithal (2013) for the problem of free convective flow and heat transfer in a square cavity that filled with pure fluid and partially heated from below, as explained in Figures 6.3 and 6.4. Figure 6.3 presents streamlines and isotherm which were visually analyzed to ensure consistency with the reference study. The streamlines were examined for similarities in flow circulation and vortex structures, confirming that the convection patterns matched expected behaviors. The isotherms were compared to check that temperature gradients and thermal boundary layers followed the same distribution as in the reference. In Figure 6.4, we compared the average Nusselt number, which measures how well heat is

Table 6.1 Thermo-physical properties of water with Al_2O_3 nanoparticles at T = 310K (Bergman et al. 2011).

Physical properties	Fluid phase (water)	Al_2O_3
C_p (J/kgK)	4178	765
ρ (kg/m^3)	993	3970
k (Wm^{-1}K^{-1})	0.628	40
$\beta \times 10^5$ (1/K)	36.2	0.85
$\mu \times 10^6$ (kg/ms)	695	–
d_p (nm)	0.385	33

transferred. Our results followed a similar trend to the reference study, meaning that the heat transfer rates were consistent. These results provide confidence to the accuracy of the present numerical method.

6.4 RESULTS AND DISCUSSION

In this part, we present numerical results concerning the streamlines, isotherms and isentropic lines (the local dimensionless entropy generation) with various values of Richardson number ($0.01 \leq Ri \leq 10$), Reynolds number ($5 \leq Re \leq 500$), nanoparticles volume fraction ($0 \leq \phi \leq 0.04$), dimensionless radius of solid cylinder ($0.05 \leq S \leq 0.25$) and dimensionless location of solid cylinder (D) [$D1 = (X = 0.5, Y = 0.5), D2 = (X = 0.35, Y = 0.5), D3 = (X = 0.65, Y = 0.5), D4 = (X = 0.5, Y = 0.2), D5 = (X = 0.5, Y = 0.45)$]. Values of Prandtl number, thermal conductivity of the solid cylinder and side surface inclination angle are fixed at Pr = 4.623, $k_s = 0.76$ and $\varphi = 22.5°$. The thermophysical properties of the used base fluid (water) and solid Al_2O_3 phases are described in Table 6.1.

Figure 6.5 shows distributions of streamlines, isotherms and isentropic lines for different values of Richardson number for $\phi = 0.02$, $R = 0.15$, $Re = 100$ and the inner solid located at the center of the solid. Therefore, an increase in Ri is due to a growth of Grashof number. Natural convection is negligible if Richardson number is less than 1.0. Due to the motion direction of the upper wall, one small cell appear at the top of the solid wall in Figure 6.5 (a) and (b). As Ri increase, the streamlines are extending downwards as in Figure 6.5 (c) since both natural and forced convection exist. When

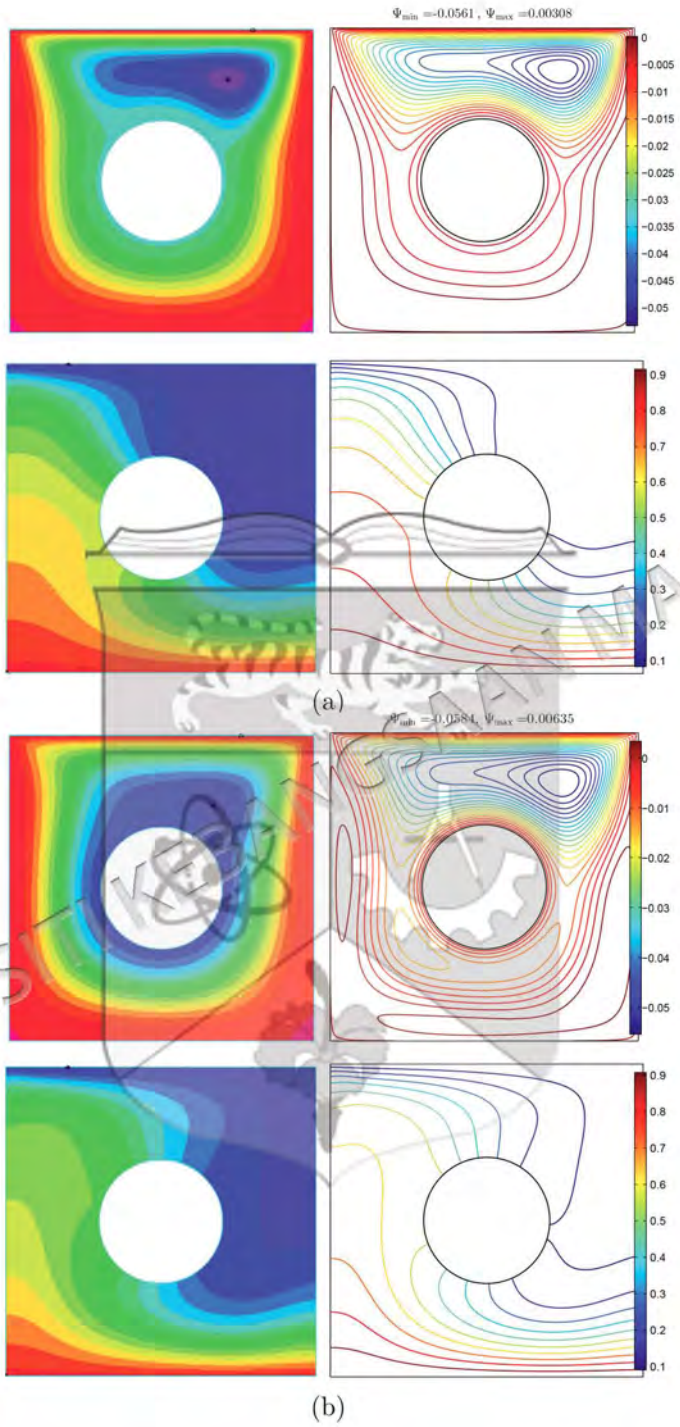

Figure 6.3 Comparison of results by Khanafer & Aithal (2013) (left) and (right) present study for (a) streamlines at $Ra = 10^6$ and $H = 0.4$, (b) isotherms at $Ra = 10^5$ and $H = 0.8$ and (c) isotherms at $Ra = 1.836 \times 10^5$ and $H = 0.8$ for the case of numerical and experimental results of Khanafer & Aithal (2013) at $\phi = 0$ and $D = 0$.

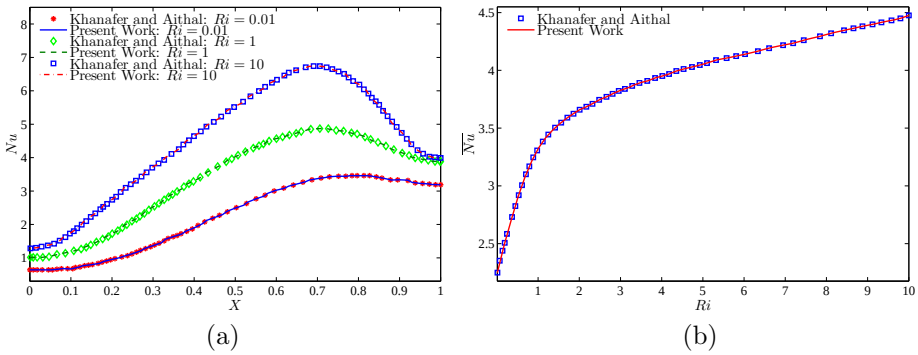

Figure 6.4 Comparison of the average Nusselt number interface with Ra for different H with Khanafer & Aithal (2013) at $\phi = 0$ and $D = 0$.

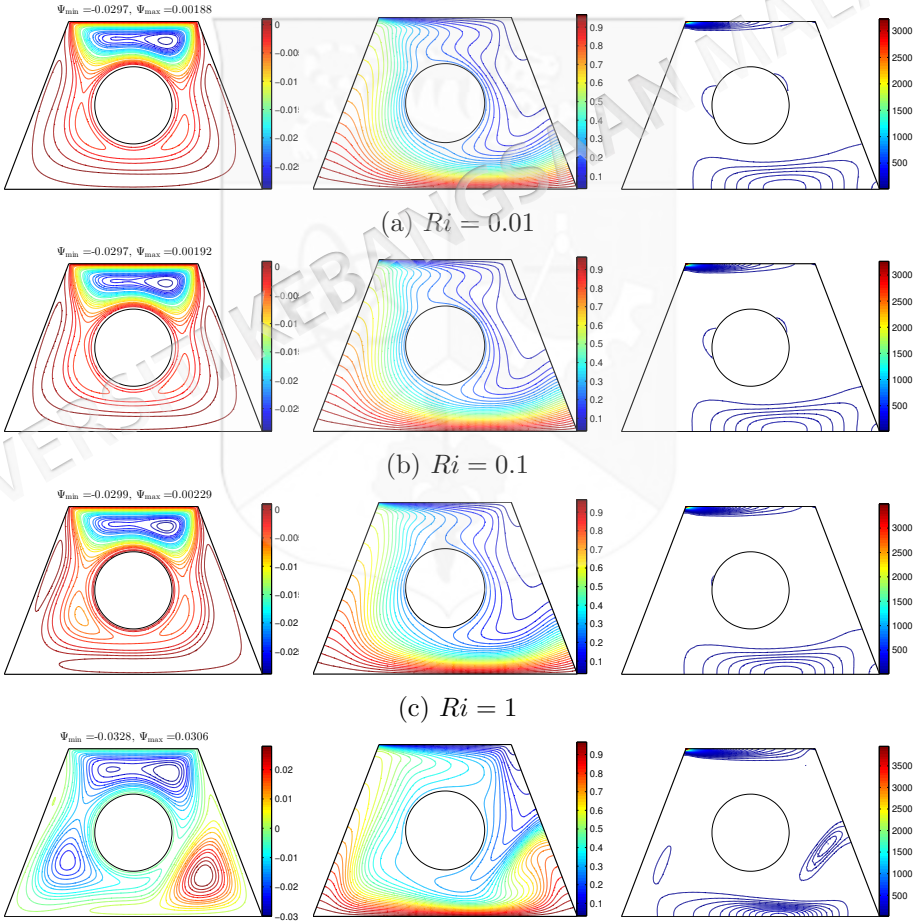

Figure 6.5 Variation of the streamlines (left), isotherms (middle), and isentropic (right) evolution by Richardson number (Ri) for $Re = 100$, $\phi = 0.02$, $R = 0.15$ and $D1$.

the Ri increases to 10, multi cellular appear at the top of the wall as well as the bottom of the wall.Since the bottom wall is heated and the upper wall is cooled, the isotherm patterns appear with curved lines. We can see that the curved lines appear at the top left and the bottom right of the solid as in Figure 6.5 (a). There is no change in the isotherm patterns as Ri increase. But, at $Ri = 10$, the isotherm curved lines elongated to the right of the solid. The entropy regions produced by the heat transfer irreversibility (HTI) and the nanofluid flow irreversibility (NFI) that arise for high temperatures and the velocity gradients. The isentropic lines depict a concentrated entropy generation close to three regions, namely top and right bottom of the enclosure and surface of the solid cylinder.There is no change of the isentropic lines at smaller Ri number. Only at $Ri = 10$, the isentropic lines slightly change as the lines appear at the center bottom of the solid and the sloping surfaces wall.

Figure 6.6 shows the effect of variations Reynold number on streamlines, isotherm, and isentropic with $Ri = 1$, $\phi = 0.02$, $R = 0.15$. In Figure 6.6 (a) , the streamlines appear with two rotating cells at the top of the wall and one rotating cell at the bottom of the wall. The reason of this is the shear force and buoyant force dominate at smaller Reynolds number.As Re increases, the cell at bottom of the wall and top right shrink while the cell at top left expands as in Figure 6.6(b). Furthermore, the cell at top right and bottom do not exist while the cell at top left expands at higher Re as in Figure 6.6 (c) and (d). These happen because the forced convection dominates compared to the buoyant force as Reynolds number increase. Since the cooling activity occurs at the top wall while the heating activity occurs at the bottom wall, thick thermal boundary layers clustered at the top left and bottom right of the cavity wall. The isotherms are approximately horizontal. Increase Re disturbs the isotherm inside the cavity.As $Re = 50$, we can see that the intensity of the isotherm patterns increased at the top left and bottom right walls and decreased at the right side of the cavity. Furthermore, intensity of the isotherm pattern decreased in the cavity as Re increases. The isentropic lines show a concentrated entropy generation inside the cavity and around the solid cylinder. These entropy regions result from the heat transfer irreversibility(HTI) and the nanofluid irreversibility (NFI) that arise from shear force and buoyant force. As Re increases, the intensity of isentropic lines decrease especially

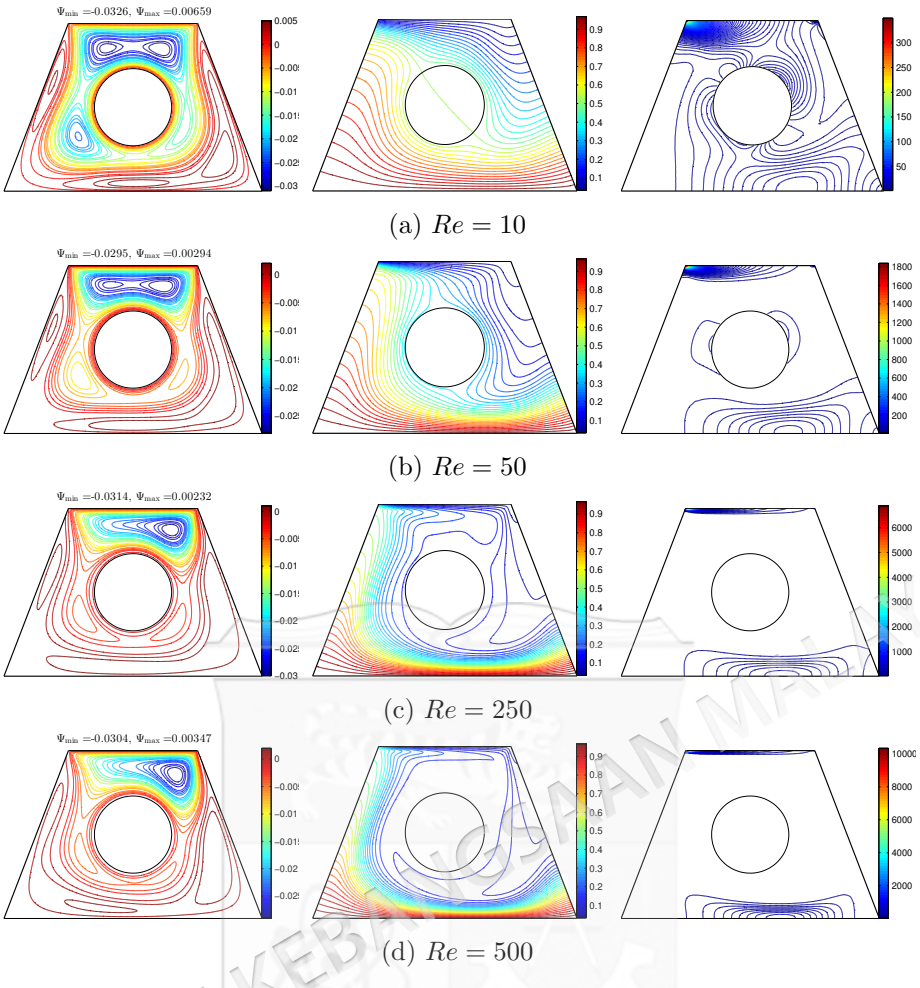

Figure 6.6 Variation of the streamlines (left), isotherms (middle), and isentropic (right) evolution by Reynolds number (Re) for $Ri = 1$, $\phi = 0.02$, $R = 0.15$ and $D1$.

around the solid cylinder. When $Re = 500$, the isentropic lines only appear at the top and bottom of the wall. The reason why this happens is the intensity of isentropic lines are high at the top of the wall due to shear force dominate as Re increase.

Figure 6.7 depicts the local Nusselt number interface with X and local entropy generation at the outer cylinder surface for different Richardson number. Local Nusselt number is maximum for all Richardson number at $X = 0.4$. The highest local Nusselt number is when $Ri = 10$ because the system is dominant with natural convection. At lowest Richardson number, we can see that the local entropy generation is highest at both vertical walls. Figure 6.8 depicts the distribution of the local Nusselt number, exhibits maximum heat transfer at $X = 0.4$ for all Reynolds number. Higher Reynold number gives maximum heat transfer compared to small Reynolds number.

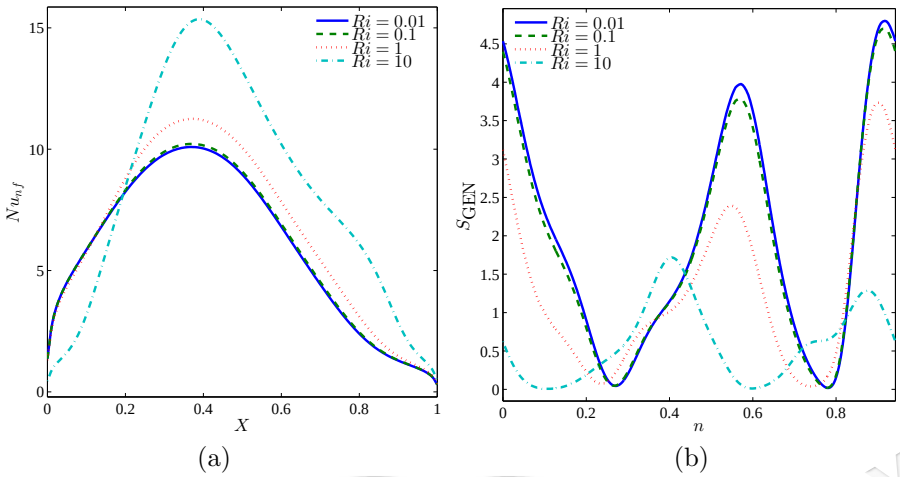

Figure 6.7 Variation of (a) local Nusselt number interfaces with X and (b) local entropy generation at the outer solid cylinder surface for different Ri at $Re = 100$, $\phi = 0.02$, $R = 0.15$ and $D1$.

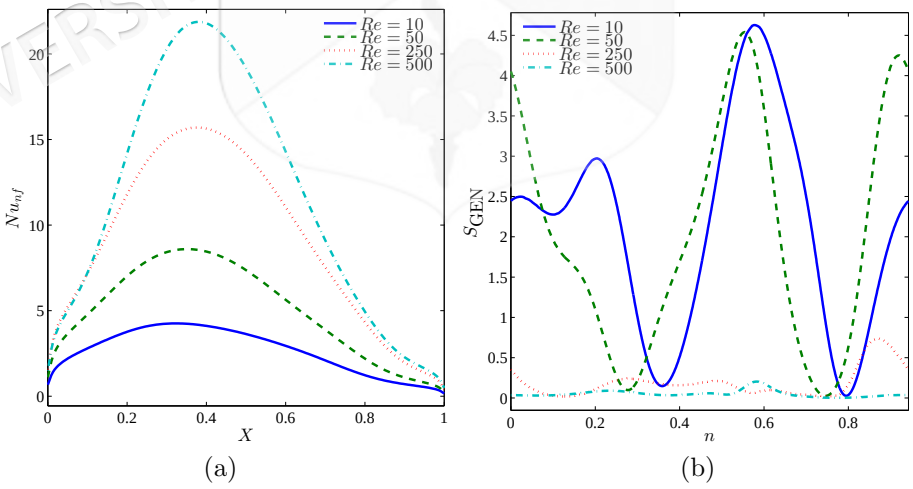

Figure 6.8 Variation of (a) local Nusselt number interfaces with X and (b) local entropy generation at the outer solid cylinder surface for different Re at $Ri = 1$, $\phi = 0.02$, $R = 0.15$ and $D1$.

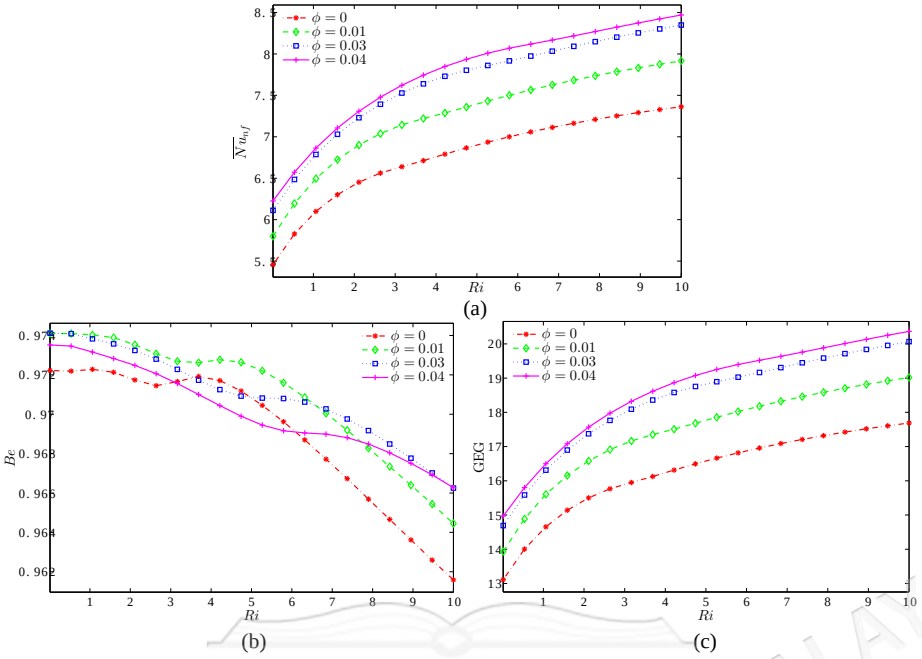

Figure 6.9 Variation of (a) average Nusselt number ($\overline{Nu}_{nf}$), (b) Bejan number (Be) and (c) the global entropy generation (GEG) with Ri for different values of ϕ at $Re = 100$, $R = 0.15$ and $D1$.

Figure 6.9 illustrates the effect of different nanoparticle volume fraction on average Nusselt number, Bejan number and global entropy generation with Richardson number at $Re = 100$, $R = 0.15$ and the location of inner solid at the center of the enclosure.As Ri increases, the average Nusselt number also increase for all nanoparticles volume fraction. We observed that the best performance of the average Nusselt number is at higher nanoparticles volume fraction. Since the value of Be is close to 1, it shows that the system is heat tranfer irreversibility dominant compared to nanofluid irreversibility. The value of Be is decreases for all nanoparticle volume fraction. The system is forced convection dominant if Richardson number is small. As the system changed to natural convection, we can see that the GEG increases. Higher nanoparticle volume fraction gives best result for global entropy generation compared to smaller nanoparticle volume fraction.

Figure 6.10 depicts the effect of different nanoparticles volume fraction on the average Nusselt number, Bejan number and the global entropy generation with different Reynolds number at $Ri = 1$, $R = 0.15$ and same position of inner solid as in Figure 6.9. As Re increases, we can see that the average Nusselt number and GEG increase. The

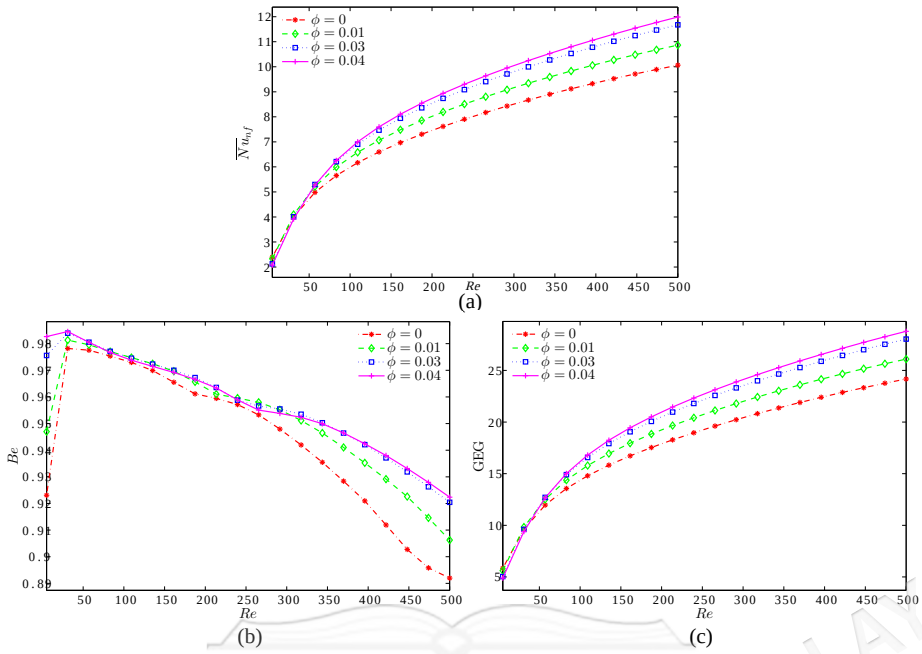

Figure 6.10 Variation of (a) average Nusselt number ($\overline{Nu}_{nf}$), (b) Bejan number (Be) and (c) the global entropy generation (GEG) with Re for different values of ϕ at $Ri = 1$, $R = 0.15$ and $D1$.

change of nanoparticle volume fraction also effect the average Nusselt number, Bejan and global entropy generation. We observed that the best performance for average Nusselt number and GEG is when the nanoparticle volume fraction is at 0.04. From graph, we noticed that the system is HTI dominant for all nanoparticle volume fraction. As Re increases to 50, we can see that the graph increases. However, the graph decreases when Re greater than 50, this may be due to combined of natural and forced convection.

The effect of various radius of cylinder on the streamlines, isotherms and isentropic are depicted in Figure 6.11 with $Ri = 1$, $Re = 100$, $\phi = 0.02$. As radius of cylinder increases, the passage width between the cylinder and the top and bottom wall decreases. Therefore, we can see that the size of cell decreases as the radius of cylinder increase. Furthermore, there are two cells appear when radius of cylinder greater than 0.2. As a result, increase in the solid cylinder shows high intensity of isotherm lines at the bottom and top of the cavity. For small radius, it shows that the intensity of isentropic are similar which the isentropic lines appear at the top and bottom of the wall. Only at higher radius, the isentropic lines appear at the solid cylinder as well.

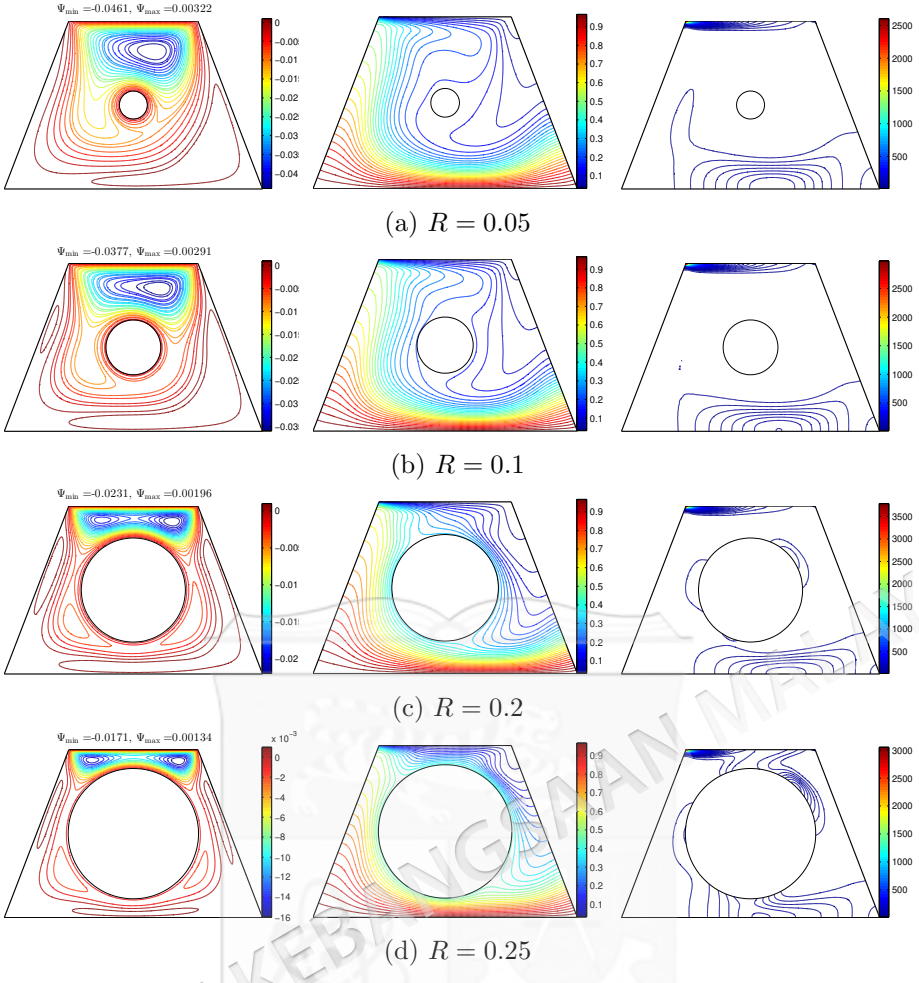

Figure 6.11 Variation of the streamlines (left), isotherms (middle), and isentropic (right) evolution by solid cylinder radius (R) for Ri = 1, Re = 100, ϕ = 0.02 and $D1$.

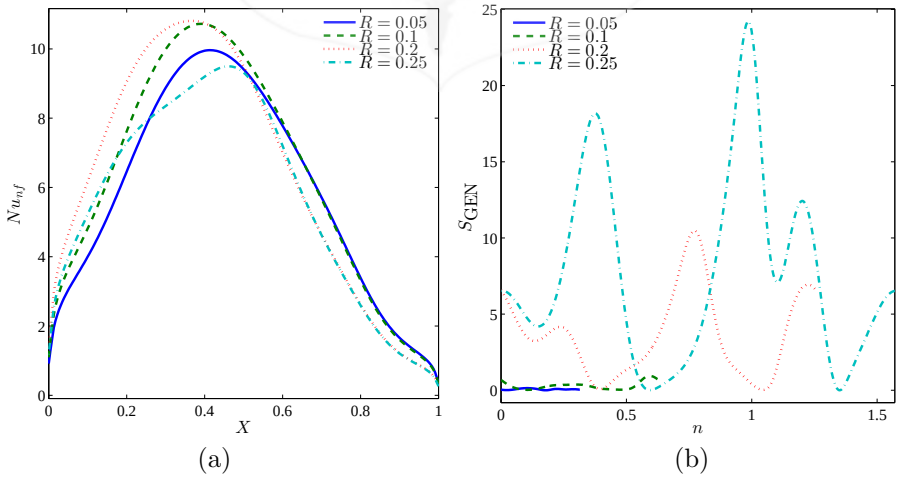

Figure 6.12 Variation of (a) local Nusselt number interfaces with X and (b) local entropy generation at the outer solid cylinder surface for different R at Ri = 1, Re = 100, ϕ = 0.02 and $D1$.

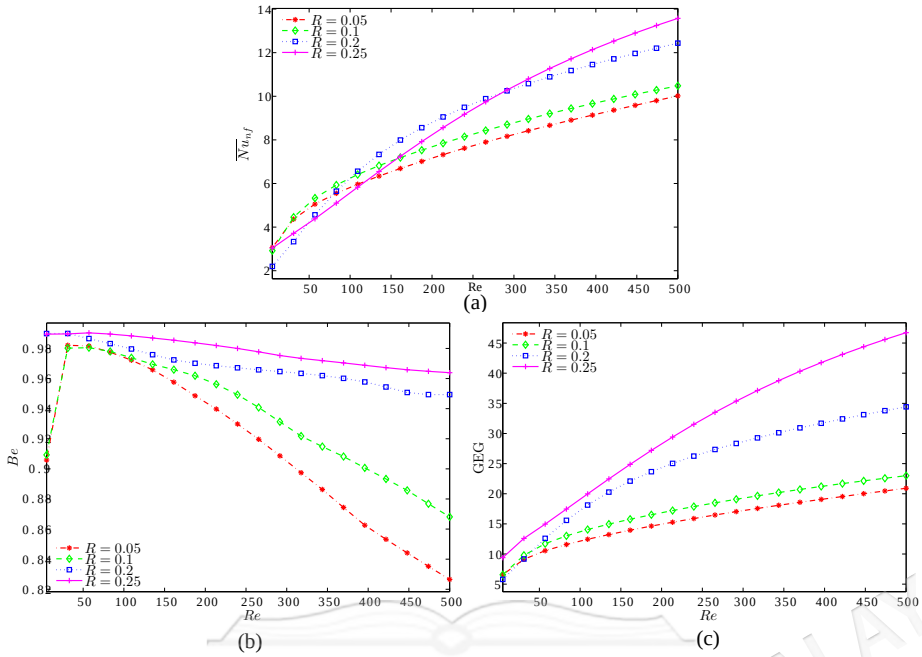

Figure 6.13 Variation of (a) average Nusselt number ($\overline{Nu}_{nf}$), (b) Bejan number (Be) and (c) the global entropy generation (GEG) with Re for different values of R at $Ri = 1$, $\phi = 0.02$ and $D1$.

Figure 6.12 depicts the local Nusselt number interfaces with X and local entropy generation at the outer solid cylinder surface with different radius of solid cylinder. Figure 6.12 (a) shows that the maximum heat transfer occur mostly at the center of the cavity. Figure 6.12 (b) illustrates that the local entropy generation has no change at smaller radius of solid cylinder. The local entropy generation has sinusoidal shape for higher radius of solid cylinder.

It is found that the changes of radius of solid cylinder affects the average Nusselt number, Bejan number and global entropy generation as in Figure 6.13. The average Nusselt number in Figure 6.13 (a) and global entropy generation in Figure 6.13 (b) were found to increase when Re number increase. This is probably due to the increase in the velocity of the top lid as Re increase, affecting thermal performance. Furthermore, the Bejan number are high for all radius and indicate that the system is HTI dominant as in Figure 6.13 (b). The graph illustrates that the Bejan number is increasing for all radius except $R = 0.25$ until $Re = 50$ and decreasing after that. This is because the fluid friction increases as Re increase and resulting Bejan number decrease.

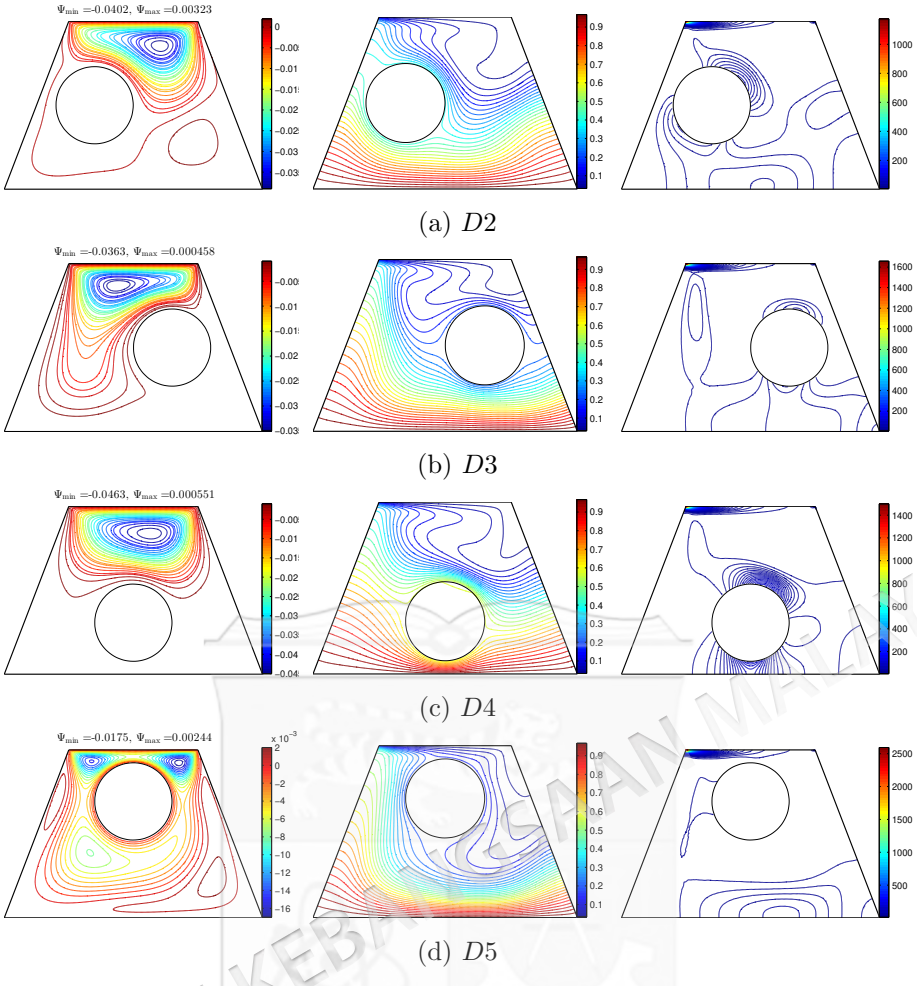

Figure 6.14 Variation of the streamlines (left), isotherms (middle), and isentropic (right) evolution by location of solid cylinder (D) for $Ri = 1$, $Re = 100$, $\phi = 0.02$ and $R = 0.15$.

Figure 6.14 illustrates the effect of various positions of solid cylinder on streamlines, isotherm and isentropic with Richardson number, Reynolds number , nanoparticle volume fraction and radius of solid cyilnder are 1, 100, 0.02 and 0.15 respectively. In Figure 6.14 (a) dan (b), the position of solid cylinder is kept constant at $y = 0.5$ but the value of x is different, where $x = 0.35$ and $x = 0.65$ respectively while in Figure 6.14 (c) and (d) the x position is kept constant, which is 0.5 but different y value where $y = 0.35$ and $y = 0.65$ respectively. The figure shows that the streamlines appear according to the position of solid cylinder. However, we can see that the streamlines also appear at the top of the enclosure for all position of solid cylinder due to the movement of the top lid wall. In addition, there is no streamline protrude in the solid cylinder. Likewise in isotherm, where we can see that the isotherm lines appear in

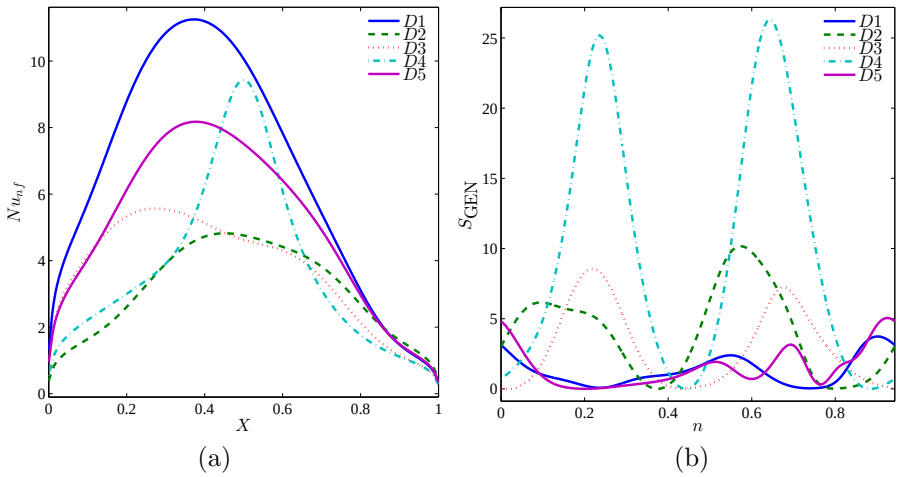

Figure 6.15 Variation of (a) local Nusselt number interfaces with X and (b) local entropy generation at the outer solid cylinder surface for different D at $Ri = 1$, $Re = 100$, $\phi = 0.02$ and $R = 0.15$.

enclosure in wavy shape. However, the intensity of isotherm is less at the top right of the enclosure for all position of solid cylinder. This maybe due to the various temperature distribution and movement of the top lid wall from left to right. For isentropic, figure depicts the isentropic lines with high intensity at the top of the enclosure for all position of solid cylinder. We also can see that the isentropic lines appear around the solid cylinder, and high density when the solid cylinder is at the bottom of the enclosure as in Figure 6.14 (d).

The various positions of solid cylinder on the local Nusselt number interfaces with X and local entropy generation at the outer solid cylinder surface is depicted in Figure 6.15. The local Nusselt number is minimum at the vertical of the cavity wall and maximum between $X = 0.2$ and $X = 0.6$ based on the position of the solid cylinder. The best thermal performance is obtained when the position of the solid cylinder is at the center of the enclosure. In addition, the local entropy generation at the outer solid cylinder is in sinusoidal shape. As we can see the local entropy generation is high when the position of the solid cylinder is at the bottom of the enclosure.

Figure 6.16 illustrates the average Nusselt number, Bejan number and the global entropy generation with nanoparticle volume fraction for different positions of solid cylinder at $Ri = 1$, $Re = 1$, and $R = 0.15$. Different solid cylinder will affect the average

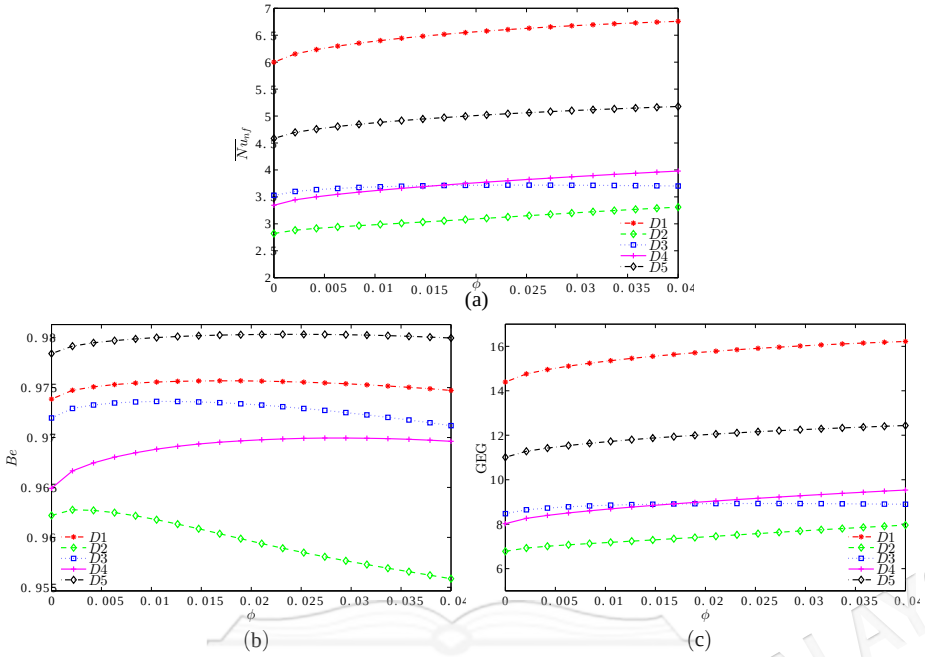

Figure 6.16 Variation of (a) average Nusselt number ($\overline{Nu}_{nf}$), (b) Bejan number (Be) and (c) the global entropy generation (GEG) with ϕ for different values of D at $Ri = 1$, $Re = 1$ and $R = 0.15$.

Nusselt number, average entropy generation and global entropy generation. We can see that the average Nusselt number and global entropy generation are high when the position of the solid cylinder is at the center of the enclosure. However, both average Nusselt number and the global entropy generation slightly increase as the nanoparticle volume fraction increased for all positions except when the solid is located at the left of the enclosure. The graph in 6.16 (b) shows that the system is HTI dominant for all positions of solid cylinder since the value of Be is greater than 0.5. As nanoparticle volume fraction number increases, we can see that the Bejan number slightly increased for all position of solid cylinder except when the solid cylinder is located at the right of the enclosure.

6.5 CONCLUSIONS

In this numerical work, the finite element method is applied to analyse the entropy generation and mixed convection in a trapezoidal cavity having differently located solid cylinder filled with Al_2O_3-water nanofluid. The detailed computational results for the

streamlines, isotherms and the local entropy generation for different values of the Ra, Re, nanoparticles volume fraction, radius and location of the solid cylinder. Some important conclusions from the study are given below.

1. The flow behaviour, which the temperature distribution and local entropy generation siginifcantly influenced by the varying position of solid cylinder in the trapezoidal enclosure.
2. Increasing both the Richardson number and Reynolds number enhances the rate of heat transfer as well as a high nanoparticles volume fraction. This phenomenon happened due to to the increased buoyancy and viscous forces within the system.
3. The global entropy generation increases with the augmentation of the Richardson and Reynolds number, while a counteractive behaviour is observed on the average Bejan number. As the Reynolds and Richardson number increase, the Bejan number tends to decrease.
4. The global entropy generation is increasing function of the solid cylinder radius for the case of intensive convection regime (Reynolds number), while the Bejan number is a decreasing function of the size of the solid cylinder radius of the same regime.
5. Both heat transfer rate and global entropy generation are significantly increased when the position of solid cylinder at the centre of the cavity. Meanwhile the Bejan number is strong when the solid cylinder located at the top in the cavity.

CHAPTER VII

MIXED CONVECTION AND ENTROPY GENERATION IN TRIANGULAR ENCLOSURE HAVING NANOFLUID WITH INNER ROTATING CYLINDER

7.1 INTRODUCTION

Food processing, solar collectors, cooling electronics, automotive are industrial that always related to heat transfer and fluid flow. Researchers have done many studies in heat transfer and fluid flow. This research is very helpful to make sure that the energy can be optimized so that the time and energy can be conserved. Mixed convection is a part of the heat transfer and fluid flow. Mixed convection is the combination between natural convection (buoyancy fluid driven) and forced convection such as magnetohydrodynamics, lid driven cavity, and radiation. Some of paper has been discussed mixed convection in various type of cavities such as square cavity (Khorasanizadeh, Nikfar and Amanip 2013), trapezoidal cavity (Arefmanesh, Aghaei and Ehteram 2016), sinusoidal cylinder (Jabbar et al. 2019) and many more.

In this chapter, we examine the thermal performance and entropy generation in a triangular enclosure with nanofluids. The bottom wall is thermally insulated while the inclined walls are cooled. To investigate the fluid flow, the 3 rotating cylinders are placed in the enclosure. Hassen et al. (2021) used double rotating cylinder under magnetic field in a porous cavity. They found that the entropy analysis is significantly increase including the rotating cylinder. Therefore, based on this study, we believed that the entropy analysis is increasing if we use three rotating cylinder. Hence, we believe that this work will be a valuable contribution in improving the thermal performance.

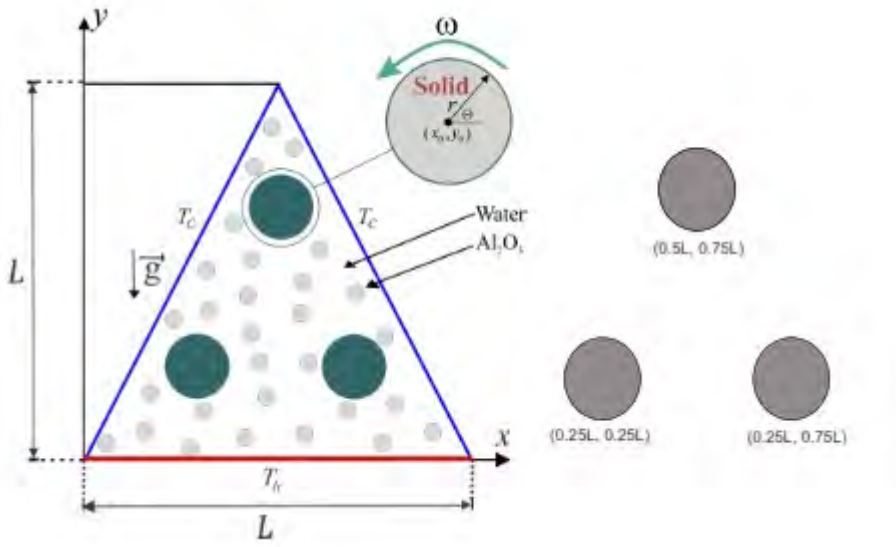

Figure 7.1 Physical model of convection in a triangular cavity together with conducting wall and coordinate system

7.2 MATHEMATICAL FORMULATION

The two-dimensional geometric design regarding mixed convection flow and heat transfer inside a triangular cavity containing three solid cylinder is described schematically in Figure 7.1. The bottom surface is assumed to be heated with a constant temperature of T_h and the inclined surface is preserved at a constant cold temperature T_c. The fluid flow in the triangular cavity was examined to hold steady, laminar, and loaded with alumina-water nanofluids. The governing equations of Navier-stokes and energy equations toward the viscous incompressible flow are indicated in the dimensional model as the following:

$$\frac{\partial u}{\partial x} + \frac{\partial v}{\partial y} = 0, \tag{7.1}$$

$$u\frac{\partial u}{\partial x} + v\frac{\partial u}{\partial y} = -\frac{1}{\rho_{nf}}\frac{\partial p}{\partial x} + \nu_{nf}\left(\frac{\partial^2 u}{\partial x^2} + \frac{\partial^2 u}{\partial y^2}\right), \tag{7.2}$$

$$u\frac{\partial v}{\partial x} + v\frac{\partial v}{\partial y} = -\frac{1}{\rho_{nf}}\frac{\partial p}{\partial y} + \nu_{nf}\left(\frac{\partial^2 v}{\partial x^2} + \frac{\partial^2 v}{\partial y^2}\right) + \beta_{nf} g(T - T_0), \tag{7.3}$$

$$u\frac{\partial T}{\partial x} + v\frac{\partial T}{\partial y} = \alpha_{nf}\left(\frac{\partial^2 T}{\partial x^2} + \frac{\partial^2 T}{\partial y^2}\right), \tag{7.4}$$

The energy equation of the conducting solid rotating cylinder is moving through external force:

$$\frac{\partial^2 T_s}{\partial x^2} + \frac{\partial^2 T_s}{\partial y^2} = \frac{k_s}{(\rho C_p)_s}\left(\frac{\partial^2 T}{\partial x^2} + \frac{\partial^2 T}{\partial y^2}\right). \tag{7.5}$$

where x and y are the Cartesian coordinates measured in the horizontal and vertical direction respectively, g is the acceleration due to gravity, ρ_{nf} is the density of the nanofluid and v_{nf} is the kinematic viscosity of the nanofluid. The β_{nf} is thermal expansion of the nanofluids, T is temperature and s is refer to inner solid cylinder. We introduced the next adopted nondimensional variables:

$$R = \frac{r'}{L'}, \omega = \frac{\omega' L^2}{\alpha_f}. \tag{7.6}$$

The following relations can describe the thermophysical features of the applied nanofluids:

$$(\rho C_p)_{nf} = (1-\phi)(\rho C_p)_f + \phi(\rho C_p)_p, \tag{7.7}$$

$$\alpha_{nf} = \frac{k_{nf}}{(\rho C_p)_{nf}}, \tag{7.8}$$

$$\rho_{nf} = (1-\phi)\rho_f + \phi\rho_p, \tag{7.9}$$

$$(\rho\beta)_{nf} = (1-\phi)(\rho\beta)_f + \phi(\rho\beta)_p, \tag{7.10}$$

$$\frac{\mu_{nf}}{\mu_f} = \frac{1}{1 - 34.87(\frac{d_p}{d_f})^{-0.3}\phi^{1.03}}, \tag{7.11}$$

$$\frac{k_{nf}}{k_f} = 1 + 4.4 Re_B^{0.4} Pr^{0.66} (\frac{T}{T_{fr}})^{10} (\frac{k_p}{k_f})^{0.03} \phi^{0.66}. \tag{7.12}$$

Here Re_B is defined as

$$Re_B = \frac{\rho_f \mu_B d_p}{\mu_f}, \mu_B = \frac{2k_b T}{\pi \mu_f d_p^2}, \tag{7.13}$$

while the molecular diameter of water (d_f) is defined by the following equation:

$$d_f = 0.1\left[\frac{6M}{N\pi\rho_f}\right]^{\frac{1}{3}}, \tag{7.14}$$

The following non-dimensional variables are introduced as follows:

$$X = \frac{x}{L}, \quad Y = \frac{y}{L}, \quad U = \frac{u}{U_0}, \; V = \frac{v}{U_0}, \quad \theta = \frac{T - T_c}{T_h - T_c}, \quad \theta_s = \frac{T_s - T_c}{T_h - T_c},$$

$$D = \frac{d}{L}, \quad \Pr = \frac{\nu_f}{\alpha_f}, \quad P = \frac{pL^2}{\rho_f \alpha_f^2} \tag{7.15}$$

This then yields the dimensionless governing equations as follows:

$$\frac{\partial U}{\partial X} + \frac{\partial V}{\partial Y} = 0, \tag{7.16}$$

$$U\frac{\partial U}{\partial X} + V\frac{\partial U}{\partial Y} = -\frac{\partial P}{\partial X} + \frac{1}{Re}\frac{\rho_f}{\rho_{nf}}\frac{\mu_{nf}}{\mu_f}\left(\frac{\partial^2 U}{\partial X^2} + \frac{\partial^2 U}{\partial Y^2}\right) + \frac{(\rho\beta)_{nf}}{\rho_{nf}\beta_f} Ri\theta \sin\gamma, \tag{7.17}$$

$$U\frac{\partial V}{\partial X} + V\frac{\partial V}{\partial Y} = -\frac{\partial P}{\partial Y} + \frac{1}{Re}\frac{\rho_f}{\rho_{nf}}\frac{\mu_{nf}}{\mu_f}\left(\frac{\partial^2 V}{\partial X^2} + \frac{\partial^2 V}{\partial Y^2}\right) + \frac{(\rho\beta)_{nf}}{\rho_{nf}\beta_f} Ri\theta \cos\gamma, \tag{7.18}$$

$$U\frac{\partial \theta}{\partial X} + V\frac{\partial \theta}{\partial Y} = \frac{\alpha_{nf}}{\alpha_f}\frac{1}{PrRe}\left(\frac{\partial^2 \theta}{\partial X^2} + \frac{\partial^2 \theta}{\partial Y^2}\right), \tag{7.19}$$

$$\frac{\partial^2 \theta_s}{\partial X^2} + \frac{\partial^2 \theta_s}{\partial Y^2} = \frac{(\rho C_p)_f k_s}{(\rho C_p)_f k_f}\left(\frac{\partial^2 \theta}{\partial X^2} + \frac{\partial^2 \theta}{\partial Y^2}\right), \tag{7.20}$$

where $Ri = \frac{Gr}{Re^2}$ is the Richardson number and $Gr = \frac{g\beta(T_h - T_c)L^3}{\nu_f^2}$ is the Grashof number. The dimensionless boundary conditions as indicated in equations (7.16) and (7.20) are shown below:

On the bottom heated surface:

$$U = V = 0, \theta = 1, 0 \le X \le 1, Y = 0, \tag{7.21}$$

On the left and right cold sloping surfaces:

$$U = V = 0, \theta = 0, \forall X, \forall Y. \tag{7.22}$$

Over the rotating cylinder :

$$U = -\Omega(X - X_0),\ V = \Omega(Y - Y_0),\ \theta = \theta_s,\ \frac{\partial \theta}{\partial \eta} = K_r \frac{\partial \theta_s}{\partial \eta}, \tag{7.23}$$

where $K_r = \frac{k_s}{k_{nf}}$ keeps the thermal conductivity ratio above the covering of the internal body. The local Nusselt number estimated through the heated base horizontal surface

does represent by:

$$N\mu_{nf} = -\left(\frac{\partial\theta}{\partial X}\right)_{Y=0}. \tag{7.24}$$

Finally, the average Nusselt number could be determined through the heated segment of the bottom horizontal surface of the cavity, which does represent by:

$$\overline{Nu}_{nf} = \int_A^B Nu_{nf}dY. \tag{7.25}$$

The entropy generation relation as indicated in dimensionless form below:

$$\begin{aligned} S_{\text{GEN}} &= \frac{k_{nf}}{k_f}\left[\left(\frac{\partial\theta}{\partial X}\right)^2+\left(\frac{\partial\theta}{\partial Y}\right)^2\right]+\frac{\mu_{nf}}{\mu_f}N_\mu\left\{2\left[\left(\frac{\partial U}{\partial X}\right)^2+\left(\frac{\partial V}{\partial Y}\right)^2\right]\right. \\ &\quad \left.+\left(\frac{\partial^2 U}{\partial Y^2}+\frac{\partial^2 V}{\partial X^2}\right)^2\right\}, \end{aligned} \tag{7.26}$$

where $N_\mu = \frac{\mu_f T_0}{k_f}\left(\frac{\alpha_f}{L(\Delta T)}\right)^2$ is the irreversibility distribution ratio and $S_{\text{GEN}} = S_{gen}\frac{T_0^2L^2}{k_f(\Delta T)^2}$. The terms of equation (7.26) can be separated based on the following formula:

$$S_{\text{GEN}} = S_\theta + S_\psi, \tag{7.27}$$

where S_θ and S_ψ are the entropy generation due to heat transfer irreversibility (HTI) and fluid fricton irrecersibility (FFI), respectively,

$$S_\theta = \frac{k_{nf}}{k_f}\left[\left(\frac{\partial\theta}{\partial X}\right)^2+\left(\frac{\partial\theta}{\partial Y}\right)^2\right], \tag{7.28}$$

$$S_\psi = \frac{\mu_{nf}}{\mu_f}N_\mu\left\{2\left[\left(\frac{\partial U}{\partial X}\right)^2+\left(\frac{\partial V}{\partial Y}\right)^2\right]+\left(\frac{\partial^2 U}{\partial Y^2}+\frac{\partial^2 V}{\partial X^2}\right)^2\right\}. \tag{7.29}$$

By Integrating equations (7.27) over the domain, the global entropy generation (GEG) for the present two-dimensional study is obtained as follows:

$$\text{GEG} = \int S_{\text{GEN}}dXdY = \int S_\theta dXdY + \int S_\psi dXdY. \tag{7.30}$$

It is necessary to mention the Bejan number in determining which is dominant, either

heat transfer or fluid friction irreversibility. Bejan number is defined as:

$$Be = \frac{\int S_\theta dXdY}{\int S_{\text{GEN}} dXdY}. \tag{7.31}$$

The HTI is dominant when $Be > 0.5$, while the FFI is dominant when $Be < 0.5$.

7.3 NUMERICAL METHOD AND VALIDATION

The Galerkin weighted residual with finite element methods was employed to investigate the control equations (7.16)–(7.20) subject to the boundary conditions shown in equations (7.21)–(7.23). The finite element analysis of the momentum equations (7.17) and (7.18) is represented by the following procedure:

Firstly, the penalty finite element method was applied excluding the pressure (P) and including a penalty parameter (λ) as follows:

$$P = -\lambda \left(\frac{\partial U}{\partial X} + \frac{\partial V}{\partial Y} \right) \tag{7.32}$$

The following momentum equations towards the X- and Y-directions are shown as follows:

$$\begin{aligned} U\frac{\partial U}{\partial X} + V\frac{\partial U}{\partial Y} &= \frac{\partial \lambda}{\partial X}\left(\frac{\partial U}{\partial X} + \frac{\partial V}{\partial Y} \right) + \frac{\rho_f}{\rho_{nf}} \frac{\mu_{nf}}{\mu f} \frac{1}{Re} \left(\frac{\partial^2 U}{\partial X^2} + \frac{\partial^2 U}{\partial Y^2} \right) \\ &\quad + \frac{(\rho\beta)_{nf}}{\rho_{nf}\beta_f} Ri\theta \sin\gamma, \end{aligned} \tag{7.33}$$

$$\begin{aligned} U\frac{\partial V}{\partial X} + V\frac{\partial V}{\partial Y} &= \frac{\partial \lambda}{\partial Y}\left(\frac{\partial U}{\partial X} + \frac{\partial V}{\partial Y} \right) + \frac{\rho_f}{\rho_{nf}} \frac{\mu_{nf}}{\mu f} \frac{1}{Re} \left(\frac{\partial^2 V}{\partial X^2} + \frac{\partial^2 V}{\partial Y^2} \right) \\ &\quad + \frac{(\rho\beta)_{nf}}{\rho_{nf}\beta_f} Ri\theta \cos\gamma, \end{aligned} \tag{7.34}$$

The weak (or weighted-integral) formulation regarding the momentum equations was obtained by multiplying the equation by an internal domain (Φ) and integrating it over the computational domain which is discretised towards small triangular elements. The

following weak formulations are obtained:

$$\begin{aligned}\int_\Omega \left(\Phi_i U^k \frac{\partial U^k}{\partial X} + \Phi_i V^k \frac{\partial U^k}{\partial Y}\right) \mathrm{d}X\mathrm{d}Y &= \lambda \int_\Omega \frac{\partial \Phi_i}{\partial X}\left(\frac{\partial U^k}{\partial X} + \frac{\partial V^k}{\partial Y}\right) \mathrm{d}X\mathrm{d}Y \\ &+ \frac{\rho_f}{\rho_{nf}} \frac{\mu_{nf}}{\mu_f} \frac{1}{Re} \int_\Omega \Phi_i \left(\frac{\partial^2 U^k}{\partial X^2} + \frac{\partial^2 U^k}{\partial Y^2}\right) \mathrm{d}X\mathrm{d}Y, \\ &+ \frac{(\rho\beta)_{nf}}{\rho_{nf}\beta_f} Ri \int_\Omega \Phi_i \theta_{nf}^k \mathrm{d}X\mathrm{d}Y \sin\gamma, \end{aligned} \tag{7.35}$$

$$\begin{aligned}\int_\Omega \left(\Phi_i V^k \frac{\partial V^k}{\partial X} + \Phi_i V^k \frac{\partial V^k}{\partial Y}\right) \mathrm{d}X\mathrm{d}Y &= \lambda \int_\Omega \frac{\partial \Phi_i}{\partial Y}\left(\frac{\partial U^k}{\partial X} + \frac{\partial V^k}{\partial Y}\right) \mathrm{d}X\mathrm{d}Y \\ &+ \frac{\rho_f}{\rho_{nf}} \frac{\mu_{nf}}{\mu_f} \frac{1}{Re} \int_\Omega \Phi_i \left(\frac{\partial^2 V^k}{\partial X^2} + \frac{\partial^2 V^k}{\partial Y^2}\right) \mathrm{d}X\mathrm{d}Y \\ &+ \frac{(\rho\beta)_{nf}}{\rho_{nf}\beta_f} Ri \int_\Omega \Phi_i \theta_{nf}^k \mathrm{d}X\mathrm{d}Y \cos\gamma. \end{aligned} \tag{7.36}$$

The selection of interpolation functions as an approximation towards velocity distribution and temperature distribution as follows:

$$U \approx \sum_{j=1}^{m} U_j \Phi_j(X,Y), V \approx \sum_{j=1}^{m} V_j \Phi_j(X,Y), \theta \approx \sum_{j=1}^{m} \theta_j \Phi_j(X,Y).$$

The non-linear residual equations for the momentum equations obtained from the Galerkin weighted residual finite-element method are as follows:

$$\begin{aligned} R(1)_i = &\sum_{j=1}^{m} U_j \int_\Omega \left[\left(\sum_{j=1}^{m} U_j \Phi_j\right) \frac{\partial \Phi_j}{\partial X} + \left(\sum_{j=1}^{m} V_j \Phi_j\right) \frac{\partial \Phi_j}{\partial Y}\right] \Phi_i \mathrm{d}X\mathrm{d}Y \\ &+ \lambda \left[\sum_{j=1}^{m} U_j \int_\Omega \frac{\partial \Phi_i}{\partial X}\frac{\partial \Phi_j}{\partial X} \mathrm{d}X\mathrm{d}Y + \sum_{j=1}^{m} V_j \int_\Omega \frac{\partial \Phi_i}{\partial X}\frac{\partial \Phi_j}{\partial Y} \mathrm{d}X\mathrm{d}Y\right] \\ &+ \frac{\rho_f}{\rho_{nf}} \frac{\mu_{nf}}{\mu_f} \frac{1}{Re} \sum_{j=1}^{m} U_j \int_\Omega \left[\frac{\partial \Phi_i}{\partial X}\frac{\partial \Phi_j}{\partial X} + \frac{\partial \Phi_i}{\partial Y}\frac{\partial \Phi_j}{\partial Y}\right] \mathrm{d}X\mathrm{d}Y, \\ &+ \frac{(\rho\beta)_{nf}}{\rho_{nf}\beta_f} Ri \int_\Omega \left(\sum_{j=1}^{m} \theta_j \Phi_j\right) \Phi_i \mathrm{d}X\mathrm{d}Y \sin\gamma, \end{aligned} \tag{7.37}$$

$$\begin{aligned} R(2)_i = &\sum_{j=1}^{m} V_j \int_\Omega \left[\left(\sum_{j=1}^{m} U_j \Phi_j\right) \frac{\partial \Phi_j}{\partial X} + \left(\sum_{j=1}^{m} V_j \Phi_j\right) \frac{\partial \Phi_j}{\partial Y}\right] \Phi_i \mathrm{d}X\mathrm{d}Y \\ &+ \lambda \left[\sum_{j=1}^{m} U_j \int_\Omega \frac{\partial \Phi_i}{\partial Y}\frac{\partial \Phi_j}{\partial X} \mathrm{dXdY} + \sum_{j=1}^{m} V_j \int_\Omega \frac{\partial \Phi_i}{\partial Y}\frac{\partial \Phi_j}{\partial Y} \mathrm{dXdY}\right] \end{aligned}$$

$$+\frac{\rho_f}{\rho_{nf}}\frac{\mu_{nf}}{\mu_f}\frac{1}{Re}\sum_{j=1}^{m}V_j\int_{\Omega}\left[\frac{\partial\Phi_i}{\partial X}\frac{\partial\Phi_j}{\partial X}+\frac{\partial\Phi_i}{\partial Y}\frac{\partial\Phi_j}{\partial Y}\right]\mathrm{dXdY} \tag{7.38}$$

$$+\frac{(\rho\beta)_{nf}}{\rho_{nf}\beta_f}Ri\int_{\Omega}\left(\sum_{j=1}^{m}\theta_j\Phi_j\right)\Phi_i\mathrm{d}X\mathrm{d}Y\cos\gamma,$$

$$R(3)_i=\sum_{j=1}^{m}(\theta_s)_j\int_{\Omega}\left[\frac{\partial\Phi_i}{\partial X}\frac{\partial\Phi_j}{\partial X}+\frac{\partial\Phi_i}{\partial Y}\frac{\partial\Phi_j}{\partial Y}\right]\mathrm{d}X\mathrm{d}Y$$

$$+\frac{(\rho C_p)_f}{(\rho C_p)_s}\frac{k_s}{k_f}\sum_{j=1}^{m}(\theta)_j\int_{\Omega}\left[\frac{\partial\Phi_i}{\partial X}\frac{\partial\Phi_j}{\partial X}+\frac{\partial\Phi_i}{\partial Y}\frac{\partial\Phi_j}{\partial Y}\right]\mathrm{d}X\mathrm{d}Y, \tag{7.39}$$

where the superscript k is the relative index, subscripts i, j, and m are the residual number, node number, and iteration number, respectively. For clarifying the non-linear terms into the momentum equations, a Newton-Raphson iteration algorithm was employed. The convergence of the solution was allowed using the relative error to any of the variables that satisfy the resulting convergence criteria as follows:

$$\left|\frac{\Gamma^{m+1}-\Gamma^{m}}{\Gamma^{m+1}}\right|\leqslant 10^{-5}.$$

For data validation, a comparison is made between the resulting figures and the one provided by Ilis, Mobedi and Sunden (2008) for the case of entropy generation and natural convection in a square cavity fully heated from sides, as shown in Figure 7.2. Figure 7.3 shows alternative comparisons regarding the enhancement in the thermal conductivity due to the addition of the Al_2O_3 nanoparticles with two different experimental results and the numerical results of Corcione, Cianfrini, and Quintino (2013) as well. These results provide confidence to the accuracy of the present numerical method.

7.4 RESULTS AND DISCUSSION

The numerical results for streamlines, isotherms, and isentropic lines along with various values for Reynolds number ($5 \leq Re \leq 500$), nanoparticles volume fraction ($0 \leq \phi \leq 0.04$), angular velocities ($-4 \leq \Omega \leq 4$) and Grashof number ($5 \leq Re \leq 500$) are presented in this section. The values for Prandtl number, thermal conductivity of the

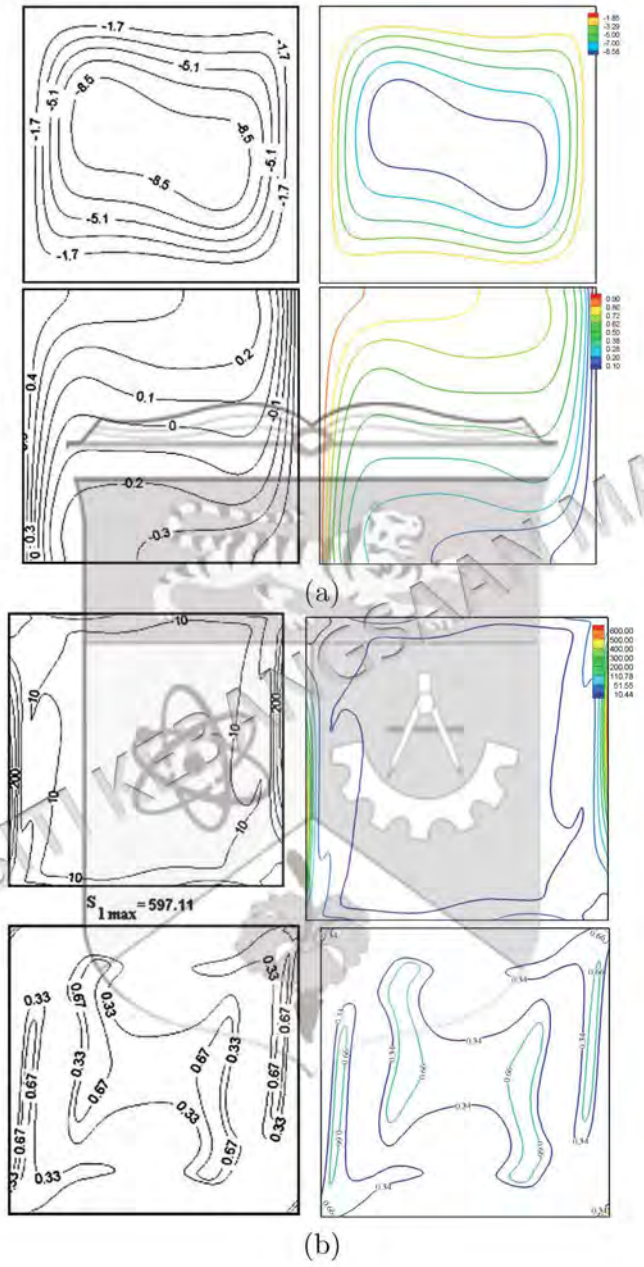

Figure 7.2 Streamlines and isotherms (a), global entropy generation and Bejan number (b), Ilis et al. (2008) (left), present study (right), for $Ra = 10^5$, $\phi = 0$, D and $H = 1$.

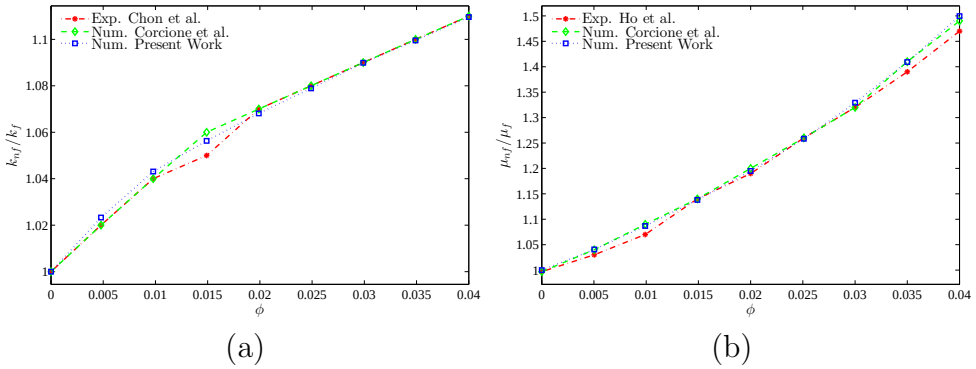

Figure 7.3 Comparison of (a) thermal conductivity ratio with Chon et al. (2005) and Corcione et al. (2013) and (b) dynamic viscosity ratio with Ho et al. (2010) and Corcione et al. (2013).

solid cylinder, and side surface inclination angle are fixed at . The thermophysical properties of the used base fluid (water) and solid Al_2O_3 phases are shown in Table. The effect of Grashof number on streamlines, isotherm and isentropic has been shown in Figure 7.4. The isotherm lines increase as Grashof number increases since the system is changed from forced convection to mixed convection. The flow intensifies as the below of the solid cylinder due to the increase in buoyancy force. The isotherm lines slightly difference as Gr increase. At $Gr = 10^5$, the isotherm vertically elongated. Due to that, at $Gr = 10^5$, we have seen slightly different where the isentropic lines is increase compared to the lower Gr due to increase in buoyancy force. The streamline, isotherm and isentropic lines influenced by the changes of rotation inner cylinder has been shown in Figure 7.5. Negative measure is when the cylinder rotates clockwise while positive measure is anti-clockwise direction. Zero value means there is no rotational happens while greater value means the rotational velocity increase. During zero rotational velocity, two rotating vortices exist at the bottom of the cavity. Since no rotation exist, the cellular appear due to the buoyancy force and temperature gradient. For non-zero rotational velocity, another one rotating vortices appear at the top of the cavity. The streamlines intensifies at the bigger value of the angular rotational velocity since the velocity increased. With no rotational, the streamlines flow just like plume like pattern. When rotational exist, the isotherm has filled the space in the enclosure, but the situation is a bit of mess. As result, we can see that the isotherm skews to the right when the cylinder rotate clockwise direction opposite the isotherm skews to the left due to the

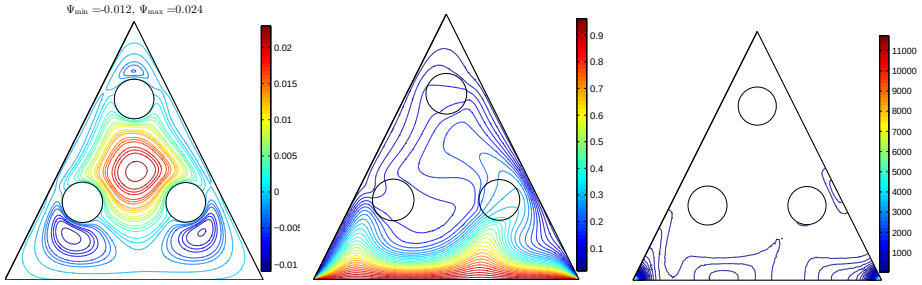

(a) $Gr = 10^2$

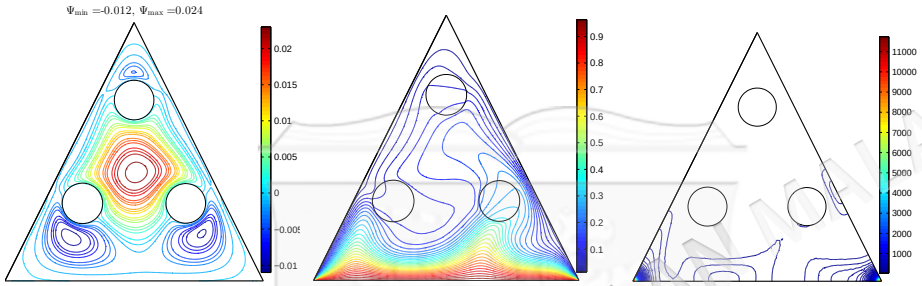

(b) $Gr = 10^3$

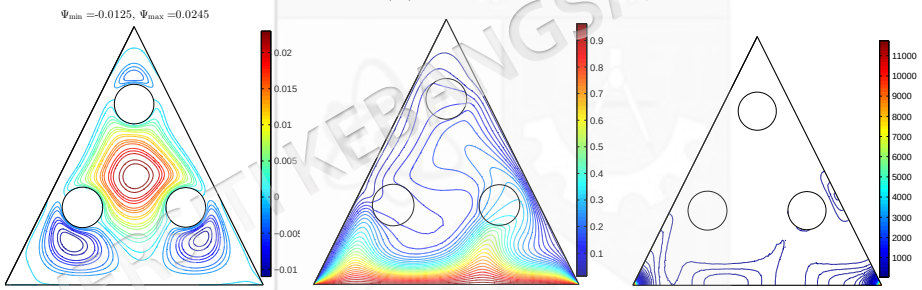

(c) $Gr = 10^4$

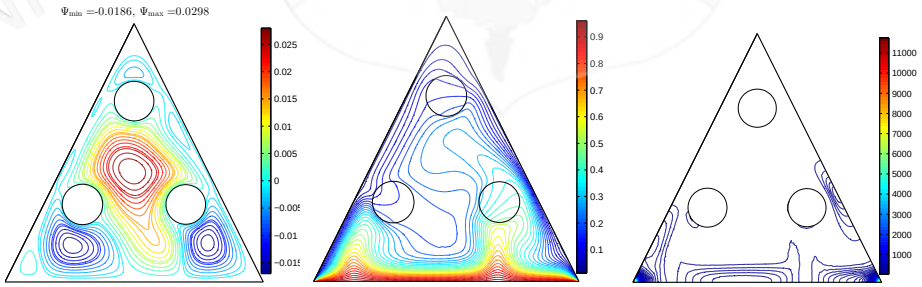

(d) $Gr = 10^5$

Figure 7.4 Variation of the streamlines (left), isotherms (middle), and isentropic (right) evolution based on the Grashof number Gr for Re = 100 and ϕ = 0.02

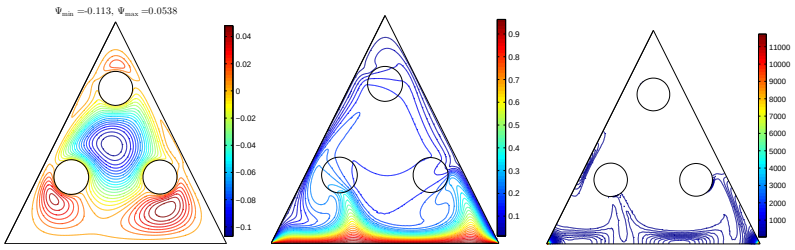

(a) $\Omega = -4$

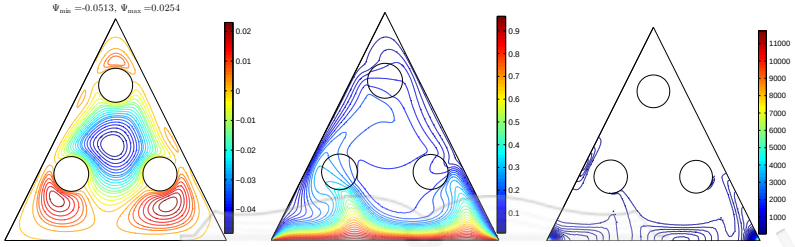

(b) $\Omega = -2$

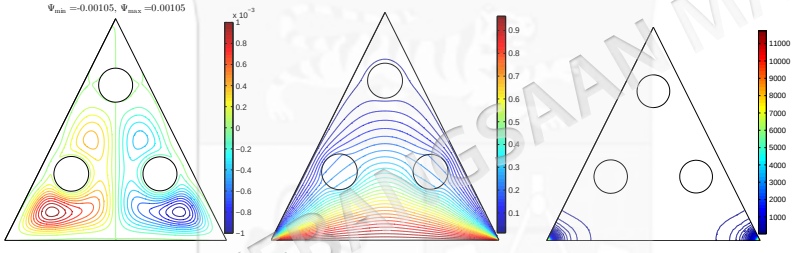

(c) $\Omega = 0$

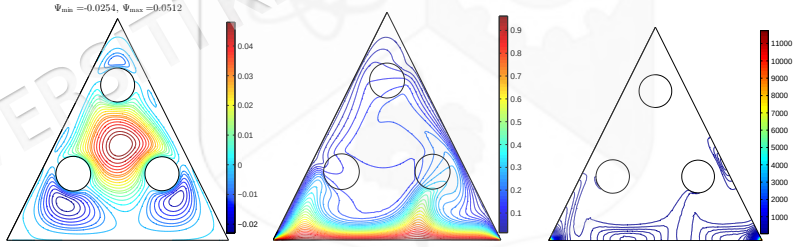

(d) $\Omega = 2$

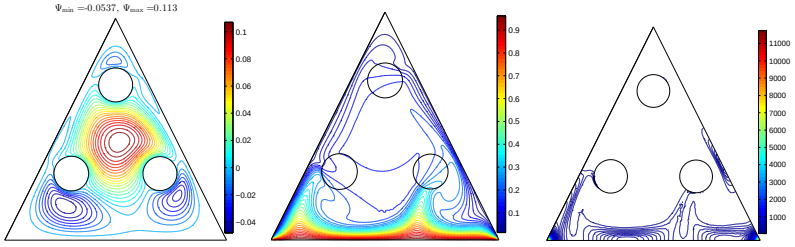

(e) $\Omega = 4$

Figure 7.5 Variation of the streamlines (left), isotherms (middle), and isentropic (right) evolution based on Ω for $Re = 100$ and $\phi = 0.02$

direction of cylinder rotate. When the system relies only with buoyancy force, the isentropic lines only appear at the edges of the cavity. Since, no force from rotational, the line appears due to temperature friction irreversibility. When rotational exist, the isentropic lines appear at the cylinder and at the bottom of the cavity due to fluid friction irreversibility compared to heat transfer irreversibility. The streamlines, isotherm and isentropic for different Reynolds number has been presented in Figure 7.6. At Re=10, the streamline is generated with unicellular appeared at the bottom right of the cavity. Since the system is more to natural convection instead of forced convection due to smaller Re, the streamline is generated by buoyancy force instead of shear force. Since the bottom of the cavity is thermally insulated, the isotherm has plume like pattern. Since then, the isentropic lines appear at the bottom of the cavity due to heat transfer irreversibility. As Re increase, the system is changed from natural convection to mixed convection. The result is the streamlines intensifies at the bottom and top of the cavity. The isotherm has skewed to the corner of the cavity. Then, the isentropic line is generated at the bottom cavity. Figure 7.7 has been shown that variation of velocity interfaces with X with different Grashof number. The result shown that the pattern like wave which is the peak of the wave at X=0.1 and X=0.4. This happen due to the existence of the rotating cylinder where it trigger the velocity of the nanofluid. The temperature is increased at the middle of the cavity due to the heated bottom of the cavity. At certain point, the temperature is decreased at the edges of the cavity due to the cold inclined wall. The local Nusselt number decrease at the middle of the cavity while at edges, the local Nusselt number high. There is no change different Grashof number. Figure 7.8 shows that the velocity of nanofluid interfaces with X. Increase Ω means increase the velocity of rotating cylinder. Negative measure means anti-clockwise direction while positive direction means clockwise direction. Zero measure means no rotating cylinder involved. We can see that the velocity has no change since no rotating involved. Increase Ω make the velocity of nanofluid increase. While the velocity of nanofluid decrease at smaller value of Ω. The temperature of the nanofluid is smaller when no rotating cylinder involved. But, at highest velocity of rotating cylinder, the temperature flows is higher. However, the temperature is highest at the middle of the Ω since at highest temperature it hinders the temperature of the nanofluid. No rotation involved, the local Nusselt number has no change. Highest velocity of rotating cylinder gives effect to the local Nusselt

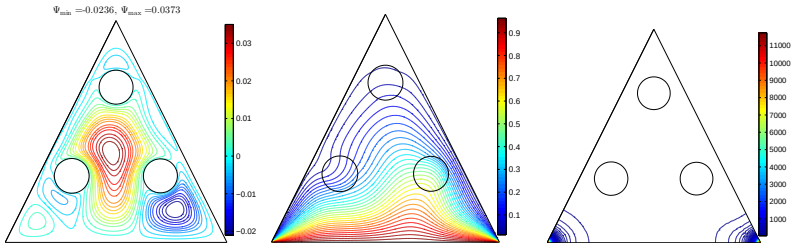

(a) $Re = 10$

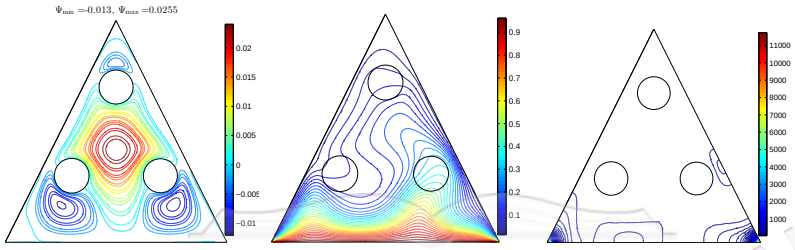

(b) $Re = 50$

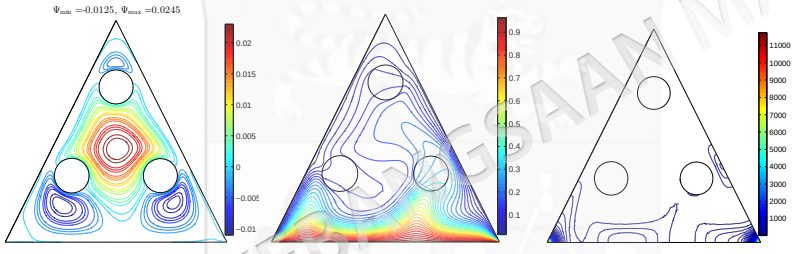

(c) $Re = 100$

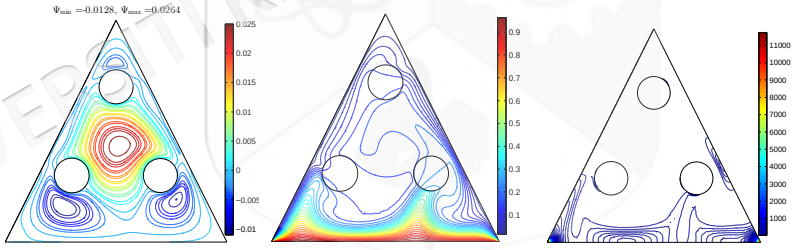

(d) $Re = 250$

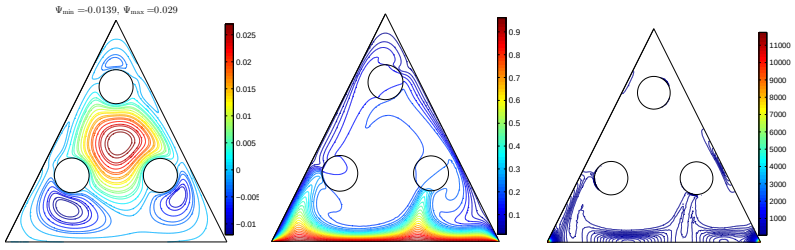

(e) $Re = 500$

Figure 7.6 Variation of the streamlines (left), isotherms (middle), and isentropic (right) evolution based on at $Ri = 1$, $Re = 100$, $\phi = 0.02$ and $D1$.

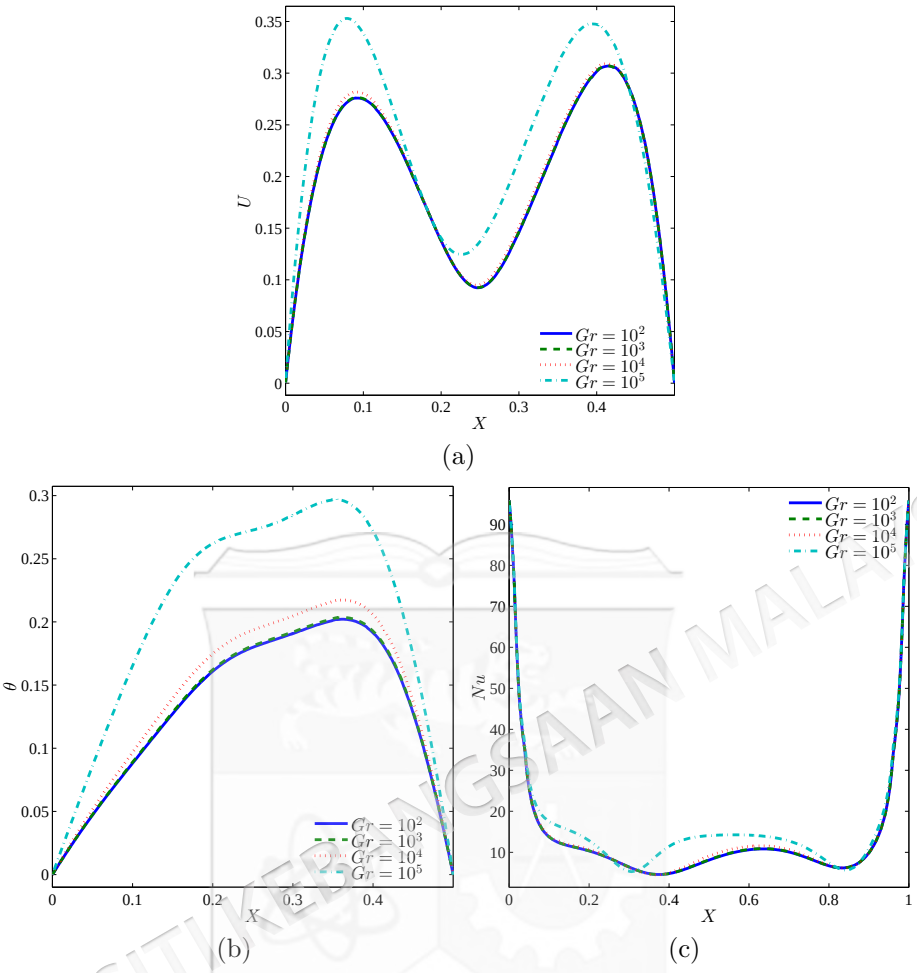

Figure 7.7 Variation of (a) velocity, (b) temperature and (c) local Nusselt number interfaces with X or different R at $Ri = 1$, $Re = 100$, $\phi = 0.02$ and $D1$.

number.

Figure 7.9 presents the effects of various Reynolds number on the local Nusselt number. With the small value of Reynolds number, the flow in the enclosure is in laminar. The velocity at the right side is high at the small Re due to movement of the rotating cylinder. While at the left side, the Re exhibit the velocity of the fluid. The temperature is high at the middle of the cavity since the bottom wall heated. While the edge of the cavity, the temperature is small due to cold inclined wall. The temperature for all Reynolds number are slightly different. The highest Reynolds number give higher temperature at the end of the cavity while the middle Reynolds number give higher

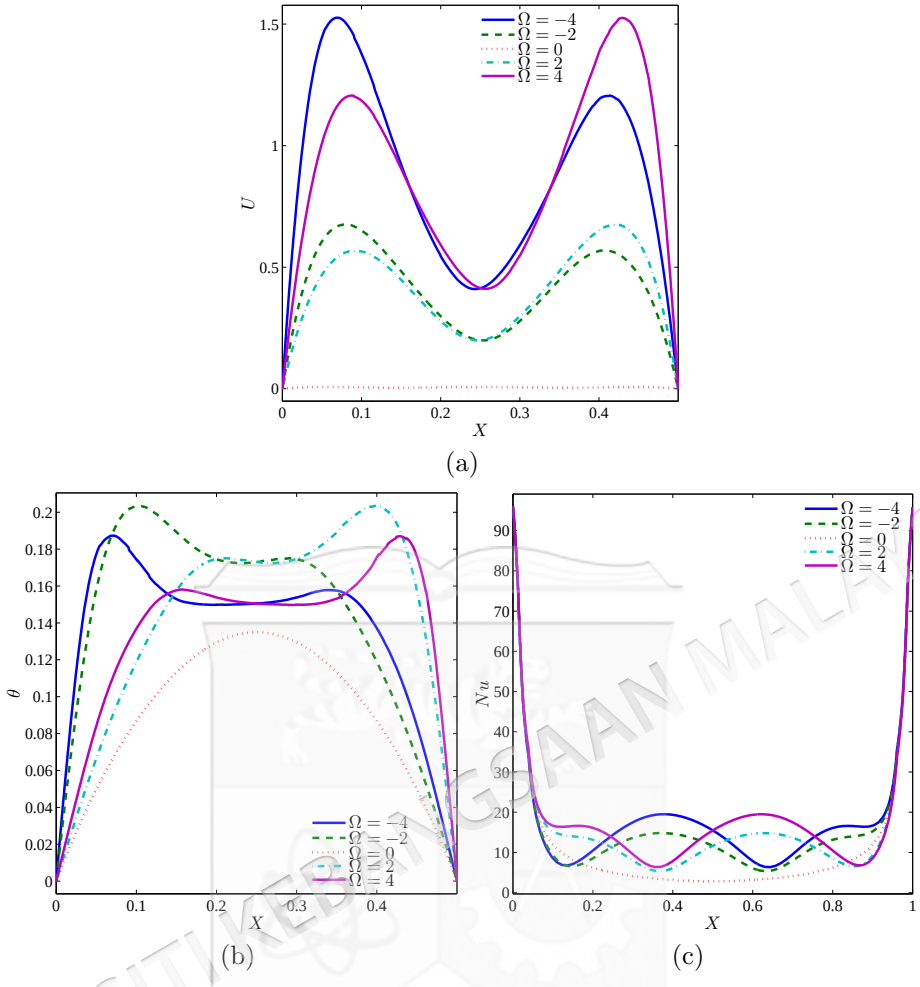

Figure 7.8 Variation of (a) velocity, (b) temperature and (c) local Nusselt number interfaces with X for different R at $Ri = 1$, $Re = 100$, $\phi = 0.02$ and $D1$.

temperature at the middle of the cavity. Local Nusselt number shows that whether the system dominant in conduction or convection. All local Nusselt number for all Reynolds number are slightly different. The highest Reynolds number accelerate the local Nusselt number compared to other Reynolds number. The result shows that convection become dominant as Reynolds number increased.

In Figure 7.10, we observe an interesting result in relation to the influence for different R. The average Nusselt number increase as Grashof number increase. However, the highest nanoparticle volume fraction accelerate the average Nusselt number since the existence of nanoparticle volume fraction enhance the convective heat transfer. For

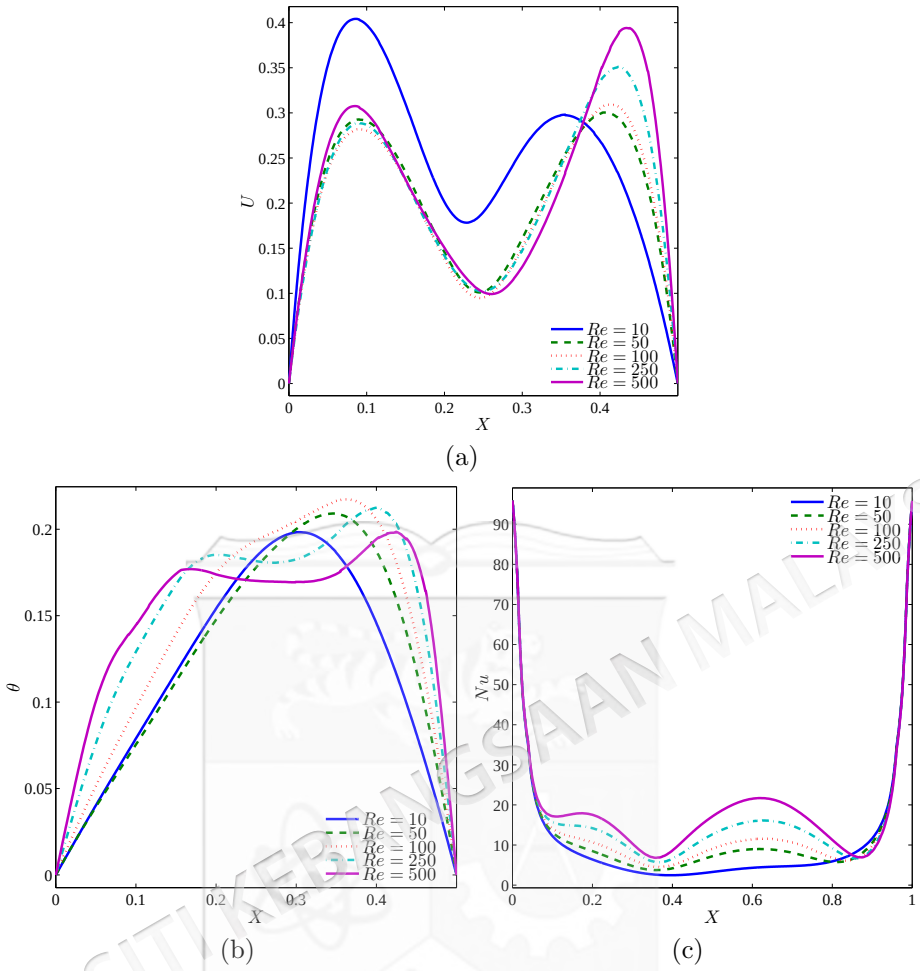

Figure 7.9 Variation of (a) velocity , (b) temperature and (c) local Nusselt number interfaces with X for different R at $Ri = 1$, $Re = 100$, $\phi = 0.02$ and $D1$.

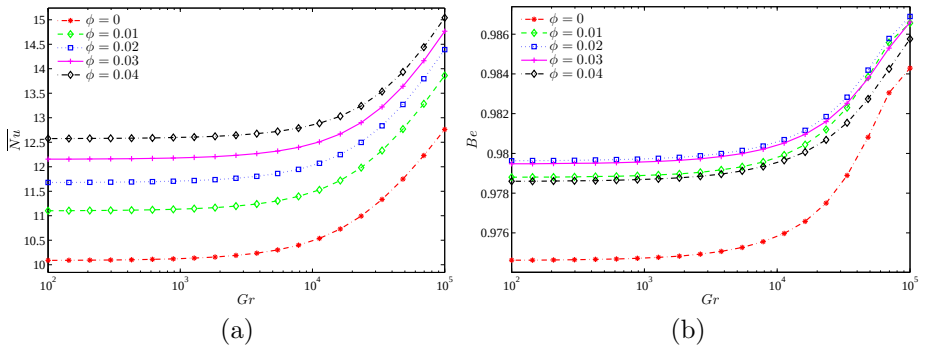

Figure 7.10 Variation of (a) average Nusselt number interfaces with X and (b) Bejan number for different R at $Ri = 1$, $Re = 100$, $\phi = 0.02$ and $D1$.

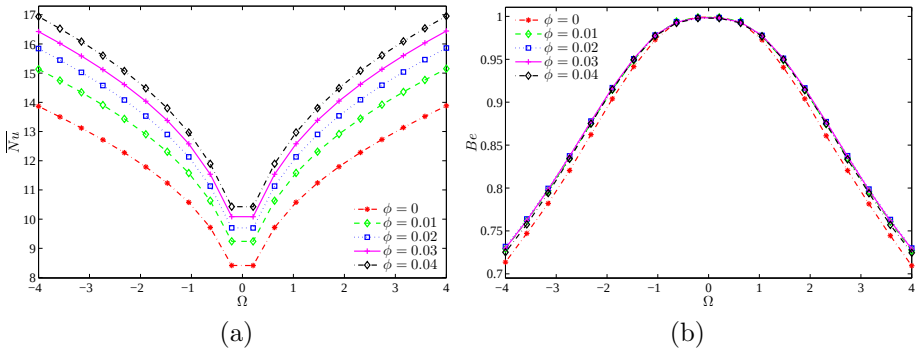

Figure 7.11 Variation of (a) average Nusselt number interfaces with X and (b) Bejan number for different R at $Ri = 1$, $Re = 100$, $\phi = 0.02$ and $D1$.

all nanoparticle volume fraction exhibit the highest Bejan number where it shows that the system are in heat transfer irreversibility. However, the Bejan number are increased after the $Gr = 10^4$.

Figure 7.11 displays the effects of various nanoparticle volume fraction on average Nusselt number and Bejan number with different velocity of rotating solid cylinder. For all nanoparticle volume fraction, the average Nusselt number is the lowest when the angular speed is close to zero. For a given angular velocity, it is observed that average Nusselt number is still high when $\phi = 0.04$. Average Nusselt number dependent on the rotational direction of the cylinder.

The contours of entropy generation do not show the relative dominance between the viscous and thermal effects. This issue can be addressed by using Bejan number. For all nanoparticle volume fraction, irreversibility are mainly due to fluid friction. The Bejan number are the highest for all nanoparticle volume fraction when there is no rotating cylinder involved. However, the Bejan number decays when the rotation of cylinder increase. Meanwhile, it is observed that only small different among all nanoparticle volume fraction except when $\phi = 0$ shows that the effect of nanoparticle to Bejan number is insignificant.

Figure 7.12 depicts the variants of average Nusselt number and Bejan number with the nanoparticle volume fraction for different Reynolds number . The average

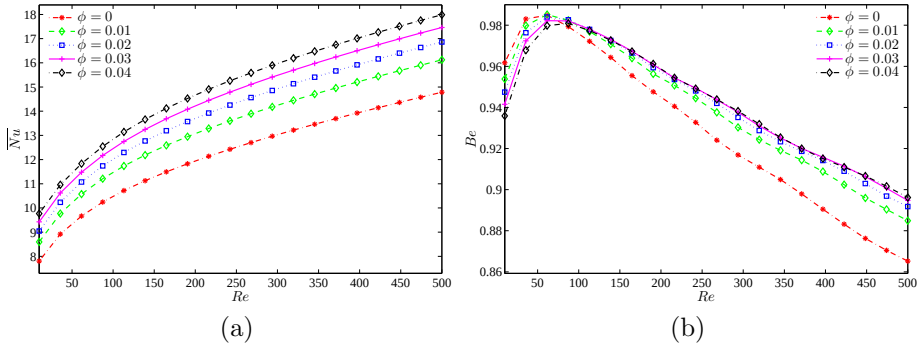

Figure 7.12 Variation of (a) average Nusselt number interfaces with X and (b) Bejan number with different nanoparticle volume fraction at $Ri = 1$, $Re = 100$, $\phi = 0.02$ and $D1$.

Nusselt number increase as Reynolds number increase. Higher nanoparticle volume fraction accelerate the average Nusselt number. Smaller Re, the Bejan number increase. After it reaches to Re=100, the Bejan number decays as the Reynolds number increase. As in average Nusselt number, higher nanoparticle volume fraction increase the Bejan number.

7.5 CONCLUSIONS

In this study, the finite element method was applied to analyse entropy generation and mixed convection in a triangular cavity with three rotating solid cylinder filled with Al_2O_3-water nanofluid. The detailed computational results for the streamlines, isotherms, and the local entropy generation for different values of Grashof number, Reynolds number, velocity of rotating cylinder. Some important conclusions from the study are given below.

1. Highest Gr influence the fluid flow and temperature distribution, fluid flow and temperature distribution increase at higher Gr. The fluid flow and temperature distribution, and local entropy generation increase at higher Gr number while local Average Nusselt number and Bejan number increase as Gr increase.
2. Existing of the rotating cylinder influence the entropy generation and flow and temperature fields. Increase the velocity of rotating cylinder increases the fluid

flow and temperature distribution as well as local entropy generation. Increase the velocity increase the average Nusselt number while decrease the Bejan number.

3. Higher nanoparticle volume fraction increase the average Nusselt number. Increase the velocity of rotating cylinder, Grashof and Reynolds number increase the average Nusselt number.

CHAPTER VIII

CONCLUSIONS AND RECOMMENDATIONS

8.1 CONCLUSIONS

Four problems of convection heat transfer has been studied in various enclosures with various inner solid. The objective of this thesis was to study the flow structures and temperature distributions as well as entropy generation under the effects of Rayleigh number, Richardson number, Reynolds number, thermal conductivity ratio, nanoparticle volume fraction, size of inner solid, source length and source position.

Geometric models chosen include square, triangular and trapezoidal enclosure with square and cylindrical inner solid that are differentially heated. It is assumed that the flows are laminar, non-Newtonian, two-dimensional, incompressible, and Newtonian. It is assumed that nanoparticles have a spherical shape. Following these presumptions and taking into account the environment, the pressure variable is eliminated, and the governing equations—the continuity equation, momentum equation, and energy equation—are nondimensionalized. The result is a set of nonlinear partial differential equations. The final equations were solved using two different approaches: one by the COMSOL finite element method and the other by a MATLAB finite difference method with an alternating direct implicit scheme and a tridiagonal matrix algorithm or Gaussian successive over-relaxation scheme.

Chapter IV considered numerically the natural convection of a nanofluid in a square enclosure with the effect of concentric solid insert and different temperature distribution using the FDM. It was found that the inner solid insertion tends to influence the flow behavior while the larger solid insert inhibits the convective heat transfer and

global entropy generation within the square cavity. Chapter V dealt with the partially heated square cavity filled with nanofluid and having a solid bottom wall to analyze the entropy generation and natural convection. It is found that the heat transfer rate is significantly enhanced by incrementing the solid wall thickness. Different values of the thermal conductivity ratio are shown to depict a variety of enhancements for the heat transfer rate.

Chapter VI numerically studied the the effect of various positions of the solid cylinder filled with nanofluid in the trapezoidal enclosure to analyze entropy generation and mixed convection. It is found that the distinct location of the solid cylinder appears to influence flow behavior, whereby temperature distribution and entropy generation are both affected.

Chapter VII dealt with the effect of three rotating solid cylinders in triangular enclosure with various temperature distribution with nanofluids where the finite difference method has been used to solve numerically. It is found that the movement of rotating cylinder influenced the entropy generation and temperature distribution.

The findings show that solid insert, thermal conductivity ratio and inner rotating cylinder significantly influence heat transfer and entropy generation. This knowledge can be applied to optimize heat industrial heat exchangers, refrigeration systems, and electronic cooling devices, ensuring maximum energy utilisation. The purpose of nanofluids in influencing heat transfer efficiency suggest potential advancements in cooling technologies for high-performance systems such as nuclear reactors, aerospace applications, and microelectronics cooling.

8.2 RECOMMENDATIONS FOR FUTURE WORK

In Chapter IV the effect of nanofluid on natural convection and entropy generation in a square enclosure with insertion inner solid was numerically considered. Obviously, the existence of inner solid influence the fluid and temperature fields. The future work may include the non-Newtonian fluids, three dimensional problems and non-uniform heating.

Chapter V presented the effect of finite wall thickness on entropy generation and natural convection in a partially heated square cavity. The future work may include non-Darcy effect in the formulation porous medium problem.

The effects of localised solid cylinder on entropy production and mixed convection in trapezoidal enclosure was numerically considered in Chapter VI. We reported the effects of non-uniform heating on the steady natural convection in a square enclosure partially-filled with nanofluid-saturated porous media in Chapter VI. Further studies may be conducted for other cases such as unsteady state flow, MHD effect and radiation. The heatline visualisation approach is worth looking into.

BIBLIOGRAPHY

Abu-Nada, E. & Chamkha, A.J. 2010. Mixed convection flow in a lid-driven inclined square enclosure filled with a nanofluid. *European Journal of Mechanics - B/Fluids* 29: 472 – 482.

Acheson, D.J. 1990. *Elementary Fluid Dynamics*. New York: Oxford University Press Inc.

Aghaei, A., Khorasanizadeh, H., Sheikhzadeh, G. & Abbaszadeh, M. 2016. Numerical study of magnetic field on mixed convection and entropy generation of nanofluid in a trapezoidal enclosure. *Journal of Magnetism and Magnetic Materials* 403: 133 – 145.

Akbarinia, A. & Behzadmehr, A. 2007. Numerical study of laminar mixed convection of a nanofluid in horizontal curved tubes. *Applied Thermal Engineering* 8: 1327 – 1337.

Al-Rashed, A.A., Kalidasan, K., Kolsi, L., Velkennedy, R., Aydi, A., Hussein, A.K. & Malekshah, E.H. 2018. Mixed convection and entropy generation in a nanofluid filled cubical open cavity with a central isothermal block. *International Journal of Mechanical Sciences* 135: 362–375.

Al-Rashed, A.A.A.A., Sheikhzadeh, G.A., Aghaei, A., Monfared, F., Shahsavar, A. & Afrand, M. 2020. Effect of a porous medium on flow and mixed convection heat transfer of nanofluids with variable properties in a trapezoidal enclosure. *Journal of Thermal Analysis and Calorimetry* 139: 741 – 754.

Alinia, M., Ganji, D. & Gorji-Bandpy, M. 2011. Numerical study of mixed convection in an inclined two sided lid driven cavity filled with nanofluid using two-phase mixture model. *International Communications in Heat and Mass Transfer* 38: 1428 – 1435.

Alloui, Z., Vasseur, P. & Reggio, M. 2011. Natural convection of nanofluids in a shallow cavity heated from below. *International Journal of Thermal Sciences* 50(3): 385–393.

Alnajem, M.H.S., Alsabery, A.I. & Hashim, I. 2019. Entropy generation and natural convection in a wavy-wall cavity filled with a nanofluid and containing an inner solid cylinder. *IOP Conference Series: Materials Science and Engineering* 518: 032044.

Alnaqi, A., Hussein, A., Kolsi, L., Al-Rashed, A., Li, D. & Ali, H. 2018. Computational study of natural convection and entropy generation in three-dimensional cavity with active lateral walls. *Thermal Science* 24: 346–346.

Alsabery, A., Chamkha, A., Saleh, H. & Hashim, I. 2017. Transient natural convective heat transfer in a trapezoidal cavity filled with non-newtonian nanofluid with sinusoidal boundary conditions on both sidewalls. *Powder Technology* 308: 214–234.

Alsabery, A., Chamkha, A., Saleh, H., Hashim, I. & Chanane, B. 2017b. Effect of spatial side-wall temperature variation on transient natural convection of a nanofluid in a trapezoidal cavity. *International Journal of Numerical Methods for Heat and Fluid Flow* 27(6): 1365–1384.

Alsabery, A., Ishak, M.S., Chamkha, A. & Hashim, I. 2018a. Entropy generation analysis and natural convection in a nanofluid-filled square cavity with a concentric solid insert and different temperature distributions. *Entropy* 20: 336.

Alsabery, A., Ismael, M., Chamkha, A. & Hashim, I. 2018b. Numerical investigation of mixed convection and entropy generation in a wavy-walled cavity filled with nanofluid and involving a rotating cylinder. *Entropy* 20: 664.

Alsabery, A., Sheremet, M., Chamkha, A. & Hashim, I. 2019. Impact of nonhomogeneous nanofluid model on transient mixed convection in a double lid-driven wavy cavity involving solid circular cylinder. *International Journal of Mechanical Sciences* 150: 637 – 655.

Alsabery, A., Siddheshwar, P., Saleh, H. & Hashim, I. 2016. Transient free convective heat transfer in nanoliquid-saturated porous square cavity with a concentric solid insert and sinusoidal boundary condition. *Superlattices and Microstructures* 100: 1006 – 1028.

Alsabery, A., Tayebi, T., Chamkha, A. & Hasim, I. 2018c. Effects of two-phase nanofluid model on natural convection in a square cavity in the presence of an adiabatic inner block and magnetic field. *International Journal of Numerical Methods for Heat and Fluid Flow* 28(7): 1613–1647.

Alsabery, A.I., Kadhim, H.T., Ismael, M.A., Hashim, I. & Chamkha, A.J. 2023. Impacts of amplitude and heat source on natural convection of hybrid nanofluids into a wavy enclosure via heatline approach. *Waves in Random and Complex Media* 33(4): 1060–1084.

Alsabery, A.I., Tayebi, T., Chamkha, A.J. & Hashim, I. 2018d. Effect of rotating solid cylinder on entropy generation and convective heat transfer in a wavy porous cavity heated from below. *International Communications in Heat and Mass Transfer* 95: 197–209.

Arani, A.A.A., Sebdani, S.M., Mahmoodi, M., Ardeshiri, A. & Aliakbari, M. 2012. Numerical study of mixed convection flow in a lid-driven cavity with sinusoidal heating on sidewalls using nanofluid. *Superlattices and Microstructures* 51: 893 – 911.

Arefmanesh, A., Aghaei, A. & Ehteram, H. 2016. Mixed convection heat transfer in a CuO–water filled trapezoidal enclosure, effects of various constant and variable properties of the nanofluid. *Applied Mathematical Modelling* 40: 815–831.

Astanina, M.S., Sheremet, M.A., Oztop, H.F. & Abu-Hamdeh, N. 2018. Mixed convection of Al_2O_3 water nanofluid in a lid-driven cavity having two porous layers. *International Journal of Heat and Mass Transfer* 118: 527 – 537.

Baytas, A. & Pop, I. 2002. Free convection in a square porous cavity using a thermal nonequilibrium model. *International Journal of Thermal Sciences* 41(9): 861–870.

Bejan, A. 2013. *Convection Heat Transfer*. Canada: John Wiley and Son Inc.

Bergman, T.L., Incropera, F.P., Lavine, A.S. & Dewitt, D.P. 2011. *Introduction to Heat Transfer*. Hoboken: New York: Wiley.

Bhattacharya, M., Basak, T., Oztop, H.F. & Varol, Y. 2013. Mixed convection and role of multiple solutions in lid-driven trapezoidal enclosures. *International Journal of Heat and Mass Transfer* 63: 366 – 388.

Billah, M., Rahman, M., Sharif, U.M., Rahim, N., Saidur, R. & Hasanuzzaman, M. 2011. Numerical analysis of fluid flow due to mixed convection in a lid-driven cavity having a heated circular hollow cylinder. *International Communications in Heat and Mass Transfer* 38: 1093 – 1103.

Bouchoucha, A., Bessaïh, R., Öztop, H., Al-Salem, K. & Bayrak, F. 2017. Natural convection and entropy generation in a nanofluid filled cavity with thick bottom wall: Effects of non-isothermal heating. *International Journal of Mechanical Sciences* 126: 95–105.

Calcagni, B., Marsili, F. & Paroncini, M. 2005. Natural convective heat transfer in square enclosures heated from below. *Applied Thermal Engineering* 25(16): 2522–2531.

Chamkha, A.J. & Abu-Nada, E. 2012. Mixed convection flow in single- and double-lid driven square cavities filled with water–Al_2O_3 nanofluid: Effect of viscosity models. *European Journal of Mechanics - B/Fluids* 36: 82 – 96.

Chamkha, A.J. & Ismael, M.A. 2016. Magnetic field effect on mixed convection in lid-driven trapezoidal cavities filled with a Cu-water nanofluid with an aiding or opposing side wall. *Journal of Thermal Science and Engineering Applications* 8(3): 31009–31021.

Chatterjee, D., Gupta, S.K. & Mondal, B. 2014. Mixed convective transport in a lid-driven cavity containing a nanofluid and a rotating circular cylinder at the center. *International Communications in Heat and Mass Transfer* 56: 71 – 78.

Chen, W.R. 2010. Natural convection heat transfer between inner sphere and outer vertically eccentric cylinder. *International Journal of Heat and Mass Transfer* 53(23): 5147–5155.

Cherif, B.M., Abderrahmane, A., Saeed, A.M., Qasem, N.A.A., Younis, O., Marzouki, R., Chung, J.D. & Shah, N.A. 2022. Hydrothermal and entropy investigation of nanofluid mixed convection in triangular cavity with wavy boundary heated from below and rotating cylinders. *Nanomaterials* 12(9): 1469.

Choi, S.U.S. & Eastman, J.A. 1995. Enhancing thermal conductivity of fluids with nanoparticles. *International mechanical engineering congress and exhibition*. Argonne National Lab. (ANL), Argonne, IL (United States).

Chon, C.H., Kihm, K.D., Lee, S.P. & Choi, S.U. 2005. Empirical correlation finding the role of temperature and particle size for nanofluid (Al_2O_3) thermal conductivity enhancement. *Applied Physics Letters* 87(15): 3107.

Corcione, M. 2011. Empirical correlating equations for predicting the effective thermal conductivity and dynamic viscosity of nanofluids. *Energy Conversion and Management* 52(1): 789–793.

Corcione, M., Cianfrini, M. & Quintino, A. 2013. Two-phase mixture modeling of natural convection of nanofluids with temperature-dependent properties. *International Journal of Thermal Sciences* 71: 182–195.

Dutta, S., Bhattacharyya, S. & Pop, I. 2022. Heat transfer enhancement compared to entropy generation by imposing magnetic field and hybrid nanoparticles in mixed convection of a Bingham plastic fluid in a ventilated enclosure. *International Journal of Numerical Methods for Heat & Fluid Flow* 32(9).

Ghasemi, B. & Aminossadati, S. 2010. Mixed convection in a lid-driven triangular enclosure filled with nanofluids. *International Communications in Heat and Mass Transfer* 37(8): 1142–1148.

Ghasemi, K. & Siavashi, M. 2017. Lattice Boltzmann numerical simulation and entropy generation analysis of natural convection of nanofluid in a porous cavity with different linear temperature distributions on side walls. *Journal of Molecular Liquids* 233: 415–430.

Gibanov, N.S., Sheremet, M.A., Oztop, H.F. & Abu-Hamdeh, N. 2018. Mixed convection with entropy generation of nanofluid in a lid-driven cavity under the effects of a heat-conducting solid wall and vertical temperature gradient. *European Journal of Mechanics - B/Fluids* 70: 148 – 159.

Goodarzi, M., Safaei, M., Vafai, K., Ahmadi, G., Dahari, M., Kazi, S. & Jomhari, N. 2014. Investigation of nanofluid mixed convection in a shallow cavity using a two-phase mixture model. *International Journal of Thermal Sciences* 75: 204 – 220.

Hashim, I., Alsabery, A., Sheremet, M. & Chamkha, A. 2019. Numerical investigation of natural convection of Al_2O_3-water nanofluid in a wavy cavity with conductive inner block using Buongiorno's two-phase model. *Advanced Powder Technology* 30(2): 399–414.

Hasib, M.H., Hossen, M.S. & Saha, S. 2015. Effect of tilt angle on pure mixed convection flow in trapezoidal cavities filled with water-Al_2O_3 nanofluid. *Procedia Engineering* 105: 388 – 397.

Hassen, W., Selimefendigil, F., Ben, K.N., Kolsi, L., Borjini, M.N. & Alresheedi, F. 2021. Control of magnetohydrodynamic mixed convection and entropy generation in a porous cavity by using double rotating cylinders and curved partition. *ACS Omega* 6(51): 35607–35618.

Hatami, M. 2017. Nanoparticles migration around the heated cylinder during the RSM optimization of a wavy-wall enclosure. *Advanced Powder Technology* 28(3): 890–899.

Ho, C., Liu, W., Chang, Y. & Lin, C. 2010. Natural convection heat transfer of alumina-water nanofluid in vertical square enclosures: An experimental study. *International Journal of Thermal Sciences* 49(8): 1345–1353.

House, J.M., Beckermann, C. & Smith, T.F. 1990. Effect of a centered conducting body on natural convection heat transfer in an enclosure. *Numerical Heat Transfer, Part A: Applications* 18(2): 213–225.

Hussain, S.M., Parveen, R., Katbar, N.M., Rehman, S., Abd-Elmonem, A., Abdalla, N.S.E., Ahmad, H., Qureshi, M.A., Jamshed, W., Amjad, A. & Ibrahim, R.W. 2024. Entropy generation analysis of MHD convection flow of hybrid nanofluid in a wavy enclosure with heat generation and thermal radiation. *Reviews on Advanced Materials Science* 63(1).

Hussein, A.K. 2018. Entropy generation due to the transient mixed convection in a three-dimensional right-angle triangular cavity. *International Journal of Mechanical Sciences* 146-147: 141–151.

Ilis, G.G., Mobedi, M. & Sunden, B. 2008. Effect of aspect ratio on entropy generation in a rectangular cavity with differentially heated vertical walls. *International Communications in Heat and Mass Transfer* 35(6): 696–703.

Ismael, M.A., Armaghani, T. & Chamkha, A.J. 2016. Conjugate heat transfer and entropy generation in a cavity filled with a nanofluid-saturated porous media and heated by a triangular solid. *Journal of the Taiwan Institute of Chemical Engineers* 59: 138–151.

Jabbar, M., Yassoub, S., Hamzah, H. & Ali, F. 2019. Heat and entropy lines visualization of natural convection between hot inner circular cylinder and cold outer sinusoidal cylinder. *International Journal of Heat and Technology* 37(4): 1151–1162.

Jiang, X., Hatami, M., Abderrahmane, A., Younis, O., Makhdoum, B.M. & Guedri, K. 2023. Mixed convection heat transfer and entropy generation of mhd hybrid nanofluid in a cubic porous cavity with wavy wall and rotating cylinders. *Applied Thermal Engineering* 226: 120302.

Jou, R.Y. & Tzeng, S.C. 2006. Numerical research of nature convective heat transfer enhancement filled with nanofluids in rectangular enclosures. *International Communications in Heat and Mass Transfer* 33(6): 727–736.

Kaluri, R. & Basak, T. 2011. Role of entropy generation on thermal management during natural convection in porous square cavities with distributed heat sources. *Chemical Engineering Science* 66: 2124–2140.

Kareem, A.K., Mohammed, H., Hussein, A.K. & Gao, S. 2016. Numerical investigation of mixed convection heat transfer of nanofluids in a lid-driven trapezoidal cavity. *International Communications in Heat and Mass Transfer* 77: 195 – 205.

Kefayati, G. 2016. Heat transfer and entropy generation of natural convection on non-Newtonian nanofluids in a porous cavity. *Powder Technology* 299: 127–149.

Khan, Z.H., Usman, M., Khan, W.A., Hamid, M. & Haq, R.U. 2022. Thermal treatment inside a partially heated triangular cavity filled with casson fluid with an inner cylindrical obstacle via fem approach. *The European Physical Journal Special Topics volume* 231: 2683–2694.

Khanafer, K. & Aithal, S. 2013. Laminar mixed convection flow and heat transfer characteristics in a lid driven cavity with a circular cylinder. *International Journal of Heat and Mass Transfer* 66: 200–209.

Khanafer, K., Vafai, K. & Lightstone, M. 2003. Buoyancy-driven heat transfer enhancement in a two-dimensional enclosure utilizing nanofluids. *International Journal of Heat and Mass Transfer* 46(19): 3639–3653.

Khorasanizadeh, H., Nikfar, M. & Amanip, J. 2013. Entropy generation of cu–water nanofluid mixed convection in a cavity. *European Journal of Mechanics - B/Fluids* 37: 143 – 152.

Kolsi, L., Mahian, O., Öztop, H.F., Aich, W., Borjini, M.N., Abu-Hamdeh, N. & Aissia, H.B. 2016. 3D buoyancy-induced flow and entropy generation of nanofluid-filled open cavities having adiabatic diamond shaped obstacles. *Entropy* 18(6): 232.

Lam, P. & Prakash, K. 2014. A numerical study on natural convection and entropy generation in a porous enclosure with heat sources. *International Journal of Heat and Mass Transfer* 69: 390–407.

Liao, C.C. & Lin, C.A. 2014. Mixed convection of a heated rotating cylinder in a square enclosure. *International Journal of Heat and Mass Transfer* 72: 9 – 22.

Long, G. & Xu, G. 2017. The effects of perforation erosion on practical hydraulic-fracturing applications. *SPE Journal* 22: 645–659.

Mahapatra, P.S., De, S., Ghosh, K., Manna, N.K. & Mukhopadhyay, A. 2013. Heat transfer enhancement and entropy generation in a square enclosure in the presence of adiabatic and isothermal blocks. *Numerical Heat Transfer, Part A: Applications* 64(7): 577–596.

Mahmoodi, M. & Sebdani, S.M. 2012. Natural convection in a square cavity containing a nanofluid and an adiabatic square block at the center. *Superlattices and Microstructures* 52(2): 261 – 275.

Majdi, H., Abed, A. & Habeeb, L. 2020. Mixed convection heat transfer of CuO-H_2O nanofluid in a triangular lid-driven cavity with circular inner body. *Journal of Mechanical Engineering Research and Developments* 44: 164–175.

Man, Y.H., Mi, J.J. & Young, S.K. 1999. Numerical study on transient heat transfer and fluid flow of natural convection in an enclosure with a heat-generating conducting body. *Numerical Heat Transfer, Part A: Applications* 35(4): 415–433.

Maneengam, A., Bouzennada, T., Abderrahmane, A., Ghachem, K., Kolsi, L., Younis, O., Guedri, K. & Weera, W. 2022. Numerical study of 3D MHD mixed convection and entropy generation in trapezoidal porous enclosure filled with a hybrid nanofluid: Effect of zigzag wall and spinning inner cylinder. *Nanomaterials* 12(12).

Manna, N., Biswas, N., Mandal, D.K., Sarkar, U.K., Öztop, F.H. & Nidal, H.A. 2022. Impacts of heater-cooler position and lorentz force on heat transfer and entropy generation of hybrid nanofluid convection in quarter-circular cavity. *International Journal of Numerical Methods for Heat and Fluid Flow* 33(3): 1249–1286.

Mehmood, K., Hussain, S. & Sagheer, M. 2017. Mixed convection in alumina-water nanofluid filled lid-driven square cavity with an isothermally heated square blockage inside with magnetic field effect: Introduction. *International Journal of Heat and Mass Transfer* 109: 397 – 409.

Mezrhab, A., Bouali, H., Amaoui, H. & Bouzidi, M. 2006. Computation of combined natural-convection and radiation heat-transfer in a cavity having a square body at its center. *Applied Energy* 83(9): 1004–1023.

Mobedi, M. 2008. Conjugate natural convection in a square cavity with finite thickness horizontal walls. *International Communications in Heat and Mass Transfer* 35(4): 503–513.

Monisha, R., Basak, T., Roy, S. & Pop, I. 2015. Analysis of entropy generation for mixed convection in a square cavity for various thermal boundary conditions. *Numerical Heat Transfer, Part A: Applications* 68(1): 44–74.

Nasrin, R. & Parvin, S. 2012. Investigation of buoyancy-driven flow and heat transfer in a trapezoidal cavity filled with water-Cu nanofluid. *International Communications in Heat and Mass Transfer* 39(2): 270–274.

Nayak, R., Bhattacharyya, S. & Pop, I. 2016. Numerical study on mixed convection and entropy generation of a nanofluid in a lid-driven square enclosure. *Journal of Heat Transfer* 138(1): 12503–12514.

Nguyen, C., Desgranges, F., Roy, G., Galanis, N., Mare, T., Boucher, S. & Mintsa, H. 2007. Temperature and particle-size dependent viscosity data for water-based nanofluids – hysteresis phenomenon. *International Journal of Heat and Fluid Flow* 28: 1492–1506.

Oosthuizen, P.H. & Naylor, D. 1999. *An Introduction to Convection Heat Transfer Analysis*. Singapore: McGraw–Hill.

Pepper, D.W. & Heinrich, J. 2017. *The Finite Element Method: Basic Concepts and Applications with MATLAB, MAPLE, and COMSOL.* Boca Raton: CRC Press.

Probert, S. & Thirst, T. 1977. Thermal insulation provided by triangular sectioned attic spaces. *Applied Energy* 3(1): 41–50.

Rahimi, A., Kasaeipoor, A., Malekshah, E., Palizian, M. & Kolsi, L. 2018. Lattice Boltzmann numerical method for natural convection and entropy generation in cavity with refrigerant body filled with DWCNTs-water nanofluid-experimental thermo-physical propertiesl. *Journal of Thermal Science and Engineering Progress* 5: 372–387.

Rahman, M., Alim, M.A., Saha, S. & Chowdhury, M. 2008. Mixed convection in a vented square cavity with a heat conducting horizontal solid circular cylinder. *Journal of Naval Architecture and Marine Engineering* 5: 37–46.

Rahman, M.M. & Alim, M. 2010. MHD mixed convection flow in a vertical lid-driven square enclosure including a heat conducting horizontal circular cylinder with joule heating. *Nonlinear Analysis: Modelling and Control* 15: 199 – 211.

Rahman, M.M., Alim, M. & Mamun, M.A.H. 2009. Finite element analysis of mixed convection in a rectangular cavity with a heat-conducting horizontal circular cylinder. *Nonlinear Analysis: Modelling and Control* 14: 217 – 247.

Rashid, U., Lu, D. & Iqbal, Q. 2023. Nanoparticles impacts on natural convection nanofluid flow and heat transfer inside a square cavity with fixed a circular obstacle. *Case Studies in Thermal Engineering* 44: 102829.

Roslan, R., Saleh, H. & Hashim, I. 2011. Buoyancy-driven heat transfer in nanofluid-filled trapezoidal enclosure with variable thermal conductivity and viscosity. *Numerical Heat Transfer* Part A: Applications: 867–882.

Roy, M., Biswal, P., Roy, S. & Basak, T. 2017. Heat flow visualization during mixed convection within entrapped porous triangular cavities with moving horizontal walls via heatline analysis. *International Journal of Heat and Mass Transfer* 108: 468–489.

Roy, N. 2022. MHD natural convection of a hybrid nanofluid in an enclosure with multiple heat sources. *Alexandria Engineering Journal* 61(2): 1679–1694.

Salah, T., Mansour, M., Gorla, R., Siddiqa, S. & Rashad, A. 2021. Unsteady MHD natural convection flow of a nanofluid inside an inclined square cavity containing a heated circular obstacle. *International Journal of Nonlinear Sciences and Numerical Simulation* 24.

Santra, A.K., Sen, S. & Chakraborty, N. 2008. Study of heat transfer augmentation in a differentially heated square cavity using Cu–water nanofluid. *International Journal of Thermal Sciences* 47(9): 1113–1122.

Sebdani, S.M., Mahmoodi, M. & Hashemi, S.M. 2012. Effect of nanofluid variable properties on mixed convection in a square cavity. *International Journal of Thermal Sciences* 52: 112 – 126.

Selimefendigil, F., Chouikhi, H. & Oztop, H.F. 2023. Natural convection and entropy generation of hybrid nanofluid in double annulus separated by a thin rotating partition under magnetic field. *Journal of Magnetism and Magnetic Materials* 582: 170974.

Selimefendigil, F. & Öztop, H.F. 2017. Mixed convection in a partially heated triangular cavity filled with nanofluid having a partially flexible wall and internal heat generation. *Journal of the Taiwan Institute of Chemical Engineers* 70: 168–178.

Selimefendigil, F. & Öztop, H.F. 2018. Modeling and optimization of MHD mixed convection in a lid-driven trapezoidal cavity filled with alumina–water nanofluid: Effects of electrical conductivity models. *International Journal of Mechanical Sciences* 136: 264 – 278.

Selimefendigil, F., Öztop, H.F. & Chamkha, A.J. 2017. Analysis of mixed convection of nanofluid in a 3D lid-driven trapezoidal cavity with flexible side surfaces and inner cylinder. *International Communications in Heat and Mass Transfer* 87: 40 – 51.

Shahid, H., Yaqoob, I., Khan, W.A. & Rafique, A. 2021. Mixed convection in an isosceles right triangular lid driven cavity using multi relaxation time Lattice Boltzmann method. *International Communications in Heat and Mass Transfer* 128: 105552.

Shariat, M., Akbarinia, A., Nezhad, A.H., Behzadmehr, A. & Laur, R. 2011. Numerical study of two phase laminar mixed convection nanofluid in elliptic ducts. *Applied Thermal Engineering* 31: 2348 – 2359.

Shariat, M., Akbarinia, A., Nezhad, A.H., Behzadmehr, A. & Laur, R. 2014. MHD mixed convection of nanofluid filled partially heated triangular enclosure with a rotating adiabatic cylinder. *Journal of the Taiwan Institute of Chemical Engineers* 45: 2150 – 2162.

Sheremet, M., Öztop, H., Pop, I. & Abu-Hamdeh, N. 2015. Analysis of entropy generation in natural convection of nanofluid inside a square cavity having hot solid block: Tiwari and Das' model. *Entropy* 18: 9.

Siahchehrehghadikolaei, S., Gholinia, M., Ghadikolaei, S.S. & Lin, C.X. 2022. A CFD modeling of CPU cooling by eco-friendly nanofluid and fin heat sink passive cooling techniques. *Advanced Powder Technology* 33(11): 103813.

Soomro, F.A., Haq, R.U., Algehyne, E.A. & Tlili, I. 2020. Thermal performance due to magnetohydrodynamics mixed convection flow in a triangular cavity with circular obstacle. *Journal of Energy Storage* 31: 101702.

T. Javed, Z. Mehmood, I.P. 2017. MHD-mixed convection flow in a lid-driven trapezoidal cavity under uniformly/non-uniformly heated bottom wall. *International Journal of Numerical Methods for Heat & Fluid* 27: 1231–1248.

Tasnim, S., Mitra, A., Saha, H., Quamrul, M. & Saha, S. 2023. MHD conjugate natural convection and entropy generation of a nanofluid filled square enclosure with multiple heat-generating elements in the presence of joule heating. *Results in Engineering* 17: 100993.

Thirst, T. & Probert, S. 1978. Heat transfer versus pitch angle for nonventilated, triangular-sectioned, apex-upward air-filled spaces. *Thermal transmission measurements of insulation*. ASTM International.

Tmartnhad, I., El Alami, M., Najam, M. & Oubarra, A. 2008. Numerical investigation on mixed convection flow in a trapezoidal cavity heated from below. *Energy Conversion and Management* 49(11): 3205 – 3210.

Wang, Y., Xu, X., Tian, T., Fan, L., Wang, W.l. & Yu, Z.t. 2015. Laminar mixed convection heat transfer of SiC-EG nanofluids in a triangular enclosure with a rotating inner cylinder: simulations based on the measured thermal conductivity and viscosity. *Journal of Zhejiang University Science A* 16: 478–490.

Xiao, B., Chen, H., Xiao, S. & Cai, J. 2017a. Research on relative permeability of nanofibers with capillary pressure effect by means of Fractal-Monte Carlo technique. *Journal of Nanoscience and Nanotechnology* 17: 6811–6817.

Xiao, B., Wang, W., Fan, J., Chen, H., Hu, X., Zhao, D., Zhang, X. & Ren, W. 2017b. Optimization of the fractal-like architecture of porous fibrous materials related to permeability, diffusivity and thermal conductivity. *Fractals* 25: 1750030.

Xiao, B., Zhang, X., Wang, W., Long, G., Chen, H., Kang, H. & Ren, W. 2018. A fractal

model for water flow through unsaturated porous rocks. *Fractals* 26: 1840015.

Xiong, P.Y., Hamid, A., Iqbal, K., Irfan, M. & Khan, M. 2021. Numerical simulation of mixed convection flow and heat transfer in the lid-driven triangular cavity with different obstacle configurations. *International Communications in Heat and Mass Transfer* 123: 105202.

Yu, Z.T., Xu, X., Hu, Y.C., Fan, L.W. & Cen, K.F. 2010. Transient natural convective heat transfer of a low-Prandtl-number fluid inside a horizontal circular cylinder with an inner coaxial triangular cylinder. *International Journal of Heat and Mass Transfer* 53(23): 5102–5110.

Çiçek, O., Baytaş, A.F. & Baytaş, A.C. 2024. Entropy generation minimization of hybrid nanofluid mixed convection flow in lid-driven square enclosure with heat-generating porous layer on inner walls. *International Journal of Numerical Methods for Heat & Fluid Flow* 34(2).

Öztop, H.F., Estellé, P., Yan, W.M., Al-Salem, K., Orfi, J. & Mahian, O. 2015. A brief review of natural convection in enclosures under localized heating with and without nanofluids. *International Communications in Heat and Mass Transfer* 60: 37–44.

APPENDIX A

LIST OF PUBLICATIONS

Journals:

1. Alsabery, A.I., Ishak, M.S., Chamkha, A.J., & Hashim, I. 2018. Entropy generation analysis and natural convection in a nanofluid-filled square cavity with a concentric solid insert and different temperature distributions. Entropy, 20(5): (Accepted) (MDPI, ISSN 1099–4300, 2018 Impact Factor: 2.7), ISI, Q2.
2. Ishak, M.S., Alsabery, A.I., Chamkha, A.J., & Hashim, I. 2019. Effect of finite wall thickness on entropy generation and natural convection in a nanofluid-filled partially heated square cavity. International Journal of Numerical Methods for Heat and Fluid Flow, 30(3):(Accepted) (Emerald Publishing LTD, ISSN 0961–5539, 2020 Impact Factor: 4.2), ISI, Q1.
3. Ishak, M.S., Alsabery, A.I., Hashim, I., & Chamkha, A.J. 2021. Entropy production and mixed convection within trapezoidal cavity having nanofluids and localised solid cylinder. Scientific Reports, 100: 001-022 (Nature Portfolio, ISSN 2045–2322, 2021 Impact Factor: 4.6), ISI, Q1.